

COMBUSTION AND ATOMIZATION STUDIES OF  
COAL-WATER FUEL IN A LAMINAR FLOW REACTOR AND  
IN A PILOT-SCALE FURNACE

by

SHIN-WON KANG

B.S., Mechanical Engineering  
Seoul National University  
(1979)

S.M., Mechanical Engineering  
Massachusetts Institute of Technology  
(1984)

SUBMITTED TO THE DEPARTMENT OF MECHANICAL ENGINEERING  
IN PARTIAL FULFILLMENT OF THE REQUIREMENTS FOR THE  
DEGREE OF

DOCTOR OF PHILOSOPHY

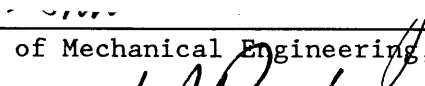
at the

MASSACHUSETTS INSTITUTE OF TECHNOLOGY

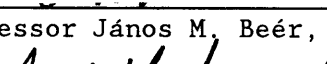
December 1987

© Massachusetts Institute of Technology

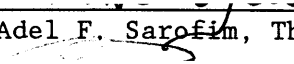
Signature of Author

  
Department of Mechanical Engineering, December 1987


Certified by

  
Professor János M. Beér, Thesis Supervisor

Certified by

  
Professor Adel F. Sarofim, Thesis Supervisor

Accepted by

  
Professor Ain A. Sonin  
Chairman, Departmental Committee on Graduate Students  
Department of Mechanical Engineering

MASSACHUSETTS INSTITUTE  
OF TECHNOLOGY

MAR 18 1988

LIBRARIES Archives

Vol. 1

COMBUSTION AND ATOMIZATION STUDIES OF  
COAL-WATER FUEL IN A LAMINAR FLOW REACTOR AND  
IN A PILOT-SCALE FURNACE

by

SHIN-WON KANG

Submitted to the Department of Mechanical Engineering  
in December 1987 in partial fulfillment of the  
requirements for the Degree of Doctor of Philosophy in  
Mechanical Engineering

ABSTRACT

The thesis is composed of two separate but related topics which are discussed separately in Part 1 and Part 2.

PART 1: "Fundamental Study of Coal-Water Fuel Droplet Combustion  
in a Laminar Flow Reactor"

The processes of devolatilization and char burnout were studied in a laminar flow reactor (LFR) by two experimental procedures. In the first of these, a coal-water fuel (CWF) droplet generator was developed and used to feed CWF droplets directly into the LFR. The CWF droplet generator, which consisted of a twin-fluid, internally mixed atomizer and a series of skimmers to reduce the feed rate of CWF droplets into the LFR, was capable of producing CWF droplets in the size range of 5-500 micrometers at feed rates of less than 3 mg/sec.

In the second parallel study, solid samples withdrawn from a CWF spray flame, close to the atomizing nozzle, were size graded and fed into the LFR in low particle concentrations. Their combustion history in the LFR was determined by the use of high-speed cinematography and by monitoring the intensity of radiation emitted by individual CWF agglomerate during combustion (by fiber optic radiometry).

The Part 1 study has established the importance of rotation induced by the volatile evolution on the breakup of coal-aggregates and the release of ash particles. The centrifugal force due to particle rotation promotes the separation of both weakly adhering coal particles and char fragments during devolatilization and char burnout.

The results show that there is competition between centrifugal force which favors the breakup of coal-aggregates and adhesive force between coal particles during the plastic stage of coal pyrolysis. Based upon the theoretical model of agglomeration, the adhesive force on the process

of coalescence of coal particles is strongly dependent on the duration of the plasticity of coal particles. It is also found that rapid heating reduces the tendency of coal particles to form aggregates during the CWF droplet evaporation. Therefore, whether coal particles burn individually or as aggregates can be influenced by the time-temperature history of the CWF agglomerate and hence by burner design.

PART 2: "(Flash-) Atomization and Combustion Studies of Coal-Water Fuel in a Spray Test Facility and in a Pilot-Scale Furnace"

During CWF droplet combustion, coal particles tend to agglomerate within CWF droplets. Hence, the resulting coal particle size distribution (p.s.d.) is determined more by the p.s.d. of the atomized fuel spray than by the initial p.s.d. of the coal particles. Therefore, the atomization quality, (i.e., fineness of CWF spray droplets), is considered to be the most important variable affecting the combustion quality of CWF combustion including: ignition, carbon burnout, and the resultant fly-ash particle size.

In the Part 2 study, the atomization quality of CWF was investigated in a Spray Test Facility (STF) equipped with a laser diffraction spray analyzer. A capillary viscometer was also developed to measure a viscosity of CWF at high shear rate. The viscosity of CWF was found to be dependent upon shear rate (i.e., non-Newtonian fluid), and the atomization quality of CWF was correlated with rheological properties of CWF.

Convective tube bank erosion due to impaction of fly-ash particles could be reduced if the fly-ash particles were sufficiently small; such particles would follow the gas streamlines around tubes rather than impact on them. A finer p.s.d. of CWF droplets, and thus, a finer fly-ash p.s.d. could be obtained by the use of fuel treatments which induced flash-atomization.

The theoretical models of CWF flash-atomization and spray angle change due to flash-atomization were also developed and discussed. The experimental results of CWF flash-atomization in the STF and in a pilot-scale furnace show that a thermally assisted atomization of CWF significantly improves the quality of CWF droplets p.s.d., and thereby, flame stability, carbon conversion efficiency, and reduction of fly-ash p.s.d.

Thesis Supervisors:

János M. Beér, Professor of Chemical and Fuel Engineering  
Adel F. Sarofim, Professor of Chemical Engineering

*DEDICATION*

*This thesis is dedicated to my parents, my grandmother,  
my daughter So-Yeun (Janet R.) and my wife Kyung-Hee.*

## ACKNOWLEDGEMENTS

I would like to express my deepest appreciation to Professor János M. Beér, who introduced me to the field of combustion, and to Professor Adel F. Sarofim, my co-supervisor. During my doctoral program at M.I.T. they supported and guided me enthusiastically through many difficult times and were always accessible and patient.

I would also like to thank Professor Peter Griffith for being the chairman of my thesis committee. As thesis supervisor of my master program and as chairman of my doctoral thesis committee, Professor Griffith was a vital resource for me during my stay at M.I.T.

I am also deeply grateful to Dr. T.-U. Yu, Dr. D. Froelich, Dr. J.D. Teare, Dr. S.-C. Rah, Mr. L.D. Timothy, Mr. D.B. Jones, Dr. M.A. Toqan, Dr. S. Srinivasachar, and Dr. P.M. Walsh for their valuable discussions and help throughout my research.

My younger brother, Shin-Gyoo Kang, who is a doctoral student in the Department of Chemical Engineering at M.I.T., made himself indispensable to me both in the computer work and in the laboratory.

I also extend my deepest appreciation to Mr. P. Dozois and Mr. F. Woodworth in the Nuclear Machine Shop for their great help in making the apparatus, and to the technical staffs, Mr. D.E. Bash, Mr. W.T. Mason, and Mr. M.A. James for their continuous help in the experimental work in the M.I.T. Combustion Research Facility. My special thanks go to Ms. B. Caputo for typing the thesis manuscript with patience.

Financial support of this research work from the U.S. Department of Energy under Grant Number DE-FG22-84PC70268 is gratefully acknowledged.

Finally, I wish to thank my family, my family-in-law, and my wife Kyung-Hee for their infinite love and support.

## TABLE OF CONTENTS

	<u>Page</u>
ABSTRACT .....	2
ACKNOWLEDGEMENTS .....	5
TABLE OF CONTENTS .....	6
Part 1: "Fundamental Study of Coal-Water Fuel Droplet Combustion in a Laminar Flow Reactor" .....	12
LIST OF FIGURES .....	13
LIST OF TABLES .....	18
NOMENCLATURE .....	19
CHAPTER 1. INTRODUCTION .....	26
1.1 Introduction .....	26
1.2 Objectives of Investigation .....	28
CHAPTER 2. EXPERIMENTAL INVESTIGATION .....	30
2.1 Introduction .....	30
2.2 Experimental Apparatus for CWF Droplet Injection .....	30
2.2.1 CWF Droplet Generator .....	33
2.2.2 Atomizer .....	36
2.2.3 Laminar Flow Reactor .....	40
2.2.4 Feeding Probe .....	43
2.2.5 Sample Collection Probe .....	46
2.2.6 Fuel Supply Tank .....	46
2.2.7 Photographic Recording System .....	46
2.3 Experimental Apparatus for CWF Agglomerate Injection.....	47
2.3.1 Laminar Flow Reactor .....	47

2.3.2	Solid-Sample Feeding System .....	50
2.3.3	Collection Probe .....	50
2.3.4	Fiber Optic Radiometer .....	53
CHAPTER 3. EXPERIMENTAL OBSERVATIONS OF CWF DROPLET COMBUSTION ...		54
3.1	Introduction .....	54
3.2	Ignition .....	58
3.3	Volatile Combustion .....	58
3.4	Particle Rotation .....	60
3.5	Ignition of Char .....	63
3.6	Char Burnout .....	65
3.7	Fragmentation .....	65
CHAPTER 4. THEORETICAL MODELS .....		70
4.1	Model of Particle Rotation .....	70
4.1.1	Introduction .....	70
4.1.2	Derivation of Angular Velocity of Rotating CWF Agglomerate .....	70
4.1.3	Angular Velocity of Rotating CWF Agglomerate for an Isothermal Devolatilization Process .....	77
4.1.4	Geometrical Factor of Devolatilization Pores .....	79
4.1.5	Centrifugal Force Induced by Particle Rotation .....	93
4.2	Model of Particle Agglomeration.....	95
4.2.1	Introduction .....	95
4.2.2	Plasticity of Bituminous Coal .....	95
4.2.3	Contact Area during Particle Agglomeration .....	100
4.2.4	Adhesive Force during Particle Agglomeration .....	103
4.2.4.1	Surface Tension Force .....	103

4.2.4.2	Adhesive Force due to Coke Interconnection	103
4.2.4.3	Adhesive Force during Particle Agglomeration	107
4.3	Time-Temperature History of CWF Agglomerate	107
4.3.1	Introduction	107
4.3.2	Particle Heating Rate in Pre-Evaporation Stage	108
4.3.3	Particle Heating Rate in Evaporation Stage	111
4.3.4	Particle Heating Rate in Heat-Up Stage	112
4.3.5	Particle Heating Rate during Devolatilization	113
4.3.6	Particle Heating Rate during Char Burnout	117
CHAPTER 5.	RESULTS AND DISCUSSIONS	121
5.1	Particle Rotation	121
5.1.1	Model Predictions of Particle Rotation	121
5.1.2	Results of Statistical Study of Particle Rotation	128
5.2	Adhesive Force during Particle Agglomeration	135
5.3	Comparison of Centrifugal Force with Adhesive Force	143
CHAPTER 6.	CONCLUSIONS	146
REFERENCES		148
APPENDICES		151
APPENDIX A	GEOMETRICAL FACTOR OF DEVOLATILIZATION PORES WITH GAVALAS' PORE MODEL	152
A.1	Derivation of Geometrical Factor	152
A.2	Application of Gavalas' Model to Geometrical Factor	158
APPENDIX B	TEST RESULTS OF ATOMIZER	162



APPENDIX C	COMPUTER PROGRAMS	.....	164
C.1	Computer Program for Model of Particle Rotation	.....	164
C.2	Computer Program for Model of Particle Agglomeration	.....	166
C.3	Computer Program for Calculation of Geometrical Factor	....	172
Part 2:	"(Flash-) Atomization and Combustion Studies of Coal-Water Fuel in a Spray Test Facility and in a Pilot-Scale Furnace"	.....	173
TABLE OF CONTENTS	.....		174
LIST OF FIGURES	.....		177
LIST OF TABLES	.....		181
NOMENCLATURE	.....		182
CHAPTER 1.	INTRODUCTION	.....	185
1.1	Introduction	.....	185
1.2	Objectives of Investigation	.....	186
CHAPTER 2.	EXPERIMENTAL INVESTIGATION	.....	187
2.1	Experimental Apparatus for CWF Atomization Study	.....	187
2.1.1	Spray Test Facility	.....	187
2.1.2	Laser Diffraction Spray Analyzer	.....	190
2.1.3	Atomizer	.....	192
2.1.4	Capillary Tube Viscometer	.....	192
2.1.5	Fuel Treatment Systems	.....	195
2.2	Experimental Apparatus for CWF Combustion Study	.....	197
2.2.1	Combustion Research Facility	.....	197
2.2.2	Water-Quench Sampling Probe	.....	202

2.2.3	Steam-Heated Sampling Probe .....	202
CHAPTER 3.	ATOMIZATION STUDY OF CWF .....	209
3.1	Introduction .....	209
3.2	Atomization Mechanism in Twin-Fluid Atomizer .....	211
3.3	Representative Shear Rate during CWF Atomization .....	213
3.4	Experimental Results of Spray Droplet Size with CWF Viscosity .....	220
3.5	Correlation of CWF Atomization .....	231
3.5.1	Basic Form of Atomization Correlation .....	231
3.5.2	Atomization Correlation for OR-KVB Atomizer .....	233
3.6	Summary .....	239
CHAPTER 4.	FLASH-ATOMIZATION STUDY OF CWF .....	243
4.1	Introduction .....	243
4.2	Theoretical Models of CWF Flash-Atomization .....	244
4.2.1	Nucleation Sites in Coal Particle during CWF Flash-Atomization .....	244
4.2.2	Mechanism of CWF Flash-Atomization .....	245
4.2.3	Bubble Growth Dynamics .....	249
4.2.4	Effect of Superheat on CWF Flash-Atomization .....	255
4.2.5	Spray Angle Change during Flash-Atomization .....	258
4.3	Experimental Results of CWF Flash-Atomization and Discussions .....	264
4.4	Experimental Results and Correlation of Spray Angle Change during Flash-Atomization .....	270
CHAPTER 5.	COMBUSTION STUDY OF CWF WITH FUEL TREATMENTS .....	278
5.1	Introduction .....	278
5.2	Experimental Results and Discussions .....	279

5.3 Summary .....	294
CHAPTER 6. CONCLUSIONS .....	298
REFERENCES .....	300
APPENDICES .....	303
APPENDIX A PRINCIPLE OF LASER DIFFRACTION SPRAY ANALYZER .....	304
APPENDIX B PRINCIPLE OF CAPILLARY TUBE VISCOMETER .....	307
APPENDIX C EXPERIMENTAL DATA OF IN-FLAME MEASUREMENTS .....	310
BIOGRAPHICAL NOTE .....	314

PART 1

FUNDAMENTAL STUDY OF COAL-WATER FUEL DROPLET COMBUSTION  
IN A LAMINAR FLOW REACTOR

## LIST OF FIGURES

<u>Figure</u>		<u>Page</u>
1	Schematic Diagram of Experimental Apparatus (CWF Droplet Injection) .....	31
2	Photograph of Experimental Apparatus (CWF Droplet Injection) .....	32
3	Schematic Diagram of CWF Droplet Generator .....	34
4	Photographs of CWF Droplet Generator (a) Assembled, (b) Disassembled .....	35
5	Schematic Diagram of Twin-Fluid Atomizer .....	37
6	Photographs of Twin-Fluid Atomizer (a) Assembled, (b) Disassembled .....	38
7	Schematic Diagram of Spray Test Facility and Laser Diffraction Spray Analyzer .....	39
8	Schematic Diagram of Laminar Flow Reactor (CWF Droplet Injector) .....	41
9	Schematic Diagram of Furnace Casing Gas Flow .....	42
10	Schematic Diagram of Furnace Elevating Support System .....	44
11	Schematic Diagram of Feeding Probe (CWF Droplet Injection) .....	45
12	Schematic Diagram of Sample Collection Probe (CWF Droplet Injection) .....	45
13	Schematic Diagram of Experimental Apparatus (CWF Agglomerate Injection) .....	48
14	Schematic Diagram of Laminar Flow Reactor (CWF Agglomerate Injection) .....	49
15	Schematic Diagram of Solid-Sample Feeding System .....	51
16	Schematic Diagram of Sample Collection Probe (CWF Agglomerate Injection) .....	52
17	Mechanism of CWF Droplet Combustion .....	55

18	Sequential Photographs from High-Speed Cinematographs of CWF Droplet Combustion (Agglomerate Diameter = 150 $\mu\text{m}$ , Furnace Gas Temperature = 1100 K, Oxygen Partial Pressure = 100 %) .....	56
19	Sequential Photographs from High-Speed Cinematographs of CWF Droplet Combustion (Agglomerate Diameter = 200 $\mu\text{m}$ , Furnace Gas Temperature = 1100 K, Oxygen Partial Pressure = 100 %) .....	57
20	Sequential Photographs from High-Speed Cinematographs of CWF Droplet Combustion; Localized Ignition Followed by Spread of Ignition (Agglomerate Diameter = 100 $\mu\text{m}$ in Figure A and 130 $\mu\text{m}$ in Figure B, Furnace Gas Temperature = 1100 K, Oxygen Partial Pressure = 100 %) .....	59
21	Sequential Photographs from High-Speed Cinematographs of CWF Droplet Combustion; Soot Clouds and Soot Trails (Agglomerate Diameter = 50-200 $\mu\text{m}$ , Furnace Gas Temperature = 1200 K, Oxygen Partial Pressure = 20 %) ....	61
22	Sequential Photographs from High-Speed Cinematographs of CWF Droplet Combustion; Soot Clouds and Soot Trails (Agglomerate Diameter = 150 $\mu\text{m}$ , Furnace Gas Temperature = 1200 K, Oxygen Partial Pressure = 20 %) ....	62
23	Radiation Intensity Traces of Rotating CWF Agglomerate (Agglomerate Diameter = 100 $\mu\text{m}$ , Furnace Gas Temperature = 1750 K, Oxygen Partial Pressure = 100 %) (a) 800 cycles/sec, (b) 1400 cycles/sec, (c) 2800 cycles/sec .....	64
24	Sequential Photographs from High-Speed Cinematographs of CWF Droplet Combustion; Fragmentation during Char Burnout (Agglomerate Diameter = 160-180 $\mu\text{m}$ , Furnace Gas Temperature = 1400 K, Oxygen Partial Pressure = 100 %) ...	66
25	Radiation Intensity Traces of Burning CWF Agglomerate; Fragmentation during Char Burnout .....	67
26	Schematic Diagram of Rotating CWF Agglomerate .....	72
27	Scanning Electron Micrographs of CWF Agglomerates .....	81
28	Distribution of Devolatilization Pores on Outer Surface of CWF Agglomerate .....	82

29	$\left  \frac{\sum_{i=1}^N \cos\theta_i  \cos\phi_i }{N} \right $	versus Total Number of Pores N .....	86
----	---	--------------------------------------	----

30	Typical Pore Size Distribution of 100 Largest Macropores .	88
31	Probability Density Distribution of Geometrical Factor ...	89
32	Configuration of Rotating Sphere with One Pore .....	91
33	Configuration of Spherical Coordinates .....	92
34	Force Balance during CWF Agglomerate Rotation .....	94
35	Surface Tension Force at Neck Region of Two Coalescent Coal Particles in CWF Agglomerate .....	104
36	Agglomeration Process of Coal Particles in CWF Agglomerate .....	105
37	Typical Time-Temperature History of CWF Agglomerate during CWF Combustion .....	109
38	Predictions of Angular Velocity of Rotating CWF Agglomerate; Effect of Oxygen Partial Pressure (Agglomerate Diameter = 100 $\mu\text{m}$ , Furnace Gas Temperature = 1100 K) (a) 20 % $\text{O}_2$ , (b) 40 % $\text{O}_2$ , (c) 100 % $\text{O}_2$ .....	122
39	Predictions of Angular Velocity of Rotating CWF Agglomerate; Effect of Furnace Gas Temperature (Agglomerate Diameter = 100 $\mu\text{m}$ , Oxygen Partial Pressure = 20 %) (a) 1100 K, (b) 1400 K, (c) 1750 K .....	123
40	Predictions of Angular Velocity of Rotating CWF Agglomerate; Effect of Agglomerate Diameter (Furnace Gas Temperature = 1400 K, Oxygen Partial Pressure = 20 %) (a) 200 $\mu\text{m}$ , (b) 100 $\mu\text{m}$ , (c) 60 $\mu\text{m}$ .....	124
41	Predictions of Angular Velocity of Rotating CWF Agglomerate; Effect of Agglomerate Diameter (Devolatilization Rate Constant = 950 $\text{sec}^{-1}$ ) .....	125
42	Comparison between Prediction and Experimental Data of Angular Velocity of Rotating CWF Agglomerate .....	126
43	Predictions of Centrifugal Force; Effect of Furnace Gas Temperature on Centrifugal Force (Agglomerate Diameter = 100 $\mu\text{m}$ , Oxygen Partial Pressure = 20 %) (a) 1100 K, (b) 1400 K, (c) 1750 K ....	129

44	Probability Density Distributions of Angular Velocities; Effect of Oxygen Partial Pressure (Agglomerate Diameter = 90-106 $\mu\text{m}$ , Furnace Gas Temperature = 1750 K) (a) 20 % $\text{O}_2$ , (b) 40 % $\text{O}_2$ , (c) 70 % $\text{O}_2$ , (d) 100 % $\text{O}_2$ .....	130
45	Probability Density Distributions of Angular Velocities; Effect of Oxygen Partial Pressure (Agglomerate Diameter = 90-106 $\mu\text{m}$ , Furnace Gas Temperature = 1400 K) (a) 40 % $\text{O}_2$ , (b) 70 % $\text{O}_2$ , (c) 100 % $\text{O}_2$ .....	131
46	Probability Density Distributions of Angular Velocities; Effect of Furnace Gas Temperature (Agglomerate Diameter = 90-106 $\mu\text{m}$ , Oxygen Partial Pressure = 100%) (a) 1100 K, (b) 1250K, (c) 1400 K, (d) 1750 K .....	132
47	Probability Density Distributions of Angular Velocities; Effect of Agglomerate Diameter (Furnace Gas Temperature = 1400 K, Oxygen Partial Pressure = 100%) (a) 212-250 $\mu\text{m}$ , (b) 150-180 $\mu\text{m}$ , (c) 90-106 $\mu\text{m}$ , (d) 45-53 $\mu\text{m}$ .....	133
48	Predictions of C, L, E, Normalized A, F, $F_A$ , and Adhesive Force $F_A$ versus Time for Particle Heating Rate of $10^4$ K/sec .....	136
49	Predictions of C, L, E, Normalized A, F, $F_A$ , and Adhesive Force $F_A$ versus Time for Particle Heating Rate of $10^5$ K/sec .....	137
50	Comparisons of C, L, E, Normalized A, and Adhesive Force $F_A$ versus Time for Different Particle Heating Rates (a) $10^4$ K/sec, (b) $10^5$ K/sec .....	138
51	Predictions of C, L, E, Normalized A, and Adhesive Force $F_A$ versus Time for Different Furnace Gas Temperature (Agglomerate Diameter = 100 $\mu\text{m}$ , Oxygen Partial Pressure = 20 %) (a) 1100 K, (b) 1750 K .....	139
52	Predictions of C, L, E, Normalized A, and Adhesive Force $F_A$ versus Time for Different Agglomerate Diameter (Furnace Gas Temperature = 1400 K, Oxygen Partial Pressure = 20 %) (a) 200 $\mu\text{m}$ , (b) 60 $\mu\text{m}$ .....	140
53	Predictions of C, L, E, Normalized A, and Adhesive Force $F_A$ versus Time for Different Oxygen Partial Pressure (Agglomerate Diameter = 100 $\mu\text{m}$ , Furnace Gas Temperature = 1100 K) (a) 20 % $\text{O}_2$ , (b) 100 % $\text{O}_2$ .....	141



54	Comparisons of Adhesive Force $F_A$ with Centrifugal Force $F_{\text{centrif}}$ for Different Furnace Gas Temperature (Agglomerate Diameter = 100 $\mu\text{m}$ , Oxygen Partial Pressure = 20 %) (a) 1100 K, (b) 1750 K .....	144
B.1.	Mass Mean Diameter of Spray Droplet at Various AFRs .....	163

## LIST OF TABLES

<u>Table</u>		<u>Page</u>
1	Example of Typical Pore Size Distribution of the 100 Largest Pores on the Outer Surface of the CWF Agglomerate .....	88

## NOMENCLATURE

A	contact area
$\left(\frac{dA}{dt}\right)$	growth rate of contact area
$A_i$	cross-sectional exit area of devolatilization pore
$\Sigma A_i$	total cross-sectional exit area of devolatilization pores
A	surface in eqs. (3) and (4)
$\bar{A}_1 \dots \bar{A}_N$	average cross-sectional exit area of devolatilization pores for each pore group in eq. (23)
B	number of moles of combustion product per mole of oxygen in eq. (83)
$B_1, B_2$	constant in eq. (71)
cs	control surface
cv	control volume
$\bar{c}$	mass fraction of unreacted coal
$\bar{c}_i$	initial mass fraction of unreacted coal ( $= 1 - \bar{f}_a$ )
C	volume fraction of unreacted coal
$c_p$	specific heat of CWF droplet/agglomerate
$c_{p_{vol}}$	specific heat of volatiles
$D_{O_2}$	diffusion coefficient of oxygen
$D_p$	diameter of coal particle in eq. (A-15)
$D_I \dots D_V$	pore diameter for each pore group
$d_p$	diameter of CWF droplet/agglomerate
$\bar{E}$	mass fraction of coke-residue (char)
E	volume fraction of coke-residue (char)
$E_{th}$	threshold volume fraction of coke-residue (char)
	$\left( = \frac{1 - \bar{f}_a}{2} \right)$

$E_1, E_2$	activation energy
$F_A$	adhesive force between two coalescent coal particles
$F_{\text{centrif}}$	centrifugal force acting on a coal particle
$F_E$	adhesive force due to coke interconnection
$F_{E1}$	adhesive force due to coke interconnection in stage 1
$F_{E2}$	adhesive force due to coke interconnection in stage 2
$F_{E3}$	adhesive force due to coke interconnection in stage 3
$F_\gamma$	surface tension force due to liquid metaplast
$\tilde{f}_a$	mass fraction of ash (mineral matter)
$f_a$	volume fraction of ash (mineral matter)
$f_1 \dots f_N$	fraction of volatile mass per total volatile mass loss for each pore group
$f^*$	fraction of volatile mass in eq. (A-15)
$G$	acceleration of gravity
$\Delta H_{\text{char}}$	heat of combustion of coal surface
$\Delta H_{\text{devol}}$	endothermic heat of devolatilization
$\Delta H_{\text{vol}}$	heat of combustion of volatiles
$k$	devolatilization rate constant
$k_I$	rate constant in eq. (29)
$k_{II}$	rate constant in eq. (30)
$k_1, k_2$	Arrhenius type reaction rate
$k_g$	thermal conductivity of surrounding gas
$k_{\text{vol}}$	thermal conductivity of volatiles
$\tilde{L}$	mass fraction of liquid metaplast
$L$	volume fraction of liquid metaplast
$L_s$	mass fraction of solid metaplast initially existing in coal

$L_w$	latent heat of evaporation
$l_{\text{eff}}$	effective circumference
$M_F$	frictional moment of rotating CWF agglomerate
$M_o$	original mass of CWF agglomerate
$\Sigma \vec{M}$	sum of moments about origin
$m_c$	mass of coal particle
$m_p$	mass of CWF droplet/agglomerate
$\dot{m}_{\text{vol}}$	rate of volatile mass loss
$\left(\frac{dm_w}{dt}\right)$	rate of water evaporation
$m_{\text{III-IV}}$	number of intersections of $D_{\text{III}}$ - and $D_{\text{IV}}$ - pores per unit particle volume
$m_{\text{III-V}}$	number of intersections of $D_{\text{III}}$ - and $D_{\text{V}}$ - pores per unit particle volume
$Nu$	Nusselt number
$Nu_D$	Nusselt number of rotating particle
$\vec{n}$	unit vector normal to surface A
$n_1 \dots n_N$	number of pores for each pore group
$n_{\text{III}}$	number of pore-mouths of $D_{\text{III}}$ -pores per unit particle external surface area
$P$	pressure
$Pr$	Prandtl number
$Q_{\text{char}}$	energy produced by exothermic char burnout
$Q_{\text{cond}}$	energy transfer due to heat conduction
$Q_{\text{devol}}$	energy required for endothermic process of devolatilization
$Q_{\text{evap}}$	energy required for endothermic process of evaporation

$Q_{\text{flame}}$	energy feedback from volatile flame
$Q_{\text{rad}}$	energy transfer due to thermal radiation
$Q_{\text{rot}}$	energy transfer due to particle rotation
$Q_{\text{vol}}$	energy produced by remaining volatile burnout
$q_{\text{char}}$	chemical surface reaction rate of coal
$q_{\text{vol}}$	combustion rate of volatiles
$R$	radius of CWF agglomerate
$R$	ideal gas constant
$Re_D$	rotational Reynolds number $\left( \equiv \frac{\rho d_p^2 \omega}{\mu} \right)$
$Re_r$	rotational Reynolds number $\left( \equiv \frac{\rho r_p^2 \omega}{\mu} \right)$
$r$	radial distance in eq. (4)
$\vec{r}$	position vector in eq. (3)
$r_c$	radius of coal particle
$r_f$	radius of volatile flame
$r_m$	rate of physical melting
$r_p$	radius of CWF agglomerate
$r^*$	radius of contact area in neck region
$T$	temperature
$T_f$	temperature of volatile flame
$T_{fp}$	average temperature between volatile flame and CWF agglomerate
$T_g$	temperature of surrounding gas
$T_m$	mean melting temperature of coal particle
$T_p$	temperature of CWF droplet/agglomerate
$T_w$	temperature of furnace wall

$t$	time
$\left(\frac{dT}{dt}\right)_1$	heating rate of CWF droplet in pre-evaporation stage
$\left(\frac{dT}{dt}\right)_2$	heating rate of CWF droplet/agglomerate in evaporation stage
$\left(\frac{dT}{dt}\right)_3$	heating rate of CWF agglomerate in heat-up stage
$\left(\frac{dT}{dt}\right)_4$	heating rate of CWF agglomerate during devolatilization
$\left(\frac{dT}{dt}\right)_5$	heating rate of CWF agglomerate during char burnout
$v$	volume in eqs. (3) and (4)
$V$	volatile mass loss per unit original mass of CWF agglomerate
$V^*$	ultimate volatile mass loss per unit original mass of CWF agglomerate
$\frac{dV}{dt}$	rate of volatile mass loss per unit original mass of CWF agglomerate
$v_e$	exit velocity of volatile jet at devolatilization pore
$(v_e)_{\text{tangential}}$	tangential component of $v_e$
$v_i$	exit velocity of volatile jet at each devolatilization pore
$(v_i)_{\text{tangential}}$	tangential component of $v_i$
$\vec{v}_{cs}$	absolute fluid velocity on control surface
$\vec{v}_{cv}$	absolute velocity in control volume
$\vec{v}_{rel}$	local fluid velocity relative to control surface

$\bar{v}_1 \dots \bar{v}_N$	average exit velocity of volatile jet for each pore group
$X_{O_2,g}$	oxygen concentration in gas
$X_{O_2,s}$	oxygen concentration at agglomerate surface

$$\left( \frac{\sum A_i \cos \theta_i |\cos \phi_i|}{\sum A_i} \right) \quad \text{geometrical factor of devolatilization pores}$$

Normalized A                      normalized contact area, given by  $\frac{A}{\pi r_c^2}$

#### Greek Symbols

$\alpha_1, \alpha_2$	mass stoichiometric coefficient
$\beta_{vol}$	oxygen requirement of volatiles
$\gamma$	surface tension
$\gamma_c$	surface tension of liquid metaplast
$\epsilon_p$	emissivity of CWF droplet/agglomerate
$\epsilon_I \dots \epsilon_V$	pore volume fraction for each pore group
$\theta$	angle in spherical coordinate
$\theta$	contact angle
$\theta_i$	angle
$\mu$	viscosity
$\mu^*$	viscosity of liquid metaplast
$\mu_{vol}$	viscosity of volatiles
$\rho$	density
$\rho_A$	density of CWF agglomerate in eq. (4)



$\rho_a$	density of ash (mineral matter)
$\rho_c$	density of unreacted coal
$\rho_l$	density of liquid metaplast
$\rho_o$	initial apparent density of CWF agglomerate
$\rho_p$	density of CWF droplet/agglomerate
$\rho_{vol}$	density of volatiles
$\sigma$	Stefan-Boltzman's constant
$\sigma_E$	bond stress of coke-residue (char)
$\sigma_T$	standard deviation of melting temperature of coal
$\Phi$	angle in spherical coordinate
$\phi_i$	angle
$\omega$	angular velocity of rotating CWF agglomerate

CHAPTER 1  
INTRODUCTION

1.1 Introduction

The two major applications of coal-water fuel (CWF) are the replacement of petroleum fuels in existing oil-fired boilers <sup>(1)</sup>, and in coal-fired (open cycle) gas turbines <sup>(2)</sup>. Both of these applications represent relatively novel developing technologies. Boiler applications are expected in this decade and gas turbine applications in the 1990s. While many of the current problem areas in combustion of CWF are common to both applications, the more immediate concern is clearly focused on the boilers.

Coal beneficiation to the level needed for retrofit of boilers designed for oil (about 2-3 % ash) requires fine grinding of the coal (~ 80 % < 76  $\mu\text{m}$ ) and approximately 30-40 weight % water to be compatible with demands of efficient coal cleaning, favorable rheologic properties of the CWF and a limited increase in waste-gas heat losses of the boilers. The water in the CWF engenders operational difficulties in achieving ignition and good flame stability over practical ranges of the turn-down ratio (about 1:3), which sets this fuel apart from pulverized coal and even from high moisture lignite. The ignition difficulty is due mainly to the requirement that all the water in the fuel spray has to be evaporated before the coal can be heated to ignition. The conditions for ignition are more severe than for the combustion of pulverized low-rank coals with high moisture content, since for these coals most of the drying occurs in the grinding mill prior to injection of the fuel into

the combustion chamber. Another factor affecting ignition is the agglomeration of the residue of the CWF droplets. This causes a shift to larger effective particle size and loss of the potential benefits of using very fine coal particles.

Effective particle size is very important when retrofitting an oil-fired boiler, which is designed to operate with residence times much shorter than would be desirable in a unit designed for pulverized coal-firing. Burnout of the residual char from the CWF agglomerates cannot be achieved unless the particle size is maintained sufficiently small.

During CWF droplet combustion, there is a tendency for the coal particles to agglomerate within droplets. Hence, the resulting coal particle size distribution (p.s.d.) is determined by the size distribution of the atomized CWF droplet rather than by the original particle size of the coal. The coal particles in the CWF droplet are drawn together by surface tension force during the drying process, so that the particles tend to agglomerate. When the CWF is sprayed into a furnace, the drying process precedes and overlaps the early stage of pyrolysis, during which swelling of the coal particles is likely to occur. Most of the CWFs currently under production use high-volatile coals in order to aid in the ignition process, but such coals in general have a high swelling index. After the CWF agglomerate reaches a temperature around 400°C, tar-like hydrocarbons are released, and the coal particles in the CWF agglomerate become more effectively bonded. The CWF agglomerate then enters the plastic deformation stage, and volatiles are evolved through devolatilization pores. Examinations of the behavior of single droplets of coal-oil mixtures during combustion<sup>(3)</sup>

have shown that the strength of the agglomerate is dependent upon coal rank, with swelling coals fusing as described above, while non-swelling coals form loosely sintered aggregates which readily fall apart during combustion. Given that the burnout time for a particle of diameter  $d$  is proportional to  $d^n$  with  $1 < n < 2$ , it is important that the conditions under which aggregates form and survive be well understood. This is especially so for applications which use micronized coal in the CWF, as the investment in producing the ultra-fine grind is virtually wasted if agglomeration determines the p.s.d.

Another area of concern in retrofit applications is the behavior of the ash from the coal, since even after beneficiation the ash burden is considerably higher than that in most fuel oils. Factors which influence this ash behavior include the ash composition and the temperature-time environment which an ash particle encounters as it is swept through the furnace. Once again, however, it is the ash particle size which determines whether the particle will follow the gas streamlines as it passes through the convective sections, with larger particles being subject to impaction and possible entrapment within a surface deposit.

Thus, from the viewpoints of ignition/stability, of good carbon burnout, and of minimization of deposit formation, the behavior of the coal particles during combustion is seen to be of crucial importance.

## 1.2 Objectives of Investigation

During CWF droplet combustion, particle size distribution (p.s.d.) of char and ash is dependent upon whether coal particles burn

individually or as agglomerate which size is determined by the CWF droplet size.

The objectives of this study are to determine the factors that govern ash p.s.d., and examine the conditions under which coal-aggregates, produced during the CWF droplet evaporation, can be induced to break up.

The experiments will be carried out in a laminar flow reactor (LFR) which has optical access so that individual CWF droplet/agglomerate behavior during combustion can be observed in detail. High-speed cinematography and fiber optic radiometry will be used to observe and record the mechanism of CWF droplet combustion.

## CHAPTER 2

### EXPERIMENTAL INVESTIGATION

#### 2.1 Introduction

The processes of particle agglomeration, particle rotation, and fragmentation during devolatilization and char burnout were studied in a laminar flow reactor (LFR) by two experimental procedures. In the first of these, a CWF droplet generator was developed and was used to feed CWF droplets directly into the LFR. The CWF droplet generator, which consisted of a twin-fluid atomizer and a series of skimmers to reduce the feed rate of CWF droplets into the LFR, was capable of producing CWF droplets in the size range of 5-500  $\mu\text{m}$  at feed rates of less than 3 mg/sec.

In the second parallel study, solid samples withdrawn from a CWF spray flame, close to the atomizing nozzle, were size graded and fed into the LFR in low particle concentrations. Their combustion history in the LFR was determined by monitoring the intensity of radiation emitted by individual CWF agglomerates during combustion (by fiber optic radiometry) and by the use of high-speed cinematography.

The experimental apparatus for a CWF droplet injection will be discussed in Section 2.2, and that for a CWF agglomerate (solid-sample) injection will be discussed in Section 2.3.

#### 2.2 Experimental Apparatus for CWF Droplet Injection

The experimental apparatus for a CWF droplet injection, shown schematically in Figure 1 and in the photograph in Figure 2, consisted

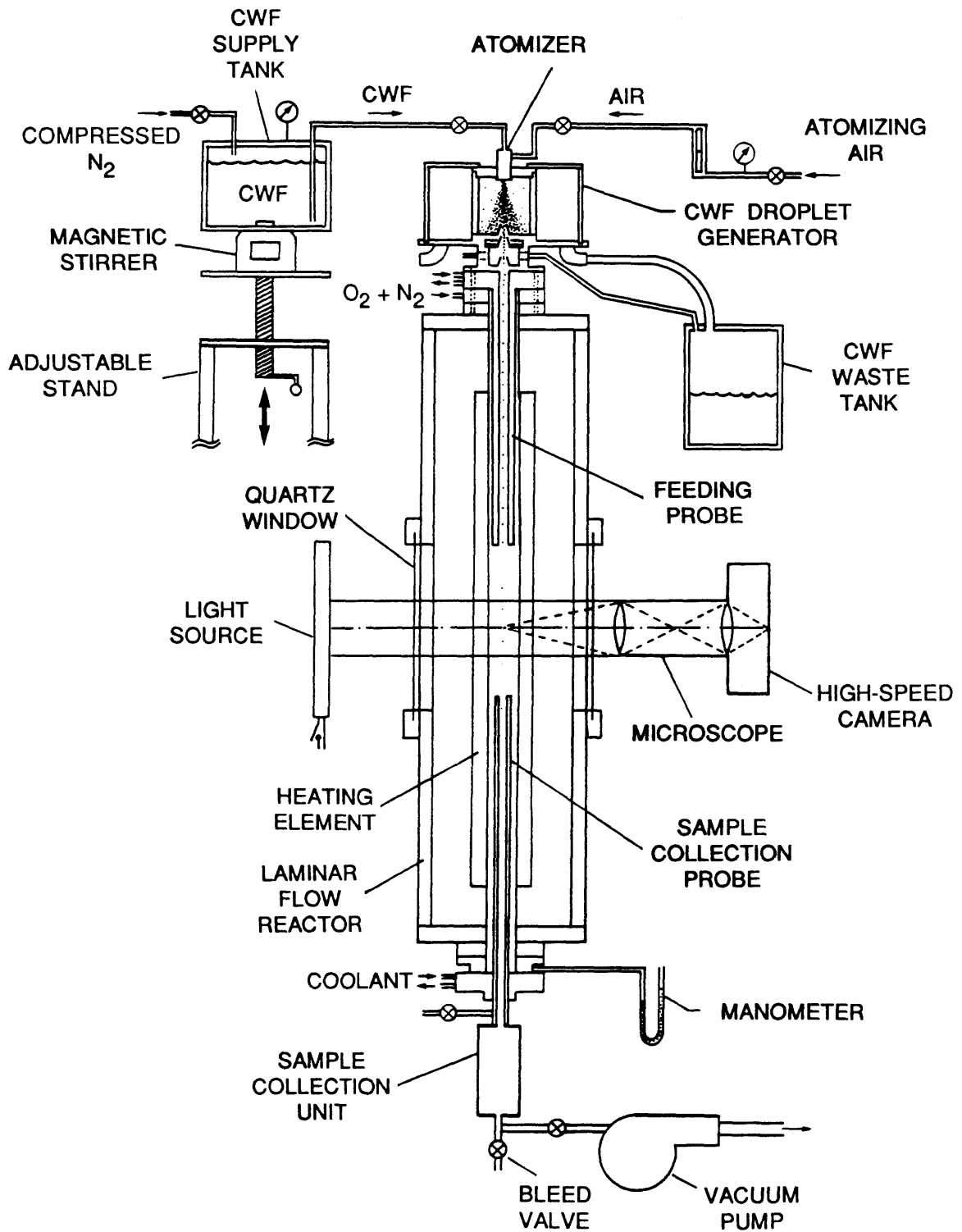


Figure 1. Schematic Diagram of Experimental Apparatus (CWF Droplet Injection)

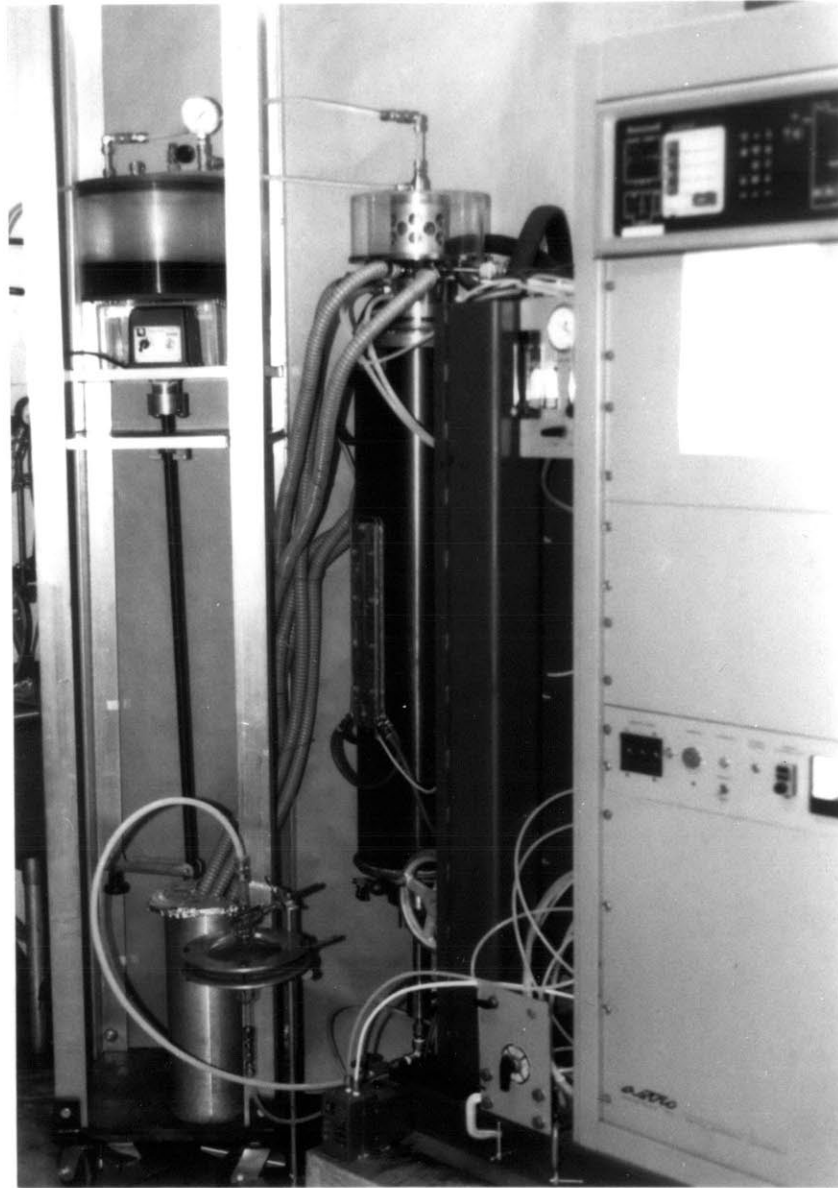


Figure 2. Photograph of Experimental Apparatus  
(CWF Droplet Injection)



of: a CWF droplet generator, a laminar flow reactor, a feeding probe, a sample collection system, a fuel supply tank, a fuel waste tank, a photographic recording system, and a digital control programmer for the laminar flow reactor.

### 2.2.1 CWF Droplet Generator

The CWF droplet generator is shown schematically in Figure 3 and in the photograph in Figure 4. It consisted of: an atomizer, an atomizer adaptor, a 25-cm-diameter plexiglas tank enclosing a 10-cm-diameter cylinder (with sixteen holes, 2 cm in diameter), a base plate, and three cone-shaped skimmers with different openings. A wide-angle CWF spray at feed rates of less than 2 g/sec, generated from the atomizer, was discharged into the cylinder, and then passed through the series of skimmers with progressively larger openings to chop most of the CWF spray. This produced a narrow dilute stream of CWF droplets at feed rates of less than 3 mg/sec which was fed directly into the LFR. The remainder of the CWF spray was discharged to the waste fuel collecting tank from the six ports in the CWF droplet generator through flexible vinyl hoses. The range of the opening diameters of the first skimmer was 0.3 cm to 0.6 cm, that of the second skimmer was 0.4 cm to 0.7 cm, and that of the third skimmer was 0.5 cm to 0.8 cm. The opening diameters of the skimmer used for a particular experiment were chosen based on the desired skimmed CWF flow rate to the LFR.

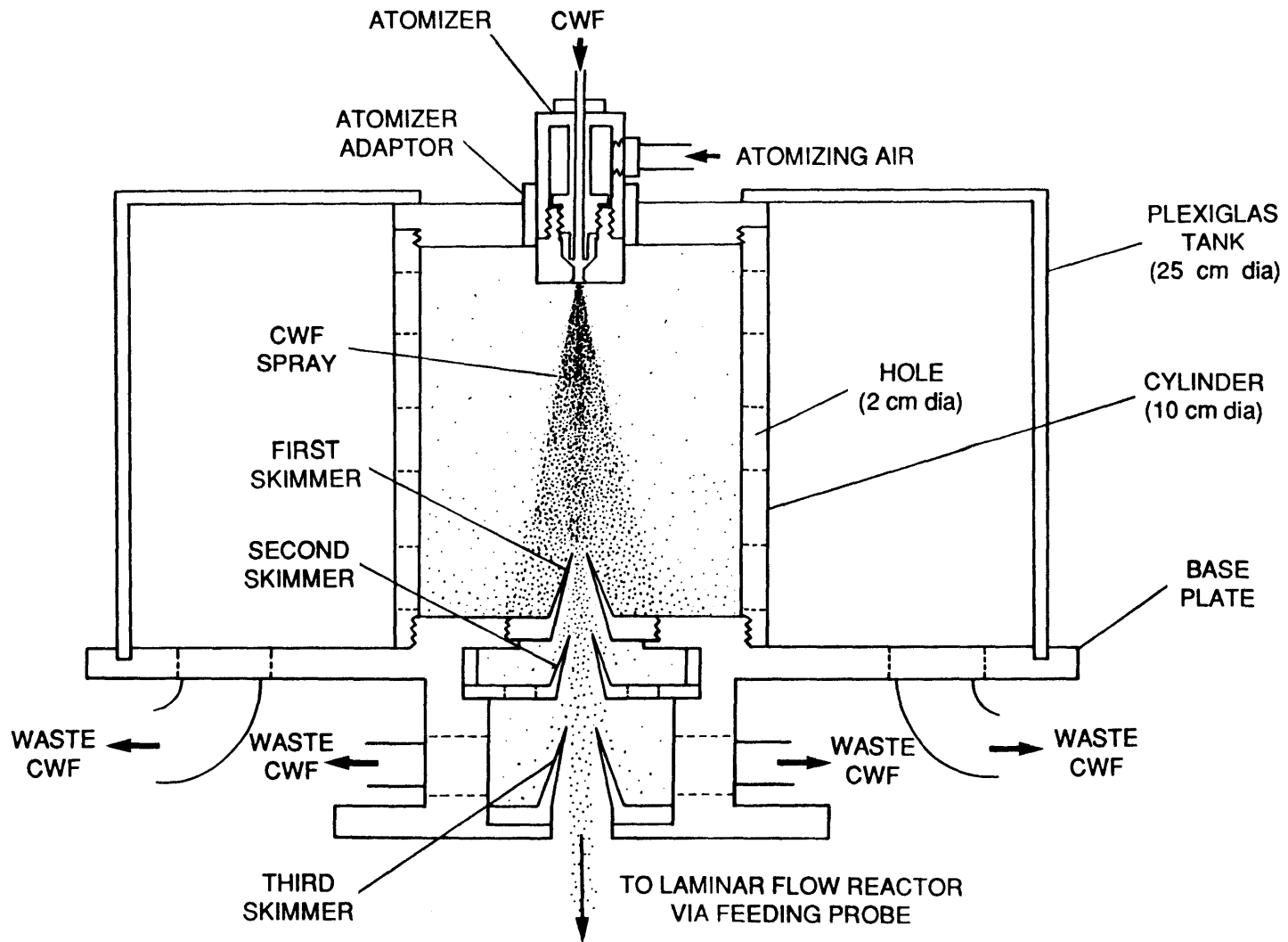
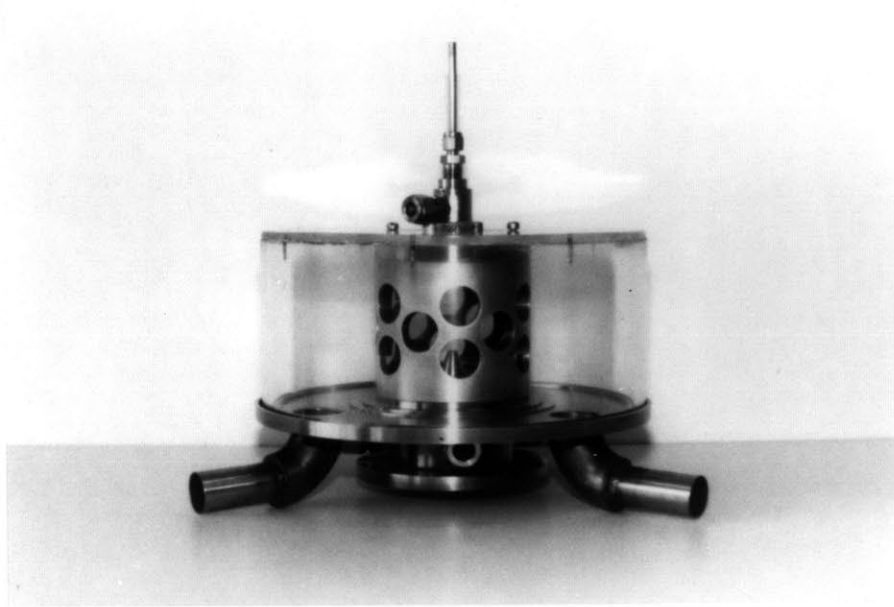
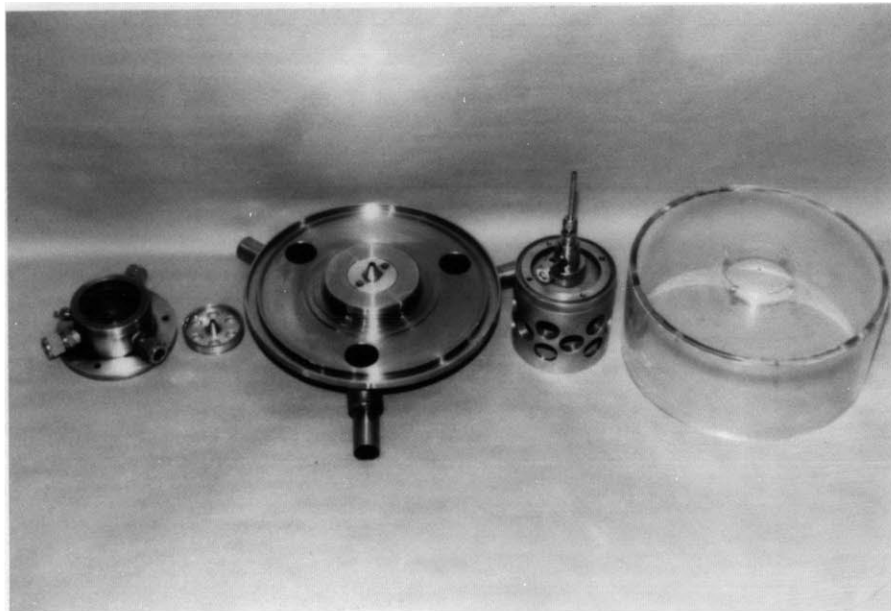


Figure 3. Schematic Diagram of CWF Droplet Generator



a



b

Figure 4. Photographs of CWF Droplet Generator  
(a) Assembled, (b) Disassembled

### 2.2.2 Atomizer

The twin-fluid, internally mixed, single-exit atomizer was developed to generate a stream of CWF droplets in the size range of 5 to 500  $\mu\text{m}$ . Figures 5 and 6 show the atomizer. It consisted: of an upper casing, a lower casing, an insert, a swirler, a spacer, O-rings, and fittings.

The atomizing air at 200-250 kPa was supplied through the air passage of the insert, the swirler, and the mixing chamber. This atomizing air entrained the CWF up to the mixing chamber by a syphon phenomenon, producing a high atomizing air-to-fuel ratio (AFR) and a fine droplet size (28  $\mu\text{m}$  Mass Mean Diameter). The CWF was supplied from the fuel tank to the atomizer through 0.6-cm-I.D. tubing. To obtain a larger mean droplet size, the CWF flow rate could be increased by supplying the CWF to the atomizer at higher fuel tank pressure (100-150 kPa).

The atomizing air and the entrained CWF were mixed internally in the mixing chamber and discharged from a common orifice (0.28 cm inside diameter) into the skimmers. The swirler in the mixing chamber increased the spray angle. The spacer, which was located between the lower casing and the insert, could adjust the cross-sectional area of the air passage leading to the mixing chamber. By adjusting this cross-sectional area, mean droplet size and particle size distribution of CWF spray could be changed. The three O-rings prevented leakage of the atomizing air, which resulted in oscillation of the CWF spray. The atomizer orifice had a full inside angle of  $40^\circ$  to increase the spray angle.

The atomizer was tested in a Spray Test Facility (Figure 7) which was equipped with a laser diffraction spray analyzer. The descriptions of the Spray Test Facility and the laser diffraction spray analyzer will

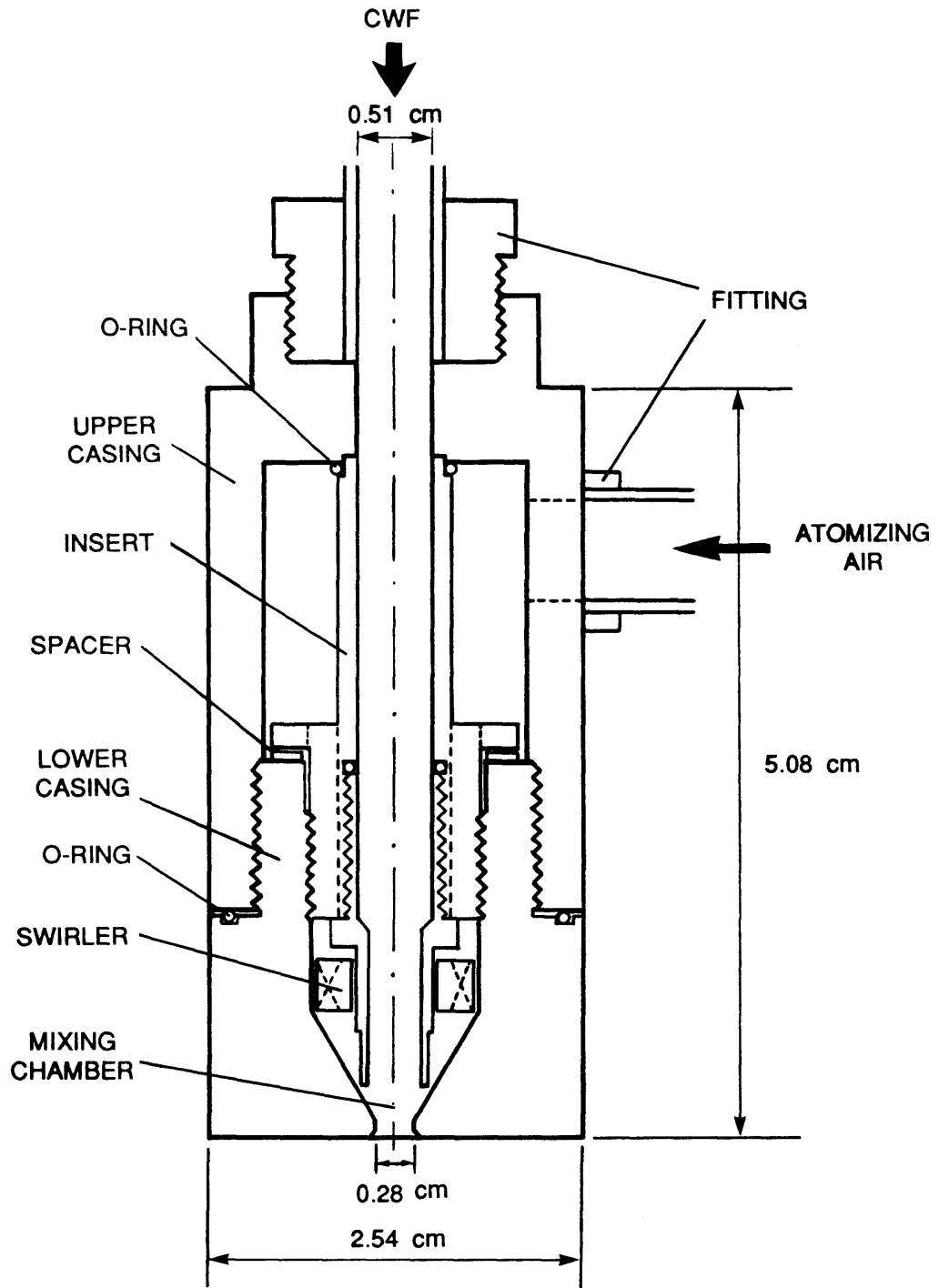
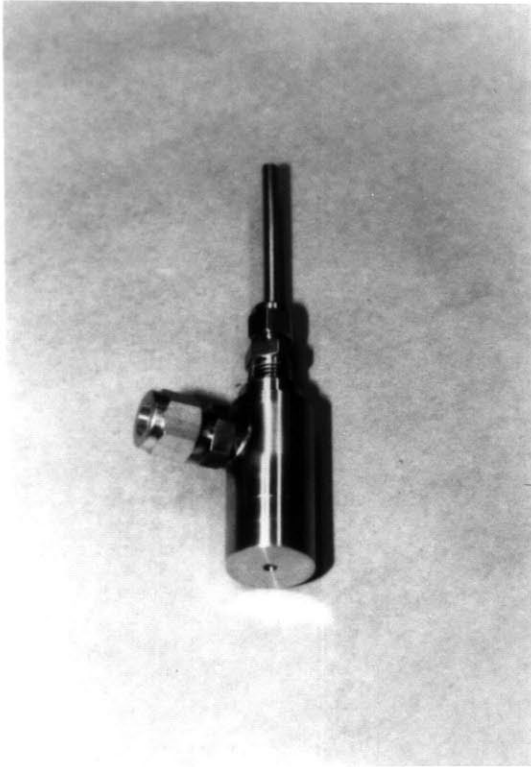
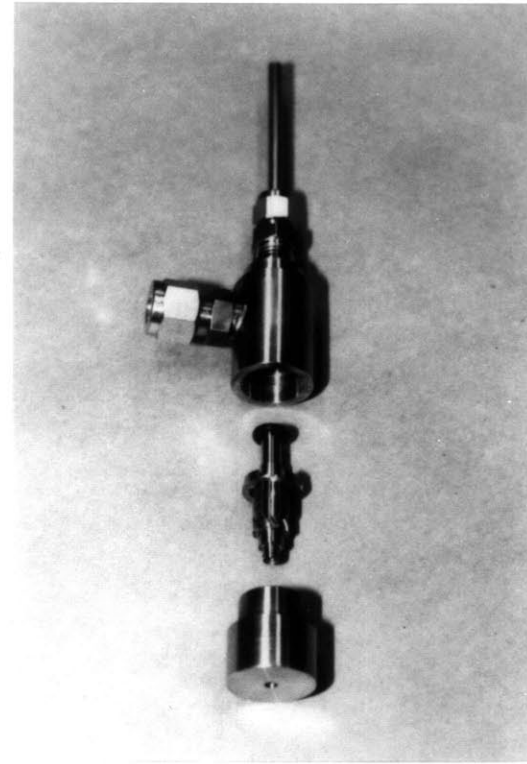


Figure 5. Schematic Diagram of Twin-Fluid Atomizer



**a**



**b**

Figure 6. Photographs of Twin-Fluid Atomizer  
(a) Assembled, (b) Disassembled

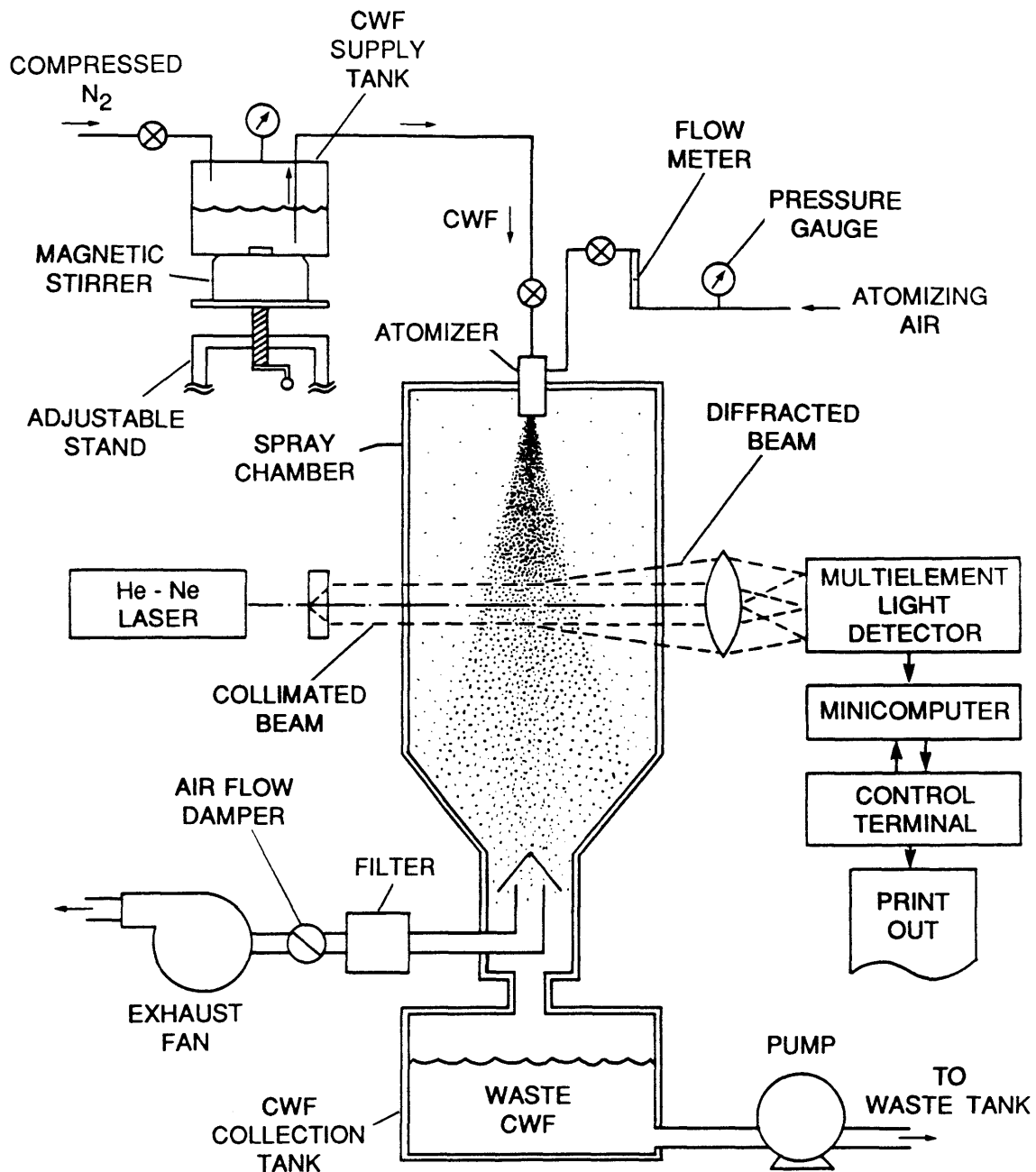


Figure 7. Schematic Diagram of Spray Test Facility and Laser Diffraction Spray Analyzer

be discussed in detail in Chapter 2 of Part 2. The test results of the atomizer will be discussed in Appendix B.

### 2.2.3 Laminar Flow Reactor

The laminar flow reactor, shown schematically in Figure 8, was manufactured by Astro Industries, Inc. (Astro Model 25-240). Overall furnace dimensions were 25.4 cm diameter by 111.8 cm length. Two windows, 1.3 cm wide by 30.5 cm long, were located on opposite sides of the furnace and symmetrically centered about the hot zone. The windows were sealed with 0.3 cm thick quartz plates. A port was provided at the center of the hot zone in a plane perpendicular to that of the windows for a Graphite/Boronated Graphite thermocouple (Astro BGT-2). A water-cooled 5.1-cm-diameter O-ring seal assembly was provided at each end of the furnace to support a quartz tube that extended the length of the furnace.

The graphite heating element was supported from two power feed-throughs at one end of the furnace. This configuration limited the furnace orientation to a length-wise vertical position. The heating element was located between the quartz tube and the graphite radiation shield. The cavity containing the heating element was continuously flushed with helium (Figure 9), which was introduced via a rotameter through orifices located in the window assembly and vented through a port in the casing at the lower end of the furnace. In the event of an over-pressurization of the casing, a pressure release valve was furnished through a port in the casing at the upper end of the furnace.



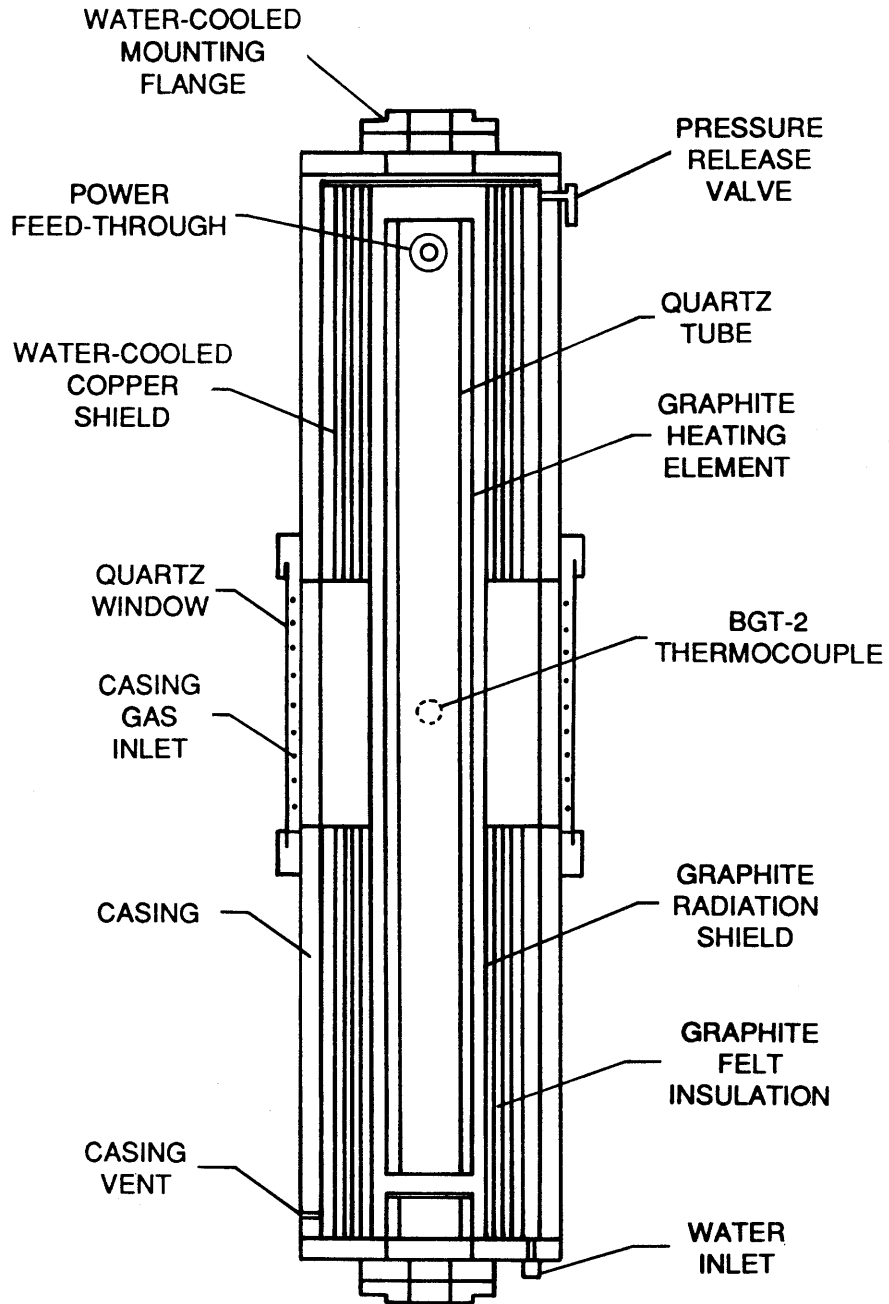


Figure 8. Schematic Diagram of Laminar Flow Reactor (CWF Droplet Injection)

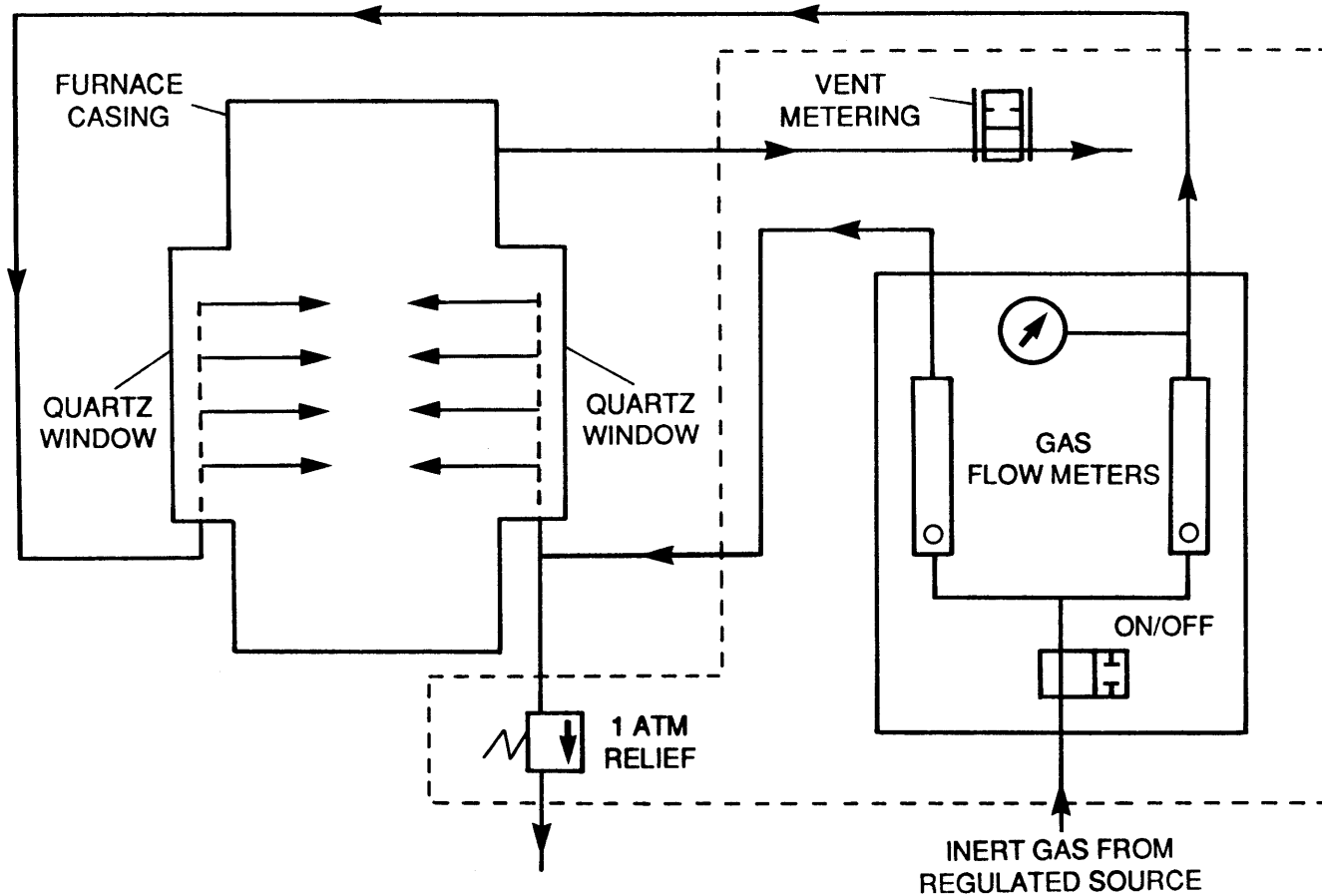


Figure 9. Schematic Diagram of Furnace Casing Gas Flow

Power for the heating element was provided by a 20-kVA power supply consisting of a phase angle fired silicon controlled rectifier power regulator and a step-down load transformer. Power might be manually or automatically adjusted by a digital control programmer (Honeywell DCP-7700).

The signal for the programmer was produced by the Graphite/Boronated Graphite thermocouple and transformed to a compatible programmer input by a signal transmitter (Rochester Instrument Systems, Model SC-1304). The BGT-2 thermocouple had an exceptionally high output and sensitivity throughout its entire operating temperature range, providing stable long-time operation to 2,250 K. All designs of this type of thermocouple had appreciable thermal mass and conduction losses along the graphite supporting elements to the water-cooled cold-junction and thus had to be calibrated.

The furnace was mounted on an elevating support stand (Figure 10). The position of the furnace might be manually adjusted through a 30-cm vertical displacement. The furnace mounting bracket on the stand, slides on hardened and ground shafts with linear ball bushings to provide smooth vibration-free operation. Adjustments could be made by a hand crank driving a lead-screw through a right angle drive.

#### 2.2.4 Feeding Probe

A narrow stream of CWF droplets was fed into the LFR through the feeding probe (Figure 11) whose inside diameter varied between 0.8 cm and 2.4 cm. The feeding probe was kept cool in the combustion zone by circulating cooling water.

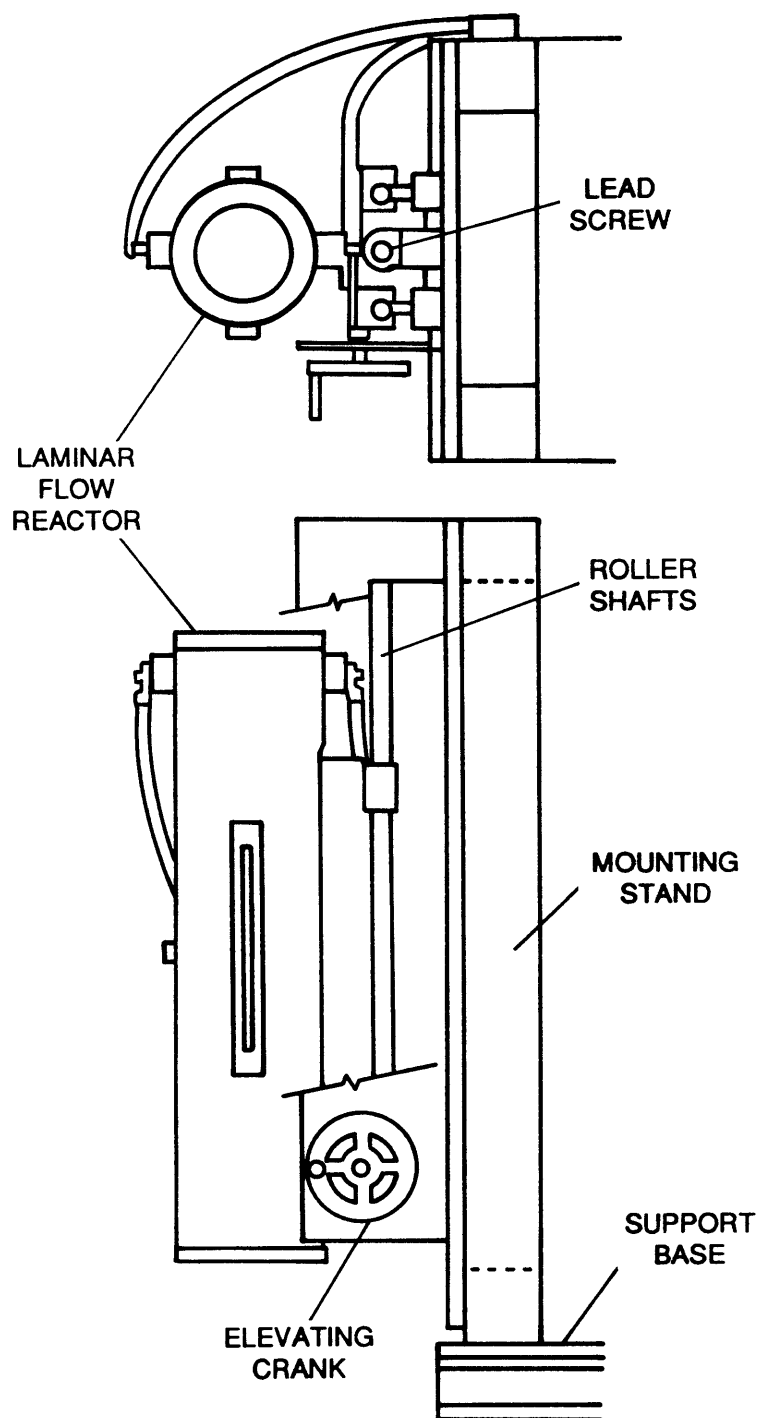


Figure 10. Schematic Diagram of Furnace Elevating Support System

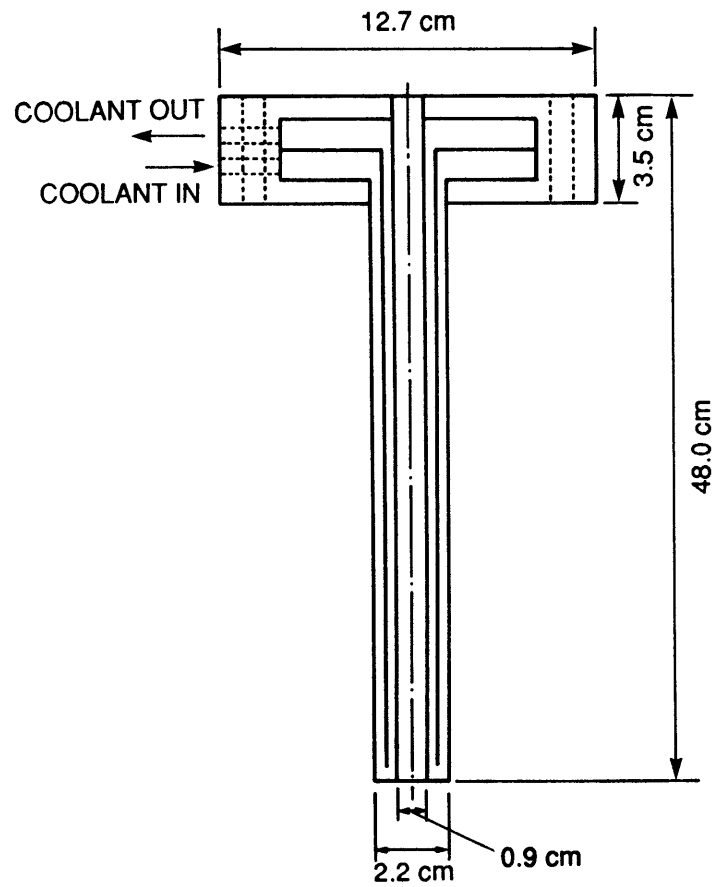


Figure 11. Schematic Diagram of Feeding Probe  
(CWF Droplet Injection)

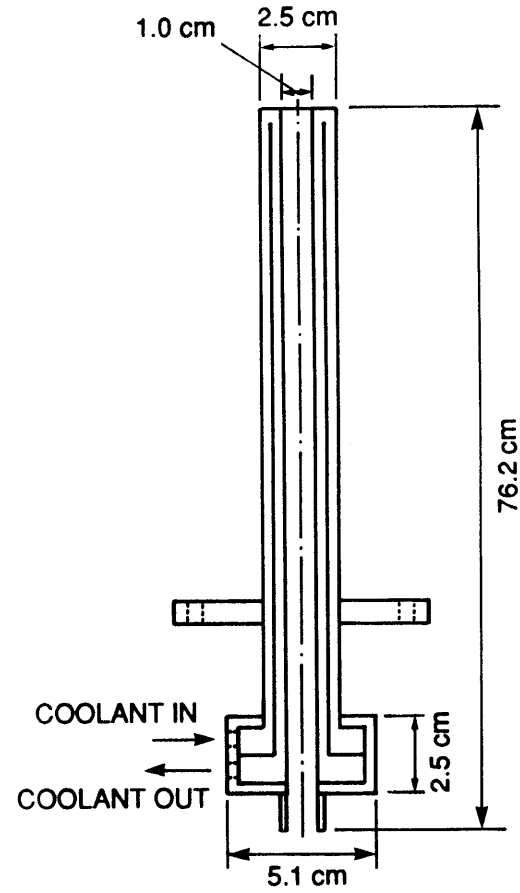


Figure 12. Schematic Diagram of Sample Collection Probe  
(CWF Droplet Injection)

### 2.2.5 Sample Collection Probe

The water-cooled sample collection probe (Figure 12) was connected to the bottom of the furnace. A vacuum pump pulled the exhaust gases and particles through the sample collection probe to a filter which removed the solid particles. The pressure inside the furnace could be changed by adjusting bleed valves between the sample collection filter and the vacuum pump. The pressure inside the furnace was monitored by a water-column manometer. The sample collection filter could be replaced by a cascade impactor to measure ash particle size distribution.

### 2.2.6 Fuel Supply Tank

The CWF was supplied from the fuel supply tank to the atomizer. The CWF flow rate could be changed by adjusting the fuel tank pressure in the range of 100-150 kPa. This pressure was controlled by adjusting the air flow rate to the fuel tank. The fuel supply tank was mounted on an adjustable-height stand. The level of CWF in the fuel tank was maintained constant, relative to the ground level, by adjusting the position of the fuel tank. This provided constant fuel tank pressure during the experiment. A magnetic stirrer was used under the fuel tank to mix CWF thoroughly.

### 2.2.7 Photographic Recording System

A high-speed cinematographic camera (HYCAM) equipped with a microscope (HEERBRUGG MDG 13) was used for observing and recording the combustion process through the quartz window on the furnace. The

microscope provided magnification of the burning CWF droplets in the range of 0.3 X to 3.7 X. A light source (shown as part of Figures 1 and 2) was located opposite the camera to give the background light for the transmission photographic study.

### 2.3 Experimental Apparatus for CWF Agglomerate Injection

The experimental apparatus for a CWF agglomerate (solid-sample) injection, shown schematically in Figure 13, consisted of: a laminar flow reactor, a solid-sample feeding system, a collection system, a two-color pyrometer, and a photographic recording system.

#### 2.3.1 Laminar Flow Reactor

Figure 14 shows a schematic diagram of the laminar flow reactor<sup>(4)</sup> (Astro Model 1000A). The furnace had electrically heated graphite elements, the temperature of which was regulated with an automated current controller. In order to protect the graphite heating elements from the oxidizing environment, the elements were isolated from the central combustion zone by an alumina muffle tube. Due to the thermal limitation imposed by the alumina, the maximum operating furnace temperature was 1800 K. The main gas, a pre-mixed oxygen inert gas, entered at a flow rate of 20-100 cm<sup>3</sup>/sec through the top of the furnace where it flowed through an alumina honeycomb at the top of the hot zone, an isothermal region of 15 cm. The honeycomb served as both a flow straightener and preheater, delivering the main gas at the specified furnace temperature with a uniform laminar velocity. The composition of oxygen/nitrogen gas mixture was regulated by dual mass flow controllers.

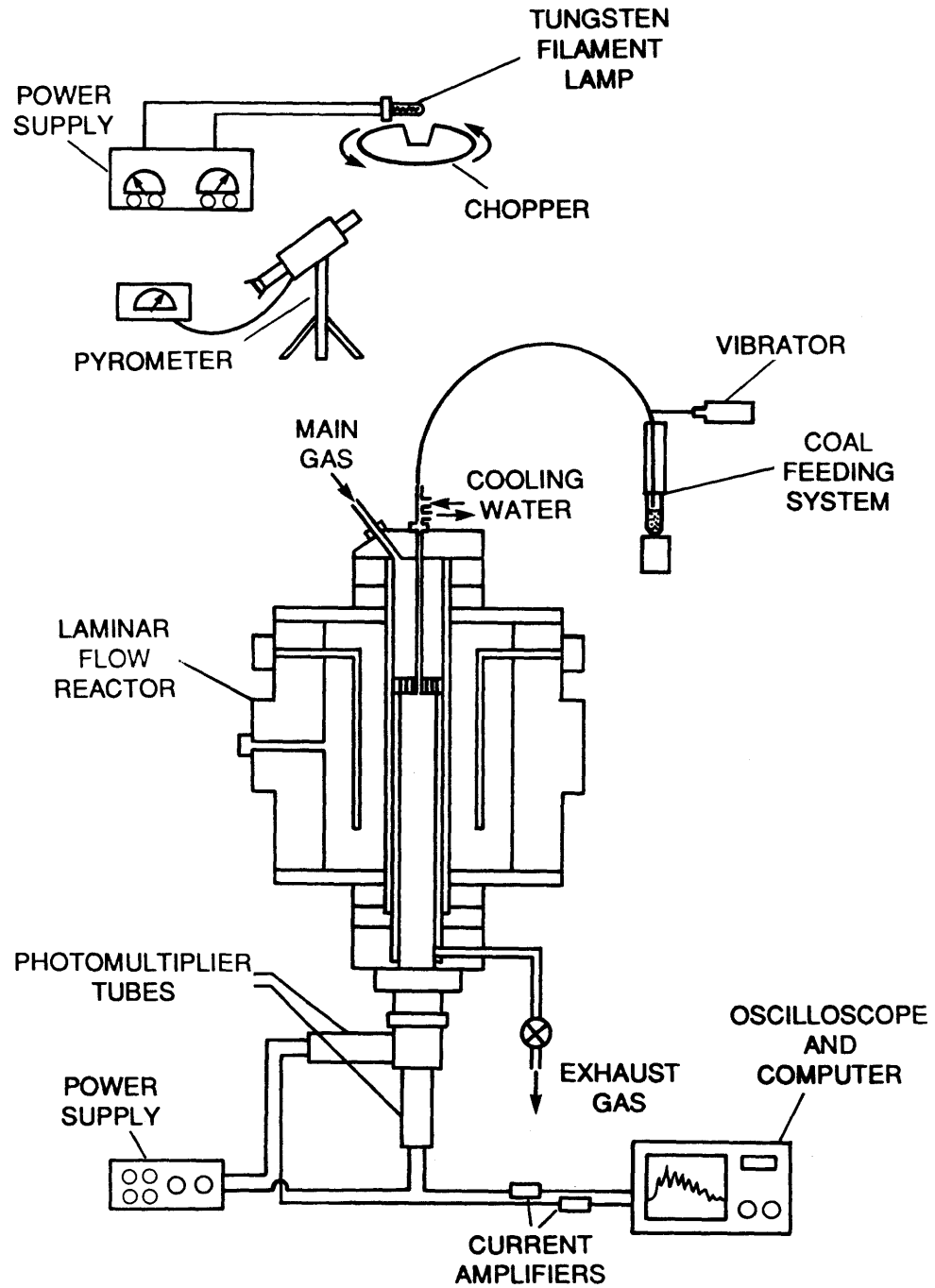


Figure 13. Schematic Diagram of Experimental Apparatus  
(CWF Agglomerate Injection)



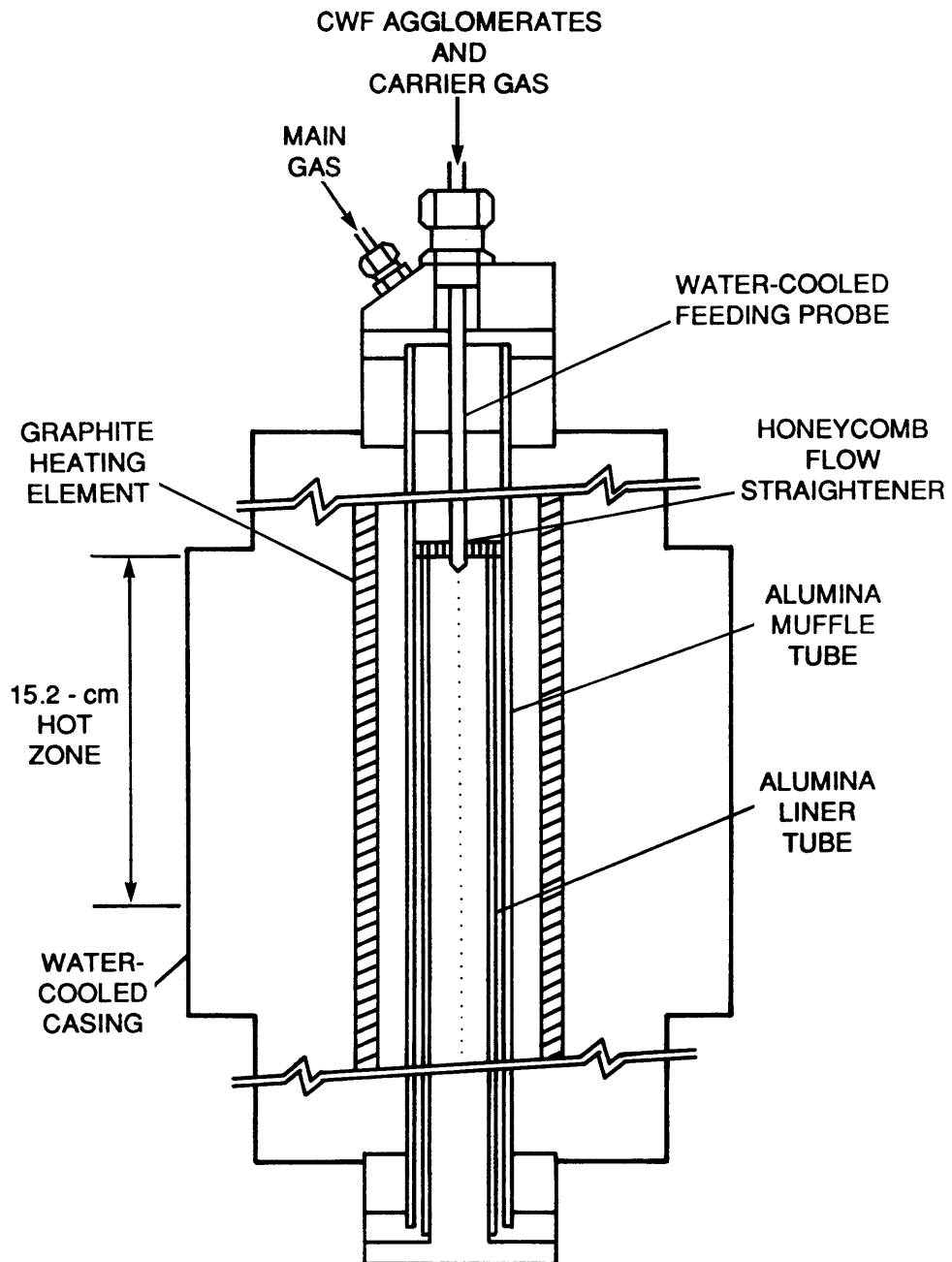


Figure 14. Schematic Diagram of Laminar Flow Reactor  
(CWF Agglomerate Injection)

Size-graded CWF agglomerates were fed through a narrow water-cooled feeder tube and injected axially into the main gas stream just below the honeycomb. The CWF agglomerates were rapidly heated and combustion began. Radial dispersion of the particles was minimized by the stable laminar flow field.

### 2.3.2 Solid-Sample Feeding System

A schematic diagram of the solid-sample feeding system is presented in Figure 15. The CWF agglomerates were entrained by the inert carrier gas, which flowed over the surface of the agitated coal bed and into the stationary fine-gauge tubing. The gas velocity in the fine-gauge tubing was sufficient to keep the particles in suspension. The rate of entrainment was established by the rate at which the coal feed vial was driven towards the stationary fine-gauge tubing by the syringe pump. A range of feeding rates from  $1.7 \times 10^{-4}$  g/sec to  $1.7 \times 10^{-3}$  g/sec was obtainable by changing the speed of the syringe pump. For a given syringe setting, a fixed clearance between the top of the coal bed and the fine-gauge tube was established after an initial transient.

### 2.3.3 Collection Probe

A schematic diagram of the collection probe is presented in Figure 16. The inner core of the water-cooled collection probe was fitted with a stainless steel porous tubing through which gas was transpired. The 1.27-cm-I.D. porous tubing was constructed from fused 5- $\mu$ m stainless steel spheres. In the top 2.5-cm section of the probe, the combustion products were rapidly quenched at a rate of  $1.0 \times 10^{-4}$  °C/sec, by a flow

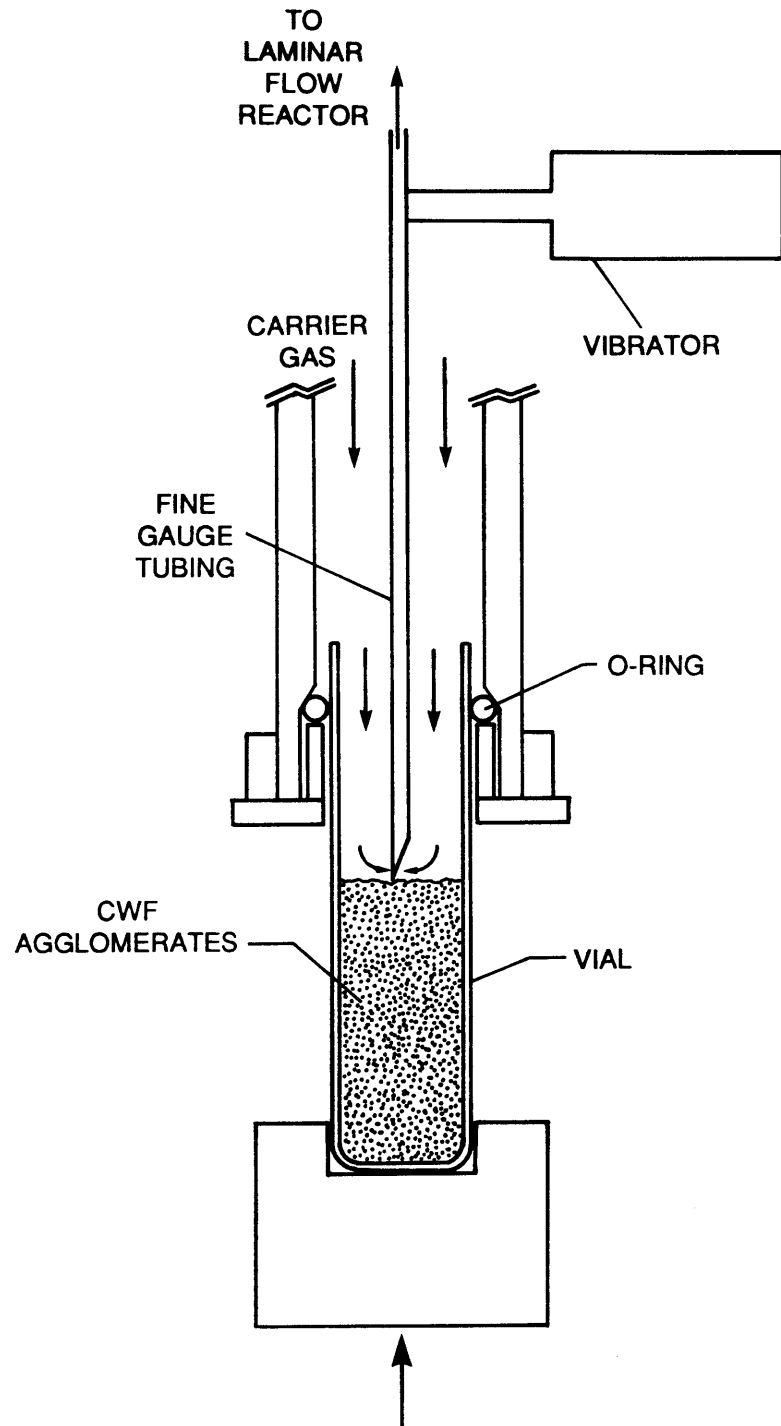


Figure 15. Schematic Diagram of Solid-Sample Feeding System

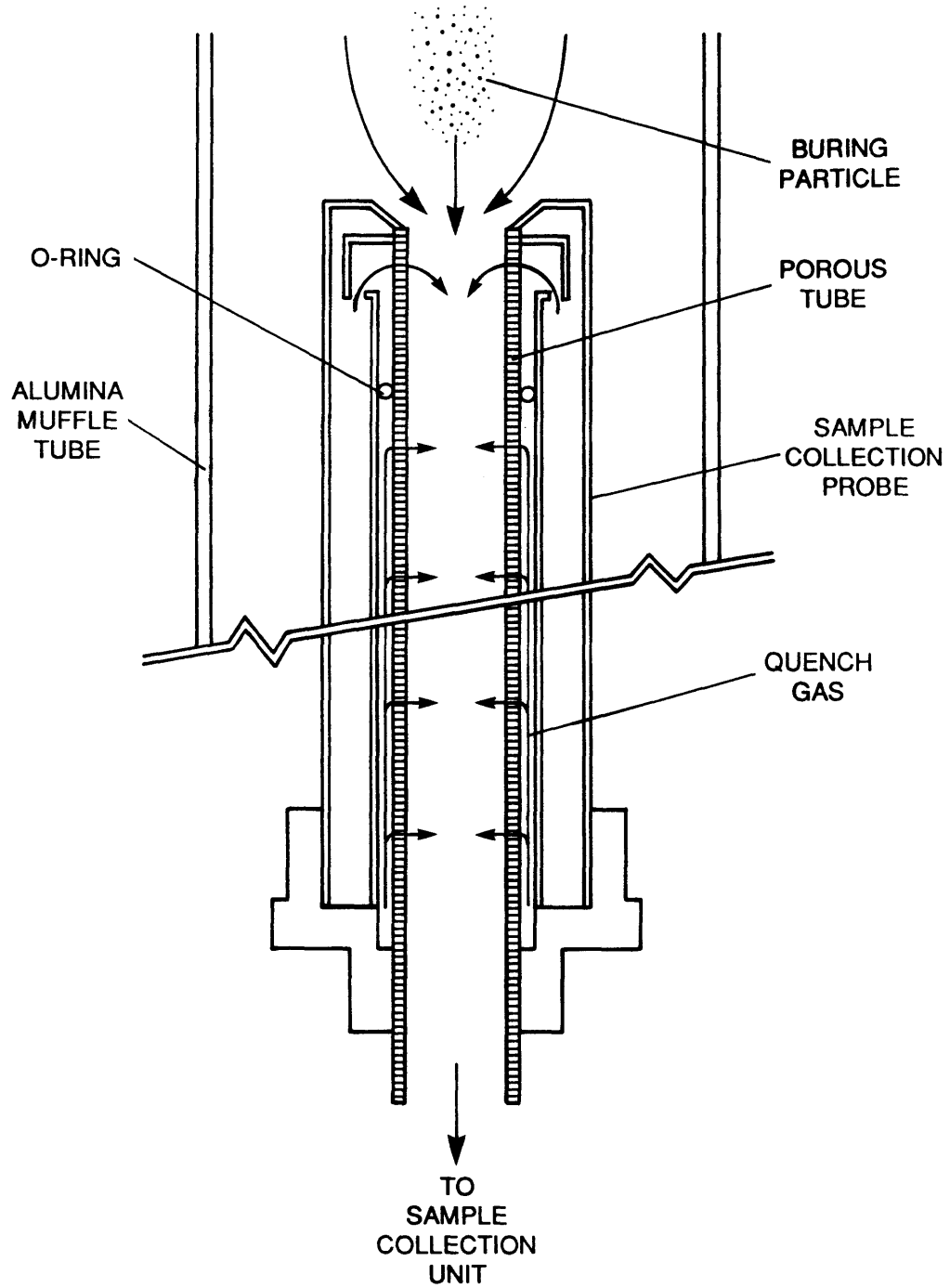


Figure 16. Schematic Diagram of Sample Collection Probe  
(CWF Agglomerate Injection)

rate of 300 cm<sup>3</sup>/sec of nitrogen. A minimal, inward radial gas flow rate of 66 cm<sup>3</sup>/sec of nitrogen, which corresponded to a gas velocity of 3.5 mm/sec, was maintained through the subsequent section of porous tubing to counter the thermophoretic velocity of the particles (e.g., 0.18 mm/sec), thereby preventing particle deposition on the inner wall of the probe.

#### 2.3.4 Fiber Optic Radiometer

Figure 13 shows a schematic diagram of the fiber optic radiometer<sup>(5)</sup> used to measure the radiation from the burning particles. A lens located at the bottom of the laminar flow reactor was used to focus the radiation from the burning particles. The particles were viewed against a dark background consisting of a water-cooled collection probe. The signals were measured by individual photomultiplier tubes, after passage through filters with effective wavelengths of 450 and 550 nm and band widths of 5 and 7 nm.

The system was calibrated with a tungsten-strip lamp, and provided a temperature resolution of 30 K at 3500 K.

## CHAPTER 3

## EXPERIMENTAL OBSERVATIONS OF CWF DROPLET COMBUSTION

3.1 Introduction

Based on high-speed cinematography and fiber optic radiometry the different stages in the CWF droplet/agglomerate\* combustion process (Figure 17) can be described as follows:

- (1) Injection of the CWF droplet
- (2) Drying of the CWF droplet
- (3) Agglomeration and swelling during the coal plasticity period
- (4) Localized ignition followed by spread of ignition
- (5) Volatile flame formation
- (6) Rotation induced by the volatile evolution
- (7) Extinction of volatile flame and ignition of char
- (8) Fragmentation both during devolatilization and char burnout
- (9) Ash shedding and completion of char burnout

The mechanism of CWF droplet/agglomerate combustion is shown in the sequential photographs which are reproduced from the high-speed cinematography in Figures 18 and 19. The time interval between each sequential photograph is labeled in these figures. The novel features of the results are the high frequency of rotation (up to 3000 cycles/sec) and fragmentation of the CWF agglomerates, which have important ramifications on the space requirements for combustion and the problems of

\* The term of CWF droplet will be used before the drying stage, and the term of CWF agglomerate, instead of CWF droplet, will be used after the drying stage.

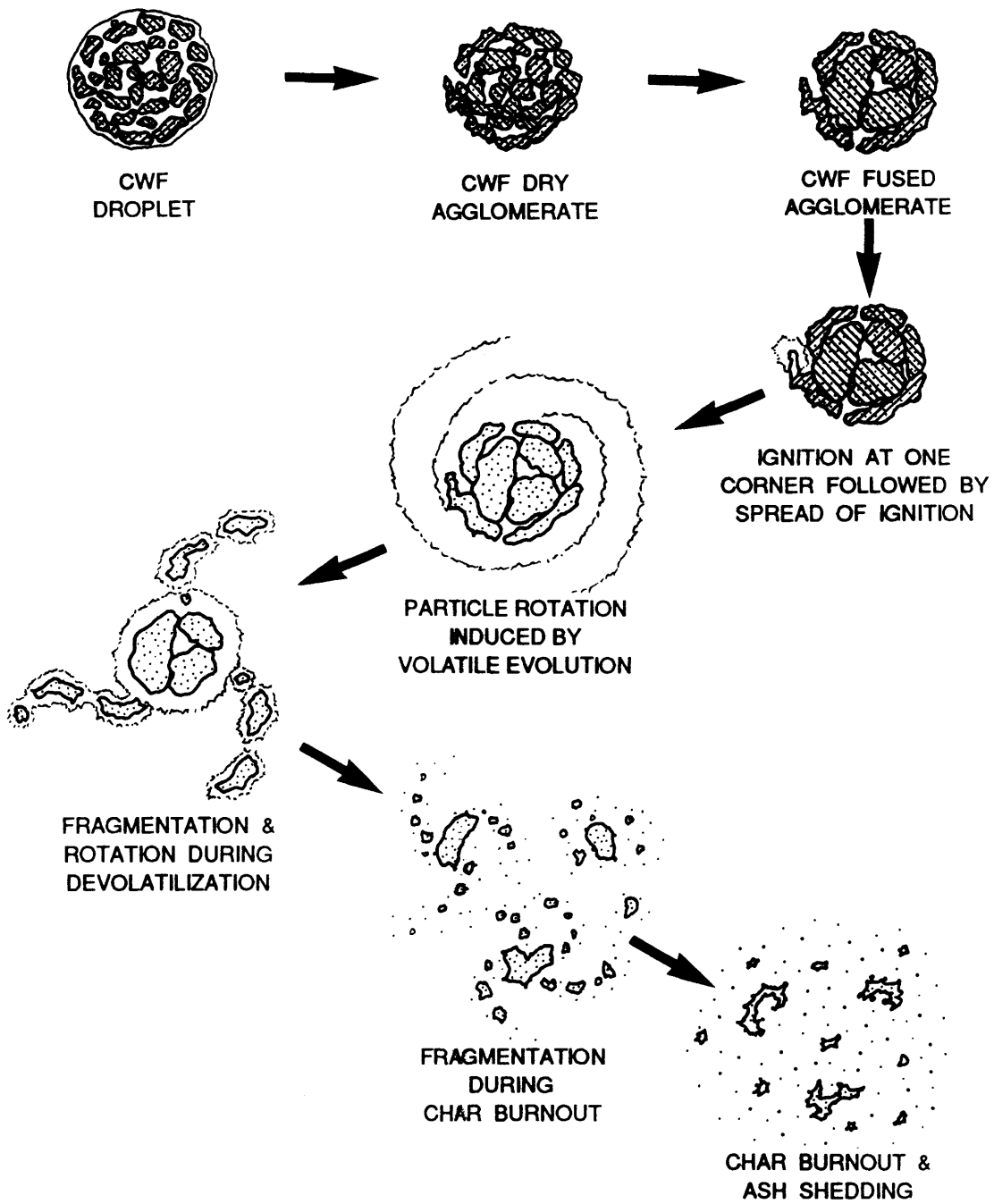


Figure 17. Mechanism of CWF Droplet Combustion

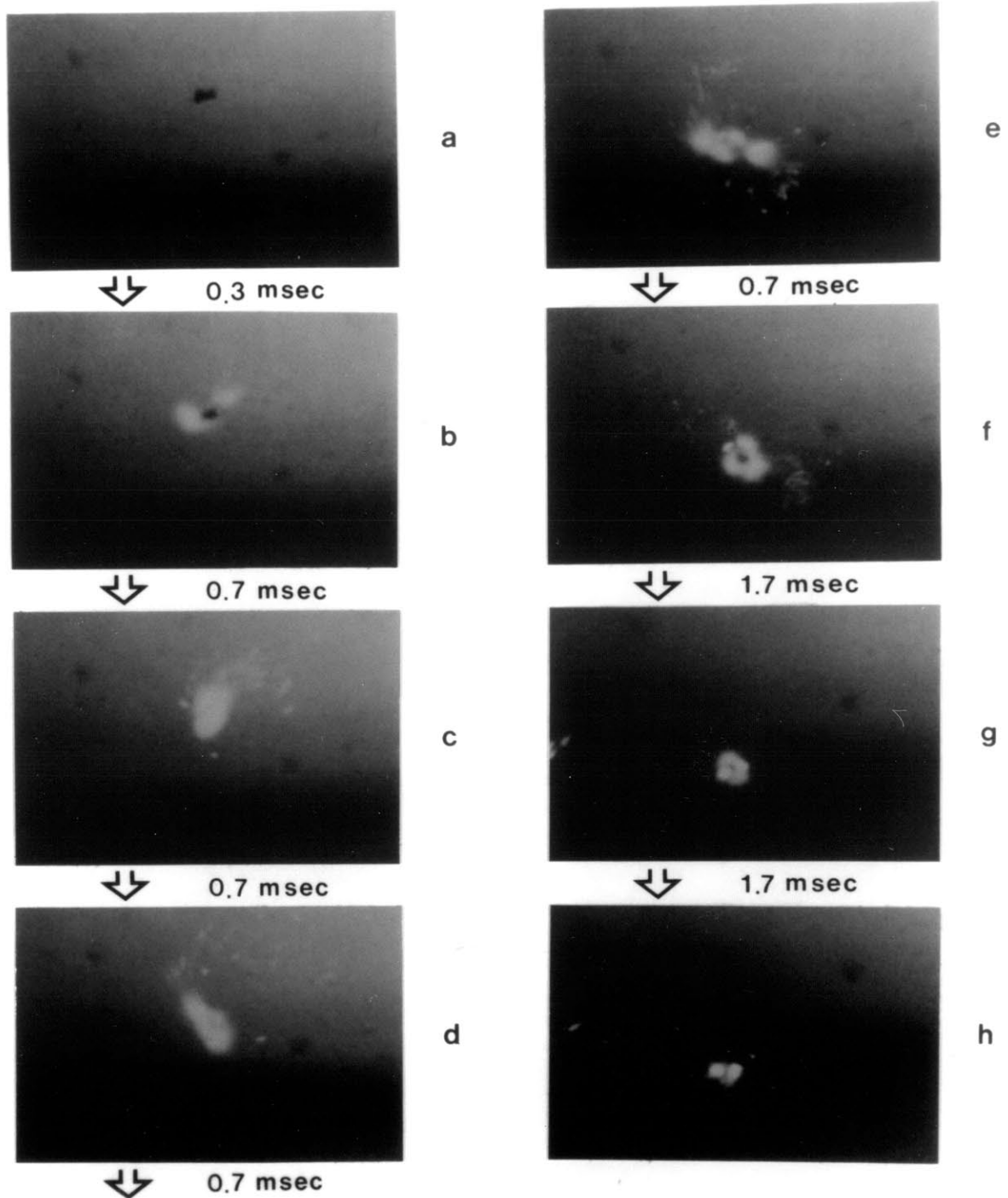


Figure 18. Sequential Photographs from High-Speed Cinematographs of CWF Droplet Combustion (Agglomerate Diameter =  $150 \mu\text{m}$ , Furnace Gas Temperature =  $1100 \text{ K}$ , Oxygen Partial Pressure =  $100 \%$ )



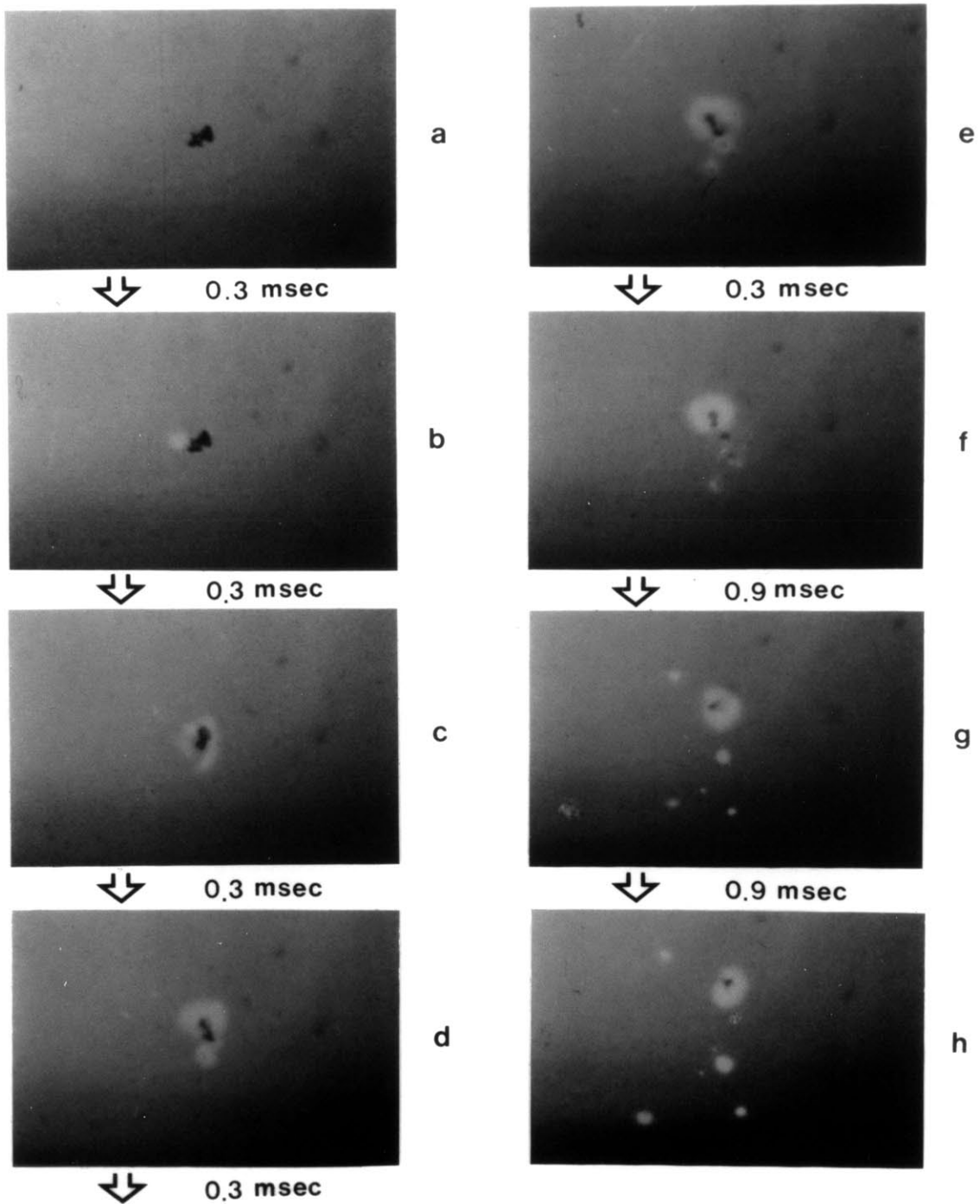


Figure 19. Sequential Photographs from High-Speed Cinematographs of CWF Droplet Combustion (Agglomerate Diameter =  $200 \mu\text{m}$ , Furnace Gas Temperature =  $1100 \text{ K}$ , Oxygen Partial Pressure =  $100 \%$ )

erosion due to ash particles. The different stages in the CWF droplet combustion process, described above, will be discussed in detail in Sections 3.2 through 3.7.

### 3.2 Ignition

Upon injection of the CWF droplet into the furnace, the interstitial water of the CWF droplet begins to evaporate. High-speed cinematography with transmission light shows that the coal particles within the CWF droplet adhere to each other, due to surface tension force. Once the outer film of water is removed, the coal particles on the surface of the CWF droplet are exposed to the hot environment. The coal particles become plastic and fuse on the outer perimeter of the CWF agglomerate. Due to the spatially non-uniform heating of the CWF agglomerate, volatile evolution and ignition occur locally at one corner of the CWF agglomerate, quickly followed by spread of ignition to the whole surface (Figures 20-A and 20-B).

### 3.3 Volatile Combustion

During devolatilization, the volatiles, emerged from the CWF agglomerate surface, burn rapidly with the available oxygen. If the volatile evolution is fast enough to displace oxygen from the CWF agglomerate surface, an envelope flame forms around the CWF agglomerate (Figures 18 and 19). The visible light emission is radiation from the soot formed by the cracking of hydrocarbon species in the fuel-rich region between the CWF agglomerate surface and the envelope flame. During this period, the CWF agglomerate is shielded from oxygen by the

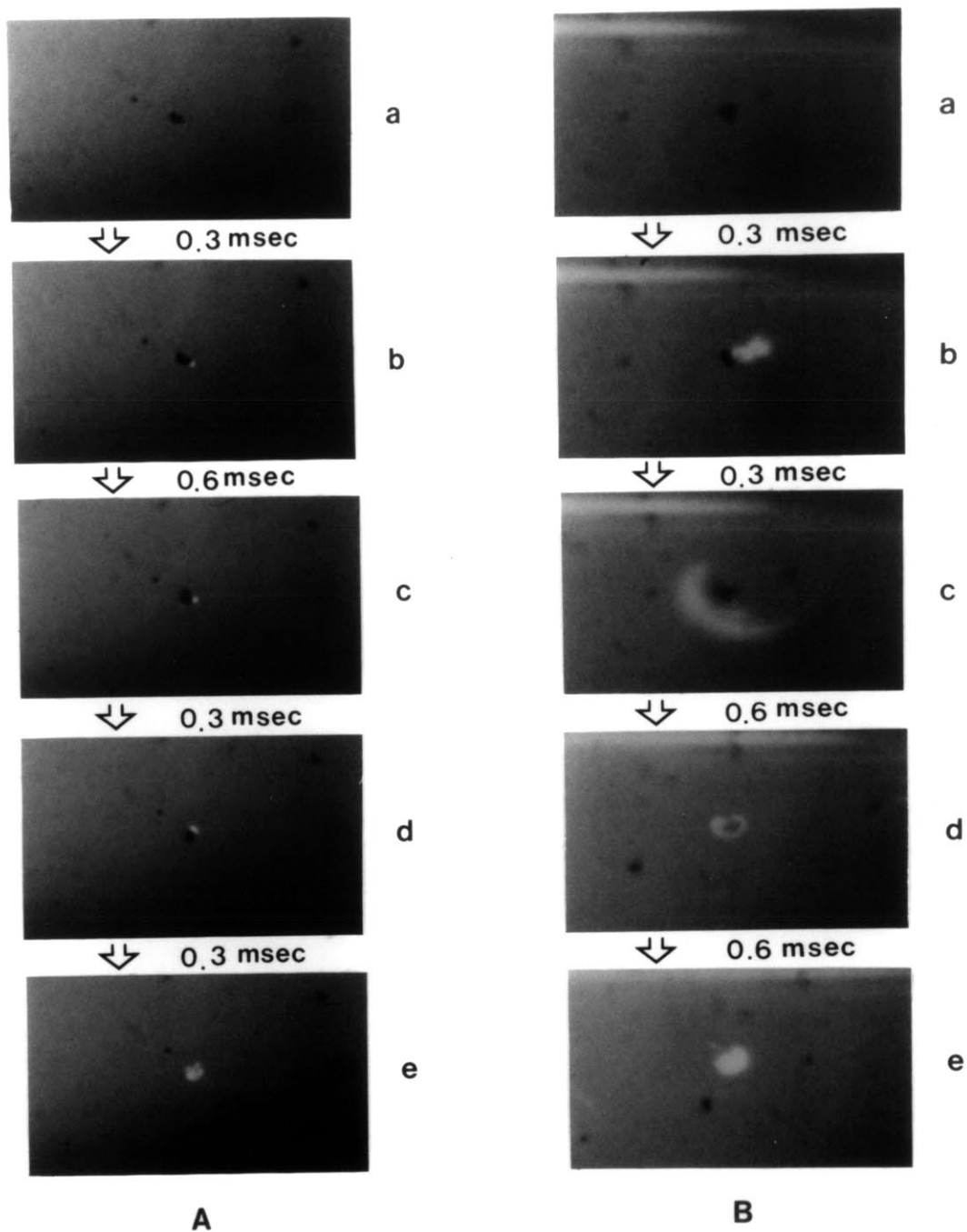


Figure 20. Sequential Photographs from High-Speed Cinematographs of CWF Droplet Combustion; Localized Ignition Followed by Spread of Ignition (Agglomerate Diameter =  $100 \mu\text{m}$  in Figure A and  $130 \mu\text{m}$  in Figure B, Furnace Gas Temperature =  $1100 \text{ K}$ , Oxygen Partial Pressure =  $100 \%$ )

volatiles and soot, but is heated by the energy fed back to the surface by the envelope flame. The radiation from the burning agglomerate is predominantly from soot particles in the high temperature zone near the flame front. The surface temperature of the CWF agglomerate is relatively low compared to the flame temperature, as evidenced by the dark core at the center of the envelope flame in the high-speed photographs (Figures 18 and 19).

The duration of the volatile flame for a CWF agglomerate diameter of 75-90  $\mu\text{m}$  and a furnace gas temperature of 1200 K ranged from 5 msec at 100 %  $\text{O}_2$  to 8 msec at 70 %  $\text{O}_2$  to 11.9 msec at 50 %  $\text{O}_2$ . There was good correspondence in the volatile combustion times between the in-situ generated CWF droplets (5.02 msec at 100 %  $\text{O}_2$ ) and re-injected CWF agglomerates (5.34 msec at 100 %  $\text{O}_2$ ), suggesting that the latter could be substituted for further experimentation<sup>(6)</sup>. At low-oxygen concentrations (less than 20 %  $\text{O}_2$ ) the volatiles evolved do not burn in a sharp flame envelope, rather, they undergo oxidation in the bulk gas phase resulting in the formation of diffuse soot clouds and trails (Figures 21 and 22).

### 3.4 Particle Rotation

Some fraction of the volatiles is ejected from the CWF agglomerate in the form of jets. The centrifugal force, generated from the momentum of the tangentially issuing jets, imparts rotation to the CWF agglomerate. High-speed photographs (Figures 18, 19, and 20-B) show that the CWF agglomerates rotate randomly in both clockwise and counter-clockwise fashion.

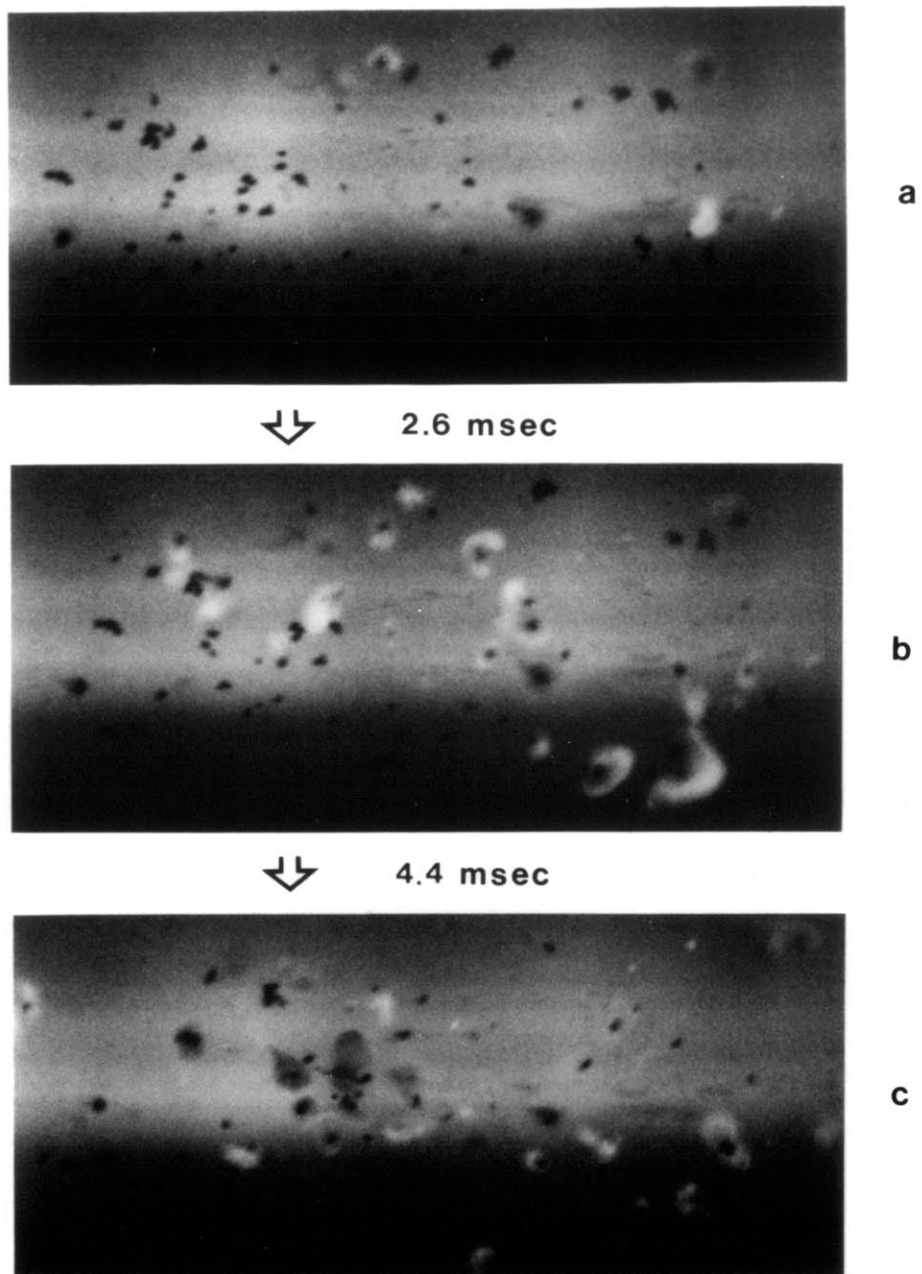


Figure 21. Sequential Photographs from High-Speed Cinematographs of CWF Droplet Combustion; Soot Clouds and Soot Trails (Agglomerate Diameter = 50-200  $\mu\text{m}$ , Furnace Gas Temperature = 1200 K, Oxygen Partial Pressure = 20 %)

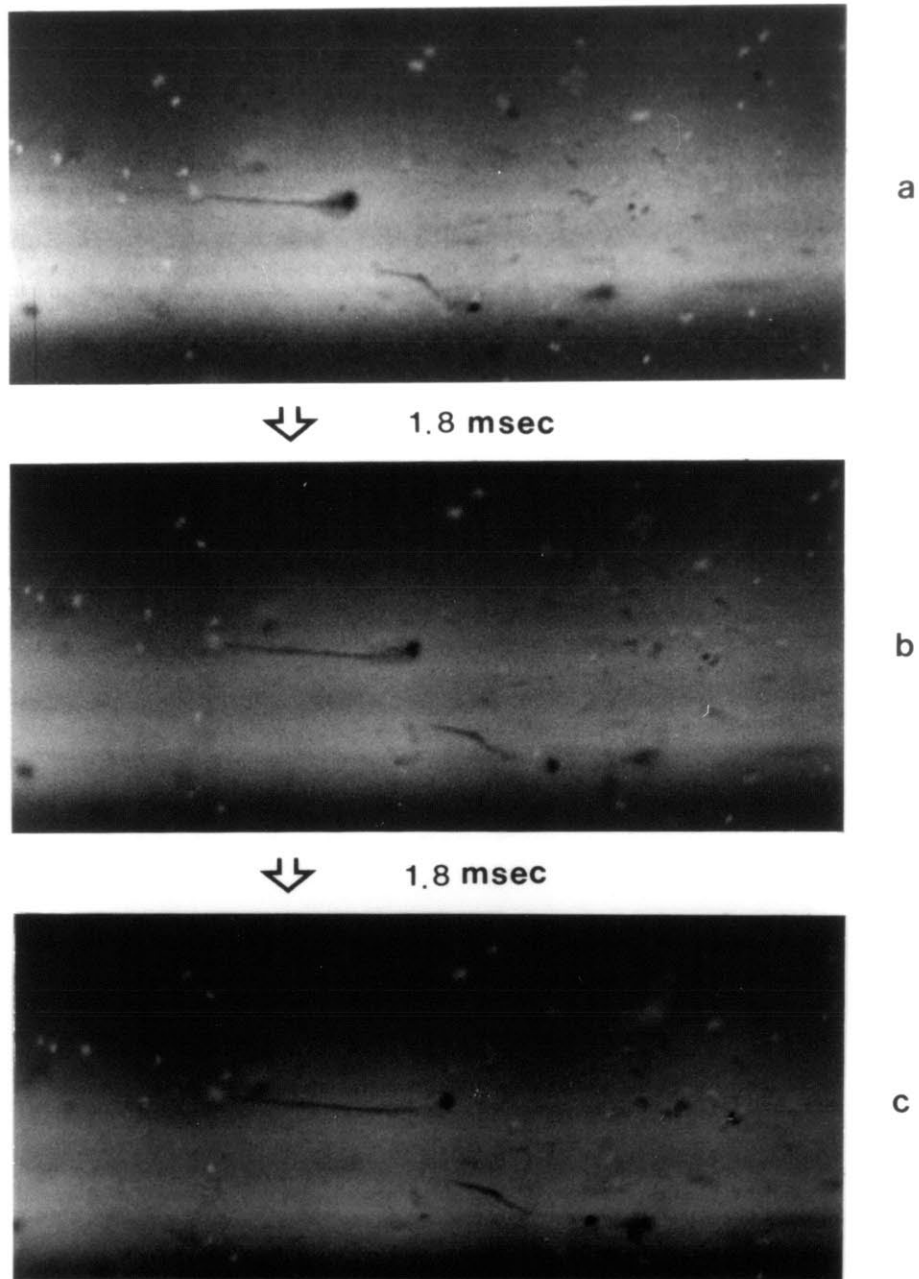


Figure 22. Sequential Photographs from High-Speed Cinematographs of CWF Droplet Combustion; Soot Clouds and Soot Trails (Agglomerate Diameter =  $150 \mu\text{m}$ , Furnace Gas Temperature =  $1200 \text{ K}$ , Oxygen Partial Pressure =  $20 \%$ )

Measurements, by fiber optic radiometry, of the radiation emitted by CWF agglomerates burning in suspension, diluted enough that only one agglomerate at a time is in the field of view, provide information about the different aspects of the combustion process and combustion time. Particle rotation can also be discerned from the intensity traces of radiation emitted by the devolatilizing/burning CWF agglomerates. Periodic oscillations in the radiation intensity traces of the CWF agglomerates are shown in Figure 23. These rotations correspond to non-spherical agglomerates which, therefore, exhibit a varying cross-sectional radiating area upon rotation. Angular velocities in Figures 23-a, 23-b, and 23-c are approximately 800, 1400, and 2800 cycles/sec, respectively, for an agglomerate diameter of 100  $\mu\text{m}$ , an oxygen partial pressure of 100 %, and a furnace gas temperature of 1750 K. An angular velocity of 1000 cycles/sec for an 100- $\mu\text{m}$ -diameter agglomerate generates centrifugal force of 200 G at the agglomerate surface. This can promote separation of weakly adhering coal particles from the CWF agglomerate during devolatilization, and of fine ash particles and fragments of char from the CWF agglomerate during char burnout. Heat and mass transfer rates to the agglomerate are, however, not significantly affected because of the relatively small rotational slip velocities (0.31 m/sec for an 100- $\mu\text{m}$ -diameter agglomerate at an angular velocity of 1000 cycles/sec) between the agglomerate surface and the surrounding gas.

### 3.5 Ignition of Char

When the rate of the volatile evolution decreases, towards the end of the devolatilization process, the flame front recedes and eventually

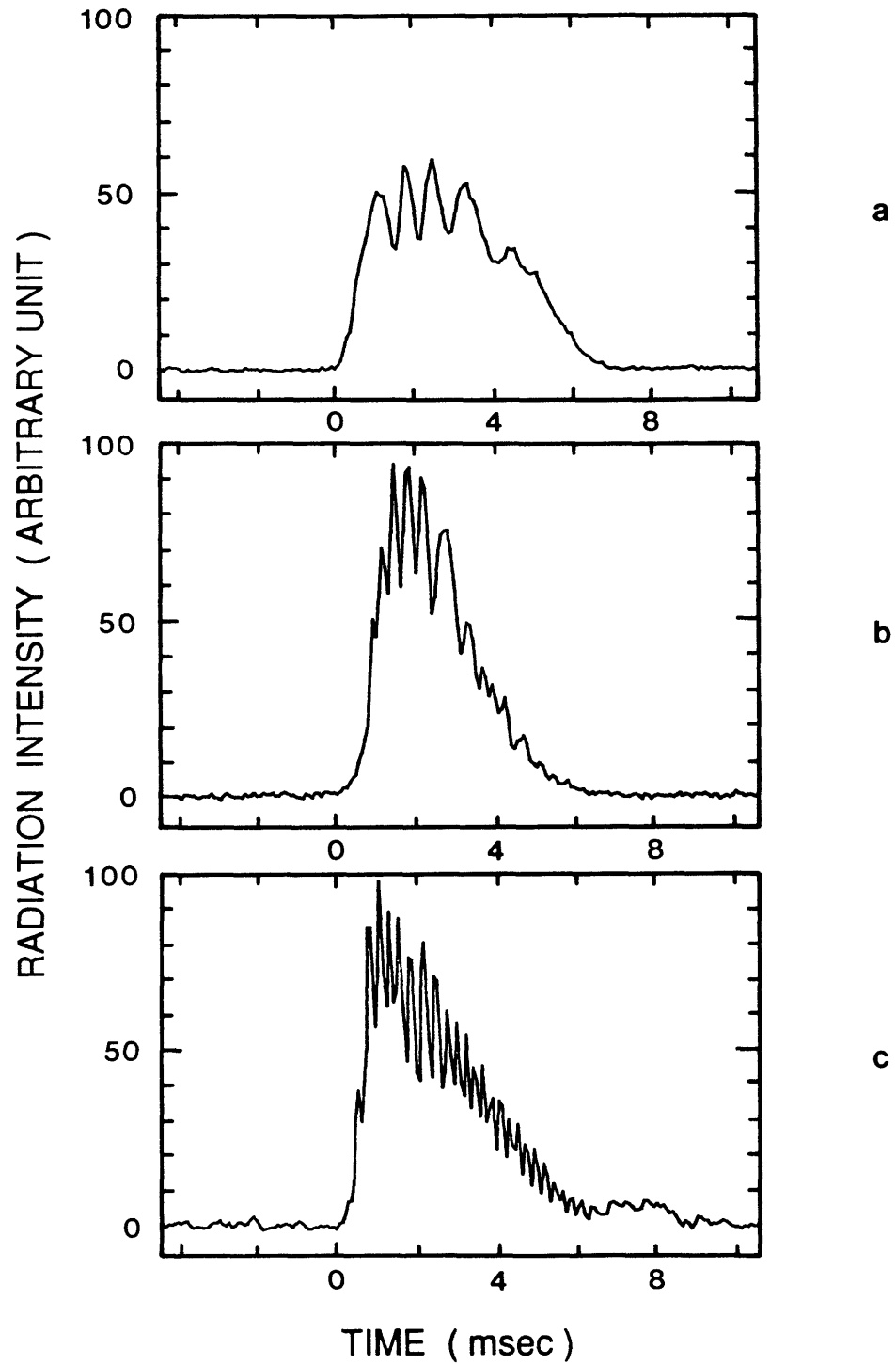


Figure 23. Radiation Intensity Traces of Rotating CWF Agglomerate (Agglomerate Diameter =  $100 \mu\text{m}$ , Furnace Gas Temperature = 1750 K, Oxygen Partial Pressure = 100 %)  
(a) 800 cycles/sec, (b) 1400 cycles/sec,  
(c) 2800 cycles/sec



the volatile flame is extinguished. The devolatilized CWF agglomerate is heated predominantly by the ambient gas, until the oxidation reaction becomes fast enough and the CWF agglomerate reignites. This ignition delay between devolatilization and char burnout is a function of the furnace gas temperature and the oxygen partial pressure. It varies from about 7 msec at 20 % oxygen partial pressure to a fraction of a millisecond at 70 % O<sub>2</sub> for a CWF agglomerate diameter of 75-90 μm at a furnace gas temperature of 1200 K<sup>(6)</sup>.

### 3.6 Char Burnout

Char burnout times can be determined by either high-speed cinematography or fiber optic radiometry. It is found that a CWF agglomerate diameter of 75-90 μm has a burnout time of 36.3 msec at 50 % O<sub>2</sub> and 20 msec at 70 % O<sub>2</sub> for a furnace gas temperature of 1200 K. Char burnout times for in-situ generated and re-injected CWF agglomerates show a close agreement, corroborating the similarity between the two cases<sup>(6)</sup>.

### 3.7 Fragmentation

The other important phenomenon, the extent of which increases with increasing furnace gas temperature and oxygen partial pressure in the furnace, is fragmentation. Fragmentation of the CWF agglomerate is seen to occur during both devolatilization (Figure 19) and char burnout (Figure 24). Some of the radiation traces (Figure 25) show bursts in intensity. These increases in radiant emissions can be attributable to the increase in the projected area of the radiating mass which is caused by fragmentation. The above inference drawn from the radiation intensity

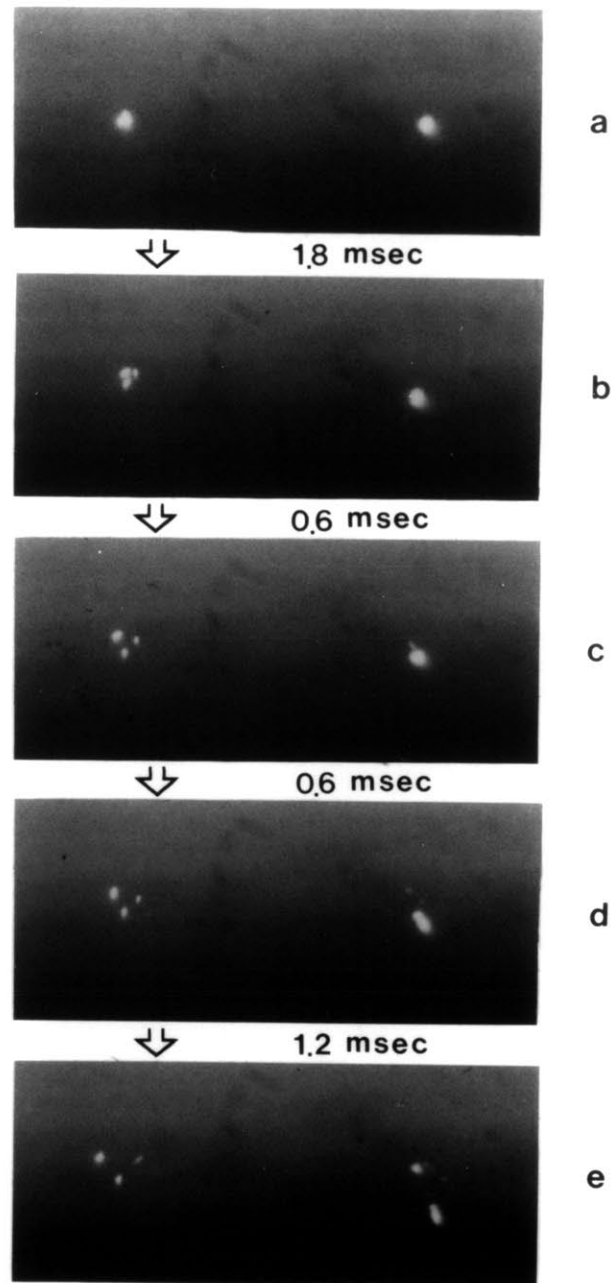


Figure 24. Sequential Photographs from High-Speed Cinematographs of CWF Droplet Combustion; Fragmentation during Char Burnout (Agglomerate Diameter = 160-180  $\mu\text{m}$ , Furnace Gas Temperature = 1400 K, Oxygen Partial Pressure = 100 %)

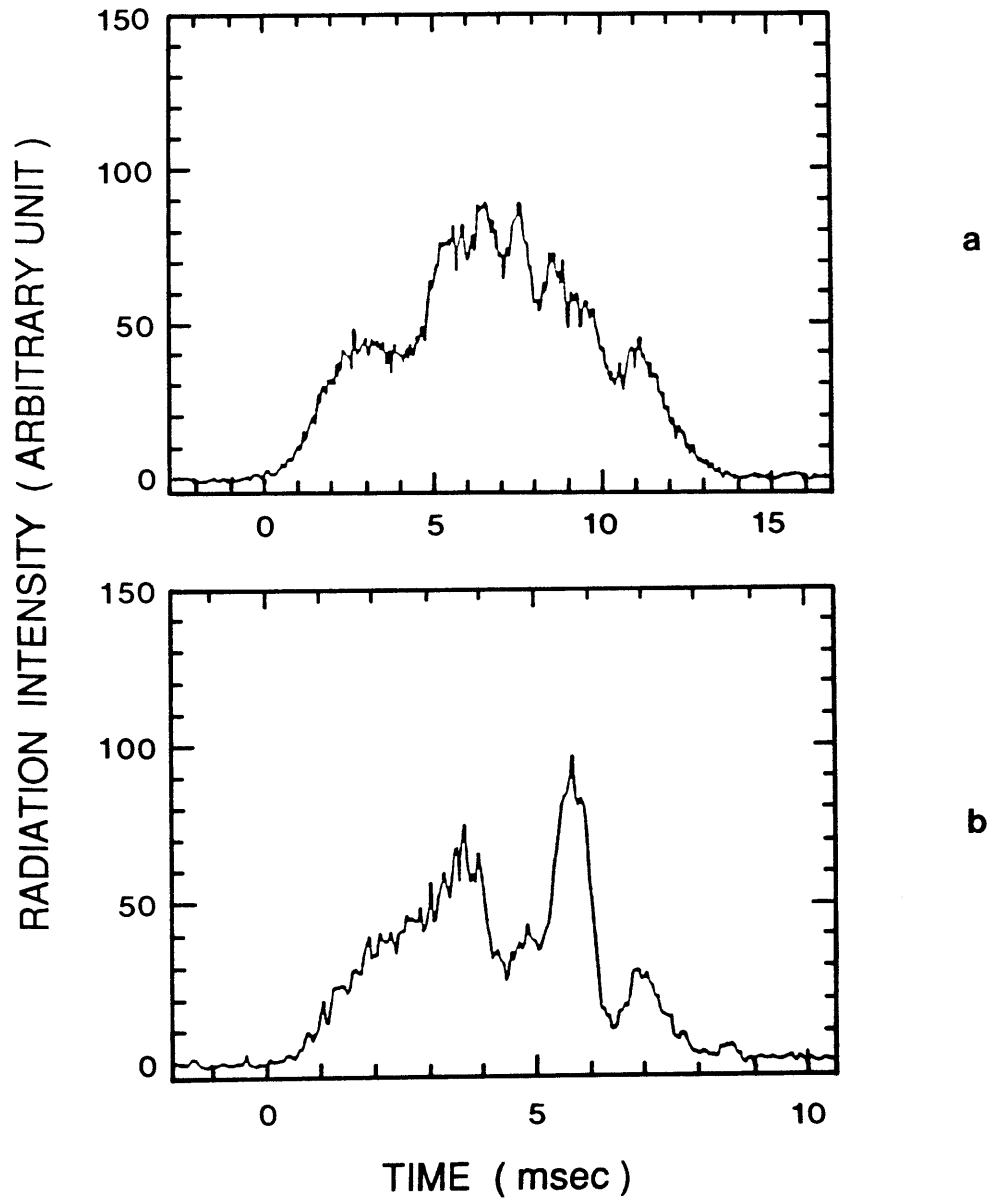


Figure 25. Radiation Intensity Traces of Burning CWF Agglomerate; Fragmentation during Char Burnout

traces is confirmed by the high-speed photographic records of the combustion history of the CWF agglomerates.

The time-temperature history of the CWF agglomerate is seen to be important in determining the extent of fragmentation. From the viscosity-temperature relationship, at higher heating rates, the period of plasticity of bituminous coal becomes shorter<sup>(7)</sup>. It is conceivable that, during pyrolysis, high heating rates can result in CWF agglomerates with lower bond strength. The centrifugal force, generated by particle rotation, can promote separation of weakly adhering coal particles (Figure 19), and the excess pressure from the combination of trapped water vapor and volatiles generated within, can also break up such CWF agglomerates into their constituent coal particles. The extent of this bulk fragmentation phenomenon (Figure 19), which results in the breakup of relatively large fragments, will strongly determine the benefits of grinding the coal to a smaller size.

The other fragmentation mechanism by which the breakup can occur is percolative perimeter fragmentation<sup>(8)</sup>, due to thin layers of carbonaceous material separating from the char particle circumference. In the pore diffusion controlled regime in which most CWF agglomerates and pulverized coal chars burn at typical conditions, oxygen penetrates only partially into the pores of the particle. As carbon is consumed in the outer regions of the particle, the porosity increases, and the structural strength of this region decreases. Beyond a critical fragmentation porosity ( $\phi^* \sim 0.85$ )<sup>(9)</sup>, the integrity of the solid matrix is lost, and satellite fragments from the outer perimeter of the parent particle, corresponding to  $\phi > \phi^*$ , escape and burn separately. This

percolative perimeter fragmentation during char burnout is shown in Figure 24.

In parallel experiments, coal particles and CWF agglomerates of the same size were burnt under the same combustion conditions. Negligible fragmentation was seen for the coal particles, as opposed to extensive fragmentation, during both pyrolysis and char burnout, for the CWF agglomerates<sup>(6)</sup>. Clearly, the fragmentation phenomenon is strongly dependent on the agglomerate formation process which is influenced by the time-temperature history of the CWF agglomerate.

Holve et al.<sup>(10)</sup> using a single particle counter have followed the size of particles generated by combustion of CWF droplets injected into a premixed methane-air flame. They report no significant particle fragmentation during combustion. However, in their experiments they obtained only fractional carbon conversion (about 70 %) and the temperature of their burning particles was reduced in the flame by radiation losses to a cold environment. It is important to determine the conditions under which fragmentation is favored since fragmentation is useful both from the point of view of burnout and obtaining finer fly-ash particle size distribution. Increasing the extent of fragmentation will reduce considerably the time required for the burnout of the CWF agglomerates and decrease the size of fly-ash particles because of their origin from smaller parent fragments, thus enhancing the potential benefits of grinding the coal to a finer size<sup>(11)</sup>.

CHAPTER 4  
THEORETICAL MODELS

4.1 Model of Particle Rotation

4.1.1 Introduction

During the devolatilization process, some fraction of the volatiles, ejected from the CWF agglomerate (or CWF particle)\* in the form of jets, imparts rotation to the CWF agglomerate. The results of high-speed cinematography and fiber optic radiometry show rotation of CWF agglomerates during devolatilization and char burnout.

The centrifugal force, generated from the resultant angular momentum due to the tangential component of the issuing volatile jets, can promote separation of weakly adhering coal particles from the CWF agglomerate during devolatilization, and of fine ash particles and fragments of char from the CWF agglomerate during char burnout. The angular velocity of a rotating CWF agglomerate, which is directly related to the centrifugal force, is correlated with the volatile yield and the rate of volatile evolution.

4.1.2 Derivation of Angular Velocity of Rotating CWF Agglomerate

Volatiles given off during the heating of a coal particle will impart a torque depending on their velocity and on the orientation and size of the pores through which they evolve. The angular rotation of a particle will be determined by the net torque produced by all of the volatile jets, and will vary from particle to particle.

\* The terms CWF agglomerate and CWF particle are used interchangeably.

Figure 26 shows a schematic diagram of a rotating CWF agglomerate. In this model, the CWF agglomerate is assumed to be spherical, and the exit velocity of the volatile jet at each devolatilization pore is assumed to be uniform. A derivation of angular velocity without this assumption of uniform exit velocity will be discussed in Appendix A.

The angular momentum of the rotating CWF agglomerate is generated by the tangential component of the volatile jet issuing at angles  $\phi_i$  and  $\theta_i$ .  $\phi_i$  is the angle between the volatile jet and the horizontal plane, perpendicular to the rotational axis, and  $\theta_i$  is the angle between two lines on the horizontal plane: the line perpendicular to the particle radius at the pore mouth and the projection of the volatile jet on the same plane. The tangential component of the exit velocity of the issuing volatile jet is expressed as

$$(v_e)_{\text{tangential}} = v_e \cos\theta_i |\cos\phi_i| \quad \text{eq. (1)}$$

Here, the exit velocity ( $v_e$ ) of volatile jet at each devolatilization pore with the assumption of the uniform exit velocity is derived as

$$v_e = \frac{M_o \left( \frac{dV}{dt} \right)}{\rho_{\text{vol}} \sum_{i=1}^n A_i} \quad \text{eq. (2)}$$

where  $\sum_{i=1}^n A_i$  is the total cross-sectional exit area of all the devolatilization pores on the outer surface of the CWF agglomerate, which can be obtained from the experimental data of the agglomerate porosity, (i.e., total cross-sectional exit area = total exit area + 2 = outer surface area of agglomerate x agglomerate apparent porosity + 2).<sup>(12)</sup> The rate of mass loss of volatiles per unit original agglomerate mass is given by

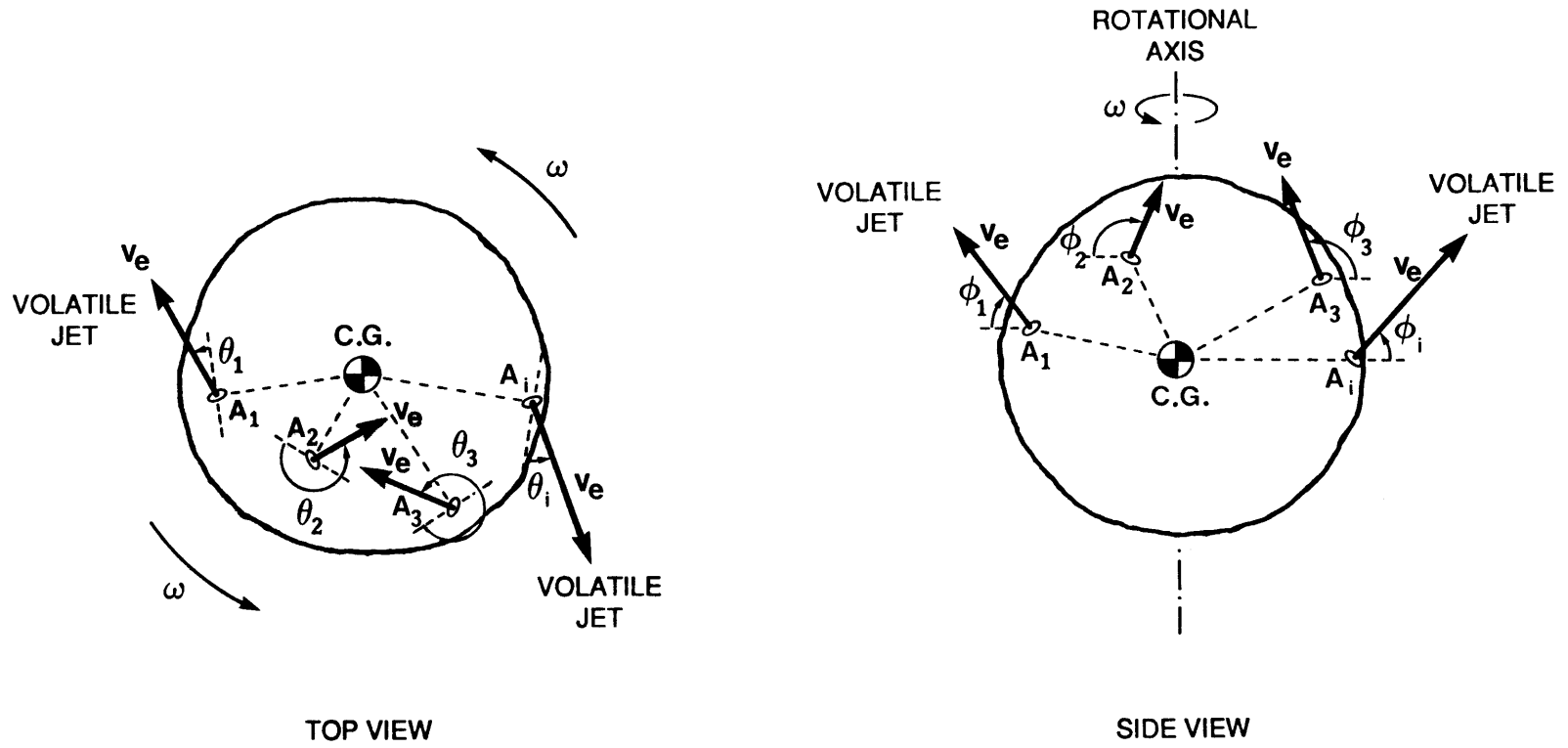


Figure 26. Schematic Diagram of Rotating CWF Agglomerate



$dV/dt$ , while  $M_0$  and  $\rho_{vol}$  denote the original mass of CWF agglomerate and the density of the volatiles, respectively.

In order to derive the differential equation for the angular velocity of the rotating CWF agglomerate, the angular momentum equation in an inertial reference frame is applied as

Angular Momentum Equation

$$\frac{d}{dt} \left[ \int_{cv} \vec{r}_{cv} \times \rho_{cv} \vec{v}_{cv} dV \right] + \int_{cs} \vec{r}_{cs} \times \vec{v}_{cs} \rho_{cs} (\vec{v}_{rel} \cdot \vec{n}) dA = \Sigma \vec{M}$$

eq. (3)

where  $cv$  = control volume of the CWF agglomerate

$cs$  = control surface which is defined as the outer surface of the CWF agglomerate and cross-sectional surface of each devolatilization pore on the outer surface of the CWF agglomerate

$V$  = volume

$A$  = surface

$\rho$  = density

$\vec{r}_{cv}$  = position vector from the origin of the center of gravity (CG) in the control volume, and given by  $r\vec{i}_r$

$\vec{r}_{cs}$  = position vector from the origin of CG to the control surface, and given by  $R\vec{i}_r$

$\vec{v}_{cv}$  = absolute velocity in the control volume as observed in the inertial reference frame, and given by  $r\omega\vec{i}_\theta$

$\vec{v}_{cs}$  = absolute fluid velocity on the control surface as observed in the inertial reference frame, and given by  $(R\omega - v_e \cos\theta_i |\cos\phi_i|)\vec{i}_\theta$

$\vec{v}_{rel}$  = local fluid velocity relative to the control surface

$\vec{\Sigma} M =$  sum of the moments about the origin of CG

$\vec{n} =$  unit vector normal to surface A

$\vec{i}_r =$  r-directional unit vector

$\vec{i}_\theta =$   $\theta$ -directional unit vector

$\vec{i}_z =$  z-directional unit vector

$$(\vec{r}_{cv} \times \vec{v}_{cv}) = r^2 \omega \vec{i}_z$$

$$(\vec{r}_{cs} \times \vec{v}_{cs}) = R (R\omega - v_e \cos\theta_i |\cos\phi_i|) \vec{i}_z$$

$$(\vec{v}_{rel} \cdot \vec{n}) = v_e$$

R = radius of the CWF agglomerate

r = radial distance from the origin of CG

t = time

The angular momentum equation for the rotational axis (i.e., axial z-component) of the CWF agglomerate in the inertial reference frame is

$$\frac{d}{dt} \left( \int_{cv} \rho_A r^2 \omega \, dV \right) + \int_{cs} R (R\omega - v_e \cos\theta_i |\cos\phi_i|) \rho_{vol} v_e \, dA = -M_F \quad \text{eq. (4)}$$

where  $\rho_A$  denotes the apparent density of the CWF agglomerate at time t, and  $M_F$  denotes the frictional moment of the CWF agglomerate during particle rotation. According to Lamb<sup>(13)</sup>, the frictional moment  $M_F$  of the particle during particle rotation for the low Reynolds number flow condition is expressed as

$$M_F = 8 \pi R^3 \mu_{vol} \omega \quad \text{eq. (5)}$$

where  $\mu_{vol}$  denotes the viscosity of the volatiles.

The above expression for the frictional moment applies when the rotational Reynolds number  $Re_r$  is much smaller than five<sup>(14)</sup>; i.e., when

$$\text{Re}_r = \frac{\rho R^2 \omega}{\mu} \ll 5$$

where  $\rho$  and  $\mu$  denote the density and the viscosity, respectively, of the surrounding gas. In the present model, the rotational Reynolds number of the rotating CWF agglomerate is found to be smaller than one.

From eqs. (4) and (5), the angular momentum equation is expressed as

$$\begin{aligned} \frac{d\omega}{dt} + \left( \frac{1}{\rho_A} \frac{d\rho_A}{dt} + \frac{5 \rho_{\text{vol}} v_e \left( \sum_{i=1}^n A_i \right)}{4 \pi R^3 \rho_A} + \frac{10\mu_{\text{vol}}}{\rho_A R^2} \right) \omega \\ = \frac{5 \rho_{\text{vol}} v_e^2}{4 \pi R^4 \rho_A} \left( \sum_{i=1}^n A_i \cos\theta_i |\cos\phi_i| \right) \end{aligned} \quad \text{eq. (6)}$$

where  $A_i$  denotes the cross-sectional exit area of each devolatilization pore. During the devolatilization process, the density of the CWF agglomerate ( $\rho_A$ ) can be expressed as

$$\rho_A = \frac{M_o [1-V]}{\frac{4}{3} \pi R^3} \quad \text{eq. (7)}$$

where  $V$  is the mass of the volatiles evolved up to time  $t$  per unit original mass of the CWF agglomerate. The swelling of the CWF agglomerate during devolatilization is assumed to be negligible, and therefore, the agglomerate radius  $R$  is assumed to remain constant. The first time-derivative of  $\rho_A$  is expressed as

$$\frac{d\rho_A}{dt} = \frac{-M_o \left( \frac{dV}{dt} \right)}{\frac{4}{3} \pi R^3} \quad \text{eq. (8)}$$

From eqs. (2), (6), (7), and (8), the differential equation for the angular velocity of the rotating CWF agglomerate is

$$\begin{aligned} \frac{d\omega}{dt} + \left[ \frac{\frac{2}{3} M_o \left( \frac{dV}{dt} \right) + \frac{40}{3} \pi R \mu_{vol}}{M_o (1-V)} \right] \omega \\ = \frac{5M_o}{3R\rho_{vol} \sum_{i=1}^n A_i} \left[ \frac{\sum_{i=1}^n A_i \cos\theta_i |\cos\phi_i|}{\sum_{i=1}^n A_i} \right] \frac{\left( \frac{dV}{dt} \right)^2}{(1-V)} \end{aligned} \quad \text{eq. (9)}$$

Here, a geometrical factor of the devolatilization pores  $\left[ \frac{\sum A_i \cos\theta_i |\cos\phi_i|}{\sum A_i} \right]$  is dependent on the geometry and the cross-sectional exit area of the individual devolatilization pore.

The initial condition of eq. (9) is

$$\omega(0) = 0 \quad \text{eq. (10)}$$

From eqs. (9) and (10), the angular velocity of the rotating CWF agglomerate is

$$\begin{aligned} \omega(t) = \frac{5 M_o}{3 R \rho_{vol} \sum_{i=1}^n A_i} \left[ \frac{\sum_{i=1}^n A_i \cos\theta_i |\cos\phi_i|}{\sum_{i=1}^n A_i} \right] \\ \times \exp \left[ - \int_0^t \frac{\frac{2}{3} M_o \left( \frac{dV}{dt} \right) + \frac{40}{3} \pi R \mu_{vol}}{M_o (1-V)} dt \right] \\ \times \int_0^t \left[ \frac{\left( \frac{dV}{dt} \right)^2}{(1-V)} \exp \left( \int_0^t \frac{\frac{2}{3} M_o \left( \frac{dV}{dt} \right) + \frac{40}{3} \pi R \mu_{vol}}{M_o (1-V)} dt \right) \right] dt \end{aligned} \quad \text{eq. (11)}$$

Here,  $V$  and  $dV/dt$  are obtained from devolatilization and heat transfer models. Of the many models available, the Kobayashi's<sup>(15)</sup> devolatilization model has been selected because of its simplicity of use; although the kinetic parameters are subject to discussion, the use of this model was found to be adequate, in that there was a close agreement between this model and the measured devolatilization times (volatile flame duration).

#### 4.1.3 Angular Velocity of Rotating CWF Agglomerate for an Isothermal Devolatilization Process

In order to simplify the general expression [eq. (11)] of the angular velocity of the rotating CWF agglomerate during devolatilization, the following assumptions are added:

- (1) The CWF agglomerate temperature, and therefore, the devolatilization rate constant  $k$ , are assumed to remain constant during devolatilization (i.e., isothermal devolatilization).
- (2) The devolatilization process is assumed to be described by the following global single reaction model:

$$\frac{dV}{dt} = k (V^* - V)$$

where  $k$  denotes the devolatilization rate constant and  $V^*$  denotes the ultimate volatile mass loss per unit original mass of the CWF agglomerate.  $V$  and  $\frac{dV}{dt}$  have been defined in Section 4.1.2.

Based upon the above additional assumptions, the volatile mass loss per unit original agglomerate mass ( $V$ ) is derived as

$$V = V^* [1 - \exp(-kt)] \quad \text{eq. (12)}$$

and the rate of the volatile mass loss per unit original agglomerate mass is

$$\frac{dV}{dt} = k V^* \exp(-kt) \quad \text{eq. (13)}$$

From eqs. (2) and (13), the exit velocity of the volatile jet evolved at time  $t$  is derived as

$$v_e = \frac{M_o \left( \frac{dV}{dt} \right)}{\rho_{vol} \sum_{i=1}^n A_i} = \frac{M_o k V^* \exp(-kt)}{\rho_{vol} \sum_{i=1}^n A_i} \quad \text{eq. (14)}$$

From eqs. (4), (5), and (14), the angular momentum equation for the rotational axis of the CWF agglomerate in the inertial reference frame is

$$\frac{d}{dt} \left[ \frac{4}{5} \pi R^5 \rho_A \omega \right] + \sum_{i=1}^n R \left[ R \omega - v_e \cos \theta_i |\cos \phi_i| \right] \rho_{vol} v_e A_i = -8\pi R^3 \mu_{vol} \omega \quad \text{eq. (15)}$$

Here, the density of the CWF agglomerate at time  $t$  is

$$\rho_A = \frac{M_o [1 - V^* (1 - \exp(-kt))]}{\frac{4}{3} \pi R^3} \quad \text{eq. (16)}$$

From eqs. (14), (15), and (16), the differential equation for the angular velocity of the rotating CWF agglomerate is

$$\frac{d\omega}{dt} + \left[ \frac{c_1 \exp(-kt) + c_2}{c_3 \exp(-kt) + c_4} \right] \omega = \frac{c_5 \exp(-2kt)}{c_3 \exp(-kt) + c_4} \quad \text{eq. (17)}$$

where  $c_1 = \frac{2}{3} M_o V^* k$

$$c_2 = \frac{40}{3} \pi R \mu_{vol}$$

$$c_3 = M_o V^*$$

$$c_4 = M_o (1-V^*)$$

$$c_5 = \frac{5 M_o^2 V^{*2} k^2}{3 R \rho_{vol} \sum_{i=1}^n A_i} \left( \frac{\sum_{i=1}^n A_i \cos \theta_i |\cos \phi_i|}{\sum_{i=1}^n A_i} \right)$$

From eqs. (10) and (17), the angular velocity of the rotating CWF agglomerate for the isothermal devolatilization process and the devolatilization model of the global single reaction is derived as

$$\omega(t) = \frac{\frac{5 M_o^2 V^{*2} k^2}{3 R \rho_{vol} \sum_{i=1}^n A_i} \left( \frac{\sum_{i=1}^n A_i \cos \theta_i |\cos \phi_i|}{\sum_{i=1}^n A_i} \right)}{\left( M_o \{V^* \exp[-kt] - V^* + 1\} \left( \frac{40 \pi R \mu_{vol}}{3 M_o (1-V^*) k} - \frac{2}{3} \right) \exp \left( \frac{40 \pi R \mu_{vol} t}{3 M_o (1-V^*)} \right) \right)}$$

$$\times \int_0^t \left[ \left( M_o \{V^* \exp[-kt] - V^* + 1\} \left( \frac{40 \pi R \mu_{vol}}{3 M_o (1-V^*) k} - \frac{5}{3} \right) \exp \left( \frac{40 \pi R \mu_{vol} t}{3 M_o (1-V^*)} - 2kt \right) \right) \right] dt$$

eq. (18)

#### 4.1.4 Geometrical Factor of Devolatilization Pores

The geometrical factor of the devolatilization pores

$\left( \frac{\sum A_i \cos \theta_i |\cos \phi_i|}{\sum A_i} \right)$  in eqs. (11) and (18) is discussed in detail in this section.

Figure 27 shows the scanning electron micrographs<sup>(6)</sup> of the CWF agglomerates formed in the early part of a turbulent diffusion flame. It shows that the coal particles fused, and agglomerated each other.

The distribution of the devolatilization pores on the outer surface of the CWF agglomerate is illustrated in Figure 28. In this figure, the number  $n_N$  ( $\equiv n$ ) denotes the total number of devolatilization pores on the outer surface of the CWF agglomerate and  $d_1$  (or  $d_{n_N}$ ) denotes the largest (or smallest) diameter of the cross-sectional exit area of the devolatilization pore. The numbers  $n_1, n_2, \dots, n_{N-2}$ , and  $n_{N-1}$  in Figure 28 are assigned to yield equal areas, i.e.,

$$\sum_{i=1}^{n_1} A_i = \sum_{i=n_1+1}^{n_2} A_i = \dots = \sum_{i=n_{N-1}+1}^{n_N} A_i \quad \text{eq. (19)}$$

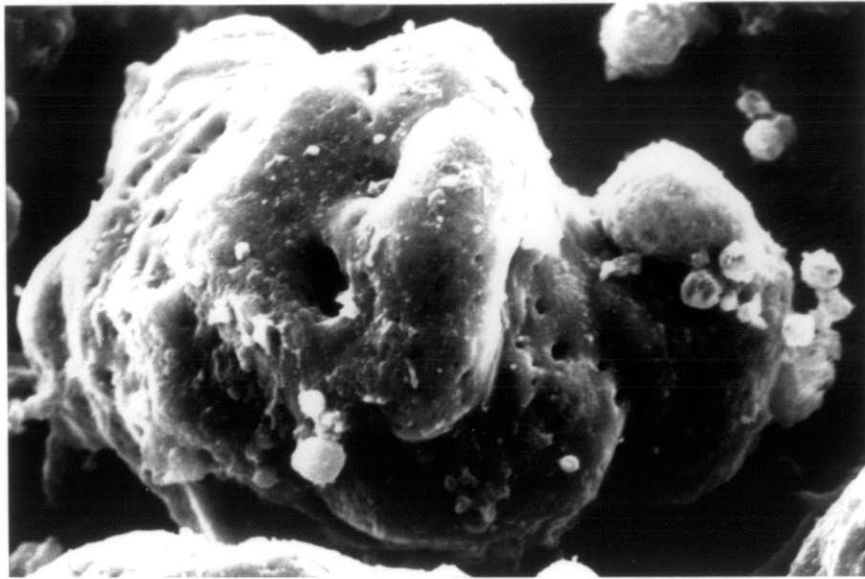
where each term denotes the sum of the cross-sectional exit area of the devolatilization pores for each pore group. It follows that the number of pores increases as pore diameter decreases, or,

$$n_1 < n_2 - n_1 < n_3 - n_2 < \dots < n_N - n_{N-1} \quad \text{eq. (20)}$$

The geometrical factor in eqs. (11) and (18) can thus be written as

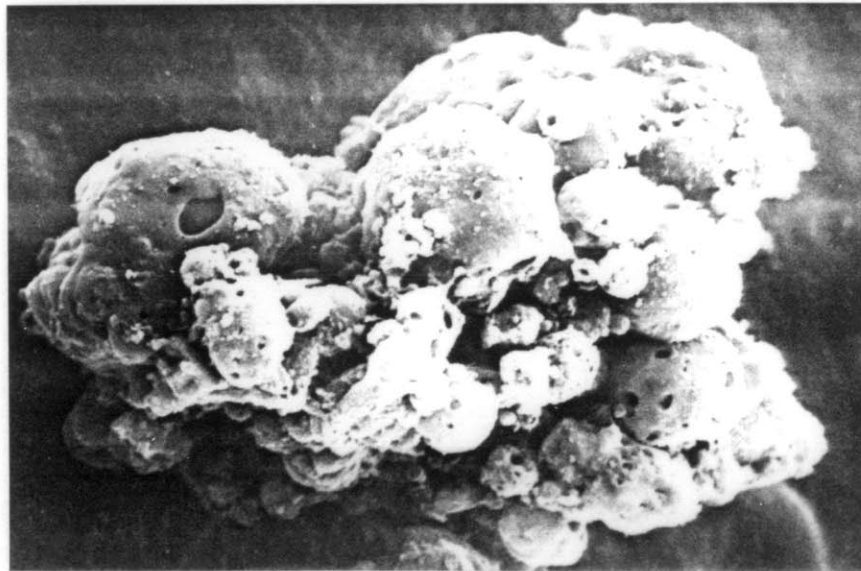
$$\frac{\sum_{i=1}^n A_i \cos \theta_i |\cos \phi_i|}{\sum_{i=1}^n A_i} = \frac{\sum_{i=1}^{n_1} A_i \cos \theta_i |\cos \phi_i|}{\sum_{i=1}^{n_N} A_i} + \frac{\sum_{i=n_1+1}^{n_2} A_i \cos \theta_i |\cos \phi_i|}{\sum_{i=1}^{n_N} A_i} + \dots$$





a

10  $\mu\text{m}$



b

10  $\mu\text{m}$

Figure 27. Scanning Electron Micrographs of CWF Agglomerates

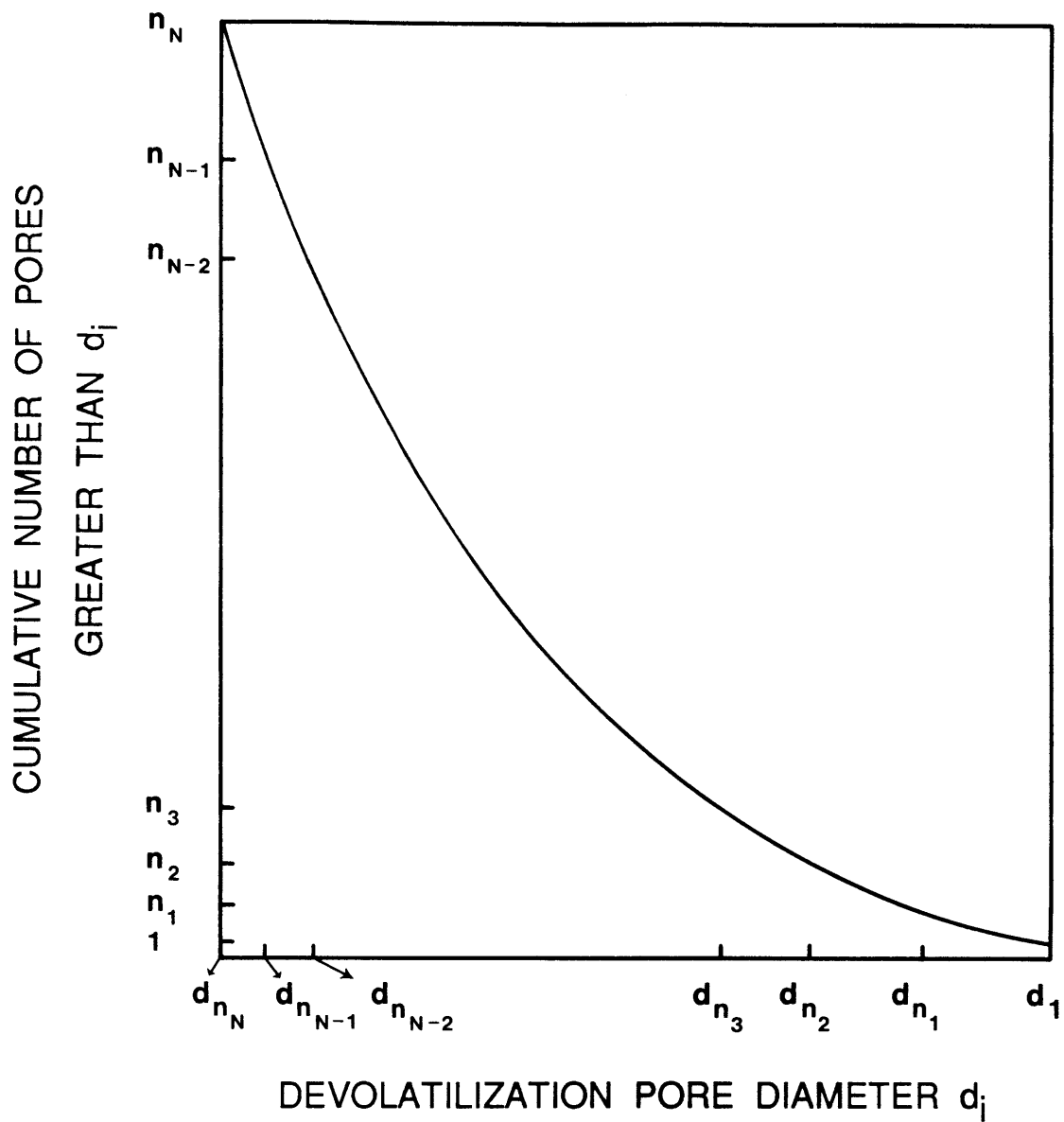


Figure 28. Distribution of Devolatilization Pores on Outer Surface of CWF Agglomerate

$$\dots + \frac{\sum_{i=n_{N-2}+1}^{n_{N-1}} A_i \cos \theta_i |\cos \phi_i|}{\sum_{i=1}^{n_N} A_i} + \frac{\sum_{i=n_{N-1}+1}^{n_N} A_i \cos \theta_i |\cos \phi_i|}{\sum_{i=1}^{n_N} A_i}$$

or, equivalently,

$$= \left( \frac{\sum_{i=1}^{n_1} A_i \cos \theta_i |\cos \phi_i|}{\sum_{i=1}^{n_1} A_i} \right) \left( \frac{\sum_{i=1}^{n_1} A_i}{\sum_{i=1}^{n_N} A_i} \right) + \left( \frac{\sum_{i=n_1+1}^{n_2} A_i \cos \theta_i |\cos \phi_i|}{\sum_{i=n_1+1}^{n_2} A_i} \right) \left( \frac{\sum_{i=n_1+1}^{n_2} A_i}{\sum_{i=1}^{n_N} A_i} \right) + \dots + \left( \frac{\sum_{i=n_{N-1}+1}^{n_N} A_i \cos \theta_i |\cos \phi_i|}{\sum_{i=n_{N-1}+1}^{n_N} A_i} \right) \left( \frac{\sum_{i=n_{N-1}+1}^{n_N} A_i}{\sum_{i=1}^{n_N} A_i} \right) \quad \text{eq. (21)}$$

From eqs. (19) and (21), the geometrical factor is written as

$$\frac{\sum_{i=1}^n A_i \cos \theta_i |\cos \phi_i|}{\sum_{i=1}^n A_i} = \left( \frac{\sum_{i=1}^{n_1} A_i}{\sum_{i=1}^{n_N} A_i} \right) \left( \frac{\sum_{i=1}^{n_1} A_i \cos \theta_i |\cos \phi_i|}{\sum_{i=1}^{n_1} A_i} \right) + \left( \frac{\sum_{i=n_1+1}^{n_2} A_i \cos \theta_i |\cos \phi_i|}{\sum_{i=n_1+1}^{n_2} A_i} \right) + \dots + \left( \frac{\sum_{i=n_{N-1}+1}^{n_N} A_i \cos \theta_i |\cos \phi_i|}{\sum_{i=n_{N-1}+1}^{n_N} A_i} \right) \quad \text{eq. (22)}$$

The average cross-sectional exit areas of the devolatilization pores for each pore group are given by

$$\bar{A}_1 = \frac{\sum_{i=1}^{n_1} A_i}{n_1}, \quad \bar{A}_2 = \frac{\sum_{i=n_1+1}^{n_2} A_i}{n_2 - n_1}, \dots, \quad \text{and} \quad \bar{A}_N = \frac{\sum_{i=n_{N-1}+1}^{n_N} A_i}{n_N - n_{N-1}} \quad \text{eq. (23)}$$

From eqs. (22) and (23), the geometrical factor is simplified as

$$\frac{\sum_{i=1}^n A_i \cos \theta_i |\cos \phi_i|}{\sum_{i=1}^n A_i} \approx \left( \frac{\sum_{i=1}^{n_1} A_i}{n_N \sum_{i=1}^{n_N} A_i} \right) \left( \frac{\sum_{i=1}^{n_1} \bar{A}_1 \cos \theta_i |\cos \phi_i|}{n_1 \bar{A}_1} + \frac{\sum_{i=n_1+1}^{n_2} \bar{A}_2 \cos \theta_i |\cos \phi_i|}{(n_2 - n_1) \bar{A}_2} + \dots + \frac{\sum_{i=n_{N-1}+1}^{n_N} \bar{A}_N \cos \theta_i |\cos \phi_i|}{(n_N - n_{N-1}) \bar{A}_N} \right)$$

or, equivalently,

$$= \left( \frac{\sum_{i=1}^{n_1} A_i}{n_N \sum_{i=1}^{n_N} A_i} \right) \left( \frac{\sum_{i=1}^{n_1} \cos \theta_i |\cos \phi_i|}{n_1} + \frac{\sum_{i=n_1+1}^{n_2} \cos \theta_i |\cos \phi_i|}{n_2 - n_1} + \dots + \frac{\sum_{i=n_{N-1}+1}^{n_N} \cos \theta_i |\cos \phi_i|}{n_N - n_{N-1}} \right) \quad \text{eq. (24)}$$

In order to compare the order of magnitude of terms of decreasing diameter (increasing pore number) in the second set of parentheses of the

right-hand side (R.H.S.) of eq. (24), the value of  $\left( \frac{\sum_{i=1}^N \cos\theta_i |\cos\phi_i|}{N} \right)$

was calculated for various numbers of pores  $N$ , assigning values of  $\theta_i$  and  $\phi_i$  at random. In order to obtain an average, the calculations were repeated 1,000 times. The effect of increasing pore number  $N$  in a pore

group of equal area on the value of  $\left| \frac{\sum_{i=1}^N \cos\theta_i |\cos\phi_i|}{N} \right|$

is shown in Figure 29. The decrease in the value of

$\left| \frac{\sum_{i=1}^N \cos\theta_i |\cos\phi_i|}{N} \right|$  with increasing  $N$  is due to the cancellation of the

contribution of pores which are oriented in random directions, and thus, yield opposing torques. The cancellation increases with increasing pore number  $N$ .

From Figure 29, it is evident that larger pores, numbering less than 100 per particle, dominate the contribution to the torque. For this reason, when the number  $n_1$  in eq. (24) is assigned a value of approximately 100, the order of magnitude of the first term in the second set of parentheses of R.H.S. of eq. (24) is found to be much greater than that of the other terms in those parentheses. Therefore, the value of the geometrical factor is mainly dependent upon the 100 largest macropores, and the much larger number of micropores contributes negligibly to the torque.

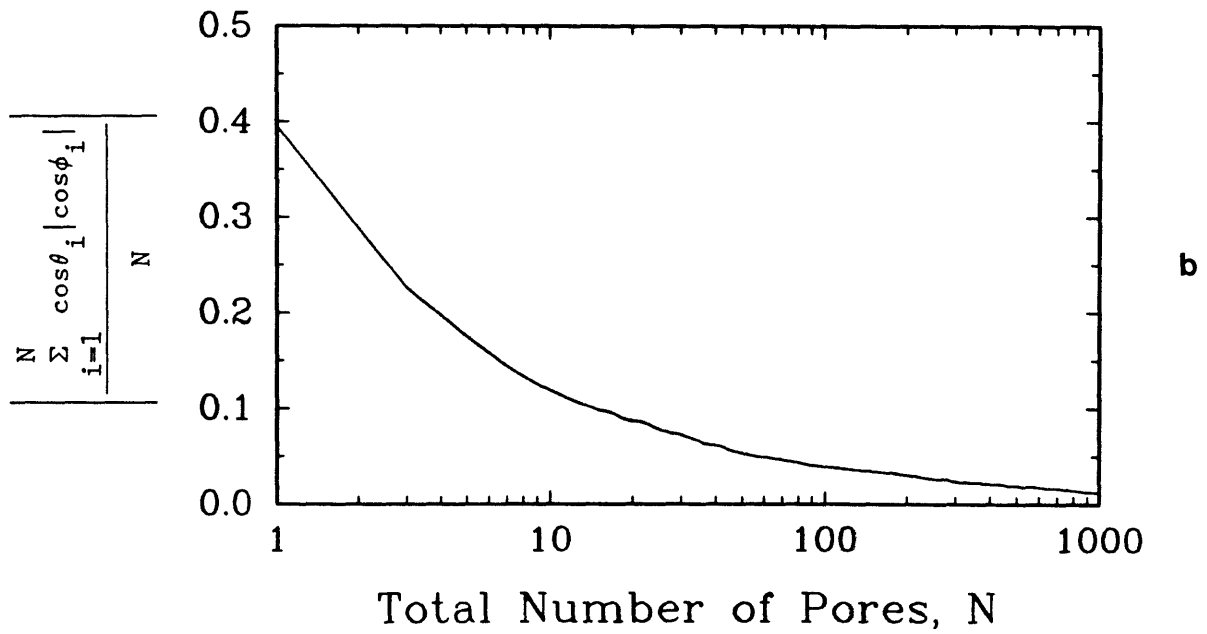
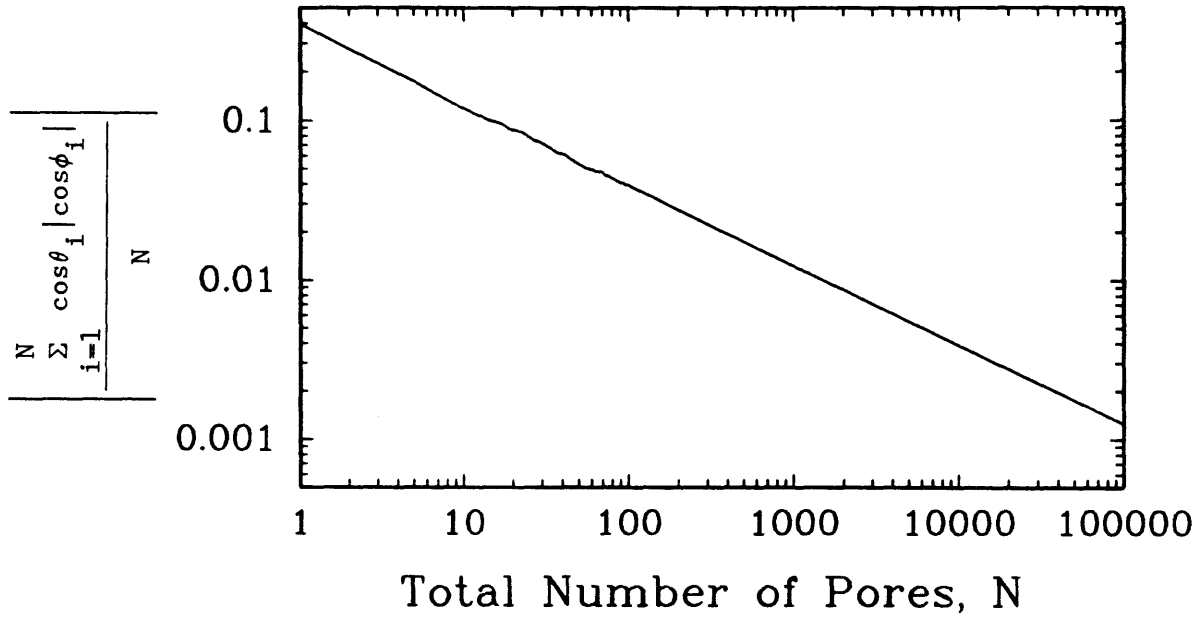


Figure 29.  $\left| \frac{N \sum_{i=1}^N \cos \theta_i |\cos \phi_i|}{N} \right|$  versus Total Number of Pores N

The pore size distribution of these 100 largest macropores on the outer surface of the CWF agglomerate is directly obtained from the scanning electron micrographs (Figure 27) of the CWF agglomerates. An example of a typical pore size distribution of the 100 largest macropores is represented in Table 1 and Figure 30.

The absolute value of the geometrical factor of the devolatilization pores is calculated and plotted in Figure 31. In this calculation, the angles  $\theta_i$  and  $\phi_i$  are chosen by the random number generation method and each cross-sectional exit area  $A_i$  is substituted for by the pore size distribution data obtained from scanning electron micrographs of CWF agglomerates.

The absolute value of the geometrical factor is found to be distributed in the range of 0 to 0.05. As the value of the geometrical factor increases, the corresponding probability tends to decrease generally, except for the range of the absolute value of the geometrical factor between 0 and 0.005 (Figure 31). The trend of the distribution curve of the geometrical factor is found to be independent of the input data of other examples of the pore size distribution of the 100 largest macropores. Inasmuch as different particles have different geometrical factors, it can be expected that they will have different rotation velocities. The distribution curves of the geometrical factor need to be compared with those for the angular velocities, and the result will be presented in Section 5.1.2.

For the additional analysis of the geometrical factor, the value of the geometrical factor for one pore is derived analytically and compared

Table 1. Example of Typical Pore Size Distribution of the 100 Largest Pores on the Outer Surface of the CWF Agglomerate

Pore Diameter ( $\mu\text{m}$ )	Number of Pores
20	1
15	2
12	4
8	5
5	6
4	8
3	9
2	15
1	50
Total 100	

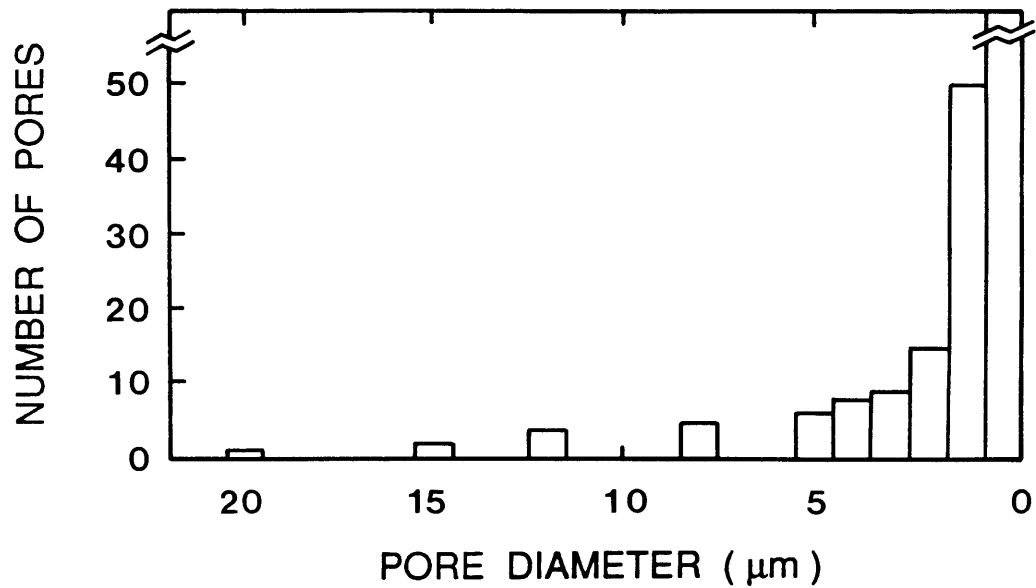


Figure 30. Typical Pore Size Distribution of 100 Largest Macropores



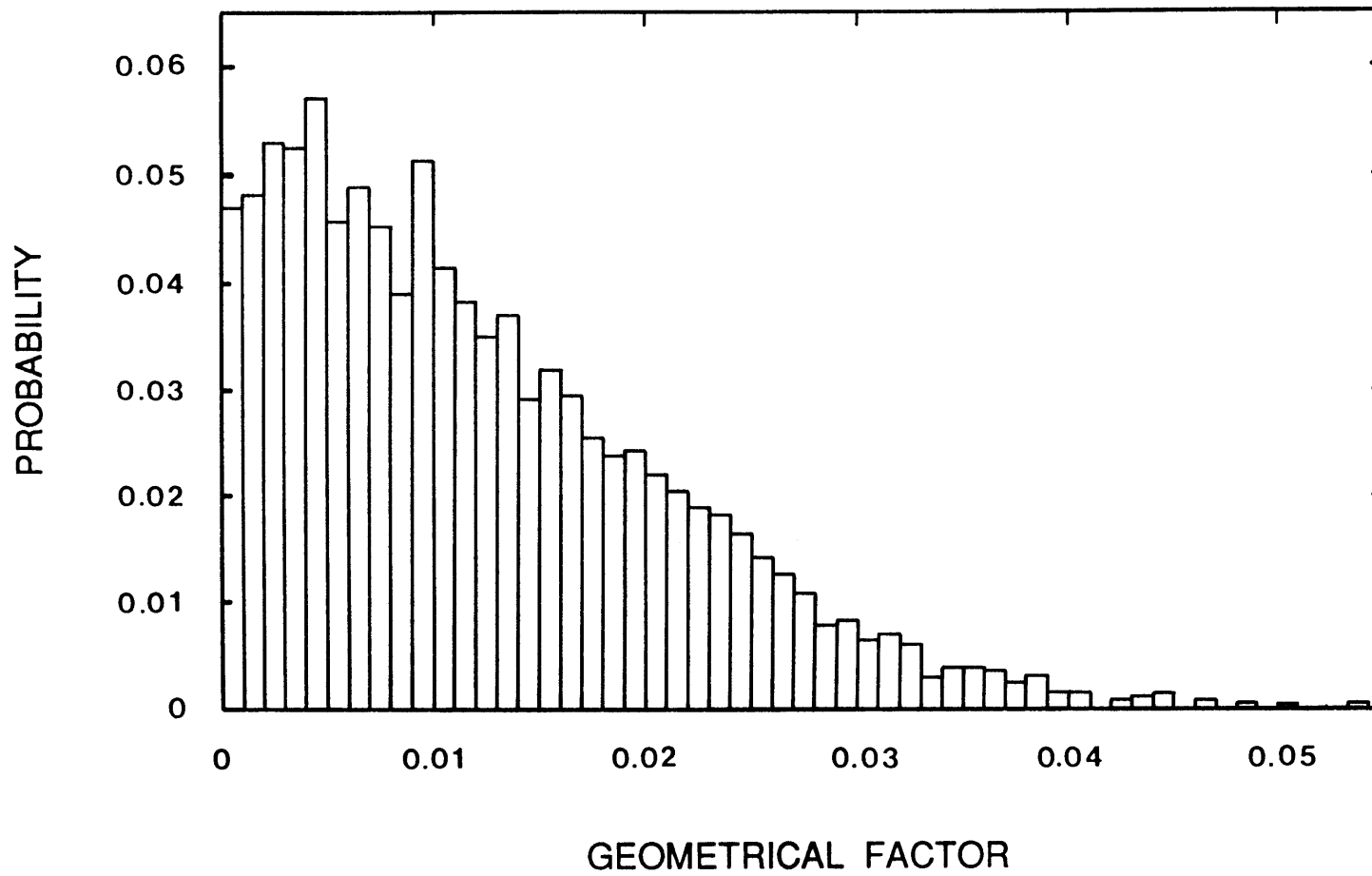


Figure 31. Probability Density Distribution of Geometrical Factor

with the value of  $\left| \frac{\sum_{i=1}^N \cos\theta_i |\cos\phi_i|}{N} \right|$  with  $N=1$  in Figure 29. Figure 32

shows the configuration of the rotating CWF agglomerate with just one pore. In this case, the rotational axis of the rotating CWF agglomerate is determined by the geometry of one pore, in other words, by the angles of the issuing volatile jet. The angles  $\theta$  and  $\phi$  in the geometrical factor in eq. (11) or (18) can be substituted by the angles  $\Theta$  and  $\Phi$  in spherical coordinates, which are defined and illustrated in Figure 33. The probability  $P(\Theta, \Phi)$  of the beam bounded by the angles  $\Theta$  to  $\Theta + d\Theta$  and  $\Phi$  to  $\Phi + d\Phi$  in Figure 33 is

$$P(\Theta, \Phi) = \frac{\sin\Theta \, d\Theta \, d\Phi}{2\pi} \quad \text{eq. (25)}$$

The value of the geometrical factor for one pore ( $\cos\theta |\cos\phi|$ ) can be given by

$$\begin{aligned} \int_{\text{surface}} \cos\theta |\cos\phi| P(\Theta, \Phi) \\ = \int_{\Phi=0}^{2\pi} \int_{\Theta=0}^{\pi/2} \cos\theta |\cos\phi| \frac{\sin\Theta}{2\pi} d\Theta \, d\Phi \quad \text{eq. (26)} \end{aligned}$$

In this one pore case, the angle  $\phi$  is always zero and the angle  $\theta$  can be substituted by  $(\frac{\pi}{2} - \Theta)$ , and therefore, the term of ( $\cos\theta |\cos\phi|$ ) in eq. (26) becomes  $\cos(\frac{\pi}{2} - \Theta)$  and the corresponding volatile jet is illustrated as two symmetrical volatile jets; one real jet and one imaginary jet, in Figure 32. Hence, eq. (26) is expressed as

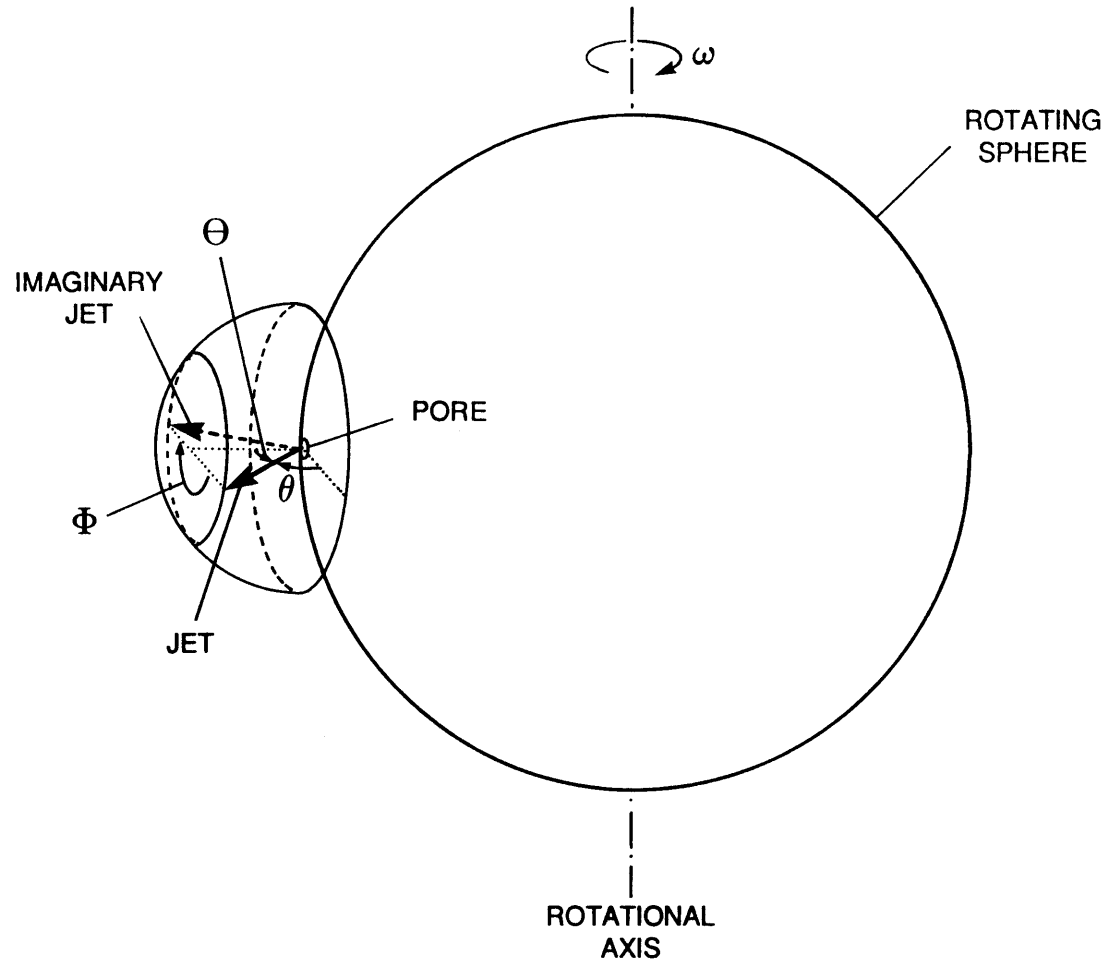


Figure 32. Configuration of Rotating Sphere with One Pore

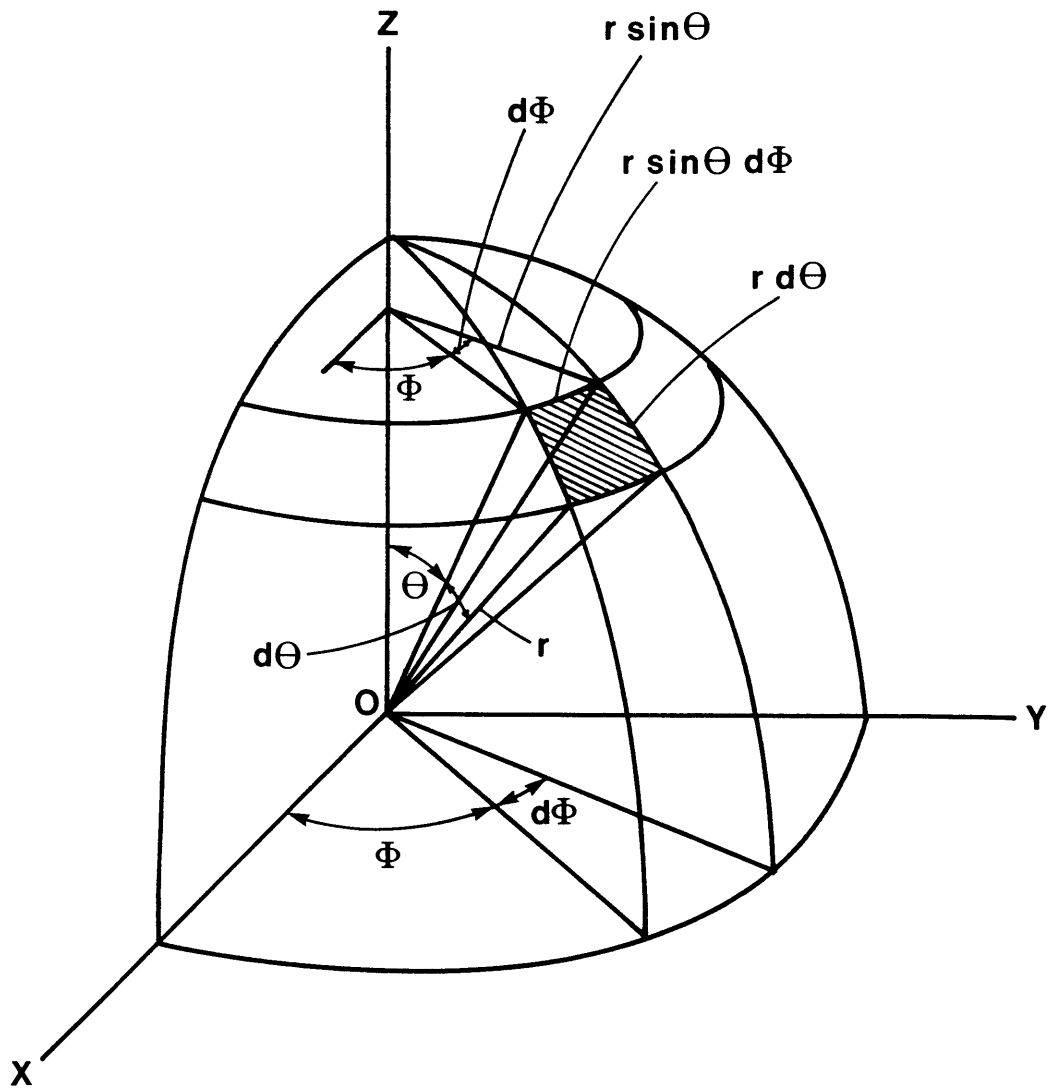


Figure 33. Configuration of Spherical Coordinates

$$\begin{aligned}
& \int_{\text{surface}} \cos\theta |\cos\phi| P(\theta, \phi) \\
&= \frac{1}{2} \int_{\phi=0}^{2\pi} \int_{\theta=0}^{\pi/2} \cos\left(\frac{\pi}{2} - \theta\right) \frac{\sin\theta}{2\pi} d\theta d\phi \\
&= \frac{\pi}{8} (= 0.393) \qquad \text{eq. (27)}
\end{aligned}$$

Therefore, the analytical solution of the geometrical factor for one

pore is found to be 0.393 which is the value of  $\left| \frac{\sum_{i=1}^N \cos\theta_i |\cos\phi_i|}{N} \right|$  with

$N = 1$  in Figure 29-b.

#### 4.1.5 Centrifugal Force Induced by Particle Rotation

Particle rotation during devolatilization and char burnout generates centrifugal force at the agglomerate surface which can promote the separation of both weakly adhering char fragments and ash particles from the CWF agglomerate.

The centrifugal force acting on a coal particle of mass  $m_c$  on the outer edge of the CWF agglomerate with a radius  $R$  (Figure 34) can be obtained by substituting the angular velocity  $\omega(t)$ , obtained from eq. (11) or (18), into:

$$F_{\text{centrif}} = m_c R [\omega(t)]^2 \qquad \text{eq. (28)}$$

The predictions of angular velocity and centrifugal force of the rotating CWF agglomerate during devolatilization and char burnout will be made by the model of particle rotation, described by eqs. (10) through (18) and eq. (28), in Section 5.1.

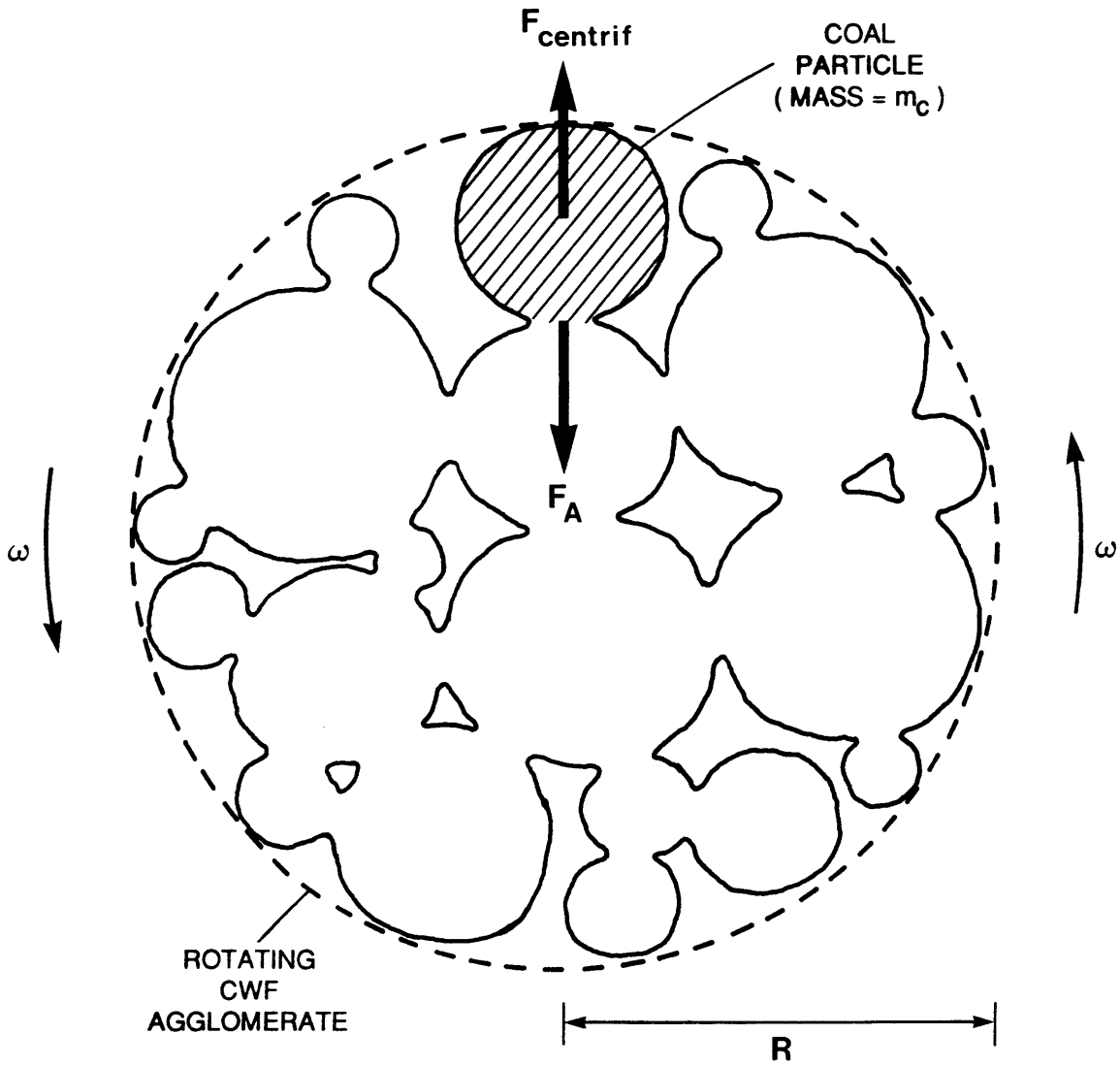


Figure 34. Force Balance during CWF Agglomerate Rotation

## 4.2 Model of Particle Agglomeration

### 4.2.1 Introduction

Upon injection of the CWF droplet into the furnace, the interstitial water in the CWF droplet begins to evaporate. As this occurs, the individual coal particles become exposed to the hot environment and are heated up rapidly. On heating to about 400°C or above, bituminous coal particles become plastic and fuse. The extent of agglomeration depends on the duration of the plastic period which is strongly affected by both the time-temperature history of the coal particles and the coal type.

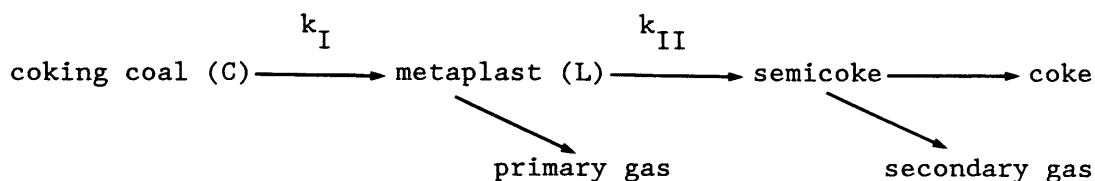
When the duration of the plastic period is long enough for particles to fuse and coalesce, a strongly fused CWF agglomerate will be formed. Due to strong adhesive force between contiguous coal particles, the CWF agglomerates will be difficult to fragment, resulting in poor combustion.

In contrast, when the duration of the plastic period is so short that coal particles cannot completely fuse and coalesce, a loosely fused CWF agglomerate will be formed, the adhesive force between contiguous coal particles will be weak, and the CWF agglomerates will easily break up, resulting in better combustion. Consequently, the plasticity-time history of the coal particles is found to be important for the study of CWF agglomeration.

### 4.2.2 Plasticity of Bituminous Coal

While heating bituminous coal to about 400°C or above, the transient occurrence of plastic behavior of coal particles can be observed. Earlier "bitumen" theory explains plastic development as a result of a fusible component (bitumen) which melts to provide a viscous slurry. The later

"metaplast" theory is more commonly accepted<sup>(16,17)</sup>. According to the metaplast theory, a liquid metaplast is generated and depleted by the following pyrolytic reactions:

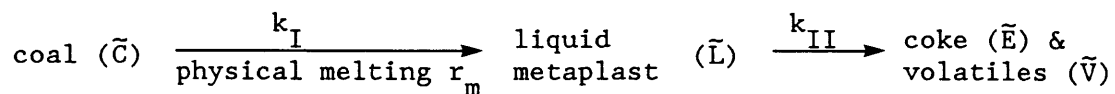


These reactions, which in a simplified form describe coke formation, are the basis for the following mathematical model:

$$\frac{dC}{dt} = -k_I C$$

$$\frac{dL}{dt} = k_I C - k_{II} L$$

The assumption of this mathematical model is that the reactions are first-order. Fong et al.<sup>(18)</sup> elaborated on this model by taking into account the liquid formed by physical melting. According to Fong et al's model, some fraction of liquid is initially formed by physical melting above a critical temperature. With further temperature increase, pyrolytic bond breaking generates additional liquid. Simultaneously, the liquid forms a volatile product which escapes from the coal and leaves a solid coke residue. The reaction scheme and corresponding rate expressions during the plasticity of bituminous coal particles are <sup>(7)</sup>



$$\frac{d\tilde{C}}{dt} = -k_I \tilde{C} - r_m \quad \text{eq. (29)}$$



$$\frac{d\tilde{L}}{dt} = k_I \tilde{C} + r_m - k_{II} \tilde{L} \quad \text{eq. (30)}$$

where  $\tilde{C}$  and  $\tilde{L}$  are the mass fractions of unreacted coal and liquid metaplast, respectively,  $r_m$  is the rate of physical melting, and  $k_I$  and  $k_{II}$  are the rate constants.

The initial conditions of eqs. (29) and (30) are

$$\tilde{C}(0) = \tilde{C}_i, \quad \text{and} \quad \text{eq. (31)}$$

$$\tilde{L}(0) = 0 \quad \text{eq. (32)}$$

where  $\tilde{C}_i$  is the initial mass fraction of unreacted coal, and given by [1 - mass fraction of mineral matter  $\tilde{f}_a$ ].

From eqs. (29) and (31), the mass fraction of unreacted coal ( $\tilde{C}$ ) is expressed as a function of the reaction rate constant  $k_I$  and the physical melting rate  $r_m$  as

$$\tilde{C} = \exp\left[-\int_0^t k_I dt\right] \left[ \int_0^t (-r_m) \exp\left(\int_0^t k_I dt\right) dt + \tilde{C}_i \right] \quad \text{eq. (33)}$$

From eqs. (30), (32), and (33), the mass fraction of liquid metaplast ( $\tilde{L}$ ) is derived as

$$\begin{aligned} \tilde{L} = \exp\left[-\int_0^t k_{II} dt\right] & \left[ \int_0^t \exp\left(\int_0^t k_{II} dt\right) \left[ r_m + \tilde{C}_i k_I \exp\left(-\int_0^t k_I dt\right) \right. \right. \\ & \left. \left. + k_I \exp\left(-\int_0^t k_I dt\right) \int_0^t (-r_m) \exp\left(\int_0^t k_I dt\right) dt \right] dt \right] \quad \text{eq. (34)} \end{aligned}$$

The rate of physical melting ( $r_m$ ) is given by the heating rate of the coal particle, multiplied by a Gaussian distribution of melting

points, centered at a mean melting temperature of 623 K with a standard deviation of 30 K. (18)

$$r_m = \left[ \frac{L_s}{\sqrt{2\pi} \sigma_T} \exp \left( -\frac{(T_p - T_m)^2}{2\sigma_T^2} \right) \right] \left( \frac{dT_p}{dt} \right) \quad \text{eq. (35)}$$

where  $T_p$  = temperature of the coal particle

$T_m$  = mean melting temperature of the coal particle (= 623 K)

$\left( \frac{dT_p}{dt} \right)$  = heating rate of the coal particle

$\sigma_T$  = standard deviation of the melting temperature (= 30 K)

$L_s$  = mass fraction of solid metaplast initially existing in coal

The rate constants  $k_I$  and  $k_{II}$  are obtained from experimental data for a Pittsburgh seam bituminous coal as follows: (18)

$$k_I = 6.6 \times 10^7 \exp(-14,500/T_p) \left( \frac{1}{\text{sec}} \right) \quad \text{eq. (36)}$$

$$k_{II} = 1.9 \times 10^{10} \exp(-21,200/T_p) \left( \frac{1}{\text{sec}} \right)$$

In the present model, it is assumed that swelling due to expansion of volatile bubbles in the liquid metaplast is not significant, and therefore, the radius of the CWF agglomerate remains constant (i.e., assumption of negligible swelling). It is also assumed that volatile bubbles, formed in the liquid metaplast, escape instantly and leave micro-porous coke-residue in the liquid metaplast, and that a coal particle during the coalescence process consists of: unsoftened coal, liquid metaplast, mineral matter, and coke-residue which has micropores. Based on the above assumptions, the volume fractions of each component will be derived as follows:

The volume fraction of unreacted coal (C) is

$$C = \frac{\rho_o}{\rho_c} \tilde{C} \quad \text{eq. (37)}$$

where  $\tilde{C}$  denotes the mass fraction of unreacted coal, given by eq (33),  $\rho_c$  denotes the density of unreacted coal, and  $\rho_o$  is the initial apparent density of the coal particle, and expressed as

$$\rho_o = \frac{\rho_c \rho_a}{\rho_a - \tilde{f}_a (\rho_a - \rho_c)} \quad \text{eq. (38)}$$

where  $\rho_a$  is the density of mineral matter and  $\tilde{f}_a$  is the mass fraction of mineral matter, given by  $\tilde{f}_a = 1 - \tilde{C}_i$ .

From eqs. (33), (37), and (38), the volume fraction of unreacted coal (C) is expressed as

$$C = \left[ \frac{\rho_a}{\rho_a - \tilde{f}_a (\rho_a - \rho_c)} \right] \exp \left[ - \int_0^t k_I dt \right] \left[ \int_0^t (-r_m) \exp \left[ \int_0^t k_I dt \right] dt + \tilde{C}_i \right] \quad \text{eq. (39)}$$

The volume fraction of liquid metaplast (L) is

$$L = \frac{\rho_o}{\rho_l} \tilde{L} \quad \text{eq. (40)}$$

where  $\tilde{L}$  denotes the mass fraction of liquid metaplast, given by eq. (34),  $\rho_l$  is the density of liquid metaplast, and  $\rho_o$  is the initial apparent density of the coal particle, given by eq. (38). From eqs. (34), (38), and (40), the volume fraction of liquid metaplast (L) is expressed as

$$L = \left[ \frac{\rho_a \rho_c}{\rho_l [\rho_a - \tilde{f}_a (\rho_a - \rho_c)]} \right] \exp \left[ - \int_0^t k_{II} dt \right] \left[ \int_0^t \exp \left( \int_0^t k_{II} dt \right) \left[ r_m \right. \right. \\ \left. \left. + \tilde{C}_I k_I \exp \left[ - \int_0^t k_I dt \right] + k_I \exp \left[ - \int_0^t k_I dt \right] \int_0^t (-r_m) \exp \left[ \int_0^t k_I dt \right] dt \right] dt \right] \quad \text{eq. (41)}$$

The volume fraction of mineral matter ( $f_a$ ) is

$$f_a = \frac{\rho_o}{\rho_a} \tilde{f}_a \quad \text{eq. (42)}$$

which may be rewritten, using eq. (38), in the form of

$$f_a = \frac{\rho_c}{\rho_a - \tilde{f}_a (\rho_a - \rho_c)} \tilde{f}_a \quad \text{eq. (43)}$$

Using the above values for C, L, and  $f_a$ , and the previously stated assumption of negligible swelling, the volume fraction of coke (E) is derived as

$$E = 1 - C - L - f_a \quad \text{eq. (44)}$$

#### 4.2.3 Contact Area during Particle Agglomeration

During the particle agglomeration process, coal particles in the CWF agglomerate fuse and coalesce, and the contact area between contiguous coal particles increases until the liquid metaplast in the coal is depleted completely.

Theoretical calculations of the sintering of a Newtonian-viscous fluid, using the approximate flow field of simple uniaxial contraction, were made by Frenkel<sup>(19)</sup>. He derived a neck growth rate law for the sintering of two spheres. This law was verified by other authors<sup>(20,21,22)</sup> to determine the accuracy of time dependency, and expressed as

$$A = \frac{3}{2} \frac{r\gamma}{\mu} t \quad \text{eq. (45)}$$

where A = contact area at time t

r = radius of the coalescent sphere

$\gamma$  = surface tension of the coalescent sphere

$\mu$  = apparent viscosity of the coalescent sphere

t = time

The growth rate of this contact area during the coalescence process for coal particle  $\left(\frac{dA}{dt}\right)$  is expressed as

$$\frac{dA}{dt} = \frac{3}{2} \frac{r\gamma}{\mu} \quad \text{eq. (46)}$$

Using a concentrated suspension model of Frankel and Acrivos<sup>(23)</sup>, the apparent viscosity of liquid ( $\mu$ ) is assumed to depend on the viscosity of the solids-free liquid ( $\mu^*$ ), and on the volume fraction of solids in the liquid (1-L), where L is the volume fraction of liquid metaplast discussed in Section 4.2.2. Their relationship for apparent viscosity is

$$\mu = \frac{\frac{9}{8} \mu^*}{\left(1-L\right)^{-\frac{1}{3}} - 1} \quad \text{eq. (47)}$$

Frankel and Acrivos found that this expression agreed well with experimental data over a wide range of volume fractions of solids (i.e.,  $0.4 < (1-L) < 1.0$ ). This implies that  $0 < L < 0.6$ , which is compatible with the calculated values of  $L$  in the present modeling effort. In the present model, the value of  $\mu^*$  is estimated from Nazem's (24) work on carbonaceous mesophase pitch. The surface tension of the liquid metaplast decreases with increasing temperature, but the experimental data on coal liquids [Hwang et al. (25)] show that the magnitude of this decrease in surface tension is small compared to the corresponding decrease in viscosity. Therefore, the surface tension of the liquid metaplast is assumed to be constant in the present model.

$$\gamma = \gamma_c \quad \text{eq. (48)}$$

From eqs. (46), (47), and (48), the growth rate of the contact area between contiguous coal particles during coalescence  $\left(\frac{dA}{dt}\right)$  is derived as

$$\frac{dA}{dt} = \frac{4 r_c \gamma_c}{3 \mu^*} \left[ (1-L)^{-1/3} - 1 \right] \quad \text{eq. (49)}$$

where  $r_c$  is the coal particle radius.

The initial condition of eq. (49) for the contact area  $A$  is

$$A(0) = 0 \quad \text{eq. (50)}$$

and therefore, the contact area  $A$  between two contiguous coal particles during coalescence is written as

$$A = \frac{4 r_c \gamma_c}{3 \mu^*} \int_0^t \left[ (1-L)^{-1/3} - 1 \right] dt \quad \text{eq. (51)}$$

#### 4.2.4 Adhesive Force during Particle Agglomeration

The adhesive force between two coalescent coal particles during the particle agglomeration process is expressed as the sum of the surface tension force due to the liquid metaplast and the adhesive force due to coke interconnection.

##### 4.2.4.1 Surface Tension Force

Figure 35 shows two coalescent coal particles in the CWF agglomerate. The surface tension force due to the liquid metaplast in the neck region is proportional to the effective circumference of the neck region ( $l_{\text{eff}}$ ), and expressed as

$$l_{\text{eff}} = 2 \pi r^* L \quad \text{eq. (52)}$$

where  $r^*$  = radius of neck region, and given by

$$r^* = \left( \frac{A}{\pi} \right)^{1/2} \quad \text{eq. (53)}$$

The surface tension force  $F_{\gamma}$  is

$$F_{\gamma} = \gamma_c \sin \theta l_{\text{eff}} \quad \text{eq. (54)}$$

where  $\theta$  is the contact angle, taken to be  $90^\circ$  as indicated in Figure 35. Hence, the surface tension force due to the liquid metaplast is derived as

$$F_{\gamma} = 2 \sqrt{\pi A} L \gamma_c \quad \text{eq. (55)}$$

##### 4.2.4.2 Adhesive Force due to Coke Interconnection

Figure 36 shows the agglomeration process of two coalescent coal particles in the CWF agglomerate, with the period of plasticity being

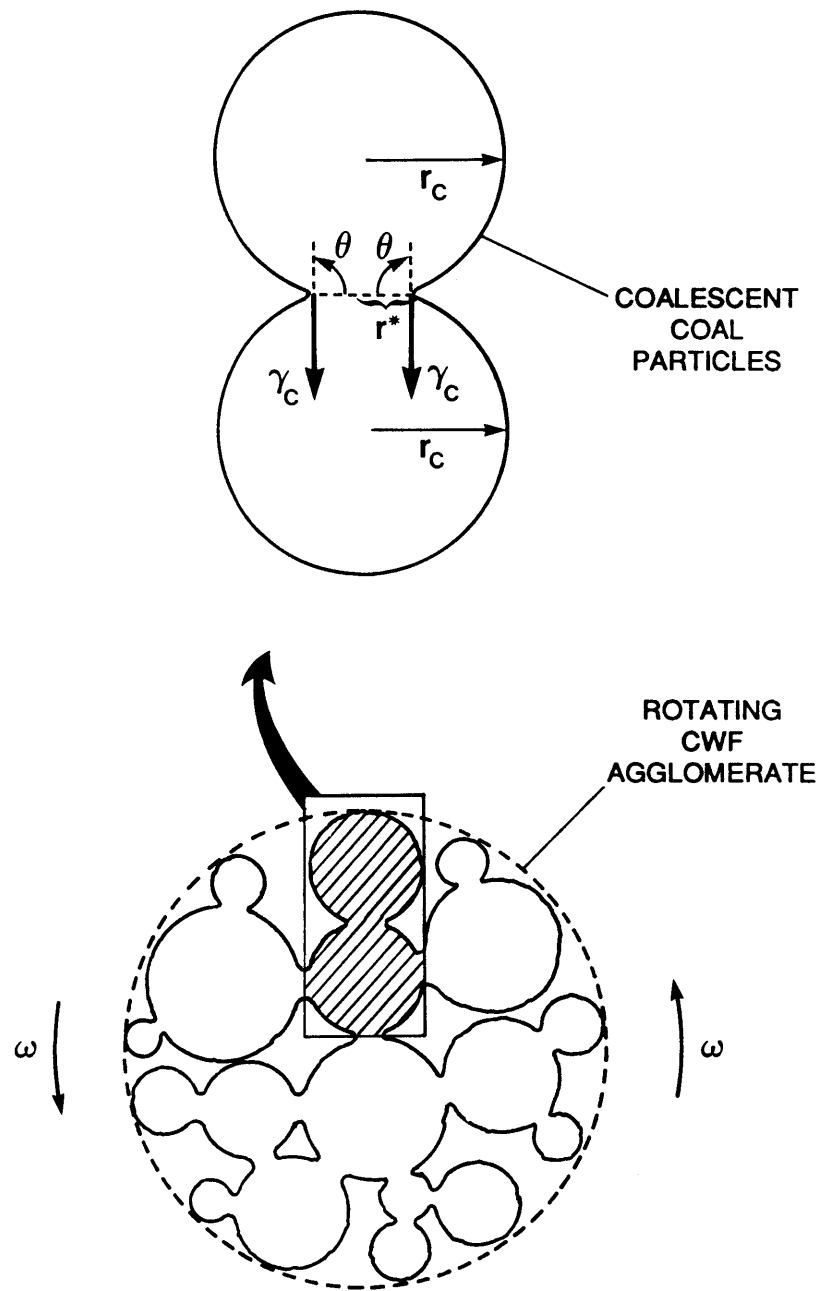


Figure 35. Surface Tension Force at Neck Region of Two Coalescent Coal Particles in CWF Agglomerate



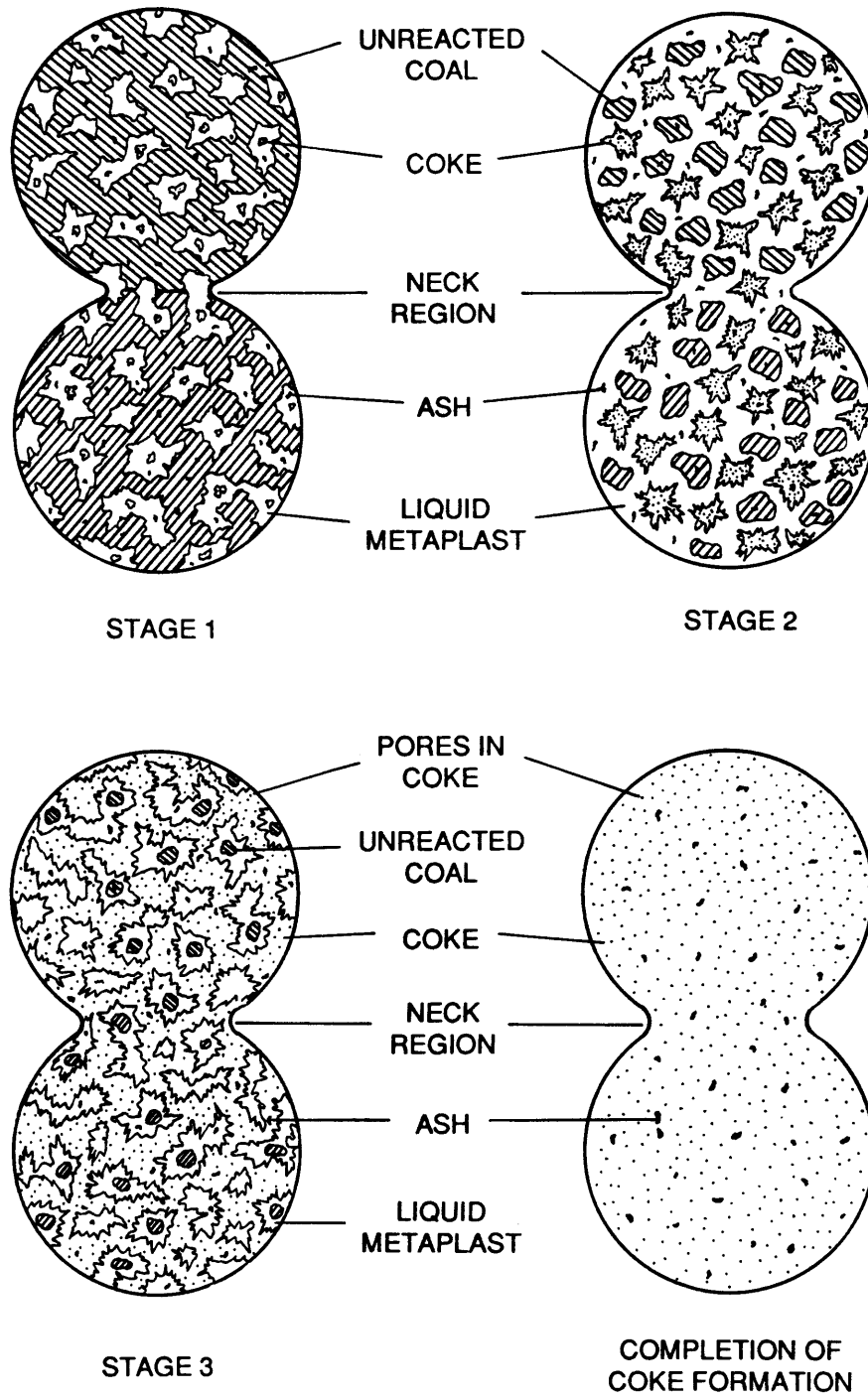


Figure 36. Agglomeration Process of Coal Particles in CWF Agglomerate

divided into three stages. The classification of each of these stages depends upon the solids in suspension of the liquid metaplast, and these solids are: coke & ash; coke & ash & unreacted coal; unreacted coal & ash, in stages 1, 2, and 3, respectively.

According to Taylor<sup>(26)</sup> and Friel et al.<sup>(27)</sup>, a characteristic "mosaic" structure of coke is found to develop during the carbonization of vitrinite. The spherical bodies, each of which has a single crystallographic orientation, become enlarged until they begin to interfere with one another's growth as the mosaic-type structure starts to form. Completion of the mosaic formation coincides with completion of the resolidification of the coal. Taylor also found that when the proportion of the coke-residue (char) was increased to about one half, the spherical bodies began to interfere with one another's growth. Hence, in the present study, the threshold volume fraction of coke-residue ( $E_{th}$ ), which is a border between stage 2 and stage 3, is defined as 50 % of  $(1-f_a)$ .

$$\text{(i.e., } E_{th} = \frac{1-f_a}{2}\text{)}.$$

In stage 1 and stage 2, when the volume fraction of coke-residue ( $E$ ) is smaller than the threshold volume fraction of coke-residue ( $E_{th}$ ), each mosaic-type coke-residue grows separately, and therefore, there is no adhesive force due to the coke interconnection. However, in stage 3, when  $E$  is larger than  $E_{th}$ , the coke-residue starts interlocking and the adhesive force due to the coke interconnection begins to be affected. The coke-residue (char), which is formed after the initiation of the coke interlock, strengthens the connection between individual coke crystalline structures. Hence, the adhesive force due to the coke interconnection ( $F_{E_3}$ ) is assumed to be proportional to the fraction  $(E-E_{th})$  of coke-

residue (char) which is formed after the initiation of the coke interconnection. Thus, the adhesive force  $F_{E_3}$  is written as

$$F_{E_3} = \sigma_E A \left( \frac{E - E_{th}}{1 - f_a - E_{th}} \right) \quad \text{eq. (56)}$$

in stage 3, where  $\sigma_E$  denotes the bond stress of the coke-residue (char), and the normalizing factor leads to  $F_{E_3} \rightarrow \sigma_E A$  when  $E \rightarrow E_{max} = 1 - f_a$ , from eq. (44). It is also assumed that, in stages 1 and 2

$$F_{E_1} = F_{E_2} = 0 \quad \text{eq. (57)}$$

#### 4.2.4.3 Adhesive Force during Particle Agglomeration

During the particle agglomeration process, the adhesive force  $F_A$  between two coalescent coal particles in the CWF agglomerate is expressed as the sum of the surface tension force ( $F_\gamma$ ) and the adhesive force due to the coke interconnection ( $F_E$ ) discussed above. Thus, using eqs. (55), (56), and (57), the adhesive force is written as

$$F_A = F_\gamma + F_E \quad \text{eq. (58)}$$

The prediction of the adhesive force during particle agglomeration for the different particle heating rates will be made by the model of particle agglomeration, described by eqs. (29) through (58), in Section 5.2.

### 4.3 Time-Temperature History of CWF Agglomerate

#### 4.3.1 Introduction

When a CWF droplet is injected into the hot combustion zone of the laminar flow reactor (LFR), the CWF droplet is heated up by thermal

radiation from the reactor wall and by heat conduction from the surrounding gas (or flame).

Figure 37 shows the typical time-temperature history of the CWF droplet/agglomerate during CWF combustion. The history can be divided into five stages: pre-evaporation, evaporation, heat-up, devolatilization, and char burnout. The temperature and the heating rate of the CWF droplet/agglomerate during CWF combustion is determined from the energy balance for the CWF droplet/agglomerate based upon the following assumptions:

- (1) CWF agglomerate is assumed to be spherical.
- (2) CWF agglomerate is assumed to have no radial temperature gradient (i.e., internally isothermal).
- (3) All the water in the CWF droplet is assumed to be evaporated before the coal particles are heated to over 100°C.
- (4) CWF agglomerate is assumed to have uniform properties.
- (5) The swelling effect is assumed to be negligible.

#### 4.3.2 Particle Heating Rate in Pre-Evaporation Stage

Energy balance for the CWF droplet upon injection into the hot combustion zone is expressed as

$$m_p c_p \left( \frac{dT_p}{dt} \right)_1 = Q_{\text{rad}} + Q_{\text{cond}} \quad \text{eq. (59)}$$

where  $m_p$  = mass of the CWF droplet

$c_p$  = specific heat of the CWF droplet

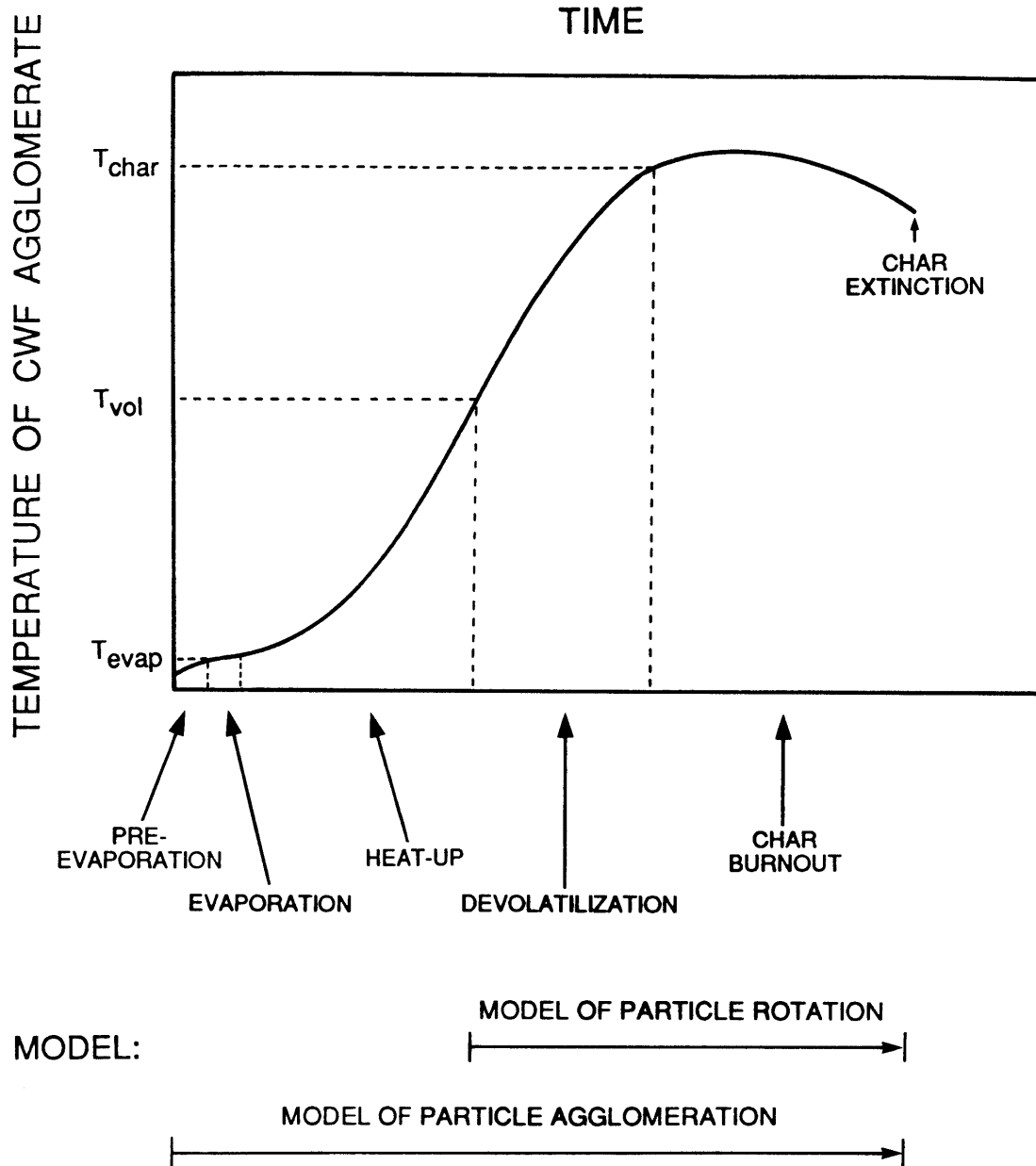


Figure 37. Typical Time-Temperature History of CWF Agglomerate during CWF Combustion

$\left(\frac{dT_p}{dt}\right)_1$  = heating rate of the CWF droplet in the pre-evaporation stage

$Q_{\text{rad}}$  = thermal radiation from the furnace wall to the CWF droplet

$Q_{\text{cond}}$  = heat conduction from the surrounding gas to the CWF droplet surface which is proportional to the temperature gradient at the CWF droplet surface, and expressed as

$$Q_{\text{cond}} = \pi d_p^2 \frac{\text{Nu } k_g}{d_p} (T_g - T_p) \quad \text{eq. (60)}$$

where  $d_p$  = diameter of the CWF droplet

$k_g$  = thermal conductivity of the surrounding gas

$T_g$  = temperature of the surrounding gas

$T_p$  = temperature of the CWF droplet

Nu = Nusselt number (in the case of stagnant medium, Nu = 2.0)

From eqs. (59) and (60), energy balance is written as

$$\left(\frac{\pi}{6} d_p^3 \rho_p\right) c_p \left(\frac{dT_p}{dt}\right)_1 = \pi d_p^2 \sigma \epsilon_p (T_w^4 - T_p^4) + \pi d_p^2 \left(\frac{\text{Nu } k_g}{d_p}\right) (T_g - T_p) \quad \text{eq. (61)}$$

where  $\rho_p$  = density of the CWF droplet

$\sigma$  = Stefan-Boltzman's constant

$\epsilon_p$  = emissivity of the CWF droplet

$T_w$  = temperature of the furnace wall

Here, Nu = 2.0 for a particle in a stagnant medium. Hence, the heating

rate of the CWF droplet in the pre-evaporation stage  $\left(\frac{dT_p}{dt}\right)_1$  is expressed

as

$$\left(\frac{dT_p}{dt}\right)_1 = \frac{6}{\rho_p c_p d_p} \sigma \epsilon_p (T_w^4 - T_p^4) + \frac{12 k_g}{\rho_p c_p d_p^2} (T_g - T_p) \quad \text{eq. (62)}$$

#### 4.3.3 Particle Heating Rate in Evaporation Stage

Energy balance for the CWF droplet/agglomerate during the evaporation process is expressed as

$$m_p c_p \left(\frac{dT_p}{dt}\right)_2 = Q_{\text{rad}} + Q_{\text{cond}} - Q_{\text{evap}} \quad \text{eq. (63)}$$

where  $\left(\frac{dT_p}{dt}\right)_2$  = heating rate of the CWF droplet/agglomerate in the evaporation stage

$Q_{\text{evap}}$  = energy required for the endothermic process of evaporation

Eq. (63) is also expressed as

$$\left(\frac{\pi}{6} d_p^3 \rho_p\right) c_p \left(\frac{dT_p}{dt}\right)_2 = \pi d_p^2 \sigma \epsilon_p (T_w^4 - T_p^4) + \pi d_p^2 \left(\frac{\text{Nu} k_g}{d_p}\right) (T_g - T_p) - L_w \frac{dm_w}{dt} \quad \text{eq. (64)}$$

where  $L_w$  = latent heat of evaporation

$\frac{dm_w}{dt}$  = rate of water evaporation

During the evaporation process, all the interstitial water in the CWF droplet is assumed to be evaporated, before the coal particles are heated to over 100°C. Hence, the temperature of the CWF droplet remains

constant (i.e.,  $T_p = T_{\text{evap}}$ ), and therefore, the heating rate of the CWF droplet/agglomerate during evaporation  $\left(\frac{dT_p}{dt}\right)_2$  will be zero,

$$\left(\frac{dT_p}{dt}\right)_2 = 0 \quad \text{eq. (65)}$$

#### 4.3.4 Particle Heating Rate in Heat-Up Stage

Once all the water in the CWF droplet evaporates, the temperature of the CWF agglomerate increases due to thermal radiation from the furnace wall and heat conduction from the surrounding gas. Energy balance for the CWF agglomerate during the heat-up stage is

$$m_p c_p \left(\frac{dT_p}{dt}\right)_3 = Q_{\text{rad}} + Q_{\text{cond}} \quad \text{eq. (66)}$$

or, equivalently,

$$\left(\frac{\pi}{6} d_p^3 \rho_p\right) c_p \left(\frac{dT_p}{dt}\right)_3 = \pi d_p^2 \sigma \epsilon_p (T_w^4 - T_p^4) + \pi d_p^2 \left(\frac{\text{Nu } k_g}{d_p}\right) (T_g - T_p) \quad \text{eq. (67)}$$

Here,  $\text{Nu} = 2.0$  for a particle in a stagnant medium. Hence, the heating

rate of the CWF agglomerate during the heat-up stage  $\left(\frac{dT_p}{dt}\right)_3$  is expressed as

$$\left(\frac{dT_p}{dt}\right)_3 = \frac{6}{\rho_p c_p d_p} \sigma \epsilon_p (T_w^4 - T_p^4) + \frac{12 k_g}{\rho_p c_p d_p^2} (T_g - T_p) \quad \text{eq. (68)}$$



where  $\rho_p$  = density of the CWF agglomerate  
 $c_p$  = specific heat of the CWF agglomerate  
 $d_p$  = diameter of the CWF agglomerate  
 $\epsilon_p$  = emissivity of the CWF agglomerate  
 $T_p$  = temperature of the CWF agglomerate

#### 4.3.5 Particle Heating Rate during Devolatilization

The particle heating rate during devolatilization is determined by an energy balance which contains: thermal radiation from the furnace wall ( $Q_{rad}$ ), energy feedback from the volatile flame to the agglomerate ( $Q_{flame}$ ), energy required for the endothermic process of devolatilization ( $Q_{devol}$ ), and energy transfer due to particle rotation ( $Q_{rot}$ ).

$$m_p c_p \left( \frac{dT_p}{dt} \right)_4 = Q_{rad} + Q_{flame} - Q_{devol} + Q_{rot} \quad \text{eq. (69)}$$

During devolatilization, the volatiles emerged from the agglomerate surface burn rapidly with the available oxygen, consequently, the volatile flame is infinitely thin and the volatiles burn completely to form  $CO_2$ ,  $NO$ , and  $H_2O$ . When the rate of the volatile evolution is faster than that of oxygen diffusion to the agglomerate, the volatiles will accumulate around the agglomerate and the volatile flame will detach from the agglomerate surface. The position of the detached volatile flame can be determined from the relative rates of devolatilization and oxygen diffusion to the volatile flame front, and the heating value and oxygen requirement of the volatiles. The expression of energy feedback from the volatile flame to the particle ( $Q_{flame}$ ) is obtained from the detached

volatile flame model derived by Timothy et al.<sup>(5)</sup>, and written as

$$Q_{\text{flame}} = \frac{\pi d_p^2 k_{\text{vol}} (T_f - T_p) \frac{1}{r_f^2} \frac{c_{p_{\text{vol}}} \dot{m}_{\text{vol}}}{4 \pi k_{\text{vol}}}}{\exp \left[ \frac{c_{p_{\text{vol}}} \dot{m}_{\text{vol}}}{4 \pi k_{\text{vol}}} \left( \frac{1}{r_p} - \frac{1}{r_f} \right) \right]} - 1 \quad \text{eq. (70)}$$

where  $r_f$  = radius of the volatile flame

$r_p$  = radius of the CWF agglomerate ( $= \frac{d_p}{2}$ )

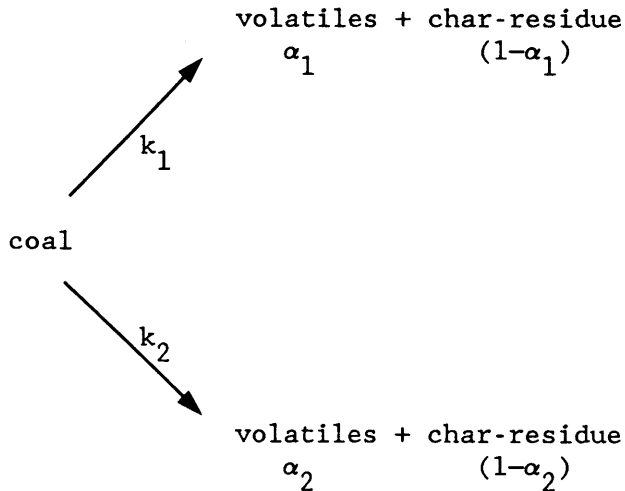
$T_f$  = temperature of the volatile flame

$k_{\text{vol}}$  = thermal conductivity of the volatiles

$c_{p_{\text{vol}}}$  = specific heat of the volatiles

$\dot{m}_{\text{vol}}$  = rate of the volatile mass loss, given by  $\left( \dot{m}_{\text{vol}} = M_o \frac{dV}{dt} \right)$

Several devolatilization models have been established to predict the devolatilization process. In the present study, Kobayashi's<sup>(15)</sup> competing reaction model is used to describe the devolatilization process. This reaction model is shown as follows:



The model consists of two competing reactions. The constants  $\alpha_1$  and  $\alpha_2$  are the mass fractions of coal produced as volatiles via paths 1 and 2. The rate constants  $k_1$  and  $k_2$  are first order with respect to the residual coal, and are assumed to follow an Arrhenius temperature dependence, and expressed as

$$k_1 = B_1 \exp(-E_1/RT_p), \text{ and} \quad \text{eq. (71)}$$

$$k_2 = B_2 \exp(-E_2/RT_p)$$

The volatile mass loss per unit original mass of the CWF agglomerate  $V(t)$  is expressed as

$$V(t) = \int_0^t \left[ (\alpha_1 k_1 + \alpha_2 k_2) \exp \left( - \int_0^t (k_1 + k_2) dt \right) \right] dt \quad \text{eq. (72)}$$

The rate of the volatile mass loss per unit original mass of the CWF agglomerate ( $dV/dt$ ) is expressed as

$$\frac{dV(t)}{dt} = (\alpha_1 k_1 + \alpha_2 k_2) \exp \left( - \int_0^t (k_1 + k_2) dt \right) \quad \text{eq. (73)}$$

Therefore, the rate of the volatile mass loss  $\dot{m}_{vol}$  in eq. (70) is expressed as

$$\begin{aligned} \dot{m}_{vol} &= M_o \frac{dV}{dt} \\ &= M_o (\alpha_1 k_1 + \alpha_2 k_2) \exp \left( - \int_0^t (k_1 + k_2) dt \right) \end{aligned} \quad \text{eq. (74)}$$

During devolatilization and char burnout, the particle rotation induced by the volatile evolution can be observed.<sup>(28)</sup> The convective heat transfer ( $Q_{rot}$ ) from the volatiles to the agglomerate due to the particle rotation is derived as

$$Q_{\text{rot}} = \pi d_p^2 \left( \frac{\text{Nu}_D k_{\text{vol}}}{d_p} \right) (T_{\text{fp}} - T_p) \quad \text{eq. (75)}$$

where  $T_{\text{fp}}$  = average temperature between the volatile flame and the CWF agglomerate

Here, Nusselt number  $\text{Nu}_D$  of a rotating sphere of diameter  $d_p$  is

$$\text{Nu}_D = 0.33 \text{Re}_D^{0.5} \text{Pr}^{0.4} \quad \text{eq. (76)}$$

$$\text{where } \text{Re}_D = \frac{\rho_{\text{vol}} d_p^2 \omega}{\mu_{\text{vol}}} \quad \text{and} \quad \text{Pr} = \frac{c_{p_{\text{vol}}} \mu_{\text{vol}}}{k_{\text{vol}}}$$

Finally, energy required for the endothermic process of devolatilization ( $Q_{\text{devol}}$ ) is given by

$$Q_{\text{devol}} = \pi d_p^2 \dot{m}_{\text{vol}} \Delta H_{\text{devol}} \quad \text{eq. (77)}$$

where  $\Delta H_{\text{devol}}$  = endothermic heat of devolatilization

From eqs. (69) through (77), energy balance for the CWF agglomerate during the devolatilization process is given by

$$\begin{aligned} \left( \frac{\pi}{6} d_p^3 \rho_p \right) c_p \left( \frac{dT}{dt} \right)_4 &= \pi d_p^2 \sigma \epsilon_p (T_w^4 - T_p^4) \\ &+ \frac{\pi d_p^2 k_{\text{vol}} (T_f - T_p) \frac{1}{r_f} \frac{c_{p_{\text{vol}}} \dot{m}_{\text{vol}}}{4 \pi k_{\text{vol}}}}{\exp \left[ \frac{c_{p_{\text{vol}}} \dot{m}_{\text{vol}}}{4 \pi k_{\text{vol}}} \left( \frac{1}{r_p} - \frac{1}{r_f} \right) \right]} - 1 \\ &- \pi d_p^2 \dot{m}_{\text{vol}} \Delta H_{\text{devol}} + \pi d_p^2 \left( \frac{\text{Nu}_D k_{\text{vol}}}{d_p} \right) (T_{\text{fp}} - T_p) \end{aligned} \quad \text{eq. (78)}$$

Hence, the heating rate of the CWF agglomerate during devolatilization

$\left(\frac{dT_p}{dt}\right)_4$  is

$$\begin{aligned} \left(\frac{dT_p}{dt}\right)_4 &= \frac{6}{\rho_p c_p d_p} \sigma \epsilon_p (T_w^4 - T_p^4) \\ &+ \frac{6}{\rho_p c_p d_p} \frac{k_{vol} (T_f - T_p) \frac{1}{r_f^2} \frac{c_{p_{vol}} \dot{m}_{vol}}{4 \pi k_{vol}}}{\exp \left[ \frac{c_{p_{vol}} \dot{m}_{vol}}{4 \pi k_{vol}} \left( \frac{1}{r_p} - \frac{1}{r_f} \right) \right] - 1} \\ &- \frac{6}{\rho_p c_p d_p} \dot{m}_{vol} \Delta H_{devol} + \frac{6}{\rho_p c_p d_p} \left( \frac{Nu_D k_{vol}}{d_p} \right) (T_{fp} - T_p) \end{aligned}$$

eq. (79)

However, the term of convective heat transfer due to particle rotation ( $Q_{rot}$ ) in eqs. (69), (78), and (79) is found to be negligibly small compared to the other terms in these equations.

#### 4.3.6 Particle Heating Rate during Char Burnout

Toward the end of devolatilization, as the rate of the volatile evolution decreases, the volatile flame will recede and reattach to the agglomerate surface. As the rest of the volatiles emerges from the agglomerate, they will burn at the agglomerate surface. At this point the char particle ignites and burns under chemical and diffusional limitations. The energy balance during char burnout has the terms of thermal radiation from the furnace wall ( $Q_{rad}$ ), energy produced by the exothermic char burnout ( $Q_{char}$ ), energy produced by the remaining

volatile burnout ( $Q_{vol}$ ), and energy transfer due to particle rotation ( $Q_{rot}$ ).

$$m_p c_p \left( \frac{dT_p}{dt} \right)_5 = Q_{rad} + Q_{char} + Q_{vol} + Q_{rot} \quad \text{eq. (80)}$$

The terms of  $Q_{rad}$  and  $Q_{rot}$  were discussed earlier, and the term of energy produced by the remaining volatile burnout ( $Q_{vol}$ ) is given by

$$Q_{vol} = \pi d_p^2 q_{vol} \Delta H_{vol} \quad \text{eq. (81)}$$

where  $q_{vol}$  = combustion rate of the volatiles

$\Delta H_{vol}$  = heat of combustion of the volatiles

The energy produced by the combustion reaction of coal at the CWF agglomerate surface ( $Q_{char}$ ) is given by

$$Q_{char} = \pi d_p^2 q_{char} \Delta H_{char} \quad \text{eq. (82)}$$

where  $\Delta H_{char}$  = heat of combustion of the coal surface

$q_{char}$  = rate of the chemical surface reaction of coal, given by<sup>(5)</sup>

$$q_{char} = \frac{PD_{O_2}}{RTBr_p} \ln \left( \frac{1+BX_{O_2,s}}{1+BX_{O_2,g}} \right) - \frac{\dot{m}_{vol} \beta_{vol}}{4 \pi r_p^2} \quad \text{eq. (83)}$$

where P = pressure

R = ideal gas constant

T = temperature

$D_{O_2}$  = diffusion coefficient of oxygen

$X_{O_2,s}$  = oxygen concentration at the agglomerate surface

$X_{O_2,g}$  = oxygen concentration in gas

$\beta_{vol}$  = oxygen requirement of the volatiles

$B$  = number of moles of combustion product per mole of oxygen

From eqs. (80) through (83), energy balance for the CWF agglomerate during char burnout is given by

$$\begin{aligned} \left(\frac{\pi}{6} d_p^3 \rho_p\right) c_p \left(\frac{dT_p}{dt}\right)_5 &= \pi d_p^2 \sigma \epsilon_p (T_w^4 - T_p^4) \\ &+ \pi d_p^2 \left[ \frac{PD_{O_2}}{RTBr_p} \ln \left( \frac{1+BX_{O_2,s}}{1+BX_{O_2,g}} \right) - \frac{\dot{m}_{vol} \beta_{vol}}{4 \pi r_p^2} \right] \Delta H_{char} \\ &+ \pi d_p^2 q_{vol} \Delta H_{vol} \\ &+ \pi d_p^2 \left( \frac{Nu_D k_{vol}}{d_p} \right) (T_{fp} - T_p) \end{aligned} \quad \text{eq. (84)}$$

Hence, the heating rate of the CWF agglomerate during char burnout is

$$\begin{aligned} \left(\frac{dT_p}{dt}\right)_5 &= \frac{6}{\rho_p c_p d_p} \sigma \epsilon_p (T_w^4 - T_p^4) \\ &+ \frac{6}{\rho_p c_p d_p} \left[ \frac{PD_{O_2}}{RTBr_p} \ln \left( \frac{1+BX_{O_2,s}}{1+BX_{O_2,g}} \right) - \frac{\dot{m}_{vol} \beta_{vol}}{4 \pi r_p^2} \right] \Delta H_{char} \\ &+ \frac{6}{\rho_p c_p d_p} q_{vol} \Delta H_{vol} \\ &+ \frac{6}{\rho_p c_p d_p} \left( \frac{Nu_D k_{vol}}{d_p} \right) (T_{fp} - T_p) \end{aligned} \quad \text{eq. (85)}$$

As mentioned in Section 4.3.5, the term of convective heat transfer due to particle rotation ( $Q_{rot}$ ) in eqs. (80), (84), and (85) is also found to be negligibly small compared to the other terms in these equations.



CHAPTER 5  
RESULTS AND DISCUSSIONS

5.1 Particle Rotation

The angular velocity of the rotating CWF agglomerate during devolatilization and char burnout for different agglomerate diameters, furnace gas temperatures, and oxygen partial pressures in the furnace was predicted by the model of particle rotation, described by eqs. (1) through (18), in Section 5.1.1.

The experimental results of high-speed cinematography and fiber optic radiometry showed that the angular velocity and the fraction of rotating agglomerates per total number of burning agglomerates vary with agglomerate diameter, furnace gas temperature, and oxygen partial pressure in the furnace. The results of the statistical study of particle rotation will be discussed in Section 5.1.2.

5.1.1 Model Predictions of Particle Rotation

The predictions of the angular velocity of the rotating CWF agglomerate were made by the model of particle rotation, described in Section 4.1, and shown in Figures 38 through 42.

Figure 38 shows the effect of the oxygen partial pressure in the furnace on the angular velocity for an agglomerate diameter of 100  $\mu\text{m}$  and a furnace gas temperature of 1100 K. Figures 38-a, 38-b, and 38-c correspond to oxygen partial pressures of 20 %, 40 %, and 100 %, respectively. The value of the geometrical factor in eq. (11) was chosen 0.03 during the model prediction in Figures 38 through 40. Figure 38 shows

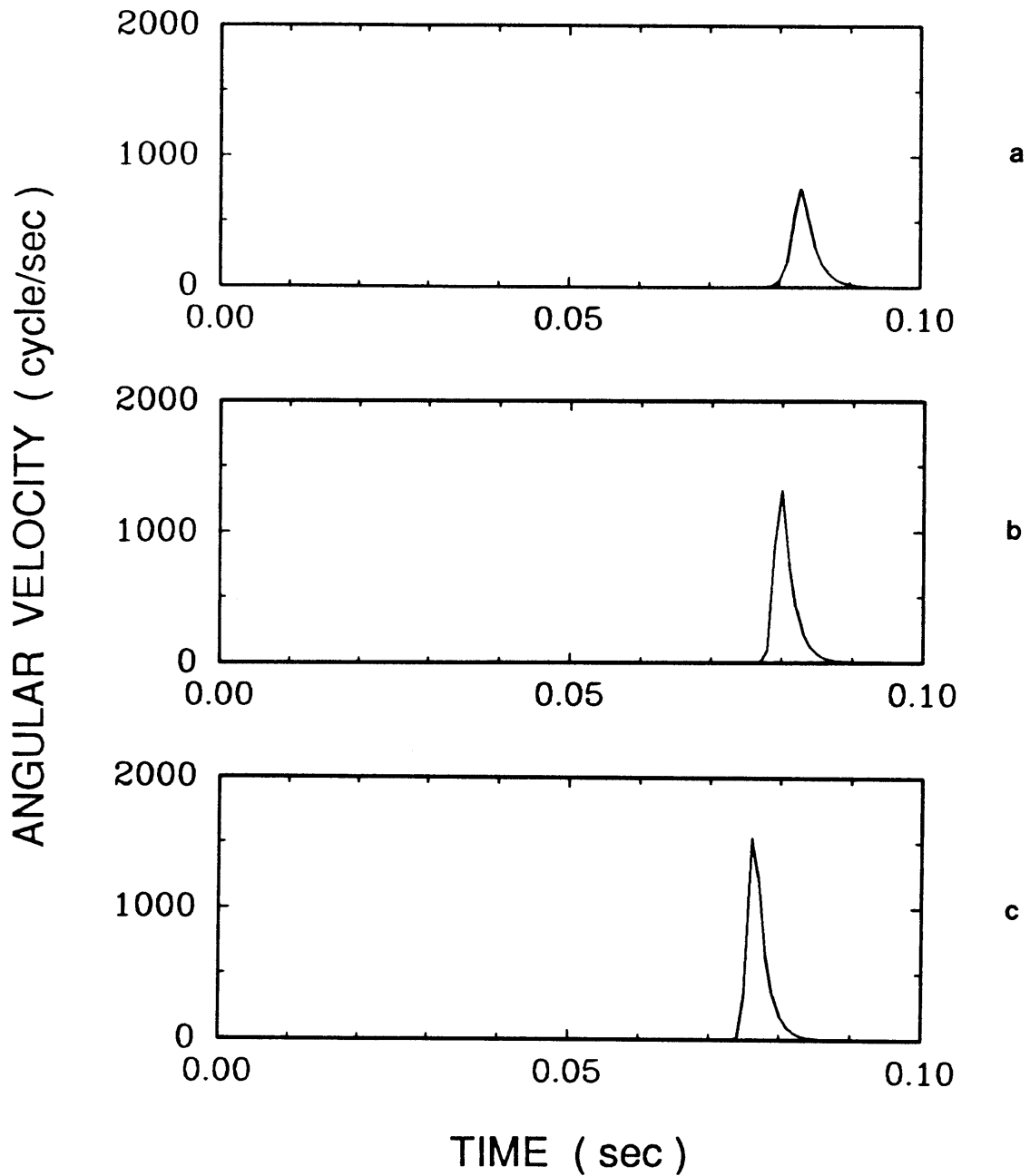


Figure 38. Predictions of Angular Velocity of Rotating CWF Agglomerate; Effect of Oxygen Partial Pressure (Agglomerate Diameter =  $100 \mu\text{m}$ , Furnace Gas Temperature = 1100 K)  
(a) 20 %  $\text{O}_2$ , (b) 40 %  $\text{O}_2$ , (c) 100 %  $\text{O}_2$

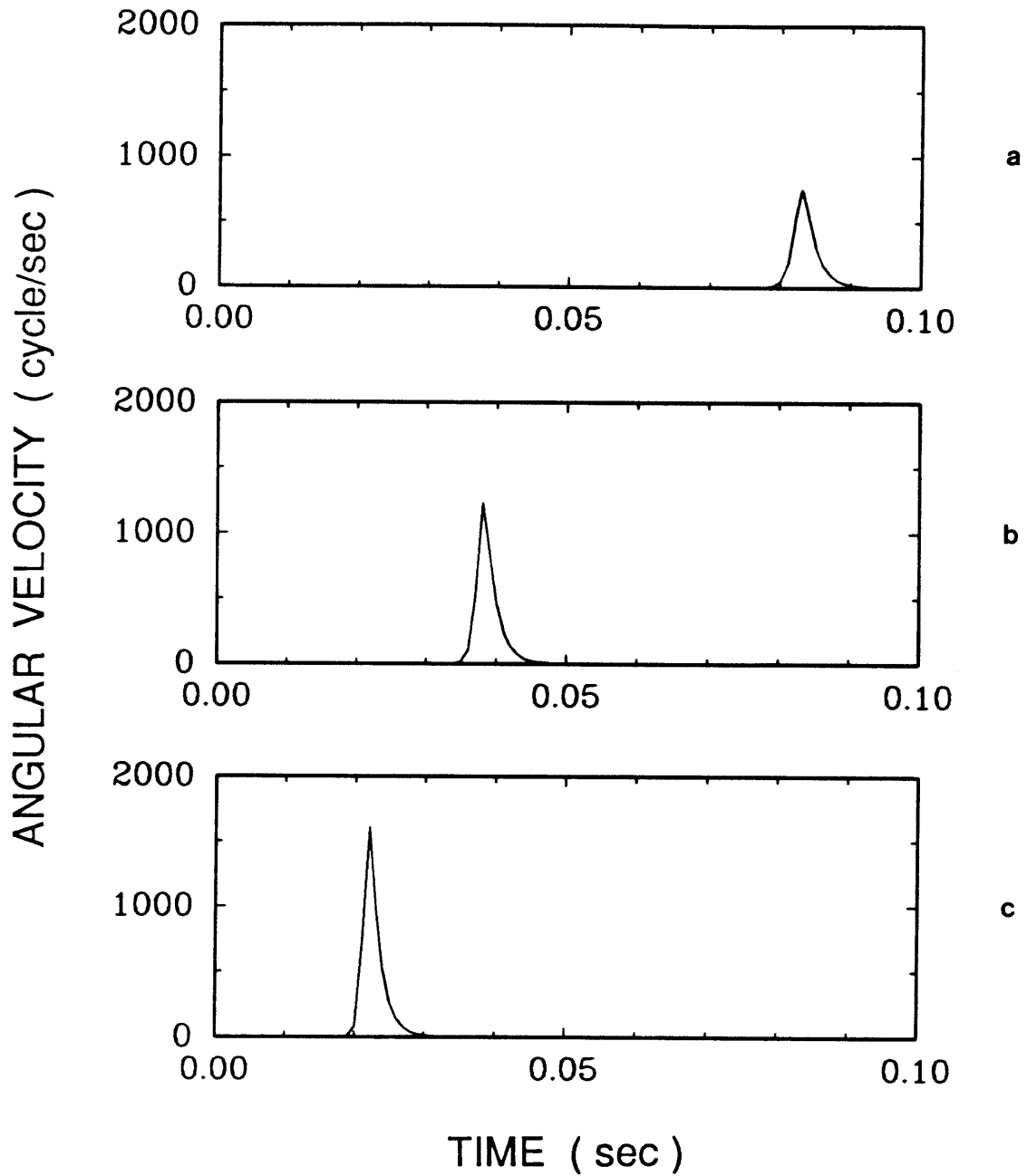


Figure 39. Predictions of Angular Velocity of Rotating CWF Agglomerate; Effect of Furnace Gas Temperature (Agglomerate Diameter =  $100 \mu\text{m}$ , Oxygen Partial Pressure = 20 %)  
(a) 1100 K, (b) 1400 K, (c) 1750 K

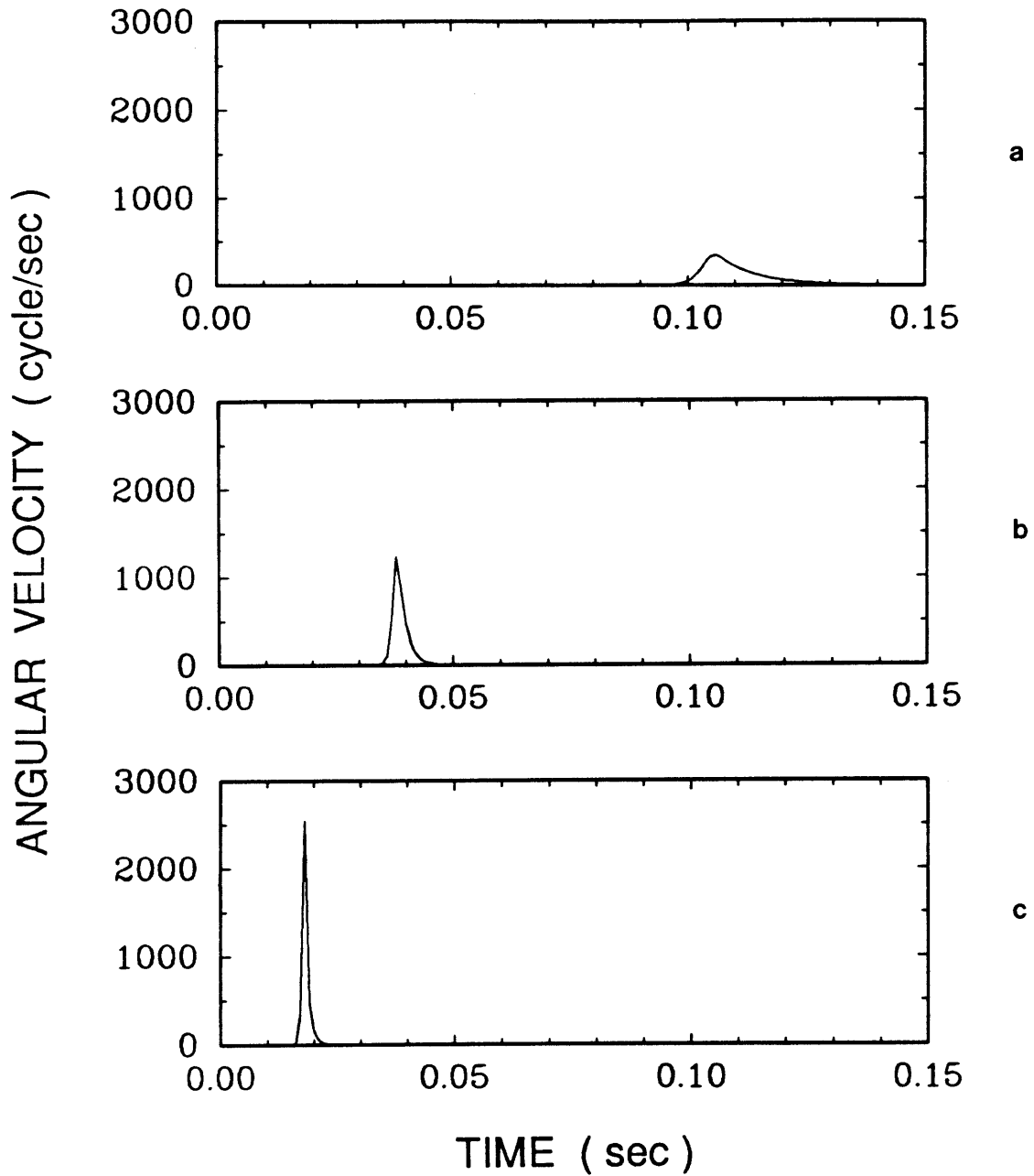


Figure 40. Predictions of Angular Velocity of Rotating CWF Agglomerate; Effect of Agglomerate Diameter (Furnace Gas Temperature = 1400 K, Oxygen Partial Pressure = 20 %)  
(a) 200  $\mu\text{m}$ , (b) 100  $\mu\text{m}$ , (c) 60  $\mu\text{m}$

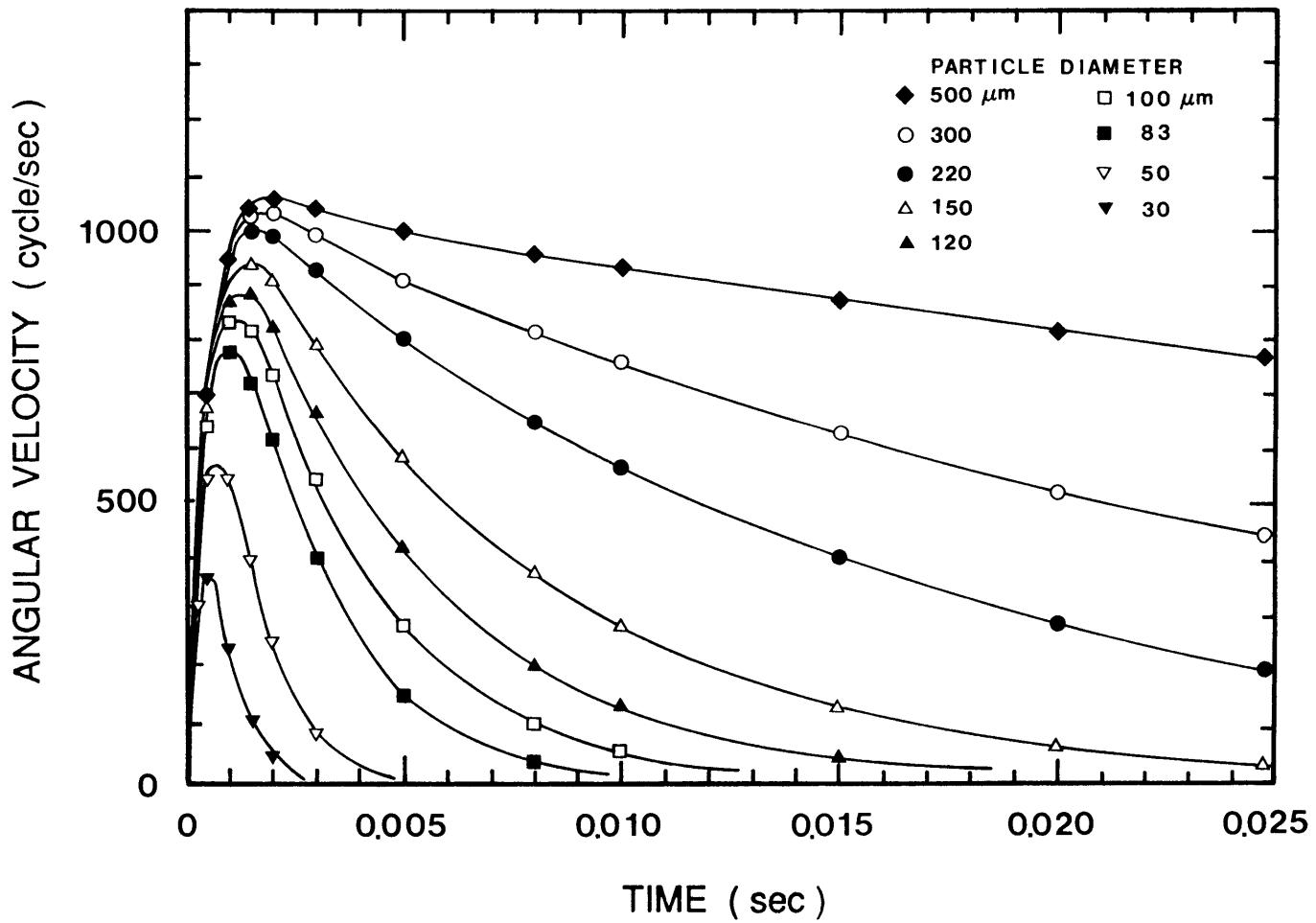


Figure 41. Predictions of Angular Velocity of Rotating CWF Agglomerate; Effect of Agglomerate Diameter (Devolatilization Rate Constant =  $950 \text{ sec}^{-1}$ )

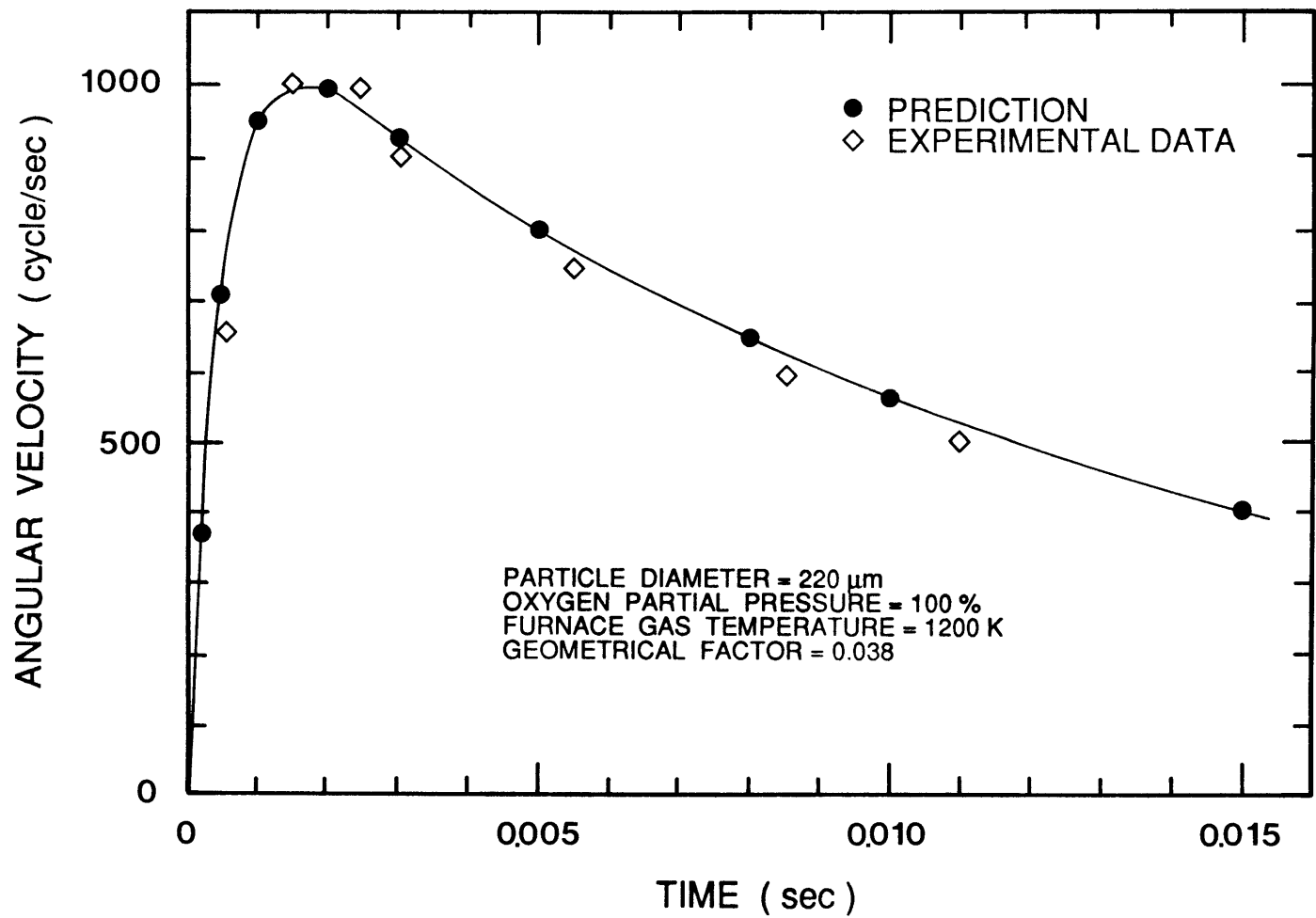


Figure 42. Comparison between Prediction and Experimental Data of Angular Velocity of Rotating CWF Agglomerate

that, as the oxygen partial pressure increases, the angular velocity of the CWF agglomerate increases, due to the increases in the particle heating rate (especially after the heat-up stage), the devolatilization rate  $dV/dt$ , and the total volatile yield  $V^*$ .

The effect of the furnace gas temperature on the angular velocity for an agglomerate diameter of  $100 \mu\text{m}$  and an oxygen partial pressure of 20 % is illustrated in Figures 39-a, 39-b, and 39-c, which correspond to the furnace gas temperatures of 1100 K, 1400 K, and 1750 K. As the furnace gas temperature increases, the angular velocity of the CWF agglomerate increases due to the increase in the particle heating rate and the increases in  $dV/dt$  and  $V^*$ .

Figure 40 shows the effect of the agglomerate diameter on the angular velocity at a furnace gas temperature of 1400 K and an oxygen partial pressure of 20 %. Figures 40-a, 40-b, and 40-c correspond to CWF agglomerate diameters of  $200 \mu\text{m}$ ,  $100 \mu\text{m}$ , and  $60 \mu\text{m}$ , respectively. As the agglomerate diameter decreases, the angular velocity of the CWF agglomerate increases due to the increase in the particle heating rate and the increases in  $dV/dt$  and  $V^*$ .

Figure 41 shows the predictions of the angular velocity of the CWF agglomerate for the isothermal devolatilization process as functions of time and agglomerate diameter by the model of particle rotation, described by eqs. (12) through (18). The devolatilization rate constant ( $k$ ) in eq. (18) was set at the value of  $950 \text{ sec}^{-1}$  for each agglomerate diameter and the value of the geometrical factor in eq. (18) was set at the value of 0.038 in Figure 41. Figure 42 shows the comparison between the prediction and the experimental data for an oxygen partial pressure

of 100 %, a furnace gas temperature of 1200 K, and an agglomerate diameter of 220  $\mu\text{m}$ . It shows a close agreement between the prediction and the experimental data.<sup>(28)</sup>

The centrifugal force of the rotating CWF agglomerate can be obtained by substituting the angular velocity, obtained from eq. (11) or (18) and shown in Figures (38) through (41), into eq. (28). The predictions of the centrifugal force acting on a coal particle with a diameter of 30  $\mu\text{m}$  and a mass of  $2.0 \times 10^{-11}$  kg located on the outer edge of a CWF agglomerate with a diameter of 100  $\mu\text{m}$  are shown in Figures 43-a, 43-b, and 43-c. The oxygen partial pressure is 20 %; the furnace gas temperature for the three figures is 1100 K, 1400 K, and 1750 K, respectively. The geometrical factor in eq. (11) was set at the value of 0.03 for each furnace gas temperature in Figure 43. It is seen that with increasing furnace gas temperature (consequently, with increasing particle heating rate and angular velocity), the centrifugal force increases.

#### 5.1.2 Results of Statistical Study of Particle Rotation

The experimental results of a statistical study of particle rotation by high-speed cinematography and fiber optic radiometry are shown in Figures 44 through 47.

During the experiments, the oxygen partial pressure ranged from 20 % to 100 %; the furnace gas temperature ranged from 1100 K to 1750 K; the agglomerate diameter was varied from 45-53  $\mu\text{m}$  to 212-250  $\mu\text{m}$ . Each figure shows the probability density distribution of angular velocities of CWF agglomerates (i.e., probability versus angular velocities of CWF agglomerates for the above-mentioned variables).



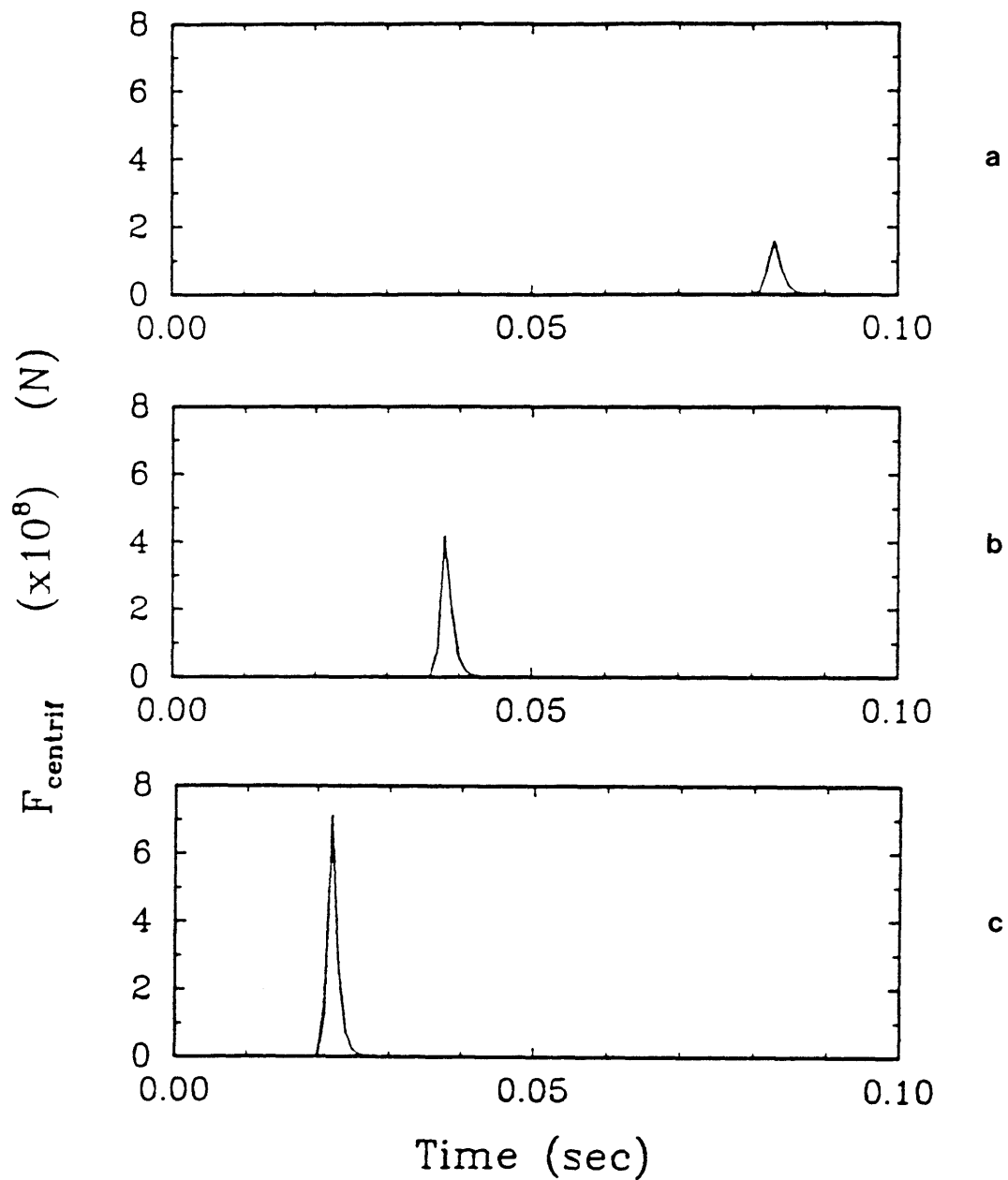


Figure 43. Predictions of Centrifugal Force; Effect of Furnace Gas Temperature on Centrifugal Force (Agglomerate Diameter =  $100 \mu\text{m}$ , Oxygen Partial Pressure = 20 %)  
(a) 1100 K, (b) 1400 K, (c) 1750 K

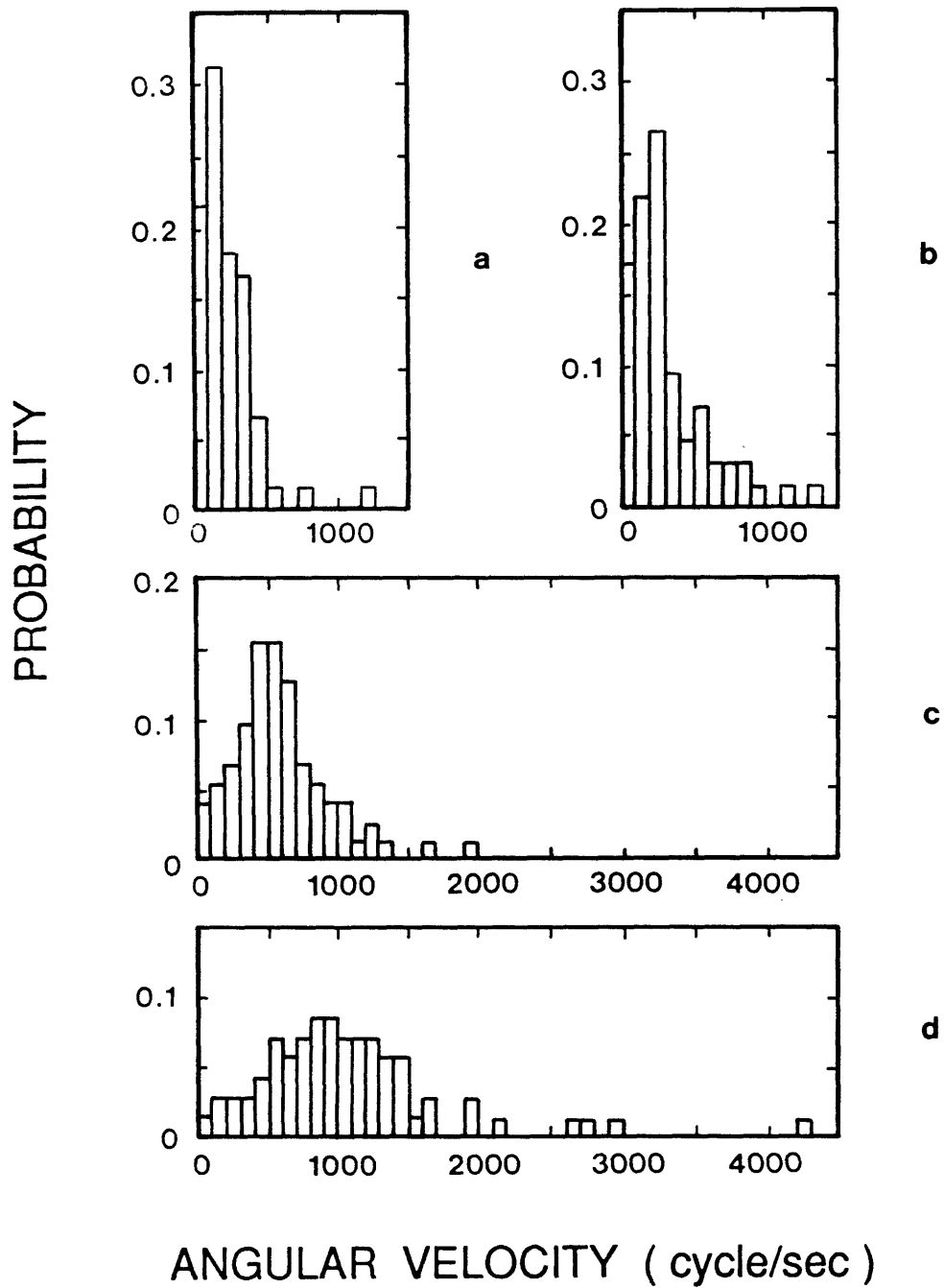


Figure 44. Probability Density Distributions of Angular Velocities; Effect of Oxygen Partial Pressure (Agglomerate Diameter = 90-106  $\mu\text{m}$ , Furnace Gas Temperature = 1750 K)  
 (a) 20 %  $\text{O}_2$ , (b) 40 %  $\text{O}_2$ , (c) 70 %  $\text{O}_2$ , (d) 100 %  $\text{O}_2$

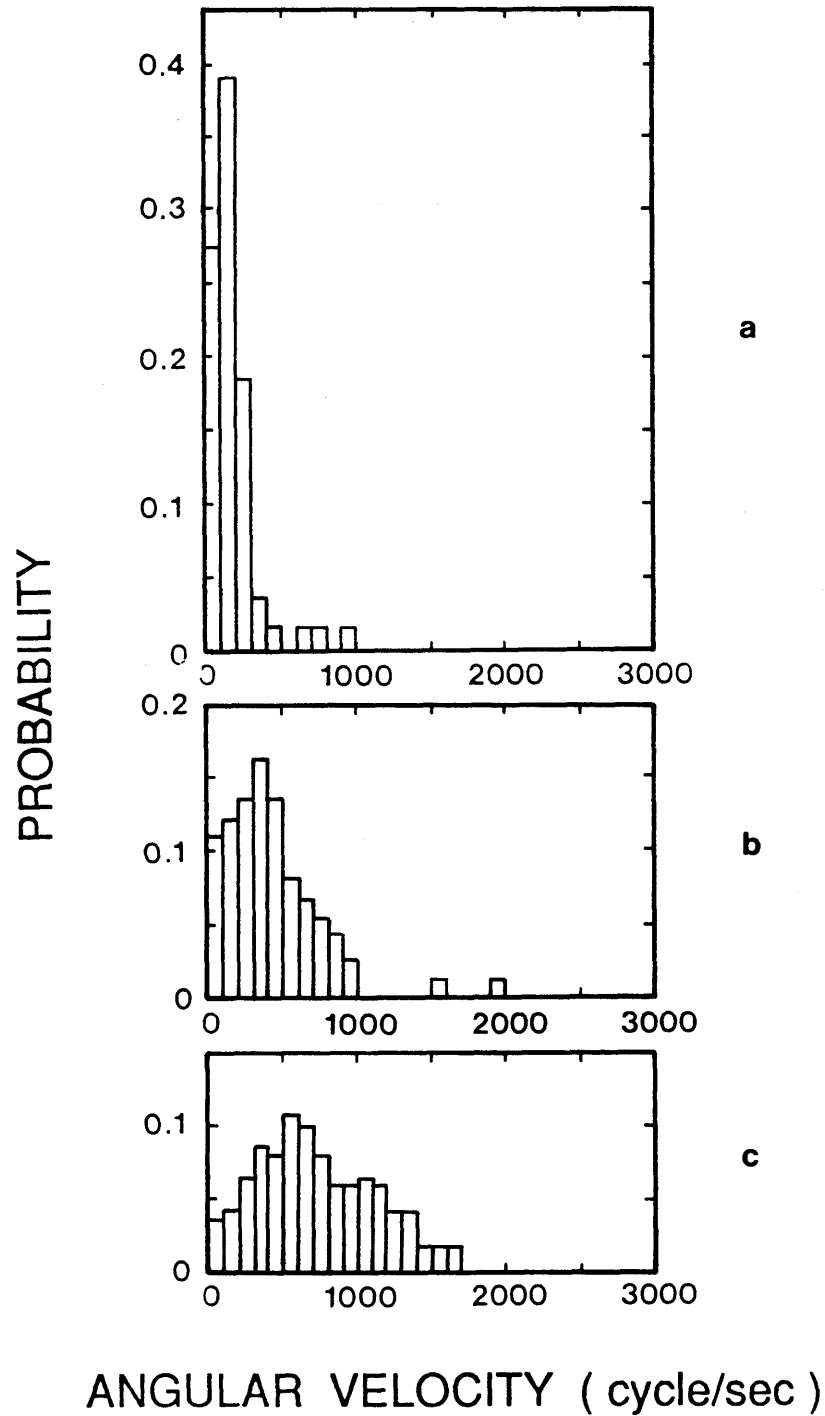


Figure 45. Probability Density Distributions of Angular Velocities;  
 Effect of Oxygen Partial Pressure (Agglomerate Diameter =  
 90-106  $\mu\text{m}$ , Furnace Gas Temperature = 1400 K)  
 (a) 40 %  $\text{O}_2$ , (b) 70 %  $\text{O}_2$ , (c) 100 %  $\text{O}_2$

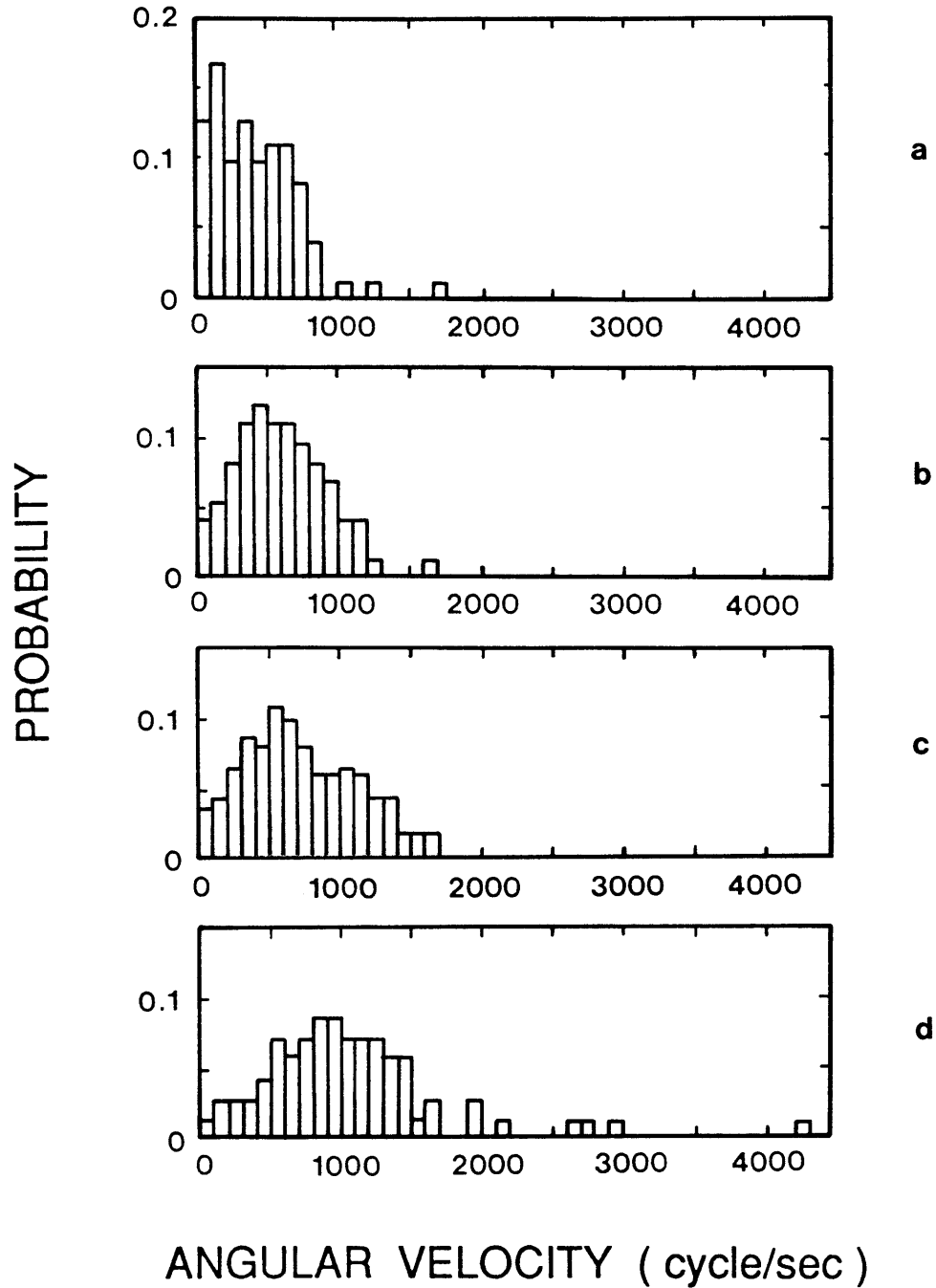


Figure 46. Probability Density Distributions of Angular Velocities;  
 Effect of Furnace Gas Temperature (Agglomerate Diameter =  
 90-106  $\mu\text{m}$ , Oxygen Partial Pressure = 100%)  
 (a) 1100 K, (b) 1250 K, (c) 1400 K, (d) 1750 K

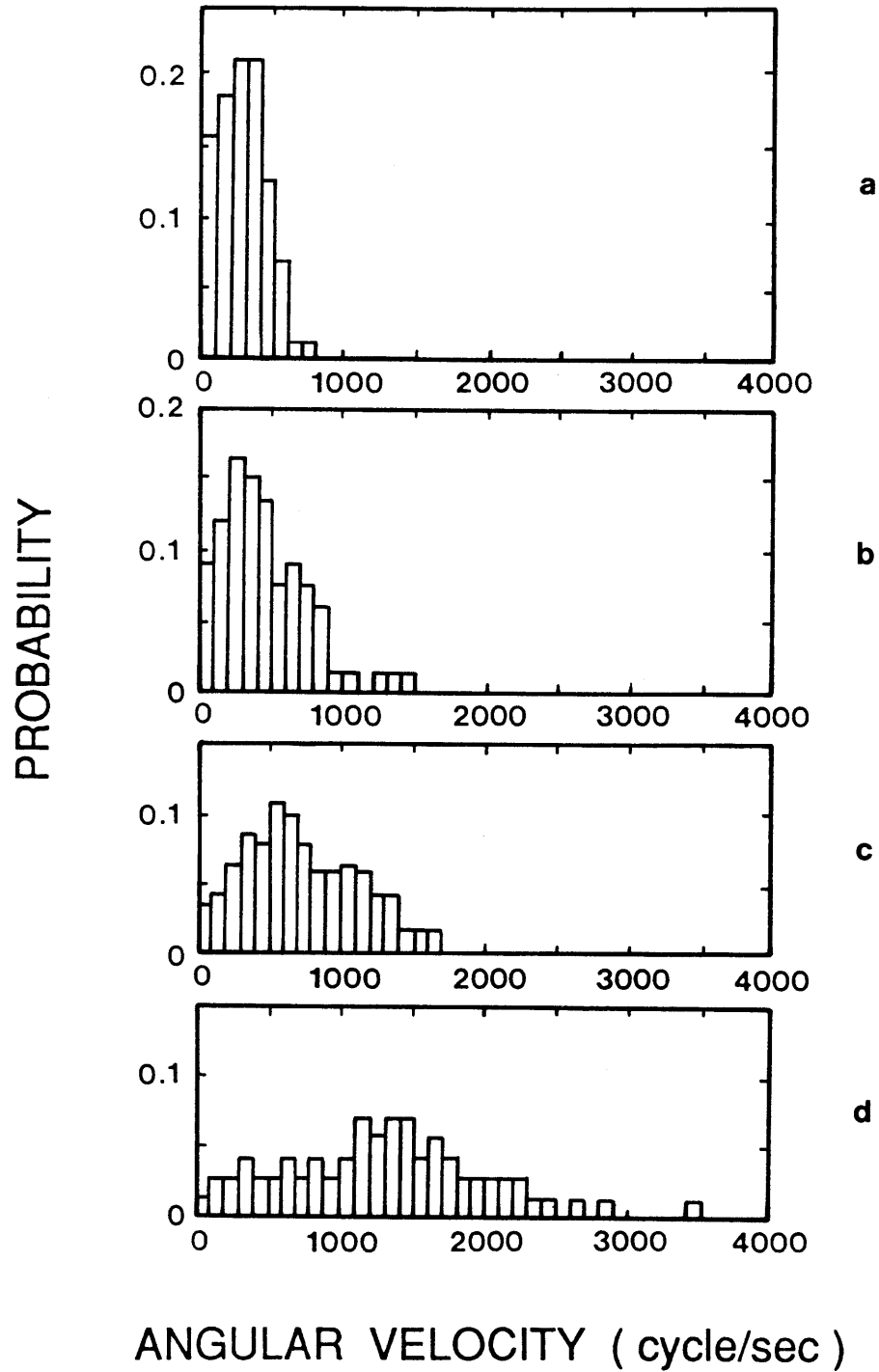


Figure 47. Probability Density Distributions of Angular Velocities;  
 Effect of Agglomerate Diameter (Furnace Gas Temperature =  
 1400 K, Oxygen Partial Pressure = 100%)  
 (a) 212-250  $\mu\text{m}$ , (b) 150-180  $\mu\text{m}$ ,  
 (c) 90-106  $\mu\text{m}$ , (d) 45-53  $\mu\text{m}$

Figures 44 and 45 show the effect of oxygen partial pressure on the angular velocity for an agglomerate diameter of 90-106  $\mu\text{m}$  at furnace gas temperatures of 1750 K and 1400 K, respectively. Oxygen partial pressure varies from 20 % to 100 % in Figure 44, and from 40 % to 100 % in Figure 45. As shown in these figures, as the oxygen partial pressure increases, the mean angular velocity of CWF agglomerates can be seen to increase due to the greater particle heating rate, and therefore higher devolatilization rate  $dV/dt$ .

Figure 46 shows the effect of furnace gas temperature on the angular velocity of CWF agglomerates for a CWF agglomerate with a diameter of 90-106  $\mu\text{m}$  and an oxygen partial pressure of 100 %. The furnace gas temperature varies from 1100 K to 1750 K. As the furnace gas temperature increases, the mean angular velocity of CWF agglomerates increases due to the increases in the particle heating and devolatilization rates.

The effect of agglomerate diameter on the angular velocity is shown in Figure 47. The furnace gas temperature and oxygen partial pressure are fixed at 1400 K and 100 %, respectively, and the agglomerate diameter varies from 45-53  $\mu\text{m}$  to 212-250  $\mu\text{m}$ . The particle heating rate increases with decreasing agglomerate diameter, resulting in increased mean angular velocity of agglomerate rotation.

Based upon the experimental results and statistical study, it is concluded that the angular velocity of the rotating CWF agglomerate and the fraction of rotating agglomerates per total number of burning agglomerates are a strong function of the particle heating rate which, in turn, is directly influenced by the oxygen partial pressure, the gas temperature in a furnace, and the agglomerate diameter. It is also found

that all of the probability density distribution curves of angular velocities of CWF agglomerates plotted in Figures 44 through 47 have the same functional form as that of the geometrical factor which is shown in Figure 31. This is apparent because only the geometrical factor affects the probability density distribution of angular velocity of CWF agglomerates when the other variables in eq. (11) or (18) are fixed.

## 5.2 Adhesive Force during Particle Agglomeration

The adhesive force during particle agglomeration for the different particle heating rates are predicted by the model of particle agglomeration, described by eqs. (29) through (58). Figures 48 and 49 show the predictions of the volume fractions of unreacted coal C, liquid metaplast L, and coke-residue (char) E, the normalized contact area A, the surface tension force  $F_\gamma$ , the adhesive force due to coke interconnection  $F_E$ , and the adhesive force  $F_A$  as functions of time and typical particle heating rates of  $10^4$  K/sec and  $10^5$  K/sec, respectively, to show the effect of particle heating rate. Figures 50-a and 50-b correspond to the particle heating rates of  $10^4$  K/sec and  $10^5$  K/sec, respectively.

The time-temperature histories of the CWF agglomerate, which are obtained for different furnace gas temperatures, agglomerate diameters, oxygen partial pressures by the model of time-temperature history in Section 4.3, are also used as input data to predict the adhesive force in Figures 51 through 53. Figures 51 and 52 show the effects of furnace gas temperature and agglomerate diameter, respectively, on the adhesive force during particle agglomeration. The particle heating rate during the

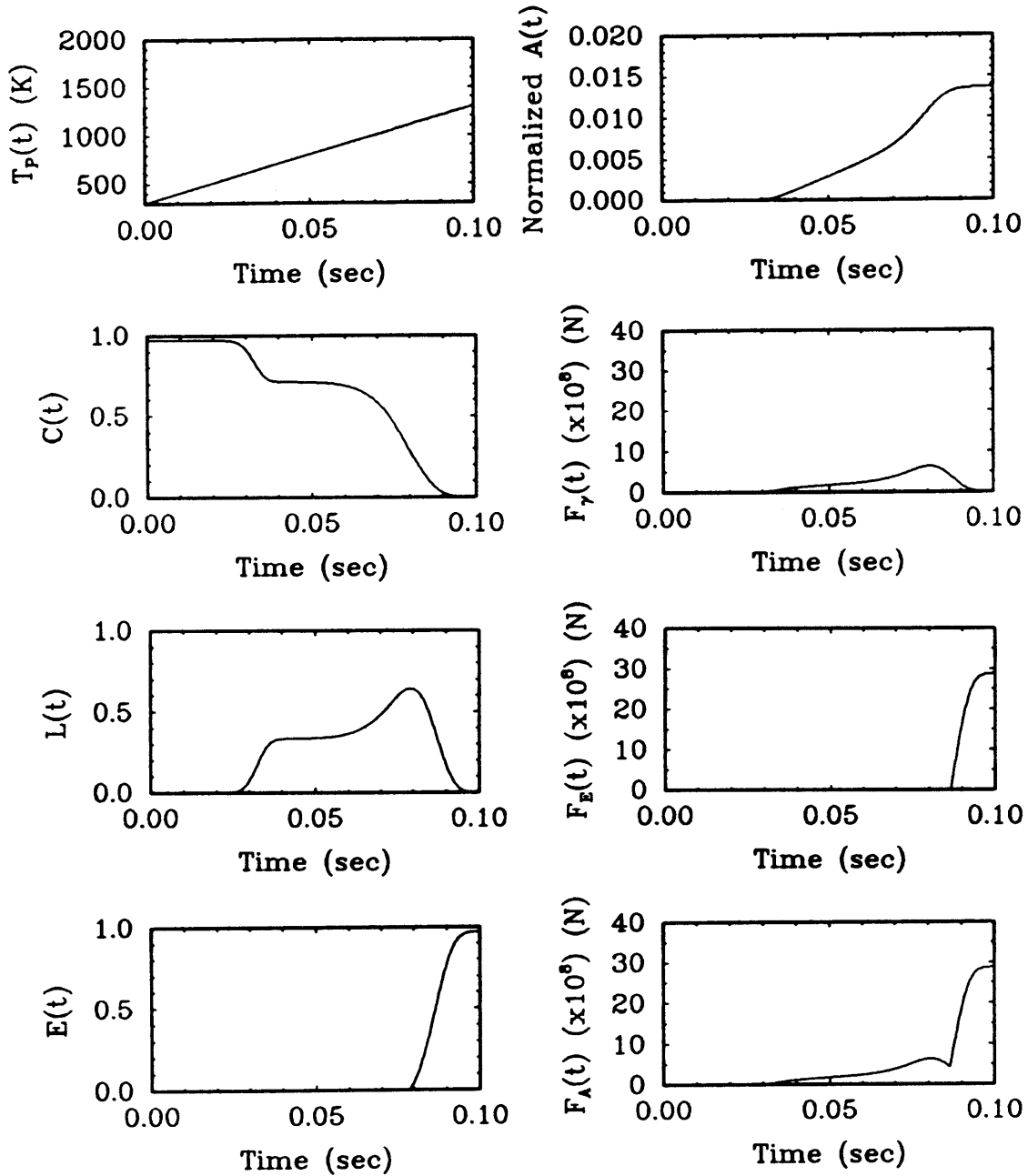


Figure 48. Predictions of  $C$ ,  $L$ ,  $E$ , Normalized  $A$ ,  $F_\gamma$ ,  $F_E$ , and Adhesive Force  $F_A$  versus Time for Particle Heating Rate of  $10^4$  K/sec



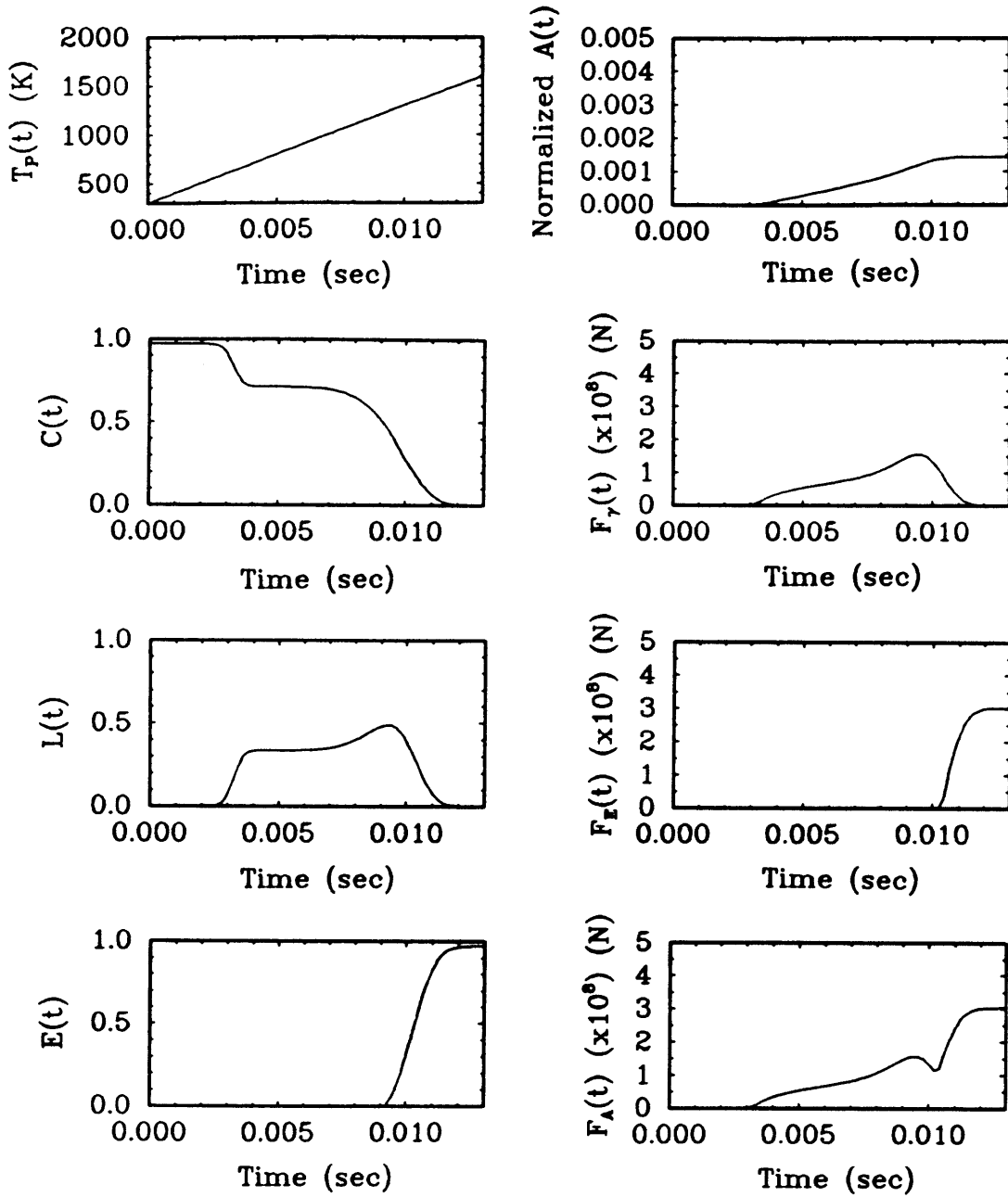


Figure 49. Predictions of  $C$ ,  $L$ ,  $E$ , Normalized  $A$ ,  $F_\gamma$ ,  $F_E$ , and Adhesive Force  $F_A$  versus Time for Particle Heating Rate of  $10^5$  K/sec

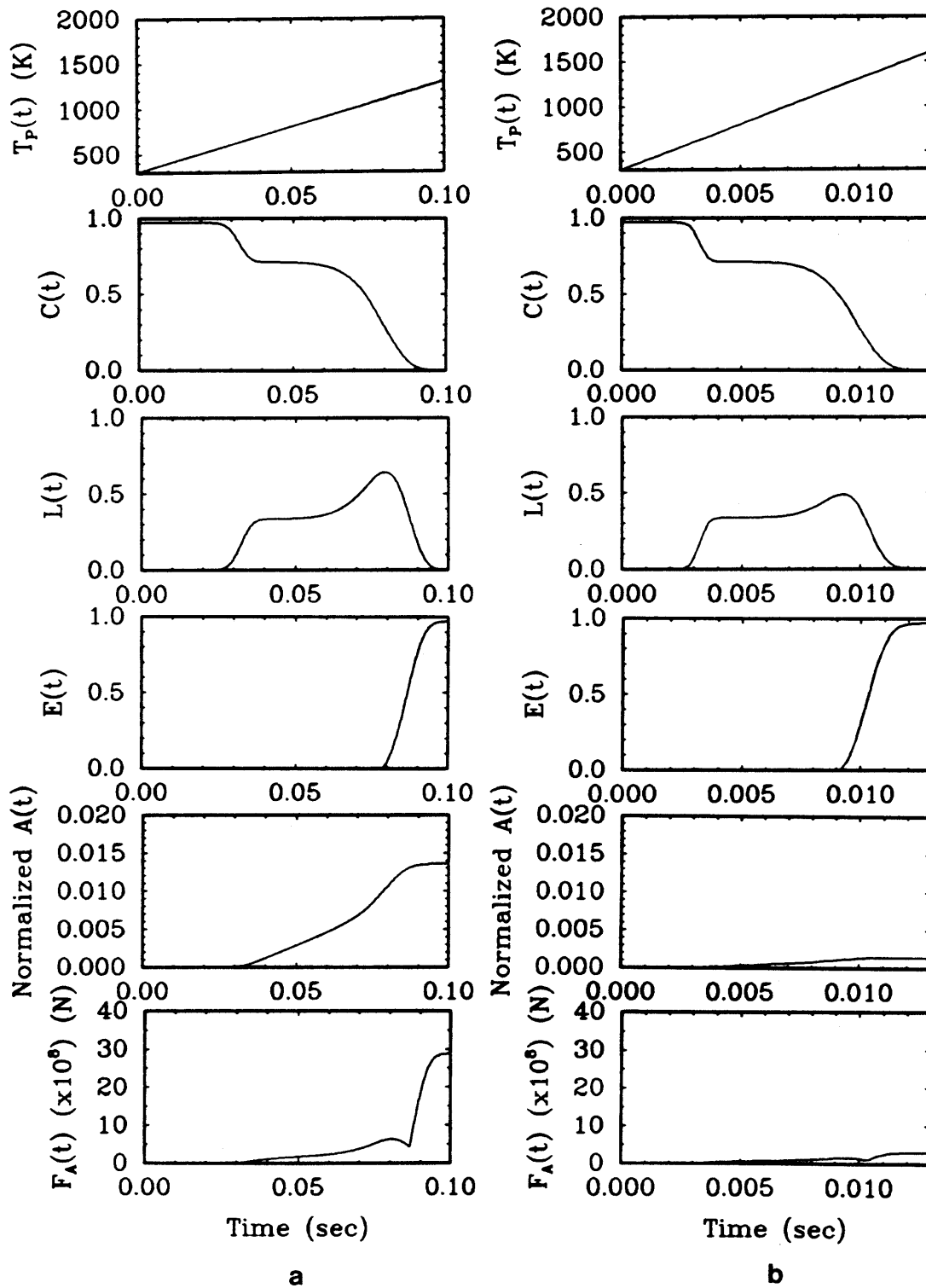


Figure 50. Comparisons of  $C$ ,  $L$ ,  $E$ , Normalized  $A$ , and Adhesive Force  $F_A$  versus Time for Different Particle Heating Rates  
 (a)  $10^4$  K/sec, (b)  $10^5$  K/sec

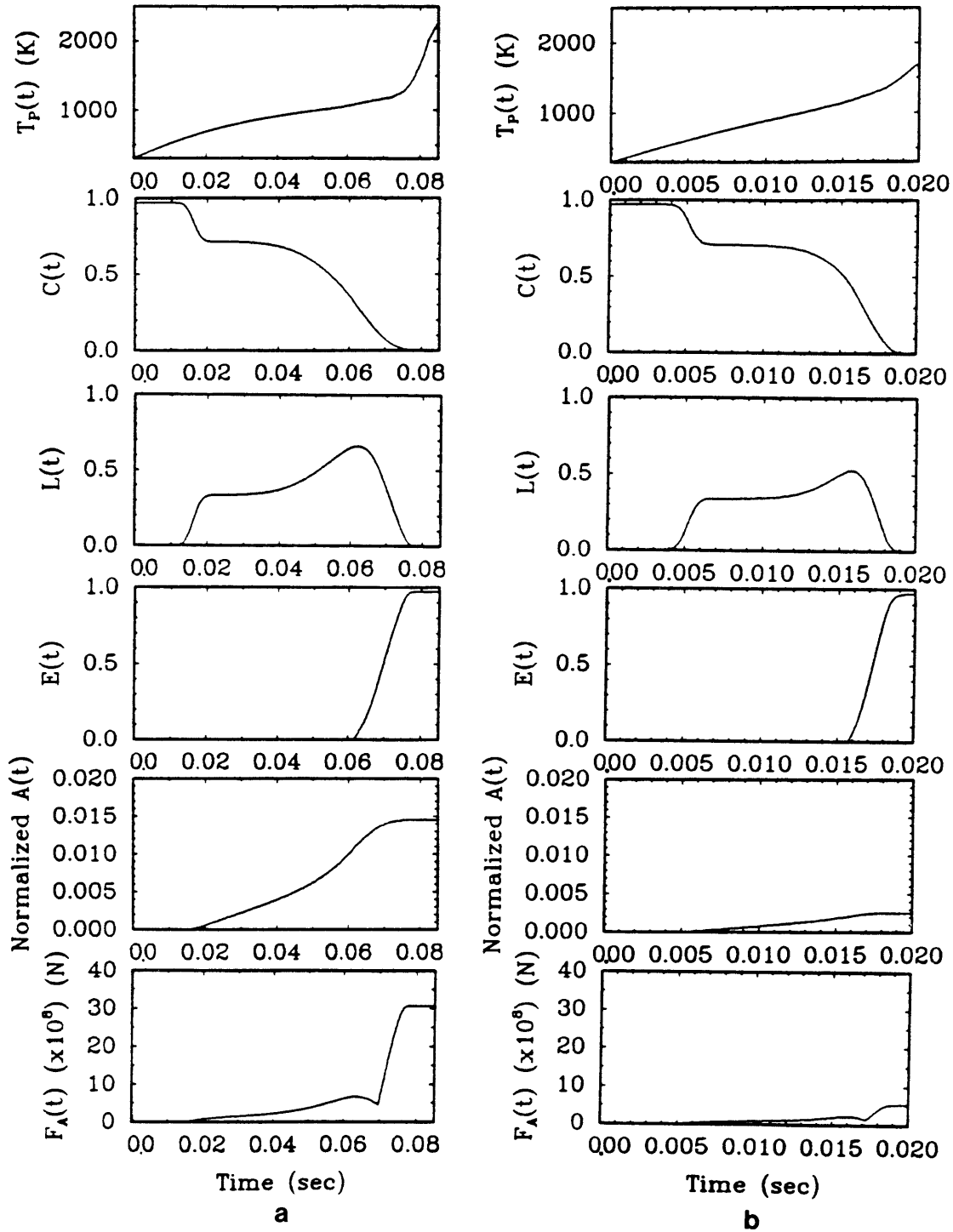


Figure 51. Predictions of  $C$ ,  $L$ ,  $E$ , Normalized  $A$ , and Adhesive Force  $F_A$  versus Time for Different Furnace Gas Temperature (Agglomerate Diameter = 100  $\mu\text{m}$ , Oxygen Partial Pressure = 20 %)  
 (a) 1100 K, (b) 1750 K

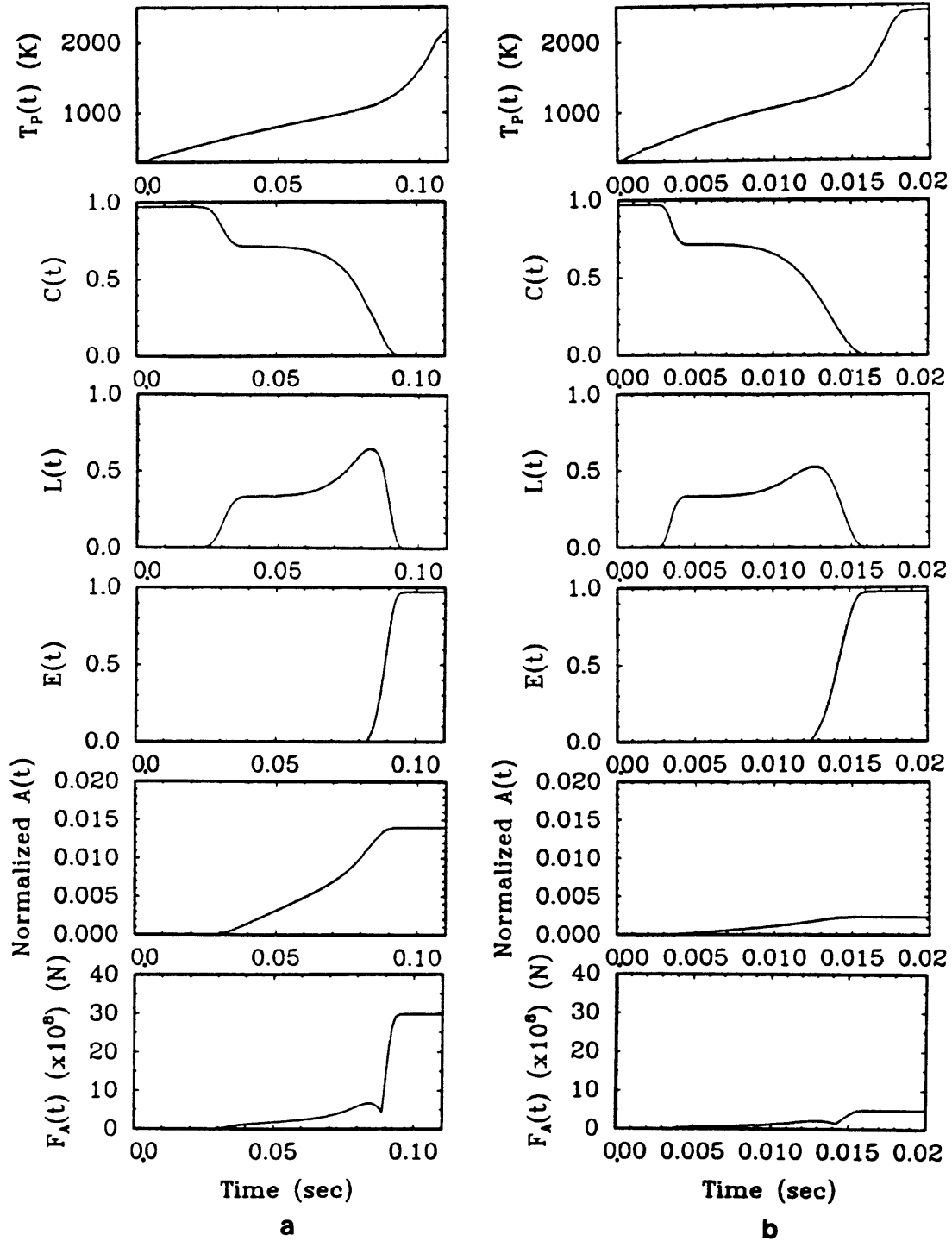


Figure 52. Predictions of  $C$ ,  $L$ ,  $E$ , Normalized  $A$ , and Adhesive Force  $F_A$  versus Time for Different Agglomerate Diameter (Furnace Gas Temperature = 1400 K, Oxygen Partial Pressure = 20 %) (a) 200  $\mu\text{m}$ , (b) 60  $\mu\text{m}$

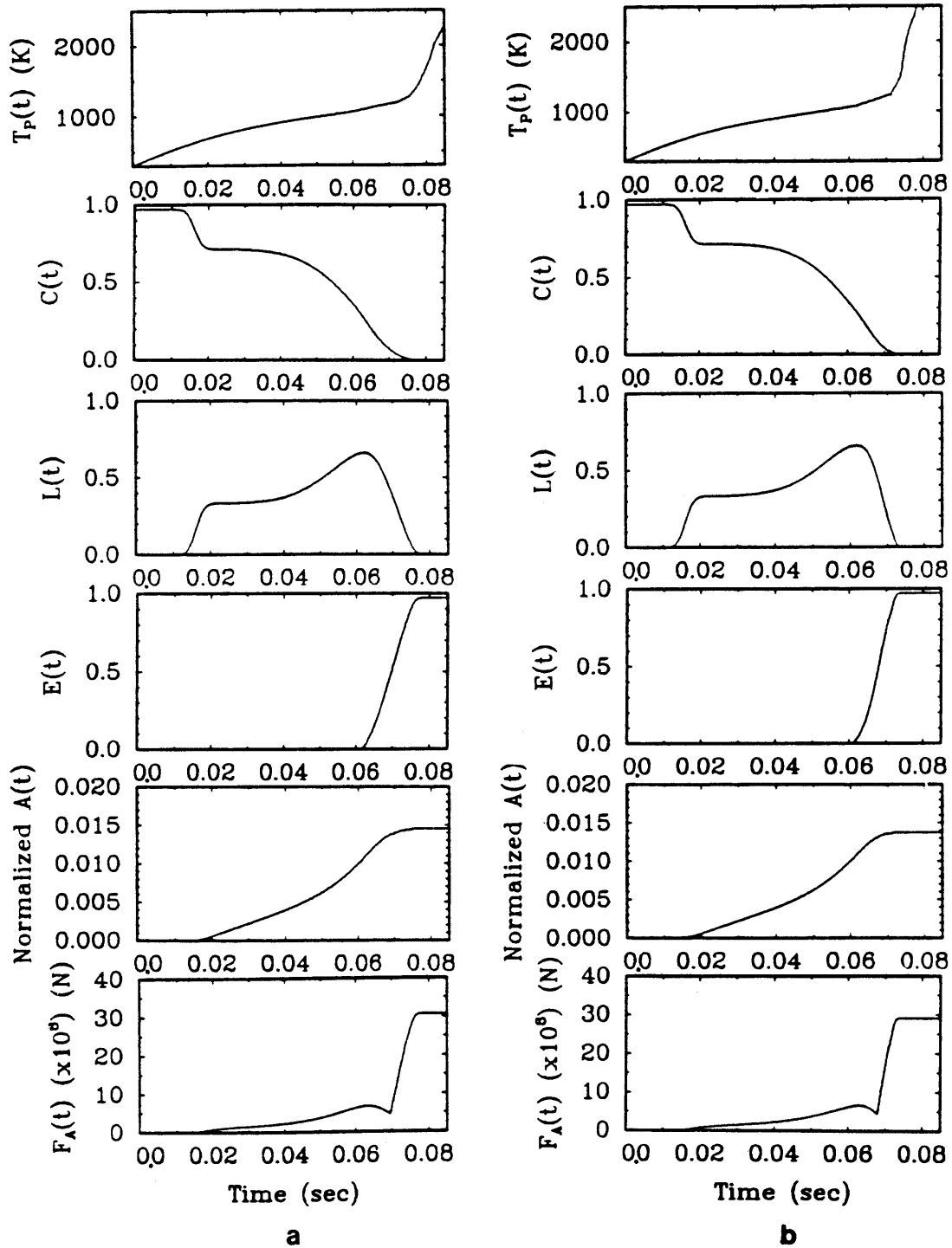


Figure 53. Predictions of  $C$ ,  $L$ ,  $E$ , Normalized  $A$ , and Adhesive Force  $F_A$  versus Time for Different Oxygen Partial Pressure (Agglomerate Diameter =  $100 \mu\text{m}$ , Furnace Gas Temperature =  $1100 \text{ K}$ )  
 (a)  $20 \% \text{ O}_2$ , (b)  $100 \% \text{ O}_2$

heat-up stage (i.e., during pyrolysis) increases with increasing furnace gas temperature and with decreasing agglomerate diameter.

As shown in Figures 48 through 52, the general trends of the curves of C, L, and E for the different particle heating rates are very similar, even though the time scales are totally different. The normalized contact area A, given by the contact area divided by the  $\pi(\text{radius of coal particle})^2$ , tends to decrease as the particle heating rate increases, mainly due to the decrease in the duration of the coal plasticity which is necessary for the particle agglomeration. Hence, the adhesive force, which is proportional to the contact area, tends to decrease as the particle heating rate increases. Consequently, it can be concluded that the higher particle heating rate (caused by a higher furnace gas temperature and a smaller agglomerate diameter) reduces the tendency of coal particles to form an agglomerate during the heat-up stage, because it both decreases the strength of the bonding of particles to each other and increases the centrifugal force during devolatilization and char burnout.

Figure 53 shows the effect of oxygen partial pressure on the adhesive force during particle agglomeration. As discussed in Section 5.1.1, the particle heating rate after the heat-up stage increases with increasing oxygen partial pressure, and consequently, the angular velocity and the centrifugal force increase with increasing oxygen partial pressure. However, the particle heating rate during the heat-up stage (i.e., during pyrolysis) is not significantly influenced by the oxygen partial pressure. Therefore, as shown in Figure 53, during pyrolysis, the curves of C, L, E, the normalized contact area A, and the adhesive force  $F_A$  are almost the same for both oxygen partial pressures

of 20 % and 100 %. Hence, it is concluded that the oxygen partial pressure does not significantly affect the adhesive force between contiguous coal particles in the CWF agglomerate.

### 5.3 Comparison of Centrifugal Force with Adhesive Force

Competition between the centrifugal force which favors the breakup of the CWF agglomerate and the adhesive force between contiguous coal particles in the CWF agglomerate in the plastic stage of coal pyrolysis through char burnout is illustrated in Figures 54-a and 54-b. The predictions of the centrifugal force and the adhesive force were made for a coal particle with a diameter of 30  $\mu\text{m}$  and a mass of  $2.0 \times 10^{-11}$  kg located on the outer edge of a CWF agglomerate with a diameter of 100  $\mu\text{m}$  in Figures 54-a and 54-b. The geometrical factor in eq. (11) was set at the value of 0.03.

Figure 54-a shows the comparison of the adhesive force with the centrifugal force for the lower particle heating rate which is represented by a furnace gas temperature of 1100 K, an oxygen partial pressure of 20 %, and an agglomerate diameter of 100  $\mu\text{m}$ . The duration of plasticity of the coal particles is long enough for coal particles to fuse and coalesce, and therefore, a strongly fused CWF agglomerate is formed and the adhesive force between contiguous coal particles in the CWF agglomerate is strong. It is also found that due to the lower particle heating rate the centrifugal force, which is directly influenced by the angular velocity of the CWF agglomerate, is weaker than the adhesive force. Consequently, the CWF agglomerates will be difficult to fragment, resulting in poor combustion.

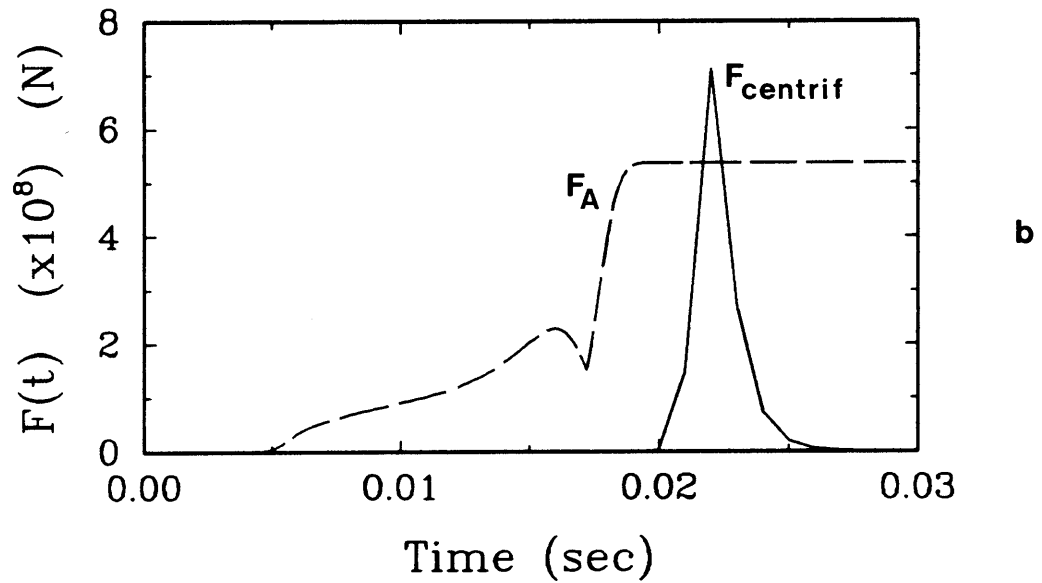
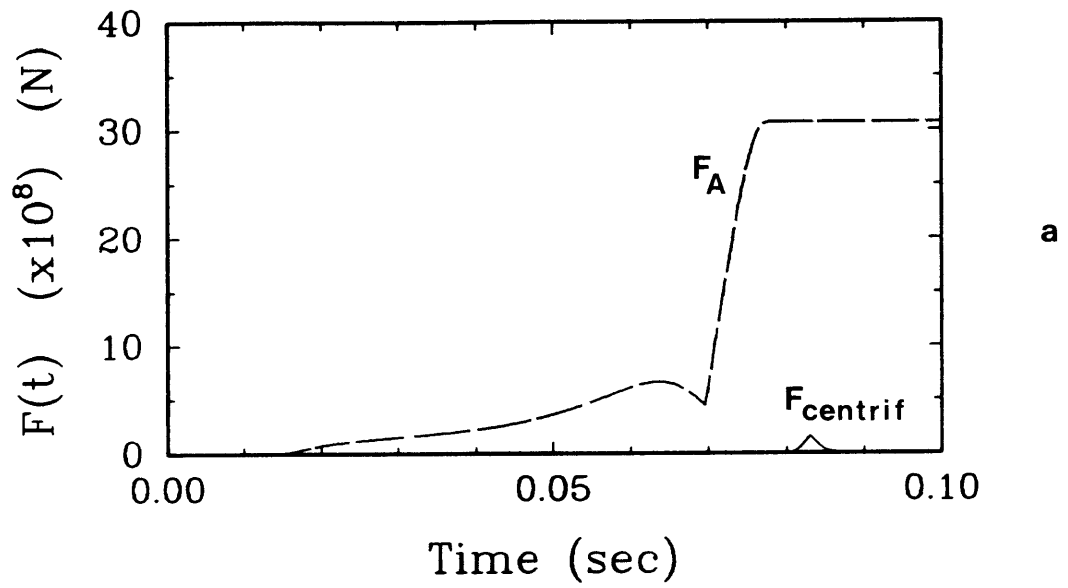


Figure 54. Comparisons of Adhesive Force  $F_A$  with Centrifugal Force  $F_{centrif}$  for Different Furnace Gas Temperature (Agglomerate Diameter = 100  $\mu\text{m}$ , Oxygen Partial Pressure = 20 %) (a) 1100 K, (b) 1750 K



In contrast, Figure 54-b shows the comparison of the adhesive force with the centrifugal force for the higher particle heating rate which is represented by a furnace gas temperature of 1750 K, an oxygen partial pressure of 20 %, and an agglomerate diameter of 100  $\mu\text{m}$ . During CWF combustion with a higher heating rate, the duration of the plastic period is so short that coal particles cannot completely fuse and coalesce, therefore a loosely fused CWF agglomerate is formed and the adhesive force between contiguous coal particles is weak. Due to the higher particle heating rate, and thus the faster angular velocity, the strong centrifugal force which can promote the separation of weakly adhering char fragments, is generated. Consequently, the CWF agglomerates will easily break up, resulting in better combustion.

CHAPTER 6  
CONCLUSIONS

Coal particles in a CWF droplet can burn individually or as agglomerates depending upon combustion conditions. The present study provides tentative criteria for determining the importance of particle agglomerates during CWF droplet combustion.

The following observations and conclusions are based upon experimental results and theoretical model predictions:

- (1) Fast rotation (up to 3000 cycles/sec), and significant fragmentation of burning CWF agglomerates, were observed and recorded by high-speed cinematography and fiber optic radiometry.
- (2) Rotation of the CWF agglomerate during devolatilization and char burnout generates centrifugal force at the agglomerate surface which can promote the separation of both weakly adhering char fragments and ash particles.
- (3) Rotation of the CWF agglomerate during devolatilization is induced by volatile ejection from a small number of macropores.
- (4) The angular velocity of the rotating CWF agglomerate is a function of the particle heating rate, which is directly influenced by the agglomerate diameter, the furnace gas temperature, and the oxygen partial pressure in the furnace.

- (5) Because of the random distribution of pores, a range of angular velocities of rotating CWF agglomerates is predicted, in general agreement with experimental observations.
- (6) The adhesive force in the process of agglomeration of coal particles is dependent upon the duration of plasticity of the coal particles.
- (7) Rapid particle heating reduces the tendency of coal particles to form agglomerates during the particle heat-up stage, because it both increases the centrifugal force during devolatilization and decreases the strength of bonding of particles to each other. The theoretical models provide a basis for calculating the separation of char fragments and ash particles as functions of coal properties and the thermal history of coal particles.
- (8) Practical implications of the present study bear on the problems of the combustion space requirement of CWF flames and the necessity of boiler performance derating when the fly-ash particle size is coarse.

## REFERENCES

1. Ehrlich S., Drenker, S., and Manfred R., "Coal Use in Boilers Designed for Oil and Gas Firing", Proc. of the Am. Power Conf., Vol. 42, 1980.
2. Crouse, F., "Combustion of Tomorrow's Fuels", Engineering Foundation Conference, Santa Barbara, CA, November 1982.
3. Lapwood, K.J., Street, P.J., and Moles, F.D., "An Examination of the Behavior and Structure of Single Droplets of Coal-Oil Fuels during Combustion", Fifth Int. Symp. on Coal-Oil Mixture Combustion, pp. 924-944, 1983.
4. Quann, R.J., Neville, M., Janghorbani, M., Mims, C.A. and Sarofim, A.F., "Mineral Matter and Trace-Element Vaporization in a Laboratory-Pulverized Coal Combustion System", Environ. Sci. Technol., Vol. 16, No. 11, pp. 776-781, 1982.
5. Timothy, L.D., Sarofim, A.F., and Beér, J.M., "Characteristics of Single Particle Coal Combustion", Nineteenth Symposium (International) on Combustion, The Combustion Institute, pp. 1123-1130, 1982.
6. Srinivasachar, S., Kang, S.W., Timothy, L.D., Froelich, D., Sarofim, A.F., and Beér, J.M., "Fundamentals of Coal-Water Fuel Combustion", Eighth International Symposium on Coal Slurry Fuels Preparation and Utilization, Orlando, FL, May 27-30, 1986.
7. Fong, W.S., Sc.D. Thesis, "Plasticity and Agglomeration in Coal Pyrolysis", Department of Chemical Engineering, M.I.T., Cambridge, MA, February 1986.
8. Srinivasachar, S., Sc.D. Thesis, "Experimental Study and Modeling of Coal-Water Fuel Combustion in a Pilot Scale Furnace", Department of Chemical Engineering, M.I.T., Cambridge, MA, October 1986.
9. Kerstein, A.R. and Niksa, S., "Fragmentation during Carbon Conversion: Predictions and Measurements", Twentieth Symposium (International) on Combustion, The Combustion Institute, pp 941-949, 1984.
10. Holve, D.J., Gomi, K., and Fletcher, T.H., "Comparative Combustion Studies of Ultrafine Coal-Water Slurries and Pulverized Coal", Seventh International Symposium on Coal Slurry Fuels Preparation and Utilization, New Orleans, LA, May 21-24, 1985.
11. Yu, T.U., Kang, S.W., Toqan, M.A., Walsh, P.M., Teare, J.D., Beér, J.M., and Sarofim, A.F., "Effect of Fuel Treatment on Coal-Water Fuel Combustion", Twenty-first Symposium (International) on Combustion, The Combustion Institute, Munich, W. Germany, Aug. 1986.

12. Simons, G.A., "The Pore Tree Structure of Porous Char", Nineteenth Symposium (International) on Combustion, The Combustion Institute, pp. 1067-1076, 1982.
13. Lamb, H., Hydrodynamics, 6th ed., Cambridge, Cambridge University Press, 1932.
14. Happel, J. and Brenner, H., Low Reynolds Number Hydrodynamics, Noordhoff Int. Publish. Leyden, 2nd Ed., 1973.
15. Kobayashi, H., Howard, J.B., and Sarofim, A.F., "Coal Devolatilization at High Temperatures", Sixteenth Symposium (International) on Combustion, The Combustion Institute, pp. 411-425, 1976.
16. Fitzgerald, D., "Kinetic Study of Coal Carbonization in the Plastic Zone", Fuel, Vol. 35, pp. 178-183, 1956.
17. Chermin, H.A.G. and Van Krevelen, D.W., "Chemical Structure and Properties of Coal XVII - Mathematical Model of Coal Pyrolysis", Fuel, Vol. 36, pp. 85-104, 1957.
18. Fong, W.S., Peters, W.A., and Howard, J.B., "Kinetics of Generation and Destruction of Pyridine Extractables in a Rapidly Pyrolyzing Bituminous Coal", Fuel, Vol. 65, pp. 251-254, 1986.
19. Frenkel, J., "Viscous Flow of Crystalline Bodies under the Action of Surface Tension", J. Phys. (USSR), Vol. 9, pp. 385-391, 1945.
20. Kingery, W.D. and Berg, M., "Study of Initial Stages of Sintering Solids by Viscous Flow, Evaporation-Condensation, and Self-Diffusion", J. Appl. Phys., Vol. 26, pp. 1205-1212, 1955.
21. Kuczynski, G.C., "Study of the Sintering of Glass", J. Appl. Phys., Vol. 20, pp. 1160-1163, 1949.
22. Huang, D.D., S.M. Thesis, "Flow Fields during Coalescence of Viscous Spheres", Department of Materials Science and Engineering, M.I.T., 1976.
23. Frankel, N.A. and Acrivos, A., "On the Viscosity of a Concentrated Suspension of Solid Spheres", Chem. Eng. Sci., Vol. 22, pp. 847, 1967.
24. Nazem, F.F., "Rheology of Carbonaceous Mesophase Pitch", Fuel, Vol. 59, pp. 851-858, 1980.
25. Hwang, S.C., Tsonopoulos, L., Cunningham, J.R., Wilson, G.W., "Density, Viscosity, and Surface Tension of Coal Liquids at High Temperatures and Pressures", Ind. Eng. Chem. Proc. Des. Div., Vol. 21, pp. 127, 1982.

26. Taylor, G.H., "Development of Optical Properties of Coke during Carbonization", *Fuel*, Vol. 40, pp. 465-471, 1961.
27. Friel, J.J., Mehta, S., Mitchell, G.D., and Karpinski, J.M., "Direct Observation of the Mesophase in Coal", *Fuel*, Vol. 59, pp. 610-616, 1980.
28. Kang, S.W., Sarofim, A.F., and Beér, J.M., "Fundamentals of Coal-Water Fuel Droplet Combustion", Third European Conference on Coal Liquid Mixtures, The Institution of Chemical Engineers, Sweden, 1987.
29. Gavalas, G.R. and Wilks, K.A., "Intraparticle Mass Transfer in Coal Pyrolysis", *AIChE Journal*, Vol. 26, No. 2, pp. 201-212, March, 1980.
30. Gavalas, G.R., "A Random Capillary Model with Application to Char Gasification at Chemically Controlled Rates", *AIChE Journal*, Vol 26, No. 4, pp 577-585, 1980.

APPENDICES

APPENDIX A  
 GEOMETRICAL FACTOR OF DEVOLATILIZATION  
 PORES WITH GAVALAS' PORE MODEL

The angular velocity of the rotating CWF agglomerate and the corresponding geometrical factor of devolatilization pores were derived with the assumption of uniform velocity of the issuing volatile jet in Section 4.1.

In this section, Gavalas et al's models <sup>(29,30)</sup> are used to derive the angular velocity and the geometrical factor instead of the previous assumption of uniform velocity of the volatile jet. The newly derived geometrical factor is compared with the previous geometrical factor.

A.1 Derivation of Geometrical Factor

The angular momentum of the CWF agglomerate is generated by the tangential component of the issuing volatile jet, which is expressed by the angles  $\phi_i$  and  $\theta_i$  which have already been defined in Section 4.1.2. The tangential component of the exit velocity of the issuing volatile jet on the surface of the rotating spherical CWF agglomerate (Figure 26) is expressed as

$$(v_i)_{\text{tangential}} = v_i \cos\theta_i |\cos\phi_i| \quad \text{eq. (A-1)}$$

In order to derive the differential equation for the angular velocity of the rotating CWF agglomerate, the angular momentum equation in an inertial reference frame is applied.

The angular momentum equation for the rotational axis of the CWF agglomerate in the inertial reference frame is



$$\frac{d}{dt} \left( \int_{cv} \rho_A r^2 \omega \, dV \right) + \int_{cs} R (R \omega - v_i \cos \theta_i |\cos \phi_i|) \rho_{vol} v_i \, dA = - 8\pi R^3 \mu_{vol} \omega$$

eq. (A-2)

where  $v_i$  denotes the exit velocity of the volatile jet at each devolatilization pore and the other symbols have already been defined in Section 4.1.2.

The angular momentum equation can be rewritten as

$$\begin{aligned} \frac{d\omega}{dt} + \left[ \frac{1}{\rho_A} \frac{d\rho_A}{dt} + \frac{5 \rho_{vol} (\sum_{i=1}^n v_i A_i)}{4 \pi R^3 \rho_A} + \frac{10\mu_{vol}}{\rho_A R^2} \right] \omega \\ = \frac{5 \rho_{vol}}{4 \pi R^4 \rho_A} \left[ \sum_{i=1}^n v_i^2 \cos \theta_i |\cos \phi_i| A_i \right] \end{aligned}$$

eq. (A-3)

The density of the CWF agglomerate  $\rho_A$  and the first time-derivative of  $\rho_A$  are expressed as

$$\rho_A = \frac{M_o [1-V]}{\frac{4}{3} \pi R^3}, \quad \text{and}$$

eq. (A-4)

$$\frac{d\rho_A}{dt} = \frac{-M_o \left( \frac{dV}{dt} \right)}{\frac{4}{3} \pi R^3}$$

eq. (A-5)

From eqs. (A-3), (A-4), and (A-5), the differential equation for the angular velocity of the rotating CWF agglomerate is

$$\frac{d\omega}{dt} + \left[ \frac{\frac{2}{3} M_o \left( \frac{dV}{dt} \right) + \frac{40}{3} \pi R \mu_{vol}}{M_o (1-V)} \right] \omega = \frac{5 \rho_{vol}}{3 R M_o (1-V)} \left[ \sum_{i=1}^n v_i^2 \cos \theta_i |\cos \phi_i| A_i \right]$$

or, equivalently,



where  $f_1, f_2, \dots$ , and  $f_N$  denote the fractions of the issuing volatile mass for each pore group. These will be discussed in detail in Section A.2. The fractions  $f_1, f_2, \dots$ , and  $f_N$  are satisfied with the following relations:

$$f_1 + f_2 + \dots + f_N = 1 \quad , \text{ and}$$

$$0 < f_N < f_{N-1} < \dots < f_2 < f_1 < 1 \quad \text{eq. (A-9)}$$

From eqs. (A-6), (A-7), and (A-8), the differential equation for the angular velocity of the CWF agglomerate is written as

$$\frac{d\omega}{dt} + \left[ \frac{\frac{2}{3} M_o \left( \frac{dV}{dt} \right) + \frac{40}{3} \pi R \mu_{vol}}{M_o (1-V)} \right] \omega$$

$$= \frac{5 \rho_{vol}}{3 R M_o (1-V)} \left[ \sum_{i=1}^{n_1} \bar{v}_1^2 \cos \theta_i |\cos \phi_i| \bar{A}_1 \right.$$

$$\left. + \sum_{i=n_1+1}^{n_2} \bar{v}_2^2 \cos \theta_i |\cos \phi_i| \bar{A}_2 + \dots + \sum_{i=n_{N-1}+1}^{n_N} \bar{v}_N^2 \cos \theta_i |\cos \phi_i| \bar{A}_N \right]$$

or, equivalently,

$$= \frac{5 M_o \left( \frac{dV}{dt} \right)^2}{3 R \rho_{vol} (1-V)} \left[ \left( \frac{f_1^2}{n_1} \right) \left( \frac{\sum_{i=1}^{n_1} \cos \theta_i |\cos \phi_i|}{n_1} \right) \right]$$

$$\begin{aligned}
& + \left( \frac{f_2^2}{\sum_{i=n_1+1}^{n_2} A_i} \right) \left( \frac{\sum_{i=n_1+1}^{n_2} \cos\theta_i |\cos\phi_i|}{n_2 - n_1} \right) + \\
& \dots\dots + \left( \frac{f_N^2}{\sum_{i=n_{N-1}+1}^{n_N} A_i} \right) \left( \frac{\sum_{i=n_{N-1}+1}^{n_N} \cos\theta_i |\cos\phi_i|}{n_N - n_{N-1}} \right)
\end{aligned}$$

or, equivalently,

$$\begin{aligned}
& = \frac{5 M_o \left(\frac{dV}{dt}\right)^2 f_1^2}{3R\rho_{vol}(1-V) \sum_{i=1}^{n_1} A_i} \left( \left( \frac{\sum_{i=1}^{n_1} \cos\theta_i |\cos\phi_i|}{n_1} \right) \right. \\
& \quad + \left. \left( \frac{f_2}{f_1} \right)^2 \left( \frac{\sum_{i=n_1+1}^{n_2} \cos\theta_i |\cos\phi_i|}{n_2 - n_1} \right) + \right. \\
& \quad \left. \dots\dots + \left( \frac{f_N}{f_1} \right)^2 \left( \frac{\sum_{i=n_{N-1}+1}^{n_N} \cos\theta_i |\cos\phi_i|}{n_N - n_{N-1}} \right) \right) \quad \text{eq. (A-10)}
\end{aligned}$$

From eq. (A-9), the following inequality can be derived:

$$0 < \left( \frac{f_N}{f_1} \right)^2 < \left( \frac{f_{N-1}}{f_1} \right)^2 < \dots < \left( \frac{f_2}{f_1} \right)^2 < 1 \quad \text{eq. (A-11)}$$

As discussed in Section 4.1.4, the first term in the second parentheses of RHS of eq. (A-10) is dominant compared to the other terms in those parentheses, and eq. (A-10) is rewritten as

$$\begin{aligned} \frac{d\omega}{dt} + \left[ \frac{\frac{2}{3} M_o \left(\frac{dV}{dt}\right) + \frac{40}{3} \pi R \mu_{vol}}{M_o (1-V)} \right] \omega \\ = \frac{5M_o}{3R\rho_{vol} \sum_{i=1}^n A_i} \left[ f_1^2 \left( \frac{\sum_{i=1}^n A_i}{n_1} \right)^2 \left( \frac{\sum_{i=1}^{n_1} A_i \cos\theta_i |\cos\phi_i|}{\sum_{i=1}^n A_i} \right) \right] \frac{\left(\frac{dV}{dt}\right)^2}{(1-V)} \end{aligned} \quad \text{eq. (A-12)}$$

The initial condition of eq. (A-12) is

$$\omega(0) = 0 \quad \text{eq. (A-13)}$$

From eqs. (A-12) and (A-13), the angular velocity of the rotating CWF agglomerate is

$$\begin{aligned} \omega(t) = \frac{5M_o}{3R\rho_{vol} \sum_{i=1}^n A_i} \left[ f_1^2 \left( \frac{\sum_{i=1}^n A_i}{n_1} \right)^2 \left( \frac{\sum_{i=1}^{n_1} A_i \cos\theta_i |\cos\phi_i|}{\sum_{i=1}^n A_i} \right) \right] \\ \times \exp \left[ - \int_0^t \frac{\frac{2}{3} M_o \left(\frac{dV}{dt}\right) + \frac{40}{3} \pi R \mu_{vol}}{M_o (1-V)} dt \right] \\ \times \int_0^t \left[ \frac{\left(\frac{dV}{dt}\right)^2}{(1-V)} \exp \left[ \int_0^t \frac{\frac{2}{3} M_o \left(\frac{dV}{dt}\right) + \frac{40}{3} \pi R \mu_{vol}}{M_o (1-V)} dt \right] \right] dt \end{aligned} \quad \text{eq. (A-14)}$$

In eq. (A-14), the newly derived geometrical factor is expressed as

$$\left( f_1^2 \left( \frac{\sum_{i=1}^n A_i}{n_1} \right)^2 \left( \frac{\sum_{i=1}^{n_1} A_i \cos \theta_i |\cos \phi_i|}{\sum_{i=1}^n A_i} \right) \right)$$

It is seen that the newly derived geometrical factor in eq. (A-14) can be obtained by the geometrical factor with the assumption of uniform

exit velocity in eq. (11) multiplied by  $(f_1)^2 \left( \frac{\sum_{i=1}^n A_i}{n_1} \right)^2$ . Here,  $\left( \frac{\sum_{i=1}^n A_i}{n_1} \right)$

denotes the ratio of the sum of the cross-sectional exit area of the whole pores on the agglomerate surface to that of the 100 largest macropores on the agglomerate surface, and  $f_1$  denotes the mass fraction of volatile products released through the 100 largest macropores per total amount of released volatile products, and will be derived in Section A.2.

#### A.2. Application of Gavalas' Model to Geometrical Factor

The mass fraction  $f_1$  of the volatile products released through the 100 largest macropores per total released volatile products in eq. (A-14) can be derived by using Gavalas et al's intraparticle mass transfer model<sup>(29)</sup> and Gavalas' random capillary model<sup>(30)</sup> which are explained as follows:

The pore volume distribution of coal is divided into five ranges, according to pore diameter. Range I consists of micropores 0.0004–0.0012  $\mu\text{m}$ ; Range II of transitional pores 0.0012 – 0.03  $\mu\text{m}$ ; Ranges III,

IV, and V consist of macropores  $0.03 - 0.3 \mu\text{m}$ ,  $0.3 - 3 \mu\text{m}$ , and  $3 - 10 \mu\text{m}$ , respectively. The first range is defined by the molecular sieve properties of these pores. The others are defined largely arbitrarily, but such that the porosities  $\epsilon_{\text{II}}, \dots, \epsilon_{\text{V}}$  are of the same order of magnitude. A representative or average diameter is assigned to each of the Ranges II-V. It is not necessary to assign a representative diameter to Range I. These averages could be chosen on the basis of theoretical considerations or treated as adjustable parameters. However, the results in many problems turn out not to be very sensitive to changes in the average diameters. Having assigned average sizes, the continuous pore size distribution is replaced with a collection of pores of diameters  $D_{\text{I}}, \dots, D_{\text{V}}$  and pore volume fractions  $\epsilon_{\text{I}}, \dots, \epsilon_{\text{V}}$ .

At temperatures of  $400 - 700^\circ\text{C}$ , the volatile gases are relatively unreactive and diffuse from Pore Range I to Pore Range II without reacting with the coal matrix. Pore Range II ( $D_{\text{II}}$ -pores) contains most of the active surface area for product generation and recombination. This pore range makes a relatively small contribution to mass transfer because of low permeability and Knudsen diffusivity, although the porosity is comparable to that of the other ranges. The volatile products generated in the  $D_{\text{II}}$ -pores are transported to the outside of the particle via the larger pores rather than directly to the surface of the particle. Hence, the  $D_{\text{II}}$ -pores will be treated as source terms for the larger pores while their contribution to transport will be neglected.

The transport of the volatile products through the  $D_{\text{III}}$ -pores occurs partly directly to the particle surface and partly via the  $D_{\text{IV}}$ -pores and

the  $D_V$ -pores. Thus, the  $D_{III}$ -,  $D_{IV}$ -, and  $D_V$ -pores must be considered interactively.

In the model used, the fraction  $f^*$  accounts for the fact that a fraction of the volatile products, generated on the surface of the  $D_{II}$ - and  $D_{III}$ -pores, is released to the  $D_{IV}$ - and  $D_V$ -pores, and the remainder escapes to the agglomerate surface directly. One hundred of the largest macropores, which play an important role in determining the angular velocity of the rotating CWF agglomerate in the present model, correspond to the  $D_{IV}$ -pores and  $D_V$ -pores in Gavalas et al's model.

The fraction  $f^*$  of the volatile products which are released to the agglomerate surface through the  $D_{IV}$ -pores and  $D_V$ -pores per total volatile products released is expressed as

$$f^* = \frac{\frac{\pi D_p^3}{6} (m_{III-IV} + m_{III-V})}{\frac{\pi D_p^3}{6} (m_{III-IV} + m_{III-V}) + \pi D_p^2 n_{III}} \quad \text{eq. (A-15)}$$

where  $D_p$  denotes the agglomerate diameter, and  $m_{III-IV}$  (or  $m_{III-V}$ ) denotes the number of intersections of the  $D_{III}$ - and  $D_{IV}$ - (or  $D_V$ -) pores per unit agglomerate volume, and given by

$$m_{III-IV} = \frac{4 \epsilon_{III} \epsilon_{IV}}{\pi D_{III}^2 D_{IV}^2} (D_{III} + D_{IV}) \quad \text{eq. (A-16)}$$

$$m_{III-V} = \frac{4 \epsilon_{III} \epsilon_V}{\pi D_{III}^2 D_V^2} (D_{III} + D_V) \quad \text{eq. (A-17)}$$

where  $n_{III}$  denotes the number of pore-mouths of the  $D_{III}$ -pores per unit agglomerate external surface area, and given by



$$n_{\text{III}} = \frac{2 \epsilon_{\text{III}}}{\pi D_{\text{III}}^2} \quad \text{eq. (A-18)}$$

where  $D_{\text{III}}$ ,  $D_{\text{IV}}$ , and  $D_{\text{V}}$  denote pore diameters, and  $\epsilon_{\text{III}}$ ,  $\epsilon_{\text{IV}}$ , and  $\epsilon_{\text{V}}$  denote pore volume fractions.

The assumption for the derivation of the fraction  $f^*$  is that the volatiles are transferred to the  $D_{\text{IV}}$ -pores and  $D_{\text{V}}$ -pores or directly to the agglomerate surface via the  $D_{\text{III}}$ -pores, thus neglecting the less important direct transfer from the  $D_{\text{II}}$ -pores to the  $D_{\text{IV}}$ -pores and  $D_{\text{V}}$ -pores or to the agglomerate surface.

Based upon Gavalas' model, the value of  $(f_1)^2$   $\left( \frac{\sum_{i=1}^n A_i}{n_1} \right)^2$  in the

geometrical factor in eq. (A-14) turns out to be in the range of 0.5 to 3.0.

## APPENDIX B

## TEST RESULTS OF ATOMIZER

The atomizer was tested in the Spray Test Facility equipped with the laser diffraction spray analyzer. ARC-fine-grind CWF (69/31 coal/water by weight %) was atomized and droplet sizes were measured. Air flow rate was varied from 600 cm<sup>3</sup>/sec to 1200 cm<sup>3</sup>/sec, and CWF flow rate was varied from 0.5 g/sec to 0.8 g/sec. Figure B.1 shows a diagram of Mass Mean Diameter (MMD) of CWF versus air-to-fuel ratio (AFR). The AFR was varied from 0.4 to 7.0. Water was also tested for comparison. The smallest MMD of CWF droplets was found to be 28.0 μm, while that of water was 20.0 μm.

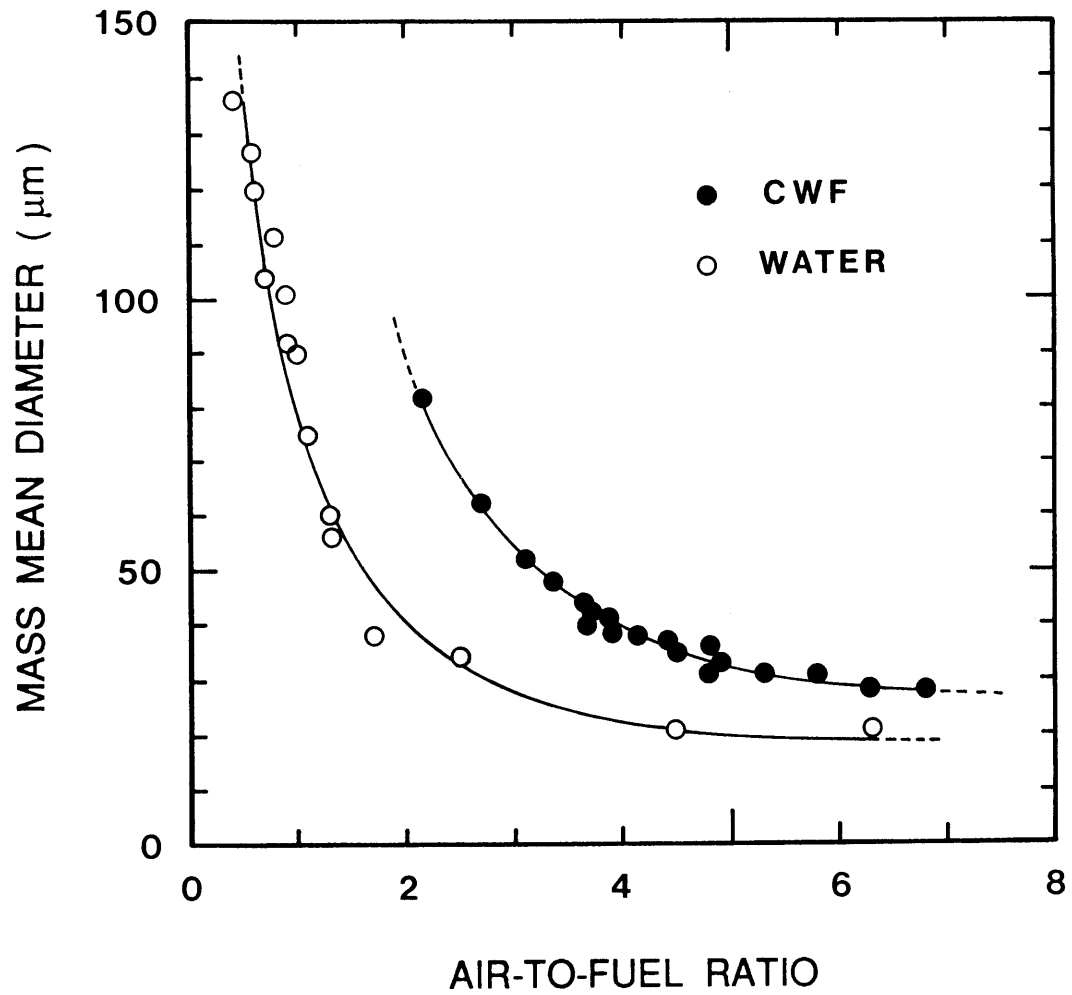


Figure B.1. Mass Mean Diameter of Spray Droplet at Various AFRs

## APPENDIX C

## COMPUTER PROGRAMS

C.1 Computer Program for Model of Particle Rotation

```

C      _____
C      PROGRAM OMEGA
C      _____
C      IMPLICIT DOUBLE PRECISION(A-H,O-Z)
C      DIMENSION OMEGA(10), DOMEGA(10), Y0(10), Q(10)
C      DIMENSION X(80),Y(80),Z(80), XX(80), ZZ(80)
C      _____
C      INITIALIZATION
C      _____
C
C      OPEN (1, FILE='NONIN',STATUS='OLD')
C      OPEN (2, FILE='NONOUT', STATUS='OLD')
C      OPEN (3, FILE='NONOUTP', STATUS='OLD')
C      DATA DENVOL,VISVOL/ .55 ,6.00E-5/
C      DATA IND/1/
C      DATA DT,TLIM/1.D-3,0.200/
C
C      PI= 4.*DATAN(1.D0)
C      T=0.
C
C      OMEGA(1)=0.
C      M=0
C      READ(1,*) AMSTAR, RSTAR
C      READ(1,*) AM0, R, SUMAI, ARATIO
C      READ(1,*) NA
C      READ(1,*)(XX(I),Y(I),ZZ(I),I=1,NA)
C
C      DO 333 I=1,NA
C          X(I)=XX(I)*1.E-3
C          Z(I)=ZZ(I)*1.E-2
333  CONTINUE
C      WRITE(2,100) T,OMEGA(1)/2./PI
C      WRITE(3,300) T,FCENT*1.E8
300  FORMAT("Time (sec)"/"F(t) (x10+8) (N)"/"HORZ"/
+ "XLEN 4."/"YLEN 2.25"/"END"/1X,F7.4,1X,E10.3)
100  FORMAT("Time (sec)"/"Dw(t)"/"HORZ"/"XLEN 6."/
+ "YLEN 2."/"END"/1X,F7.4,1X,E10.3)
C      INDEX= 1
C      CONST1= 5.*AM0*ARATIO/(3.*R*DENVOL*SUMAI)
C      CONST2= 40.*PI*R*VISVOL/AM0/3.
C      _____
C      FOURTH-ORDER RUNGE-KUTTA-GILL METHOD
C      _____
C
C      8  IF (T-TLIM) 6,6,7
C      6  CALL RUNGE(1,OMEGA,DOMEGA,T,DT,M,K,AA,Q)
C      GOTO (10,20) K
10    V=FUN1(T,NA,X,Y)
C      DVDT=FUN1(T,NA,X,Z)
C      DOMEGA(1)=DVDT/(1.-V)*(CONST1*DVDT-.6666*OMEGA(1))
C      + -OMEGA(1)/(1.-V)*CONST2
C      GOTO 6

```



C.2 Computer Program for Model of Particle Agglomeration

```

C      _____
C      PROGRAM RKG
C      _____

      IMPLICIT DOUBLE PRECISION(A-H,O-Z)
      DIMENSION Y(10), F(10), Y0(10), Q(10)

C      _____
C      INITIALIZATION
C      _____

      DATA C0,L0,A0/0.94,0.,0./
      DATA SL,SIGMA,TM,FABAR /0.25, 30., 623., 0.06D0/
      DATA RC,GAMC,VISC /15.D-6, 0.01, 250./
      DATA DENC,DENA,DENL /1300., 2600., 1000./
      DATA SIGMAE /3.D4/
      DATA SLOPE,XT,IND /1.0D5, 0.01627,20/
      DATA XLIM,DELX,M /0.013, 1.D-5 , 0/

      OPEN (1, FILE='OC', STATUS='OLD')
      OPEN (2, FILE='OL', STATUS='OLD')
      OPEN (3, FILE='OE', STATUS='OLD')
      OPEN (4, FILE='OA', STATUS='OLD')
      OPEN (7, FILE='OST', STATUS='OLD')
      OPEN (8, FILE='OAE', STATUS='OLD')
      OPEN (9, FILE='OF', STATUS='OLD')
      OPEN (10, FILE='OT', STATUS='OLD')

      PI= 4.*DATAN(1.00)
      J= 1
      X= 0.
      Y(1)= 1.-FABAR
      Y(2)= L0
      Y(3)= A0

      FACTOR= DENA/(DENA- FABAR*(DENA-DENC))
      FA= FACTOR*FABAR/DENA*DENC
      YY= (1.-FA)/2.

      C= Y(1)*FACTOR
      AL= Y(2)*FACTOR*DENC/DENL
      E= 1.-C -AL -FA
      A= Y(3)
      AN=A/PI/RC**2
      FST = 2.*DSQRT(PI)*DSQRT(A)*AL*GAMC
      FAE = 0.
      PHI= (FA*AL+E)/(AL+E)
      FSUM= FST+FAL+FAE
      TP=0.
      WRITE(1,100) X,C
      WRITE(2,200) X,AL
      WRITE(3,300) X,E
      WRITE(4,400) X,AN
      WRITE(7,700) X,FST
      WRITE(8,800) X,FAE
      WRITE(9,900) X,FSUM
      WRITE(10,1000) X,TP
100  FORMAT("Time (sec)"/"C(t)"/"HORZ"/"XLEN 1.87"/
+ "YLEN .93"/"XMAX .013"/"YMIN .00"/"YMAX 1.000"
+ "/"HNUM .1"/"HTIT .1"/"END"/1X,F7.4,1X,E10.3)
200  FORMAT("Time (sec)"/"L(t)"/"HORZ"/"XLEN 1.87"/
+ "YLEN .93"/"XMAX .013"/"YMIN 0."/"YMAX 1."/"HNUM .1"/"HTIT .1"/
+ "END"/1X,F7.4,1X,E10.3)

```

```

300  FORMAT("Time (sec)"/"E(t)"/"HORZ"/"XLEN 1.87"/"YLEN .93"/
+ "XMAX .013"/"YMIN .00"/"YMAX 1."/"HNUM .1"/"HTIT 1"/"END"/
+ 1X,F7.4,1X,E10.3)
400  FORMAT("Time (sec)"/"Normalized A(t)"/"HORZ"/"XLEN 1.87"/
+ "YLEN .93"/"XMAX .013"/"YMIN 0."/"YMAX .02"/"HNUM .1"/"HTIT .1"/
+ "END"/1X,F7.4,1X,E10.3)
700  FORMAT("Time (sec)"/"F\g(t) (x10+8) (N)"/"HORZ"/"XLEN 1.87"/
+ "YLEN .93"/"XMAX .013"/"YMIN 0."/"YMAX 40."/"HNUM .1"/"HTIT .1"
+ "/"END"/1X,F7.4,1X,E10.3)
800  FORMAT("Time (sec)"/"F\E(t) (x10+8) (N)"/"HORZ"/"XLEN 1.87"/
+ "YLEN .93"/"XMAX .013"/"YMIN 0."/"YMAX 40."/"HNUM .1"/"HTIT .1"
+ "END"/1X,F7.4,1X,E10.3)
900  FORMAT("Time (sec)"/"F\A(t) (x10+8) (N)"/"HORZ"/"XLEN 1.87"/
+ "YLEN .93"/"XMAX .013"/"YMIN 0."/"YMAX 40."/"HNUM .1"/"HTIT .1"/
+ "END"/1X,F7.4,1X,E10.3)
1000 FORMAT("Time (sec)"/"T\p(t) (K)"/"HORZ"/"XLEN 1.87"
+ "/YLEN .93"/"XMAX .013"/"YMIN 300."/"YMAX 2000."/"HNUM .1"/
+ "HTIT .1"/"END"/1X,F7.4,1X,E10.3)
INDEX= 1

```

C  
C  
C

---

FOURTH-ORDER RUNGE-KUTTA-GILL METHOD

---

```

8  IF (X-XLIM) 6,6,7
6  CALL RUNGE(3,Y,F,X,DELX,M,K,AA,Q)
   GO TO (10,20) K
10  TP= 300.+ SLOPE*X
    DTPDX= SLOPE

    RM= SL/DSQRT(2.*PI)/SIGMA*DEXP(-(TP-TM)**2/2./SIGMA**2)*DTPDX
    ALPHAK= 6.6D7 *DEXP(-14500./TP)
    BETAK= 1.9D10*DEXP(-21200./TP)

    IF (Y(1) .LE. 1.D-16) Y(1)= 0.D0
    F(1)= -ALPHAK*Y(1) -RM
    IF (Y(2) .LE. 1.D-16) Y(2)= 0.D0
    F(2)= ALPHAK*Y(1) + RM -BETAK*Y(2)
    Y2= Y(2)*DENC/DENL*FACTOR
    F(3)= 4./3.*RC*GAMC/VISC*(1./(1.-Y2)**(1./3.)-1.)
    GO TO 6

```

C  
C  
C

---

CONTROL THE INTERVAL OF PRINT

---

```

20  INDEX= INDEX+1
    IF (MOD(INDEX,IND) .NE. 1) GO TO 8
    C= Y(1)*FACTOR
    AL= Y(2)*FACTOR*DENC/DENL
    E= 1.-C -AL -FA
    A= Y(3)
    AN=A/(PI*RC**2)
    FST = 2.*DSQRT(PI)*DSQRT(A)*AL*GAMC
    IF (E .GE. YY) THEN
      FAE= SIGMAE*A*(E-YY)/(1.-FA-YY)
    ELSE
      FAE = 0.
    ENDIF

    ST=FST*1D8
    AE=FAE*1D8
    FSUM= ST+AE

    WRITE(1,150) X,C
    WRITE(2,150) X,AL

```

```

WRITE(3,150) X,E
WRITE(4,150) X,AN
WRITE(7,150) X,ST
WRITE(8,150) X,AE
WRITE(9,150) X,FSUM
WRITE(10,150)X,TP
150  FORMAT(1X,F7.4,1X,E10.3)

GO TO 8
7    STOP
END

C
C   SUBROUTINE RUNGE-KUTTA-GILL
C
SUBROUTINE RUNGE (N,Y,F,X,H,M,K,A,Q)
IMPLICIT DOUBLE PRECISION (A-H,O-Z)
DIMENSION Y(10), F(10), Q(10)

M= M+1
GO TO (1,4,5,3,7) M
1    DO 2 I=1,N
     Q(I)= 0.
2    CONTINUE
     A= .5
     GO TO 9
3    A= 1.+ 1./DSQRT(2.D0)
4    X= X+.5*H
5    DO 6 I= 1,N
     Y(I)= Y(I) + A*( F(I)*H-Q(I))
     Q(I)= 2.*A*H*F(I) +(1.-3.*A)*Q(I)
6    CONTINUE
     A= 1.- 1./DSQRT(2.D0)
     GO TO 9
7    DO 8 I= 1,N
     Y(I)= Y(I) + H*F(I)/6. -Q(I)/3.
8    CONTINUE
     M= 0
     K= 2
     GO TO 10
9    K= 1
10   RETURN
     END

```





```

+ /1X,F7.4,1X,E10.3)
300 FORMAT("Time (sec)"/"E(t)"/"HORZ"/"XLEN 2 "/"YLEN 1."
+ /"XMAX .110"/"YMIN 0."/"YMAX 1."/"HNUM .1"/"HTIT .1"/"END"
+ /1X,F7.4,1X,E10.3)
400 FORMAT("Time (sec)"/"Normalized A(t)"/"XLEN 2."/"
+ "YLEN 1."/"XMAX .110"/"YMAX .02"/"HNUM .1"/"HTIT .1"/"END"
+ /1X,F7.4,1X,E10.3)
700 FORMAT("Time (sec)"/"F\theta(t) (x10+8) (N)"/"HORZ"/"XLEN 2."
+ /"YLEN 1."/"XMAX .110"/"HNUM .1"/"HTIT .1"/"END"
+ /1X,F7.4,1X,E10.3)
800 FORMAT("Time (sec)"/"F\E(t) (x10+8) (N)"/"HORZ"/"XLEN 2."
+ /"YLEN 1."/"HNUM .1"/"HTIT .1"/"END"
+ /1X,F7.4,1X,E10.3)
900 FORMAT("Time (sec)"/"F\A(t) (x10+8) (N)"/"HORZ"/"XLEN 2."
+ /"YLEN 1."/"XMAX .110"/"YMAX 40."/"HNUM .1"/"HTIT .1"/"END"
+ /1X,F7.4,1X,E10.3)
1000 FORMAT("Time (sec)"/"T\P(t) (K)"/"XLEN 2."/"YLEN 1."/"
+ "XMAX .110"/"YMIN 300."/"YMAX 2500."/"HNUM .1"/"HTIT .1"/"END"
+ /1X,F7.4,1X,E10.3)
INDEX= 1

```

C  
C  
C

---

FOURTH-ORDER RUNGE-KUTTA-GILL METHOD

---

```

8 IF (X-XLIM) 6,6,7
6 CALL RUNGE(3,Y,F,X,DELX,M,K,AA,Q)
GO TO (10,20) K
10 TP=FUN1(X,NA,AX,AY)
DTPDX=FUN1(X,NA,AX,AZ)

RM= SL/DSQRT(2.*PI)/SIGMA*DEXP(-(TP-TM)**2/2./SIGMA**2)*DTPDX
ALPHA= 6.6D7 *DEXP(-14500./TP)
BETAK= 1.9D10*DEXP(-21200./TP)

IF (Y(1) .LE. 1.D-16) Y(1)= 0.D0
F(1)= -ALPHA*Y(1) -RM
IF (Y(2) .LE. 1.D-16) Y(2)= 0.D0
F(2)= ALPHA*Y(1) + RM -BETAK*Y(2)
Y2= Y(2)*DENC/DENL*FACTOR
F(3)= 4./3.*RC*GAMC/VISC*(1./(1.-Y2)**(1./3.)-1.)
GO TO 6

```

C  
C  
C

---

CONTROL THE INTERVAL OF PRINT

---

```

20 INDEX= INDEX+1
IF (MOD(INDEX,IND) .NE. 1) GO TO 8
C= Y(1)*FACTOR
AL= Y(2)*FACTOR*DENC/DENL
E= 1.-C -AL -FA
A= Y(3)
AN=A/(PI*RC**2)
FST = 2.*DSQRT(PI)*DSQRT(A)*AL*GAMC
IF (E .GE. YY) THEN
  FAE= SIGMAE*A*(E-YY)/(1.-FA-YY)
ELSE
  FAE = 0.
ENDIF

ST=FST*1D8
AE=FAE*1D8
FSUM= ST+AE

WRITE(1,150) X,C
WRITE(2,150) X,AL
WRITE(3,150) X,E

```

```

WRITE(4,150) X,AN
WRITE(7,150) X,ST
WRITE(8,150) X,AE
WRITE(9,150) X,FSUM
WRITE(11,150)X,TP
150  FORMAT(1X,F7.4,1X,E10.3)
      GO TO 8
      7  STOP
      END

C
C
C
SUBROUTINE RUNGE-KUTTA-GILL

SUBROUTINE RUNGE (N,Y,F,X,H,M,K,A,Q)
IMPLICIT DOUBLE PRECISION (A-H,O-Z)
DIMENSION Y(10), F(10), Q(10)

M= M+1
GO TO (1,4,5,3,7) M
1  DO 2 I=1,N
   Q(I)= 0.
2  CONTINUE
   A= .5
   GO TO 9
3  A= 1. + 1./DSQRT(2.D0)
4  X= X+.5*H
5  DO 6 I= 1,N
   Y(I)= Y(I) + A*( F(I)*H-Q(I))
   Q(I)= 2.*A*H*F(I) +(1.-3.*A)*Q(I)
6  CONTINUE
   A= 1. - 1./DSQRT(2.D0)
   GO TO 9
7  DO 8 I= 1,N
   Y(I)= Y(I) + H*F(I)/6. -Q(I)/3.
8  CONTINUE
   M= 0
   K= 2
   GO TO 10
9  K= 1
10 RETURN
   END

FUNCTION FUN1(A, N, X, Y)
IMPLICIT DOUBLE PRECISION (A-H, O-Z)
DIMENSION X(100), Y(100)
IF(A-X(1))5,5,6
6  IF(A-X(N))1,1,2
2  FUN1=Y(N)
   RETURN
5  FUN1=Y(1)
   RETURN
1  DO 3 I=2,N
   IF(A.LT.X(I)) GOTO 4
3  CONTINUE
4  FUN1=Y(I-1)+(A-X(I-1))*(Y(I)-Y(I-1))/(X(I)-X(I-1))
   RETURN
   END

```

C.3 Computer Program for Calculation of Geometrical Factor

```

c      program random
c
dimension p(101,1000)
open(5, file='rout', status='old')
do 10 i=1,100
  sum=0.
  do 10 n=1,1000
    xx=rands(iseed)*3.1415926
    yy=rands(iseed)*3.1415926/2.
    prod=cos(xx)*cos(yy)
    sum=sum+prod
    absum=abs(sum/n)
    p(i,n)=absum
10  continue
c
do 30 np=1,1000
  sump=0.
  do 20 ip=1,100
    sump=sump+p(ip,np)
20  continue
  p(101,np)=sump/100.
30  continue
do 40 i=1,1000,2
  write(5,100) i, p(101,i)
40  continue
100 format(3x,i4,5x,f6.4)
stop
end
c
C
C      FUNCTION SUBPROGRAM "RANDS": GENERATES A SEQUENCE OF RANDOM
C      NUMBERS, UNIFORMLY DISTRIBUTED IN THE INTERVAL [0,1].
C
REAL*8 FUNCTION RANDS(ISEED)
IB=ISEED/65536
IA=ISEED-IB*65536
IBC=IB*63253
IDA=IA*24301
ISUM=IBC-2147483647+IDA
IF(ISUM .LE. 0) GO TO 10
ISUM=ISUM-1
GO TO 20
10  ISUM=ISUM+2147483647
20  IFF=ISUM/32768
  IE=ISUM-IFF*32768
  IX=IE+IA
  IY=453816691-2283*IA
  IX2=IX/32768
  IX1=IX-32768*IX2
  ISEED=IX1*65536-2147483647+IY
  IF (ISEED.LE.0) GO TO 30
  ISEED=ISEED-1
  GO TO 40
30  ISEED=ISEED+2147483647
40  RANDS=ISEED/2147483647.
RETURN
END

```

PART 2

(FLASH-) ATOMIZATION AND COMBUSTION STUDIES OF  
COAL-WATER FUEL IN A SPRAY TEST FACILITY AND  
IN A PILOT-SCALE FURNACE

## TABLE OF CONTENTS

	<u>Page</u>
Part 2: "(Flash-) Atomization and Combustion Studies of Coal-Water Fuel in a Spray Test Facility and in a Pilot-Scale Furnace" .....	173
TABLE OF CONTENTS .....	174
LIST OF FIGURES .....	177
LIST OF TABLES .....	181
NOMENCLATURE .....	182
CHAPTER 1. INTRODUCTION .....	185
1.1 Introduction .....	185
1.2 Objectives of Investigation .....	186
CHAPTER 2. EXPERIMENTAL INVESTIGATION .....	187
2.1 Experimental Apparatus for CWF Atomization Study .....	187
2.1.1 Spray Test Facility .....	187
2.1.2 Laser Diffraction Spray Analyzer .....	190
2.1.3 Atomizer .....	192
2.1.4 Capillary Tube Viscometer .....	192
2.1.5 Fuel Treatment Systems .....	195
2.2 Experimental Apparatus for CWF Combustion Study .....	197
2.2.1 Combustion Research Facility .....	197
2.2.2 Water-Quench Sampling Probe .....	202
2.2.3 Steam-Heated Sampling Probe .....	202

CHAPTER 3. ATOMIZATION STUDY OF CWF .....	209
3.1 Introduction .....	209
3.2 Atomization Mechanism in Twin-Fluid Atomizer .....	211
3.3 Representative Shear Rate during CWF Atomization .....	213
3.4 Experimental Results of Spray Droplet Size with CWF Viscosity .....	220
3.5 Correlation of CWF Atomization .....	231
3.5.1 Basic Form of Atomization Correlation .....	231
3.5.2 Atomization Correlation for OR-KVB Atomizer .....	233
3.6 Summary .....	239
CHAPTER 4. FLASH-ATOMIZATION STUDY OF CWF .....	243
4.1 Introduction .....	243
4.2 Theoretical Models of CWF Flash-Atomization .....	244
4.2.1 Nucleation Sites in Coal Particle during CWF Flash-Atomization .....	244
4.2.2 Mechanism of CWF Flash-Atomization .....	245
4.2.3 Bubble Growth Dynamics .....	249
4.2.4 Effect of Superheat on CWF Flash-Atomization .....	255
4.2.5 Spray Angle Change during Flash-Atomization .....	258
4.3 Experimental Results of CWF Flash-Atomization and Discussions .....	264
4.4 Experimental Results and Correlation of Spray Angle Change during Flash-Atomization .....	270
CHAPTER 5. COMBUSTION STUDY OF CWF WITH FUEL TREATMENTS .....	278
5.1 Introduction .....	278
5.2 Experimental Results and Discussions .....	279
5.3 Summary .....	294

CHAPTER 6. CONCLUSIONS .....	298
REFERENCES .....	300
APPENDICES .....	303
APPENDIX A PRINCIPLE OF LASER DIFFRACTION SPRAY ANALYZER .....	304
APPENDIX B PRINCIPLE OF CAPILLARY TUBE VISCOMETER .....	307
APPENDIX C EXPERIMENTAL DATA OF IN-FLAME MEASUREMENTS .....	310
BIOGRAPHICAL NOTE .....	314



## LIST OF FIGURES

<u>Figure</u>		<u>Page</u>
1	Schematic Diagram of Spray Test Facility .....	188
2	Photograph of Spray Test Facility .....	189
3	Schematic Diagram of Spray Test Facility and Laser Diffraction Spray Analyzer .....	191
4	Schematic Diagram of OR-KVB Atomizer .....	193
5	Schematic Diagram of Capillary Tube Viscometer .....	194
6	Schematic Diagram of CO <sub>2</sub> Injection System .....	196
7	Schematic Diagram of MIT Combustion Research Facility and Support Systems .....	198
8	Schematic Diagram of Furnace Assembly and Air Supply System in MIT Combustion Research Facility .....	199
9	Photographs of Furnace Assembly in MIT Combustion Research Facility (a) Front View, (b) Side View .....	200
10	Schematic Diagram of Water-Quench Sampling Probe .....	203
11	Detail of Water-Quench Sampling Probe Tip .....	203
12	Schematic Diagram of Flame Solids Sampling System .....	204
13	Photograph of Modified Pilat Cascade Impactor and BCURA Cyclone Separator in Oven .....	205
14	Schematic Diagram of Pilat Mark III Cascade Impactor .....	207
15	Schematic Diagram of Cross-Section of Pilat Mark III Cascade Impactor .....	208
16	Schematic Diagram of Twin-Fluid Atomizer with Transparent Lower Casing .....	214
17	Photographs of Twin-Fluid Atomizer with Transparent Lower Casing (a) Assembled, (b) Disassembled .....	215
18	Atomization Mechanism in Twin-Fluid Atomizer .....	216
19	Control Volume of Contracted Liquid Jet in Mixing Chamber of Twin-Fluid Atomizer .....	218

20	Effect of Dilution on MMD and Viscosity of CWF (A-Reg) (a) MMD versus AFR, (b) CWF Viscosity versus Shear Rate .....	223
21	Effect of Dilution on MMD and Viscosity of CWF (B-Fine) (a) MMD versus AFR, (b) CWF Viscosity versus Shear Rate .....	224
22	Effect of Dilution on MMD and Viscosity of CWF (A-Fine) (a) MMD versus AFR, (b) CWF Viscosity versus Shear Rate .....	225
23	Effect of Chemical Additive on MMD and Viscosity of CWFs (A-Reg & C-Reg) (a) MMD versus AFR, (b) CWF Viscosity versus Shear Rate .....	226
24	Effect of Coal Particle Size Distribution on MMD and Viscosity of CWFs (A-Reg, B-Fine, & D-U-Fine) (a) MMD versus AFR, (b) CWF Viscosity versus Shear Rate .....	227
25	Effect of Coal Particle Size Distribution in CWF on CWF Viscosity at Low and High Shear Rates .....	229
26	Effect of Dilution on CWF Viscosity at Low and High Shear Rates .....	230
27	Mass Mean Diameter of Spray Droplets of Various CWFs versus CWF Viscosity for AFRs = 0.1, 0.2, & 0.3 .....	234
28	Mass Mean Diameter of Spray Droplets of Various CWFs versus CWF Viscosity for AFRs = 0.15 & 0.25.....	235
29	Mass Mean Diameter of Spray Droplets versus ( $1 + 1/AFR$ ) for A-Reg-70, 66, & 60 CWFs .....	237
30	Mass Mean Diameter of Spray Droplets versus ( $1 + 1/AFR$ ) for B-Reg-70 & 66 and C-Reg-66 & 60 CWFs .....	238
31	Comparison of Measured MMDs with Calculated MMDs .....	240
32	Comparisons of Measured MMDs with Calculated MMDs for Low Shear Viscosities and for High Shear Viscosities .....	241
33	Sequential Process of Flash-Atomization between Each Coal Particle in CWF .....	246
34	Sequential Process of Flash-Atomization on CWF Droplet Surface .....	247

35	Adhesion Process of Flash-Atomized CWF Droplets (a) Before Collision, (b) After Collision .....	250
36	Sequential Process of Vapor Bubble Growth at Nucleation Pore of Coal Particle .....	251
37	Pore Size Distribution of Coal Particle .....	256
38	Comparison of Amount of Remaining Water on Coal Particle Surface with Different Superheat $\Delta T$ (a) Small Superheat $\Delta T$ , (b) Large Superheat $\Delta T$ .....	257
39	Comparison of Surface Tension Force with Different Amount of Surrounding Water in Coalescent CWF Droplets (a) Thin Water Layer, (b) Thick Water Layer .....	259
40	Schematic Diagrams of Twin-Fluid Atomization (a) Without Flash-Atomization, (b) With Flash-Atomization .....	262
41	Effect of CWF Temperature on Mass Mean Diameter of CWF Spray .....	265
42	Effect of Water Temperature on Mass Mean Diameter of Water Spray (a) Water Viscosity versus Water Temperature, (b) MMD of Water Spray versus Water Temperature .....	267
43	Comparison of Mass Distribution on CWF Sprays and Coal Particles at Various CWF Temperatures .....	269
44	Photographs of Water Sprays Taken for AFRs of 0.1 and 0.3 and at Water Temperatures of 100°C and 160°C (a) AFR = 0.1, (b) AFR = 0.3 .....	271
45	Measurement of Spray Angle $\alpha$ .....	273
46	Variation of $(\sin\alpha - \sin\alpha_0)$ with $(2c_p)^{1/2} \left[ \Delta T - T_{sat} \ln \frac{\Delta T + T_{sat}}{T_{sat}} \right]^{1/2}$ .....	274
47	Variation of $\xi/V_a$ with Flow Rates of Water and Atomizing Air .....	275
48	Photographs of CWF Flames in CRF (a) Without Flash-Atomization, (b) With Flash-Atomization .....	277

49	Photographs of CWF Flames with Various Fuel Treatments (a) Baseline, (b) Picric Acid, (c) CO <sub>2</sub> , (d) Heating .....	282
50	Particle Size Distributions of Fly-Ash and Residual Char (Unburned Carbon) for Various Fuel Treatments (Fine-Grind CWF, Flame Thermal Input = 1.0 MW) .....	284
51	Particle Size Distributions of Fly-Ash and Residual Char (Unburned Carbon) for Various Fuel Treatments (Regular-Grind CWF, Flame Thermal Input = 1.3 MW) .....	285
52	Comparisons of Gas Temperature and Gas Velocity at Centerline of Flames of Regular- and Fine-Grind CWFs for Baseline and Thermally Assisted Flames (a) Regular-Grind CWF, Flame Thermal Input = 1.3 MW, (b) Fine-Grind CWF, Flame Thermal Input = 1.0 MW .....	286
53	Solids Concentrations and Carbon Conversion Efficiencies at Centerline of Flames of Regular- and Fine-Grind CWFs for Thermally Assisted and Baseline Flames (a) Fine-Grind CWF, Flame Thermal Input = 1.0 MW, (b) Regular-Grind CWF, Flame Thermal Input = 1.3 MW .....	287
54	SEM Photographs of Particles Collected from Centerline of Flames at X/D = 17.1 (30-45 μm Particle Size) (a) Baseline, (b) Thermally Assisted .....	289
55	SEM Photographs of Particles Collected from Centerline of Flames at X/D = 17.1 (150-212 μm Particle Size) (a) Baseline, (b) Thermally Assisted .....	290
56	SEM Photographs of Particles Collected from Centerline of Flames at X/D = 17.1 (212-250 μm Particle Size) (a) Baseline, (b) Thermally Assisted .....	291
57	SEM Photographs of Particles Collected from Centerline of Flames at X/D = 17.1 (250-355 μm Particle Size) (a) Baseline, (b) Thermally Assisted .....	292
58	Transverse Distributions of Fly-Ash Deposition Rate per Unit Area of Ceramic Tubes at Axial Distance Ratio of X/D = 17.1 for Baseline and Thermally Assisted Flames .....	293

## LIST OF TABLES

<u>Table</u>		<u>Page</u>
1	Specifications of CWFs for Atomization Study .....	221
2	Surface Tensions of CWFs .....	221
3	Specifications of CWFs for Fuel Treatment Study .....	280
4	Experimental Conditions of Combustion Tests .....	281
5	Summary of Experimental Data from Combustion Tests with Various Fuel Treatments for Fine-Grind CWF .....	295
6	Summary of Experimental Data from Combustion Tests with Various Fuel Treatments for Regular-Grind CWF .....	296
C.1	Experimental Data of In-Flame Measurements (Fine-Grind CWF, Baseline) .....	310
C.2	Experimental Data of In-Flame Measurements (Fine-Grind CWF, Heating) .....	311
C.3	Experimental Data of In-Flame Measurements (Regular-Grind CWF, Baseline) .....	312
C.4	Experimental Data of In-Flame Measurements (Regular-Grind CWF, Heating) .....	313

## NOMENCLATURE

A	cross-sectional area of liquid jet
$A_{side}$	side area of liquid jet
AFR	air-to-fuel mass flow rate ratio
a	constant in eqs. (5) and (6)
b	constant in eqs. (5) and (6)
c	constant in eqs. (5) and (6)
$c_{\ell}$	specific heat of liquid
$c_p$	specific heat at constant pressure
$D_o$	diameter of fuel port
d	constant in eqs. (5) and (6)
$d_{L1}$	diameter of fuel port
$d_{L2}$	diameter of contracted liquid jet
e	constant in eqs. (5) and (6)
f	constant in eqs. (5) and (6)
$h_{fg}$	latent heat of evaporation
$\Delta h$	enthalpy difference between superheated liquid and saturated liquid
K	consistency index
$k_{\ell}$	thermal conductivity of liquid
$\ell$	depth of cylindrical nucleation pore
MMD	mass mean diameter
$\dot{m}_a$	mass flow rate of atomizing air
$\dot{m}_f$	mass flow rate of liquid fuel
n	flow behavior index
$\Delta P$	pressure drop

$R$	bubble radius
$R_p$	radius of nucleation pore mouth
$R_1$	initial bubble radius
$R_2$	final bubble radius
$R^*$	final bubble radius
$R_\infty$	radius of bubble at pore mouth
$Re$	Reynolds number
$\frac{dR}{dt}$	bubble growth rate
$\Delta s$	entropy difference between superheated liquid and saturated liquid
$T$	temperature of superheated liquid
$T_{sat}$	saturation temperature of liquid at ambient pressure
$\Delta T$	superheat of liquid
$t$	time
$\Delta t_1$	time taken to reach top of pore from bottom of pore
$\Delta t_2$	time taken to reach hemispherical stage from bubble radius of $R_\infty$
$\Delta t_3$	time taken to reach bubble radius of $R_2$ from bubble radius of $R_1$
$\Delta t_{tot}$	total time taken to reach final bubble radius of $R^*$ from entrapped air pocket
$U_A$	velocity of atomizing air
$U_L$	velocity of liquid jet
$U_R$	relative velocity between liquid jet and atomizing air
$\frac{\partial u}{\partial y}$	representative shear rate
$V_a$	axial velocity of spray
$V_f$	radial velocity of spray generated by flash-atomization
$V_{fmax}$	maximum radial velocity of spray generated by flash-atomization
$V_r$	radial velocity of spray
$We$	Weber number

X	function of bubble radius and vapor temperature in eq. (11)
Y	function of bubble radius and vapor temperature in eq. (11)
Z	Ohnesorge number

GREEK SYMBOLS

$\alpha$	half angle of spray with flash-atomization
$\alpha_0$	half angle of spray without flash-atomization
$\alpha_\ell$	thermal diffusivity of liquid
$\dot{\gamma}$	shear rate
$\mu_L$	viscosity of liquid
$\xi$	efficiency factor
$\rho_A$	density of atomizing air
$\rho_L$	density of liquid
$\rho_\ell$	density of liquid
$\rho_V$	density of vapor
$\tau$	shear stress
$\Delta\psi$	available energy of superheated liquid



## CHAPTER 1

## INTRODUCTION

1.1 Introduction

Coal-water fuel (CWF) is primarily considered as an alternative for fuel oil in retrofit applications, and it may also be seen as a future clean fuel for new coal-fired plants. CWF can be stored, transported, pumped, and atomized in a combustion chamber similar to the handling of heavy fuel oil. Upon injection into the flame the CWF droplet dries and the coal particles in the CWF droplet are drawn together by surface tension forces. At first a loose agglomerate is formed, but, as a result of initial pyrolysis, the bituminous coal particles become more tightly bonded as they undergo plastic deformation at temperatures of 350 to 500°C. As the particle temperature rises above 600 to 700°C, the loose agglomerate hardens, usually in the form of a spherical particle commensurate in size with the CWF droplet from which it originates. This transformation of the droplet/particle during the coal pyrolysis process explains why the size distribution of the carbonaceous solids in the CWF flames bears more resemblance to that of the atomized spray rather than to the size distribution of the coal particles in the CWF. The importance of high quality (sufficiently fine) atomization of CWF lies therefore in the effects this has on the efficiency of carbon conversion and the fly-ash particle size distribution<sup>(1,2,3)</sup>. Inertial impaction of ash particles causes the erosion of convective tube banks in boilers and the formation of deposits. Because the fly-ash particle size influences

these two problems, it is therefore a parameter that directly affects the degree of derating of boiler performance in retrofit applications.

### 1.2 Objectives of Investigation

The purpose of the present investigation (Part 2) is to understand the mechanisms of CWF (flash-) atomization and to examine the effects of atomizing parameters and flash-atomization on CWF atomization quality.

The atomization quality of CWF will be investigated in the Spray Test Facility (STF) equipped with the laser diffraction spray analyzer. A capillary viscometer will be used to measure viscosity of CWF at high shear rate. Based upon the experimental results of CWF atomization, the correlation of atomization quality with rheological properties of CWF will be established.

The effect of fuel treatments which induce flash-atomization will be also investigated in the STF and in a pilot-scale furnace. Finally, the theoretical models of flash-atomization and of spray angle change due to flash-atomization will be developed.

## CHAPTER 2

## EXPERIMENTAL INVESTIGATION

2.1 Experimental Apparatus for CWF Atomization Study2.1.1 Spray Test Facility

A schematic diagram and a photograph of the Spray Test Facility (STF) used to characterize CWF spray are shown in Figures 1 and 2, respectively. CWF was delivered to the atomizer through the flow meter (Micro-Motion Model C 25) by the Moyno pump which could provide injection pressure up to 4 MPa. Fuel pressure and temperature were measured at the entrance of the spray gun. Atomizing air was supplied at pressures up to 7 MPa. It passed through the pressure regulator, the flow meter, and the flexible stainless steel hose to the atomizer. Atomizing air pressure and temperature were also measured at the entrance of the spray gun. The spray gun transporting the CWF and the atomizing air could be adjusted vertically and horizontally to permit the traversing of different segments of the conical spray by the laser beam of the optical spray analyzer.

Two sides of the 1.3 m x 0.5 m x 1.0 m chamber had plexiglas walls with a 3-cm-diameter hole on each side of the wall for optical observation and measurement. About half of the other sides of the chamber had honeycomb sections through which outside air could be entrained by the exhaust fan. The supply of outside air was necessary to suppress the recirculation of small particles into the path of the laser beam. This entrained air flow and the atomizing air were separated from the CWF at the exit of the spray chamber and then flowed through a filter

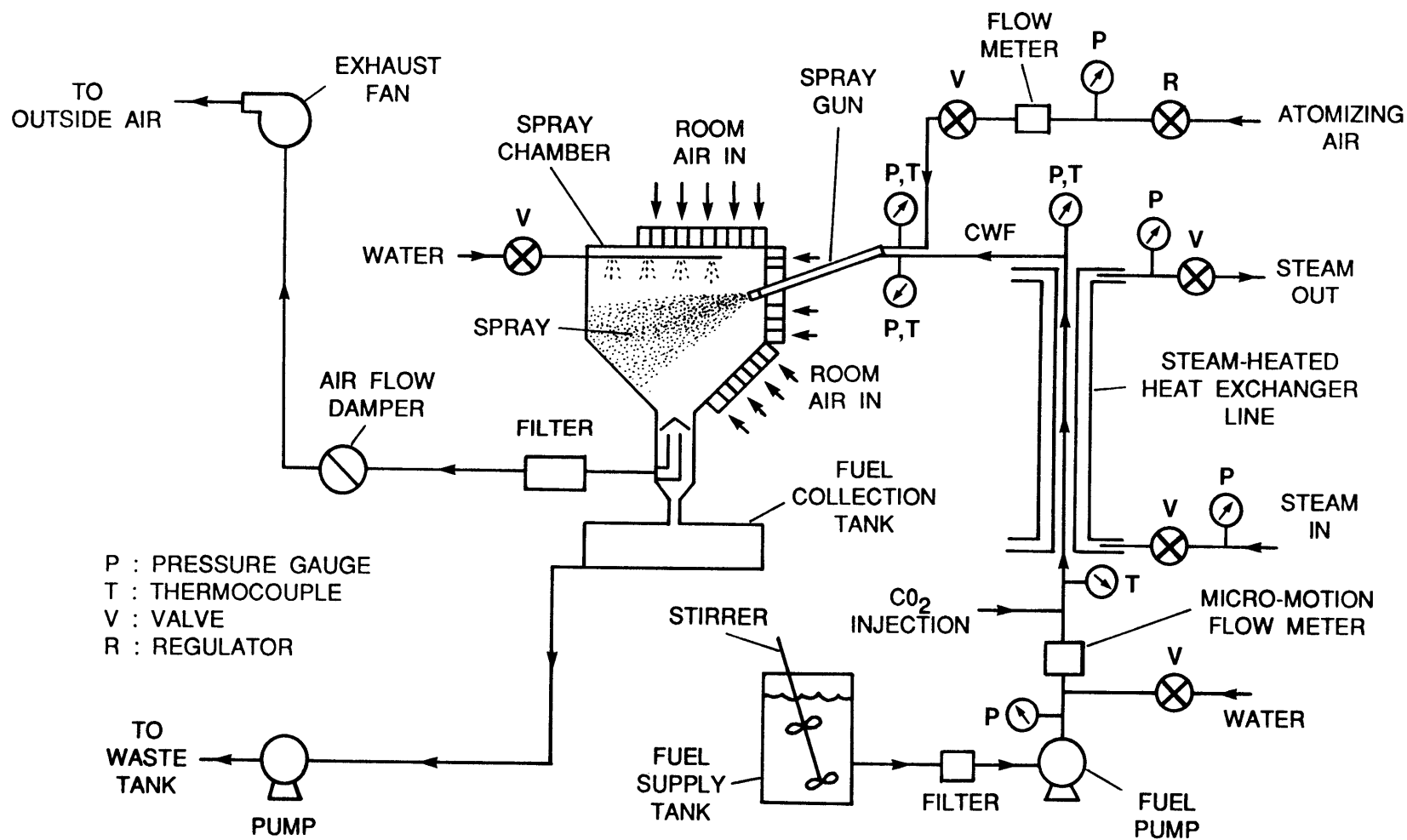


Figure 1. Schematic Diagram of Spray Test Facility

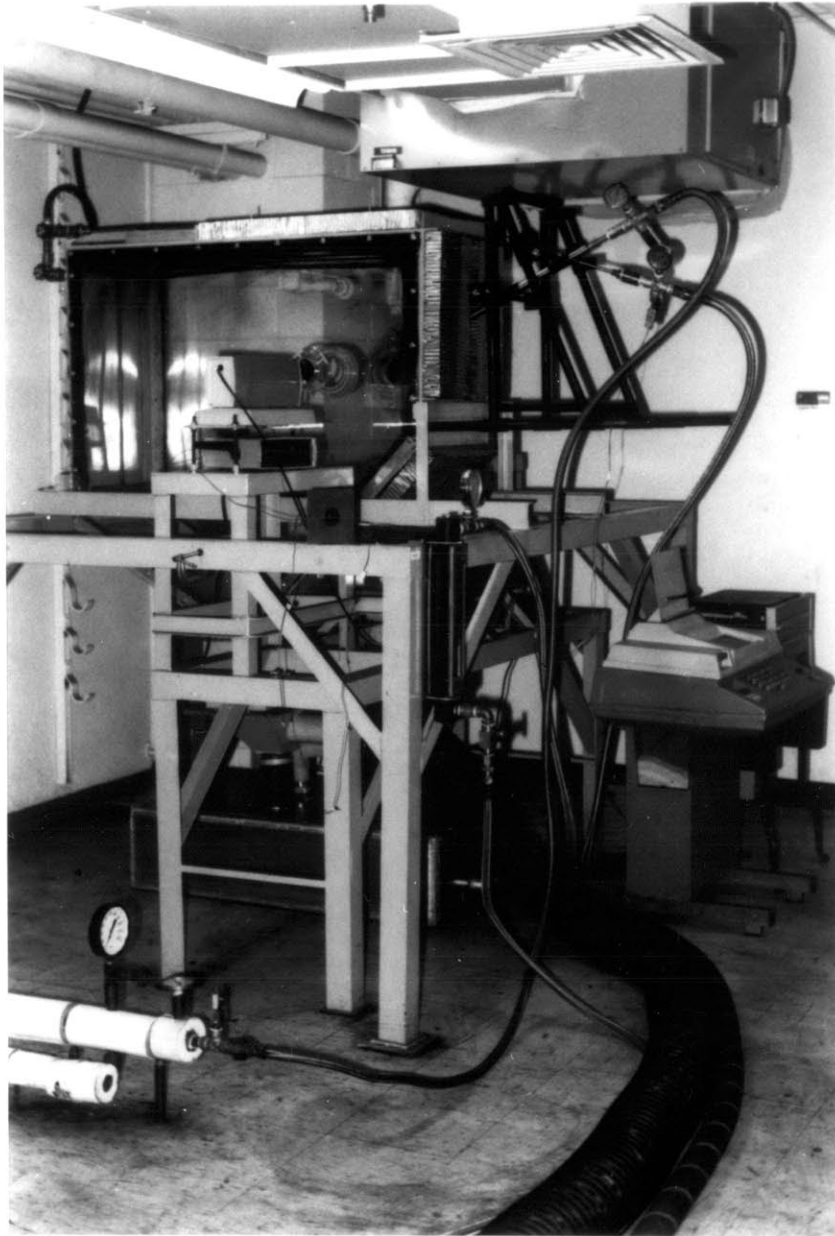


Figure 2. Photograph of Spray Test Facility

and a flexible hose en route to the exhaust system of the Combustion Research Facility (CRF). The used CWF was collected in a waste tank through a pump.

### 2.1.2 Laser Diffraction Spray Analyzer

The Spray Test Facility (STF) was equipped with the laser diffraction spray analyzer<sup>(4)</sup> for droplet size measurements. A schematic diagram of the laser diffraction spray analyzer and the STF is shown in Figure 3. The operational principle of the laser diffraction spray analyzer is based on the Fraunhofer diffraction pattern superimposed on the geometrical image produced by droplets in the path of the monochromatic light beam. This spray analyzer, manufactured by Malvern Instruments Inc., generated a laser light source which passed through the holes in two plexiglas plates in the STF. The spray analyzer consisted of: a 31 annular-element photodetector that received the light signal from the other side of the chamber, a minicomputer, and a control terminal that processed output signals from the photodetector to calculate droplet size distributions. A computer program of the spray analyzer was capable of deducing the corresponding particle size distribution responsible for producing the measured light energy distribution in various functional forms, such as Normal, Log Normal, Rosin-Rammler, or Model Independent.

During the experiments, the laser beam was aimed through the middle of the spray 30 cm away from the atomizer tip. The transmissivity of the spray was monitored, and the multiple scattering effect was determined according to the empirical calibration technique developed by Dodge<sup>(5)</sup>.

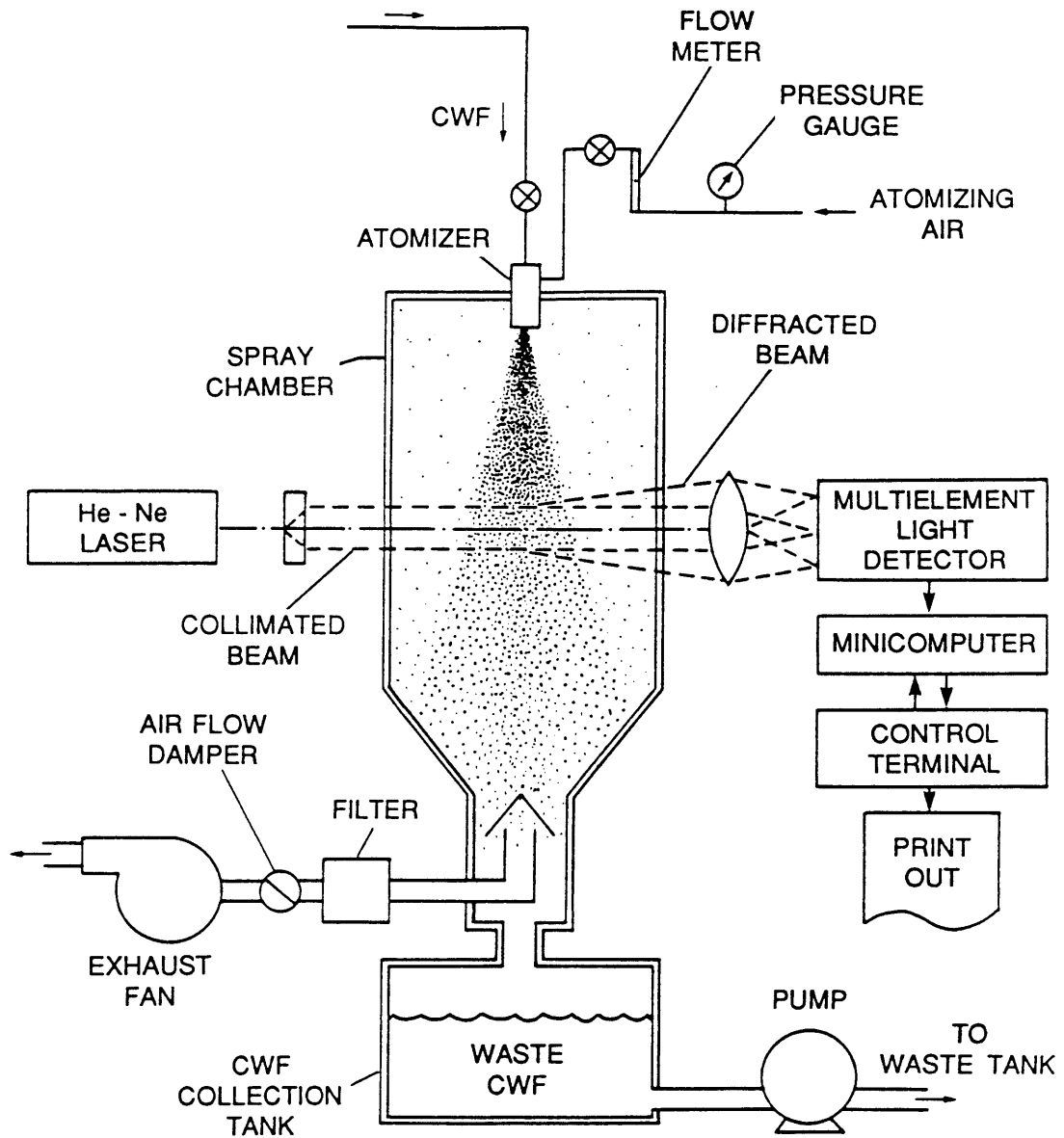


Figure 3. Schematic Diagram of Spray Test Facility and Laser Diffraction Spray Analyzer

A 300-mm focal length lens was used for the laser diffraction particle size measurements. This gave an observable size range of 5.8 to 564  $\mu\text{m}$ . The operational principle of the laser diffraction spray analyzer will be discussed in detail in Appendix A.

### 2.1.3 Atomizer

Figure 4 shows a schematic diagram of the atomizer which was used for both spray tests and combustion tests. This twin-fluid, OR-KVB atomizer (developed by Occidental Research Corp. and KVB, Inc.) had an internal-mixing and single-exit orifice. This atomizer was found to be capable of producing fine CWF sprays and stable flames in the MIT CRF<sup>(2)</sup>.

During the experiments, the diameter of the atomizer orifice was fixed at 3.175 mm and the air-to-fuel ratio (AFR) was varied from 0.1 to 0.3 which was within the normal operating AFR range for this type of the atomizer.

### 2.1.4 Capillary Tube Viscometer

A schematic diagram of the capillary tube viscometer<sup>(6)</sup> which was used to measure CWF viscosities at shear rates up to  $2 \times 10^5 \text{ sec}^{-1}$  is shown in Figure 5. A cylindrical pressure vessel, 60 cm long with a 15-cm I.D., designed for the maximum working pressure of 14.0 MPa, was used to store CWF. When the cylindrical vessel was pressurized by a compressed air, CWF in the vessel was forced to flow through a capillary tube to the Micro-Motion flow meter. The applied pressure was measured by a pressure transducer and recorded as a function of the CWF mass flow rate. In order to obtain the pressure drop along the fully developed



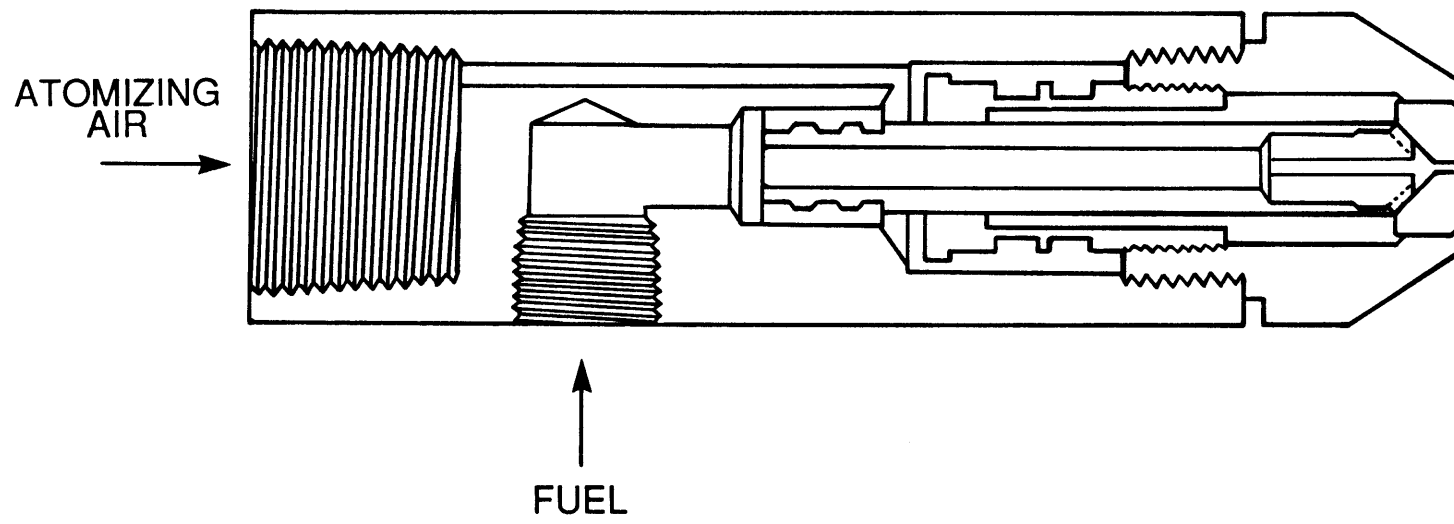


Figure 4. Schematic Diagram of OR-KVB Atomizer

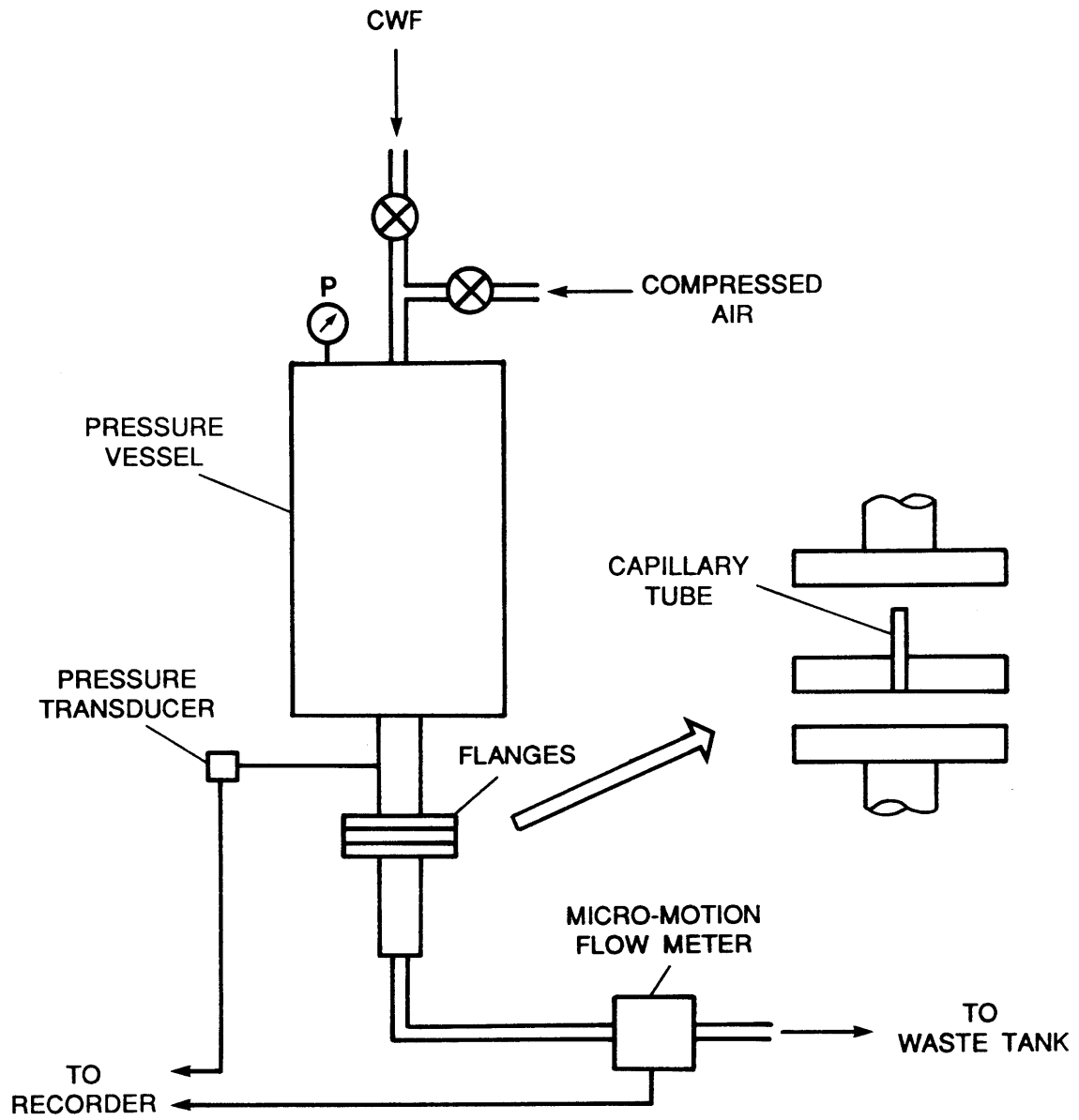


Figure 5. Schematic Diagram of Capillary Tube Viscometer

laminar tube flow region free from effects of inlet and exit losses, the measurements of applied pressure and CWF mass flow rate were repeated with another tube of the same diameter but of different length.

The capillary tubes used were of 1.5 mm in inside diameter and of 1.0 to 10.0 cm in length. Detail description of the capillary tube viscometer and procedure of viscosity measurement will be discussed in Appendix B.

#### 2.1.5 Fuel Treatment Systems

A steam-heated heat exchanger line (Figure 1) was installed between the fuel pump and the Spray Test Facility for the thermally assisted atomization study. The heat exchanger line was 12 m long, and was equipped with pressure gauges and thermocouples to monitor pressures and temperatures of both steam and CWF.

A schematic diagram of the CO<sub>2</sub> injection system is shown in Figure 6. The CO<sub>2</sub> injection system could be installed temporarily in the main fuel line for the study of fuel treatment by CO<sub>2</sub> injection. The maximum CO<sub>2</sub> mass flow rate which could be injected into the fuel line without causing pulsating sprays or flames was approximately 4 g/kg CWF.

For the study of chemical treatment of CWF, picric acid was mixed with CWF in the fuel supply tank. The nominal picric acid concentration was chosen to be 0.35 g/kg CWF.

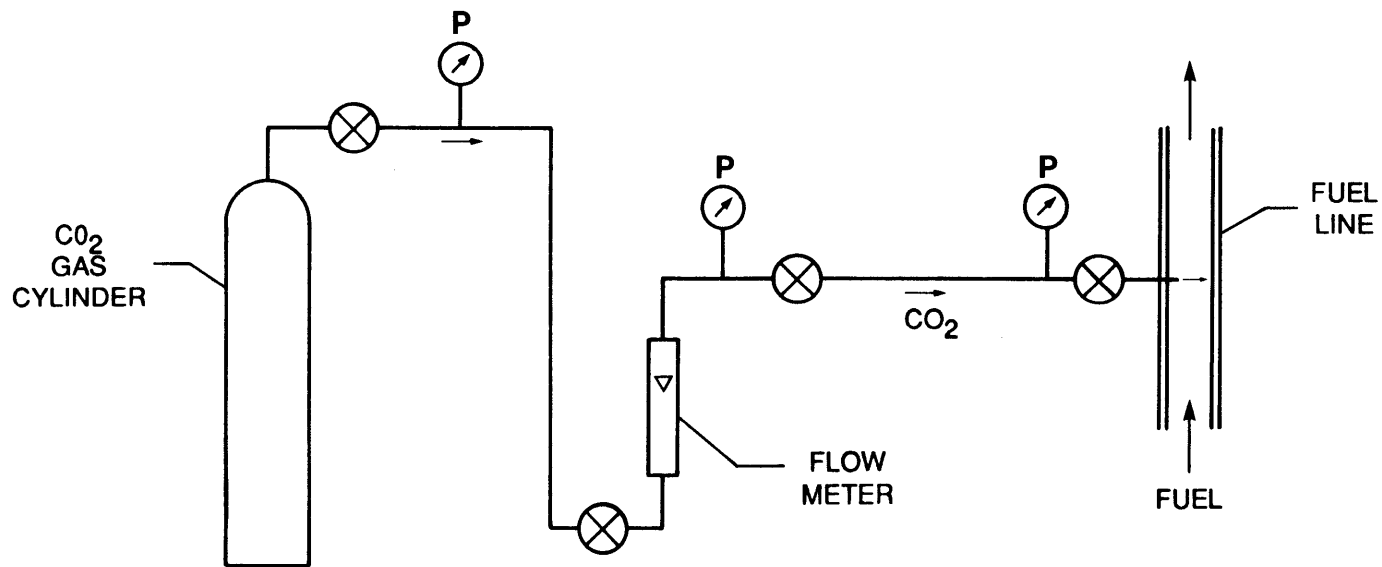


Figure 6. Schematic Diagram of CO<sub>2</sub> Injection System

## 2.2 Experimental Apparatus for CWF Combustion Study

### 2.2.1 Combustion Research Facility

The Combustion Research Facility (CRF) is shown schematically in Figures 7 and 8 and in the photograph in Figure 9. The CRF had an 1.2 m x 1.2 m cross-section. The CRF was a 10-m-long combustion tunnel made up of 30 interchangeable, separable 30-cm wide wall sections, all of which were water-cooled and instrumented to obtain a sectional heat balance. An additional section was cylindrical with 0.6 m I.D.; it might be used as an after-burner with oxygen injection, or as a transition piece to establish a staged combustion configuration which precluded upstream recirculation of second-stage combustion gases. Fifteen of the wall sections were refractory-lined to permit hot-wall operation of up to 1600°C face temperature, and the remainder of the sections had bare metal surfaces permitting cold-wall operation (100°C face temperature). The interchangeability of these wall sections permitted variable furnace length and variable heat sink distribution. The variable heat sink capability permitted simulation of a wide range of industrial- and domestic-scale furnaces while facilitating the necessary wall heat flux conditions needed to ensure thermal and/or chemical similarity for scale-up of experimental data.

The CRF was equipped with a single burner of up to 3 MW thermal, multi-fuel firing capability. The burner assembly was in accordance with IFRF (International Flame Research Foundation) design and contained an interchangeable and centrally located gas or liquid fuel/coal-water fuel gun, which carried the fuel and atomizing air for liquid fuel/coal-water fuel injection. The combustion air was supplied to an annular throat

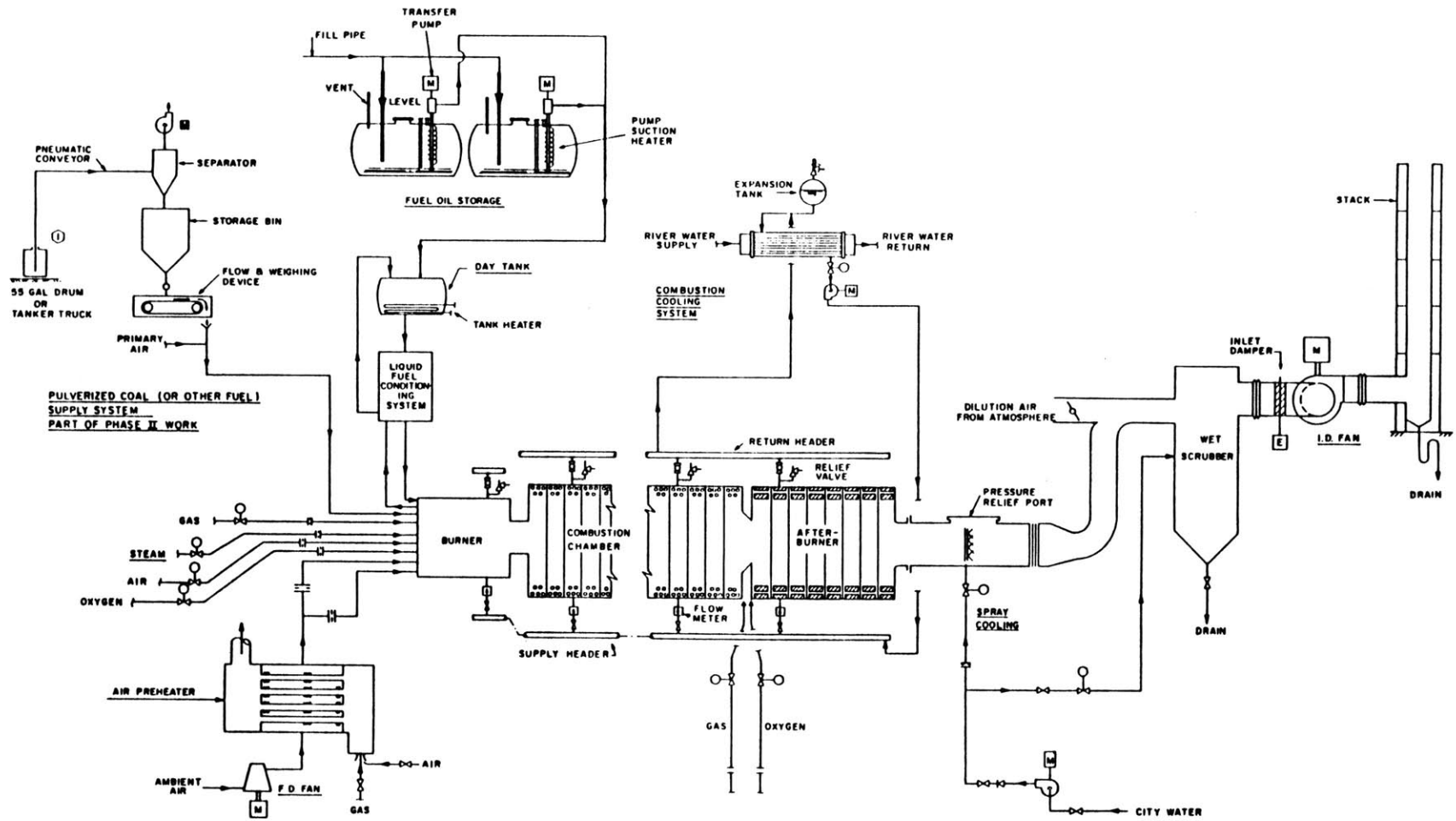


Figure 7. Schematic Diagram of MIT Combustion Research Facility and Support Systems

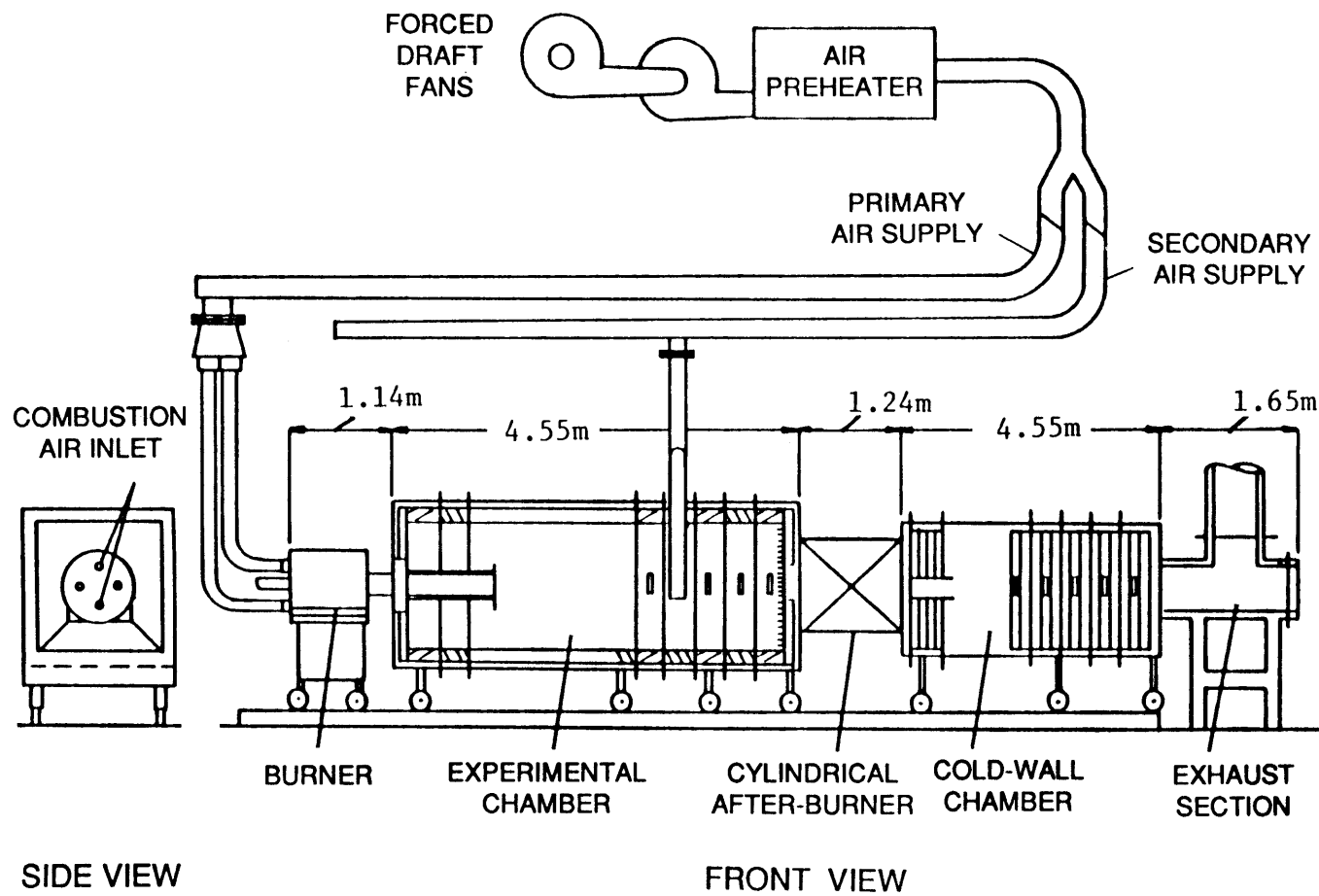
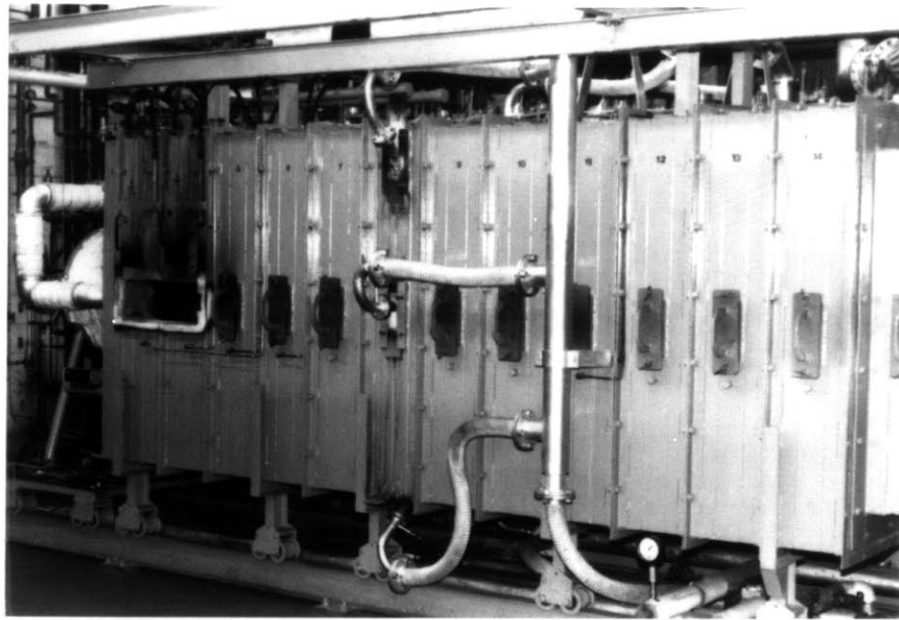
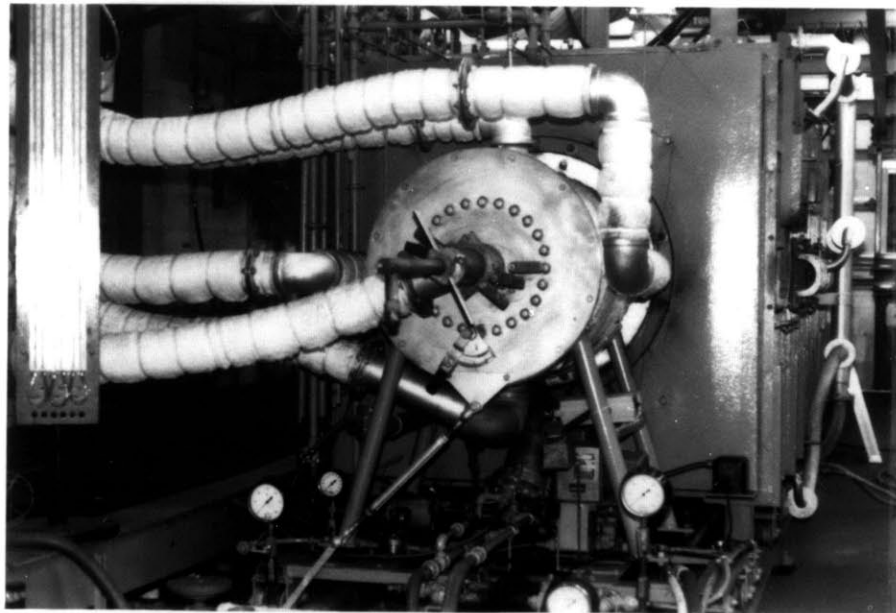


Figure 8. Schematic Diagram of Furnace Assembly and Air Supply System in MIT Combustion Research Facility



a



b

Figure 9. Photographs of Furnace Assembly in MIT Combustion Research Facility  
(a) Front View, (b) Side View



surrounding the fuel gun via a variable swirl generator which permitted the ratio of tangential to axial momentum in the combustion air to be varied over a wide range. The variation in combustion air swirl permitted significant changes in flame flow pattern and overall aerodynamics.

The fuel handling and preparation system was designed to permit use of gaseous fuels, and a range of liquid fuels including mixtures of solids and liquids, i.e., coal-oil mixtures and coal-water fuels.

All of the measurement and monitoring systems for both inputs to the furnace and experimental variables were interfaced to a computerized data acquisition and handling system. This system permitted rapid evaluation of all process variables and also rapid processing of all in-flame measurements, many of which might need to be further analyzed to provide guidance on input parameters selection for continuation of the measurements program.

The overall arrangement of the experimental plant is shown schematically in Figure 7. The multi-fuel swirl burner and the layout of the furnace itself are illustrated in Figure 8, which shows the sequential arrangement of the burner, the brick-lined experimental chamber, the after-burner, and the cold-wall chamber of the CRF. The combustion air was supplied by a fan capable of delivering  $100 \text{ m}^3/\text{min}$ , against 2.0 m WG (water gauge) pressure; the air could be preheated in an externally fired air preheater, up to  $500^\circ\text{C}$ . The preheated air could then be divided into two separately metered branches for introduction to the burner as primary and secondary air flows, as shown schematically in Figure 8.

### 2.2.2 Water-Quench Sampling Probe

Schematic diagrams of the water-quench sampling probe are shown in Figures 10 and 11. Combustion gases along with particulates were drawn by a vacuum through the probe and into a sampling unit. A controlled flow of quench water was sprayed at the tip of the probe in order to quench the reactions occurring in the sample, and to prevent deposition of organic particulates along the tube walls of the sampling probe. The probe was made of stainless steel and was water-cooled.

The sample was comprised of the quench water, particulates, and gases. These were run through the sampling unit which consisted of: 1) a filter (paper) for collection of solids, 2) absorption traps for various constituents of interest in the combustion gases, and 3) a water trap for retention of any organics/inorganics of interest that might have been dissolved in the quench water.

The total gas drawn through the sampling unit was measured with a volumetric gas flow meter, so that the constituents of interest might be quantified as well as identified.

### 2.2.3 Steam-Heated Sampling Probe

The system used to sample flame solids is shown in Figures 12 and 13. A sampling probe with a protective outer cooling-water jacket and an inner steam-heated sampling line captured flame solids. The probe had three interchangeable inlet nozzles with diameters of 14 mm, 20 mm, and 28 mm to allow for isokinetic sampling under varying conditions. A BCURA cyclone separator collected the largest particles with a minimum size of 4  $\mu\text{m}$  aerodynamic diameter. Those particles that were not captured by the

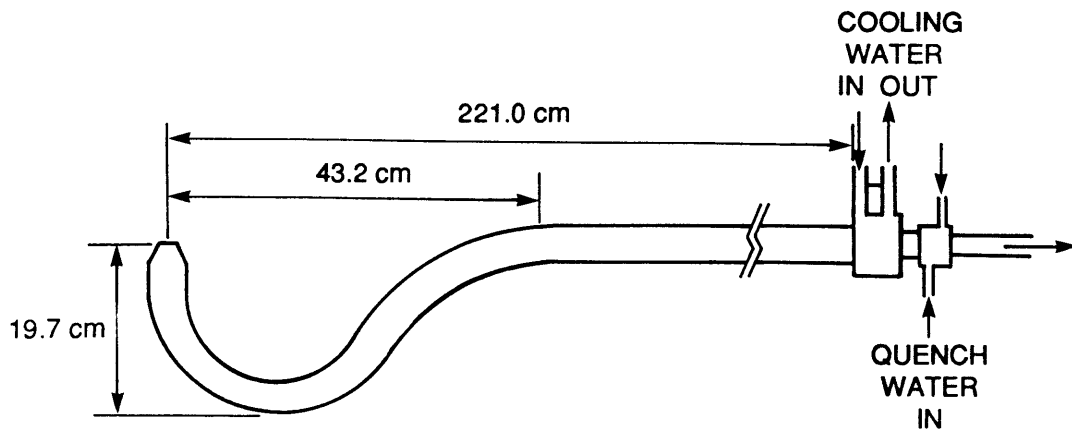


Figure 10. Schematic Diagram of Water-Quench Sampling Probe

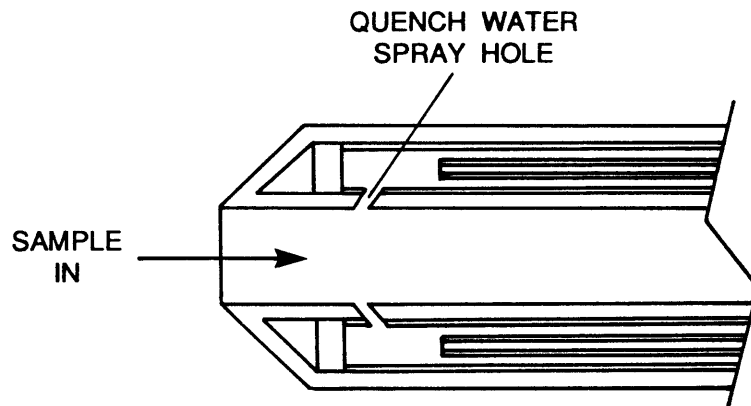


Figure 11. Detail of Water-Quench Sampling Probe Tip

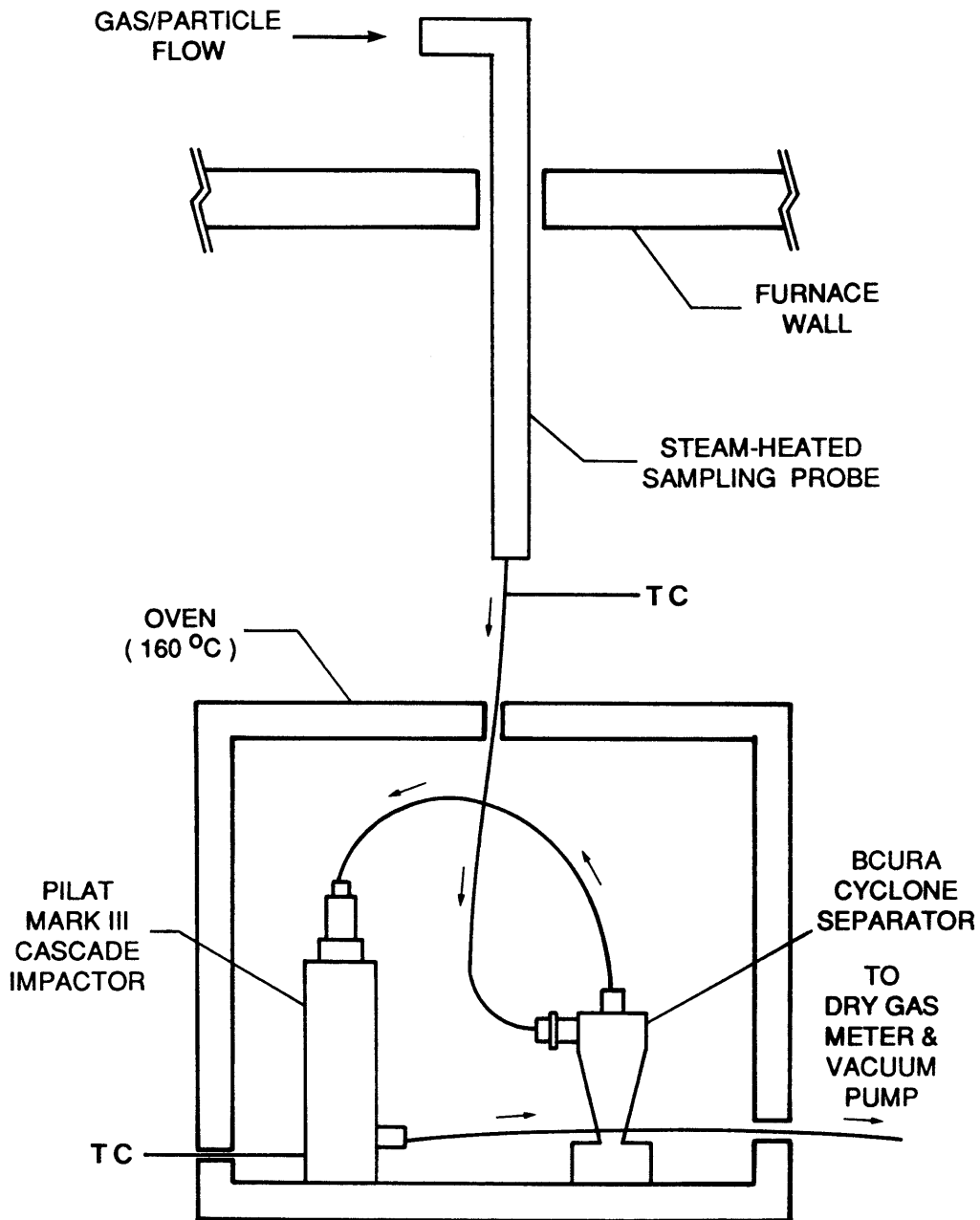


Figure 12. Schematic Diagram of Flame Solids Sampling System



Figure 13. Photograph of Modified Pilat Cascade Impactor and BCURA Cyclone Separator in Oven

cyclone separator were captured and aerodynamically size-classified by a Pilat (University of Washington) Mark III cascade impactor (Figures 14 and 15). Because the presence of sulfuric acid in the combustion gases increased the potential for condensation and its resulting errors, the probe sample line was steam-heated and the cyclone separator and cascade impactor were kept in an oven at 160°C (Figures 12 and 13). Thermocouples were installed at the probe outlet and at the base of the cascade impactor to monitor sample temperature.

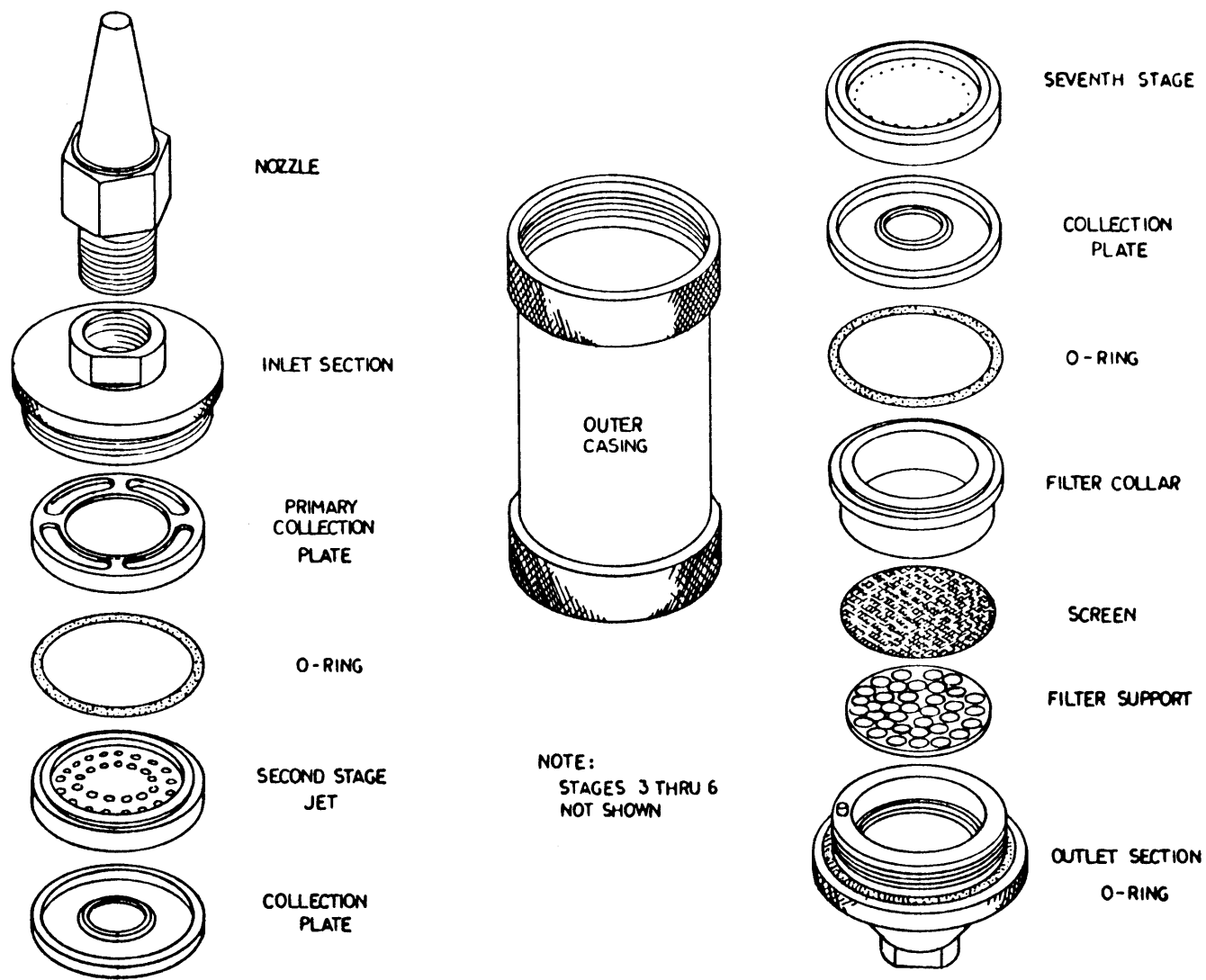


Figure 14. Schematic Diagram of Pilat Mark III Cascade Impactor

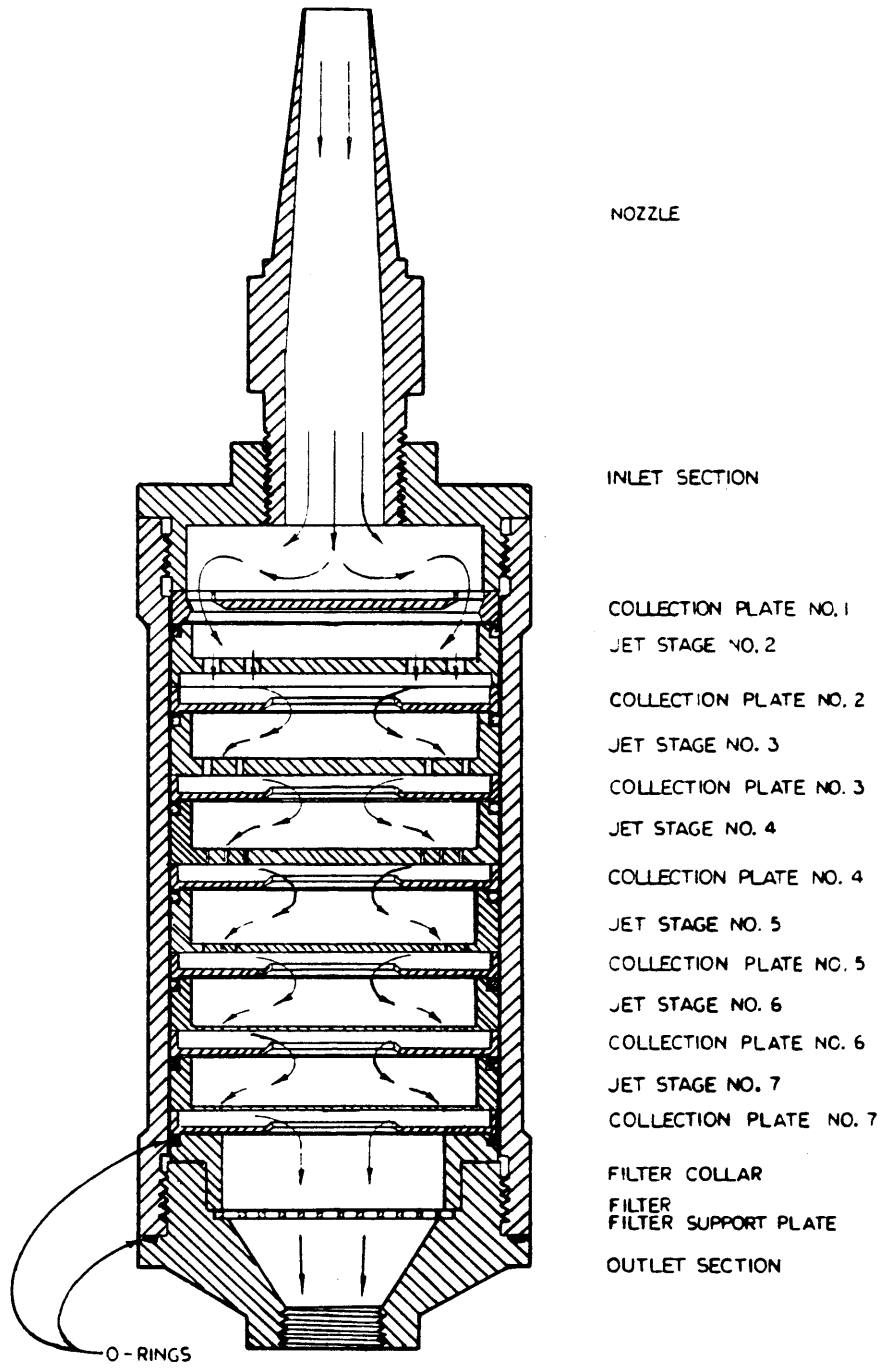


Figure 15. Schematic Diagram of Cross-Section of Pilat Mark III Cascade Impactor



CHAPTER 3  
ATOMIZATION STUDY OF CWF

3.1 Introduction

Upon atomization of CWF into a combustor, CWF droplets undergo rapid evaporation and heating, followed by ignition. During these stages coal particles tend to agglomerate within CWF droplets. The resulting coal particle size distribution is then determined more by the size distribution of the atomized CWF spray than by the initial size distribution of the coal particles. Therefore, the atomization quality (i.e., fineness of CWF spray droplets) is considered to be the most important factor for a higher carbon conversion efficiency of CWF and a finer fly-ash particle size distribution (p.s.d.) in the flame.

While there are several publications pertaining to methods and mechanisms of atomization of Newtonian fluids<sup>(7, 8)</sup>, there is a dearth of information on the atomization characteristics of strongly non-Newtonian fluids such as CWF. In non-Newtonian fluids, the effective viscosity is shear rate dependent, and this dependence can take two distinct forms; shear thinning (pseudoplastic) and shear thickening (dilatant). The shear thinning (pseudoplastic) behavior is generally favorable for the purpose of atomization, which means that as the fluid undergoes shear stress in the atomizer, its effective viscosity decreases. In the shear thickening (dilatant) case, the opposite applies; the effective viscosity increases with increasing shear rate, which is unfavorable for the purpose of atomization. The behavior of some CWFs may be further complicated by their changing from one type of behavior to the other as

the shear rate is varied. Hence, it is important to determine effective viscosities at high shear rates commensurate with those which arise in twin-fluid atomizers.

In the majority of data published on CWF atomization, no attempt was made to correlate measured droplet size distributions with rheologic properties of CWF. Where such an effort was made, low shear rate values of the viscosity were used.

Various atomizers were tested for CWF application by Borio et al.<sup>(9)</sup> and Rasfjord<sup>(10)</sup>. Photographic studies of CWF atomization were made by Chigier and Meyer<sup>(11,12)</sup>. Sommer and Matsuzaki<sup>(13)</sup> formulated an empirical equation for a twin-fluid, air-blast atomizer to predict a Sauter Mean Diameter (SMD) at a given radial location as a function of the dominant flow parameters such as air and fuel flow rates.

Smith et al.<sup>(14)</sup> studied CWF atomization at various ambient pressure, air-to-fuel ratio (AFR), and pressure drop. They found that in their experiments, dependence of SMD of CWF spray on AFR and pressure drop was consistent with that for low viscosity liquid fuels, and that SMD did not depend on ambient air pressure.

Daley et al.<sup>(15)</sup> reported experimental data showing acceptable correlation between SMD and viscosity at low shear rates (less than  $500 \text{ sec}^{-1}$ ). Spray droplet size (SMD) and viscosity at shear rates up to  $10^4 \text{ sec}^{-1}$  were measured by Tsai and Knell<sup>(16)</sup>; they reported significant changes in effective viscosity as they varied the shear rate from low to high values, and found a better correlation of atomization quality with the high shear viscosity. The apparent contradiction between the conclusions drawn by investigators of these two studies<sup>(15, 16)</sup> stems

from the limited range of fuel types tested. The shear thinning (pseudoplastic) liquids behavior at high shear rate can be predicted with reasonable approximation from low shear rate viscosity data. But, generalization of such results to a broad range of fuels may cause errors.

Hence, it is considered that predictions of rheological behavior of CWF during atomization can be made only if the representative shear rate during atomization is calculated, and the effective viscosity is experimentally determined at these representative shear rates.

In this chapter, atomization mechanism in the twin-fluid atomizer will be reviewed in Section 3.2 and an approximate assessment of shear rate at the atomizing air/fuel interface will be made in Section 3.3. The experimental results of CWF spray droplet sizes with CWF viscosities and AFRs will be discussed in Section 3.4. Finally, the correlation of atomization quality with rheological properties of CWF and flow parameters of CWF and atomizing air will be established in Section 3.5.

### 3.2 Atomization Mechanism in Twin-Fluid Atomizer

Liquid fuel requires to be broken up into small droplets before being injected into a combustion chamber in order that it can effectively burn. To produce a high ratio of surface to mass in the liquid phase, resulting in very high evaporation rates, a volume of liquid fuel should be converted into a multiplicity of small droplets, which is called atomization.

The process of atomization is simple to accomplish because it needs only the existence of a high relative velocity between the liquid fuel

and the surrounding gas. With atomizers of the pressure type, a high velocity is imparted to the fuel by discharging it under pressure through a fine orifice. An alternative approach is twin-fluid atomization which is to expose a relatively low-velocity liquid fuel to a high-velocity gas stream.

Twin-fluid atomization has many practical advantages over pressure atomization. It produces a finer spray and ensures thorough mixing of air and fuel. It also provides a sensibly constant fuel distribution over the entire range of fuel flows, and requires lower fuel pressures.

The physical process of twin-fluid atomization is composed of the following steps<sup>(17)</sup>:

- (1) Formation of thin liquid sheets on a plate or along the inner walls of an internal-mix atomizer, or free sheets unattached to walls.
- (2) Disintegration of the liquid sheet by aerodynamic forces to form ligaments, large drops, and droplets.
- (3) Breakup of ligaments and large drops into droplets.
- (4) Acceleration of droplets by high-velocity gas stream and/or deceleration of droplets by low-velocity and recirculation flows.
- (5) Formation of two-phase, liquid-gas spray, followed by spreading of a spray jet and entrainment of gas from surroundings.
- (6) Evaporation of droplets as a result of temperature and vapor pressure differentials between droplet surface and surroundings.

- (7) Agglomeration of droplets by collision can occur but, except under conditions of rapid deceleration in the regions of a spray close to the nozzle, this mechanism is not considered to be significant.

Figures 16 and 17 show the twin-fluid, internally mixed, single-exit atomizer with the transparent lower casing, which was made to observe and study the atomization process in the mixing chamber of the atomizer. This atomizer was also used during the experiments in the Part 1 study. For the purpose of the Part 2 study, the stainless steel lower casing was replaced with the transparent plexiglas one.

Based upon the observation of twin-fluid atomization of water, the atomization mechanism in the twin-fluid atomizer is shown schematically in Figure 18. It was observed that water was discharged from the fuel port to the mixing chamber as an unbroken column, and was contracted due to momentum transfer to a low-velocity liquid jet from a high-velocity atomizing air. The surface of the contracted liquid jet became uneven and then tore into many finger-shaped ligaments by the disruptive action of a high-velocity atomizing air. The ligaments were then quickly drawn into droplets due to the surface tension of the liquid.

### 3.3 Representative Shear Rate during CWF Atomization

Since CWF shows non-Newtonian fluid behavior, the shear rate should be known in order to decide the viscosity of CWF during the atomization process. The actual shear rate during the atomization process is varied with the position of the atomized liquid jet due to the changes of liquid thickness and relative velocity between atomizing air and CWF. However,

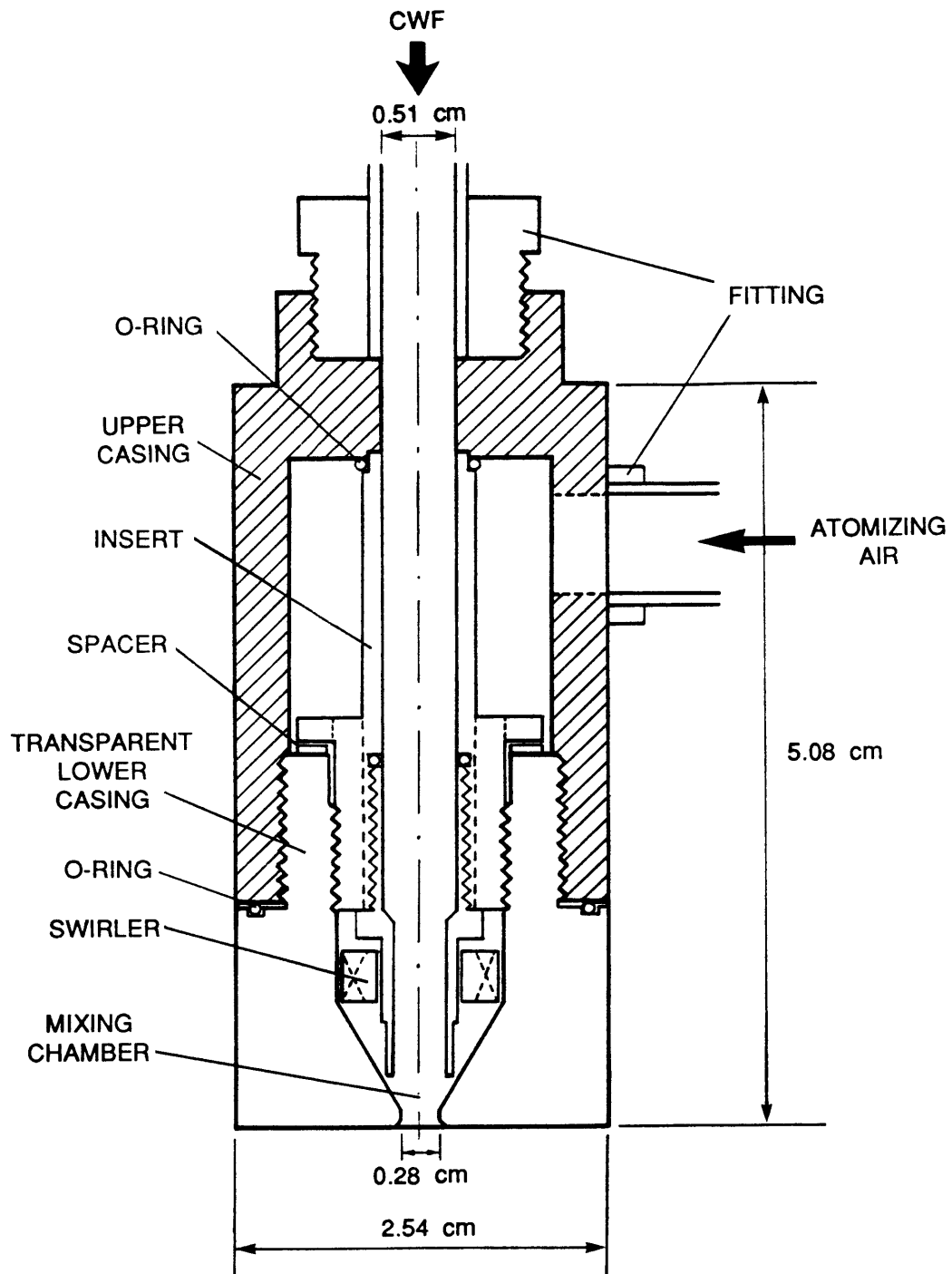
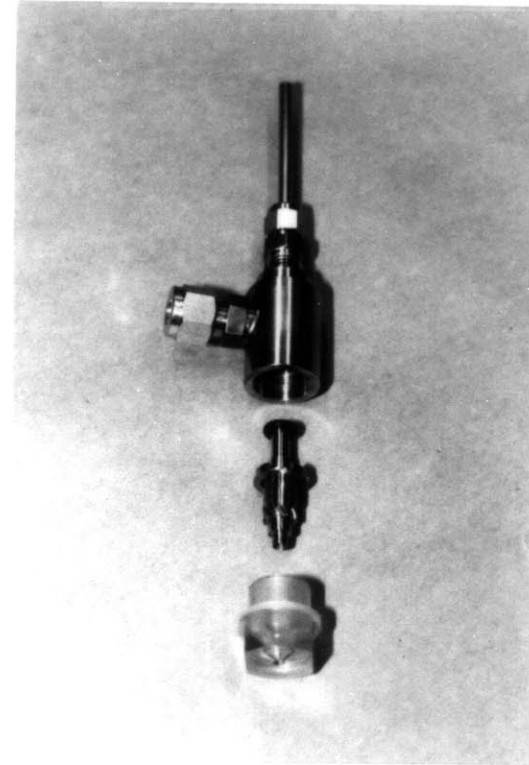


Figure 16. Schematic Diagram of Twin-Fluid Atomizer with Transparent Lower Casing



a



b

Figure 17. Photographs of Twin-Fluid Atomizer with Transparent Lower Casing  
(a) Assembled, (b) Disassembled

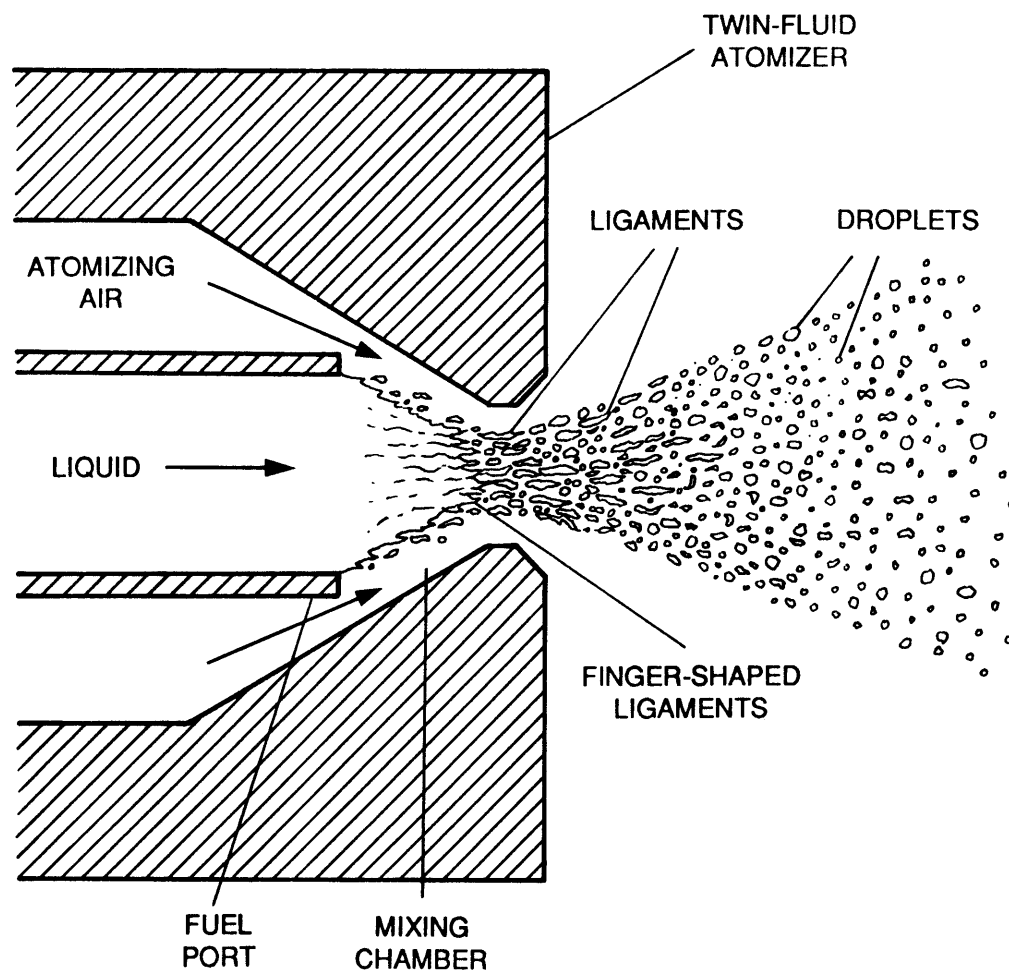


Figure 18. Atomization Mechanism in Twin-Fluid Atomizer



an accurate calculation of the continuously varying shear rate at the atomizing air/fuel interface is not possible because of the inadequate quantitative understanding of the physical process of twin-fluid atomization. Therefore, the representative shear rate during the atomization process needs to be defined in order to represent the actual continuously varying shear rate of atomized CWF.

The representative shear rate is expressed as a function of air velocity, liquid velocity, and characteristic dimension of the liquid jet in the mixing chamber and will be derived in eqs. (1) through (4) below. As mentioned in Section 3.2, during atomization, liquid fuel jet was contracted and most of the fuel broke up into ligaments, and large drops occurred in the mixing chamber by the disruptive action of the atomizing air. Figure 19 shows the control volume of contracted liquid jet in the mixing chamber of the atomizer.

The mass conservation equation and the momentum equation for the liquid jet in the mixing chamber of the atomizer (Figure 19) are expressed as

Mass Conservation Equation

$$\rho_L U_{L1} A_1 = \rho_L U_{L2} A_2 \quad \text{eq. (1)}$$

Momentum Equation

$$\frac{d}{dt} \int_{cv} \rho \vec{v} dV + \int_{cs} \rho \vec{v} (\vec{v} - \vec{v}_{cs}) \cdot \vec{n} dA = \vec{F}_{cv}(t) \quad \text{eq. (2)}$$

or, equivalently,

$$\rho_L U_{L2}^2 A_2 - \rho_L U_{L1}^2 A_1 = \Delta P A + \tau A_{side} \quad \text{eq. (3)}$$

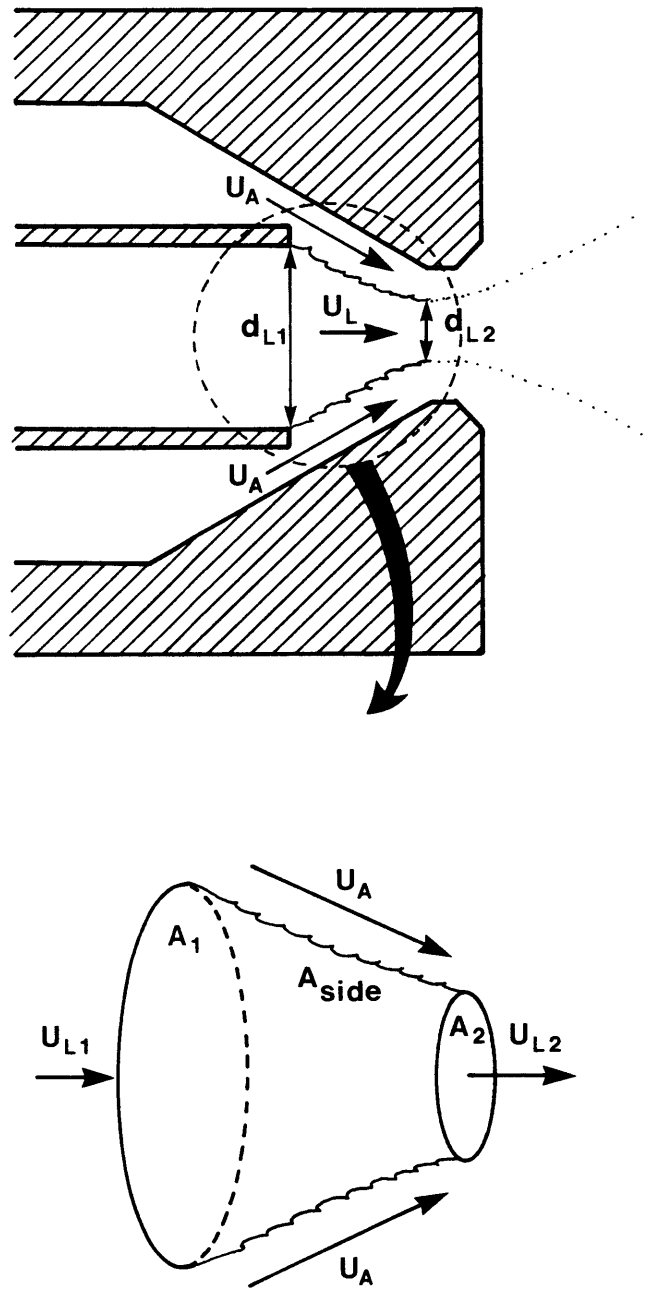


Figure 19. Control Volume of Contracted Liquid Jet in Mixing Chamber of Twin-Fluid Atomizer

where  $\rho_L$  = density of liquid

$U_{L1}$  = liquid velocity at position 1

$U_{L2}$  = liquid velocity at position 2

$A_1$  = cross-sectional area of liquid jet at position 1, given by

$$A_1 = \frac{\pi d_{L1}^2}{4}$$

$A_2$  = cross-sectional area of liquid jet at position 2, given by

$$A_2 = \frac{\pi d_{L2}^2}{4}$$

$A_{side}$  = side area of liquid jet between positions 1 and 2

$d_{L1}$  = diameter of fuel port

$d_{L2}$  = diameter of contracted liquid jet at position 2

$\tau$  = shear stress at the air/liquid interface

$\Delta P$  = pressure drop between positions 1 and 2, and assumed to be negligible

From eqs. (1) and (3), the diameter of contracted liquid jet ( $d_{L2}$ ) can be calculated.

The characteristic dimension for the representative shear rate is expressed as the average value of the contracted liquid jet radius and fuel port radius. The representative shear rate  $\partial u / \partial y$  during the atomization process is expressed as

$$\frac{\partial u}{\partial y} = \frac{U_A - U_L}{\frac{\left( \frac{d_{L1}}{2} + \frac{d_{L2}}{2} \right)}{2}} = \frac{4U_R}{d_{L1} + d_{L2}} \quad \text{eq. (4)}$$

where  $U_A$  = velocity of atomizing air in mixing chamber

$U_L$  = velocity of liquid jet in mixing chamber ( $\approx U_{L1} \approx U_{L2}$ )

$U_R$  = relative velocity between liquid jet and atomizing air

Hence, the representative shear rate, which is substituted for the actual continuously varying shear rate, can be obtained from eq. (4).

The representative shear rates for the OR-KVB atomizer (Figure 4), which was used in the present atomization study, for the air-to-fuel mass flow rate ratios (AFRs) of 0.1, 0.2, and 0.3 are calculated as  $2.0 \times 10^4$  to  $4.0 \times 10^4 \text{ sec}^{-1}$ ,  $3.0 \times 10^4$  to  $4.7 \times 10^4 \text{ sec}^{-1}$ , and  $4.0 \times 10^4$  to  $6.0 \times 10^4 \text{ sec}^{-1}$ , respectively.

#### 3.4 Experimental Results of Spray Droplet Size with CWF Viscosity

The CWF atomization characteristics were investigated for the OR-KVB twin-fluid atomizer at conditions typical in an industrial combustor. Six CWFs provided by commercial vendors were tested for measurements of spray droplet size, high shear viscosity, and surface tension. The specifications of CWFs are presented in Table 1. In the designation of CWF type, the letters A, B, C, and D refer to coal type, Reg, Fine, and U-Fine to the fineness of the coal in CWF (i.e., Regular-grind, Fine-grind, Ultra- Fine-grind), and the numbers 70, 69, 66, etc. to the weight percentage of solids loading.

The surface tensions of CWFs were measured by a Rosano Surface Tensiometer (Model LG-709827). The results of the surface tensions of CWFs are presented in Table 2. It is found that the surface tension of CWF varies little with coal particle size distribution, coal type, and chemical additive.

Table 1  
Specifications of CWFs for Atomization Study

CWF Type	Chemical Additive	Coal Type	Coal Particle MMD ( $\mu\text{m}$ )	Weight %* of Solids Loading (%)	Apparent** Viscosity (cp)
A-Regular	A	Splash Dam	19.2	70	250
A-Fine	A		7.9	69	200
B-Regular	B	Virginia Pocahontas	29.5	70	-
B-Fine	B		25.8	69	-
C-Regular	C	Splash Dam	24.3	70	-
D-Ultra-Fine	D	-	7.0	56	76

\*As received

\*\*Haake RV-12

Viscometer, Measured at shear rate of  $150 \text{ sec}^{-1}$

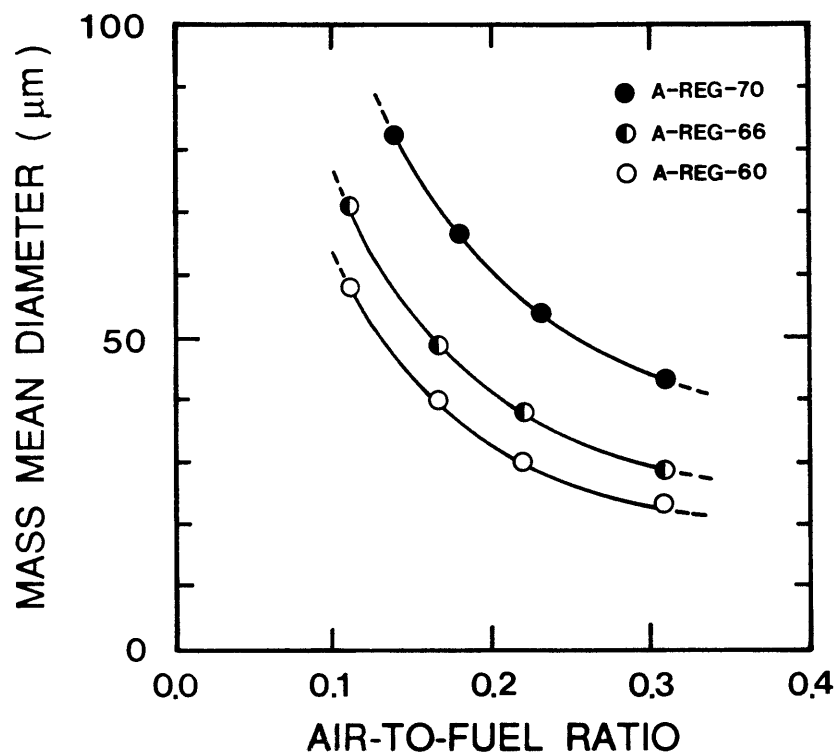
Table 2  
Surface Tensions of CWFs

CWF Type	Surface Tension (dyne/cm)
A-Regular	51.3
A-Fine	-
B-Regular	50.2
B-Fine	49.3
C-Regular	51.7
D-Ultra-Fine	50.8

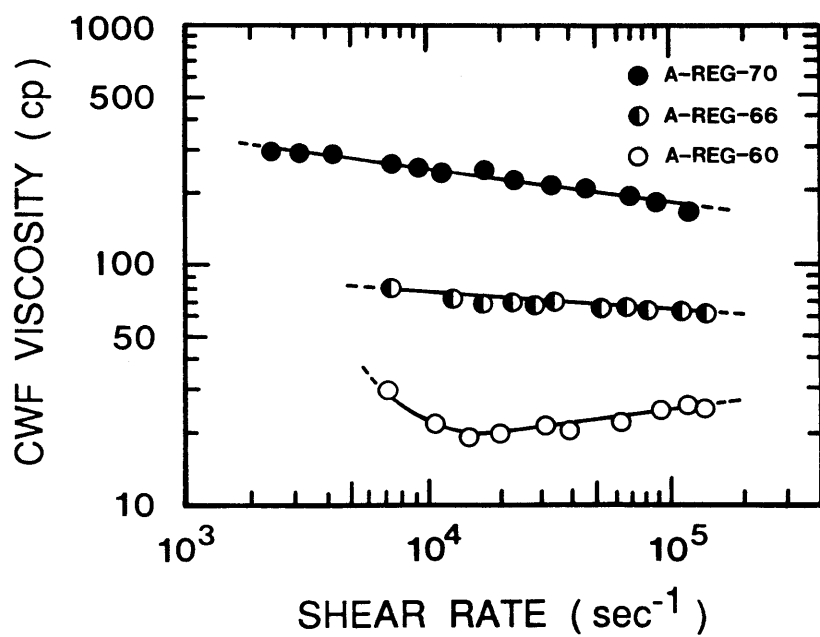
Each CWF viscosity, measured by the capillary tube viscometer, is plotted in Figures 20-b through 24-b as a function of shear rate in the range of  $10^3$  to  $10^5$   $\text{sec}^{-1}$ . These results<sup>(18,19)</sup> show that CWF viscosity is strongly dependent on shear rates (non-Newtonian characteristics of CWF viscosity). Solids loading (dilution), coal particle size distribution, and chemical additive all influence CWF viscosity. Dilution of CWF with water, in general, reduces the viscosity (Figure 20-b), but some CWFs show reverse trends at certain shear rates (Figure 21-b). One of the CWFs, A-Fine-69, is shear thinning at low shear rates, but as the shear rate increases above  $5 \times 10^4$   $\text{sec}^{-1}$ , it suddenly becomes shear thickening (Figure 22-b).

Each mass mean diameter (MMD) of CWF spray, measured by using the laser diffraction spray analyzer, is shown in Figures 20-a through 24-a plotted as a function of the atomizing air-to-fuel mass flow rate ratio (AFR). Since the fuel flow rate is maintained at 2.7 kg/min during the experiments, as AFR increases, the atomizing air flow rate increases, and therefore, the shear rate also increases. In general, as shown in Figures 20-a through 24-a, MMDs decrease with increasing AFR.

The spray droplet size does not, however, always decrease with increasing AFR (see B-Fine-69 in Figure 21-a). The leveling off of the reduction in MMD in the AFR range of 0.2 to 0.3 is consistent with the increasing viscosity of this CWF in the corresponding shear rate range of  $3 \times 10^4$  to  $5 \times 10^4$   $\text{sec}^{-1}$ . In Figure 22-a, MMDs of the A-Fine-69 are found to decrease with increasing AFR up to the AFR of 0.25, but MMD increases beyond this value of AFR because of the increasing viscosity of the fuel. Figure 20-a shows the effect of CWF dilution on MMD of CWF



a



b

Figure 20. Effect of Dilution on MMD and Viscosity of CWF (A-Reg)  
 (a) MMD versus AFR, (b) CWF Viscosity versus Shear Rate

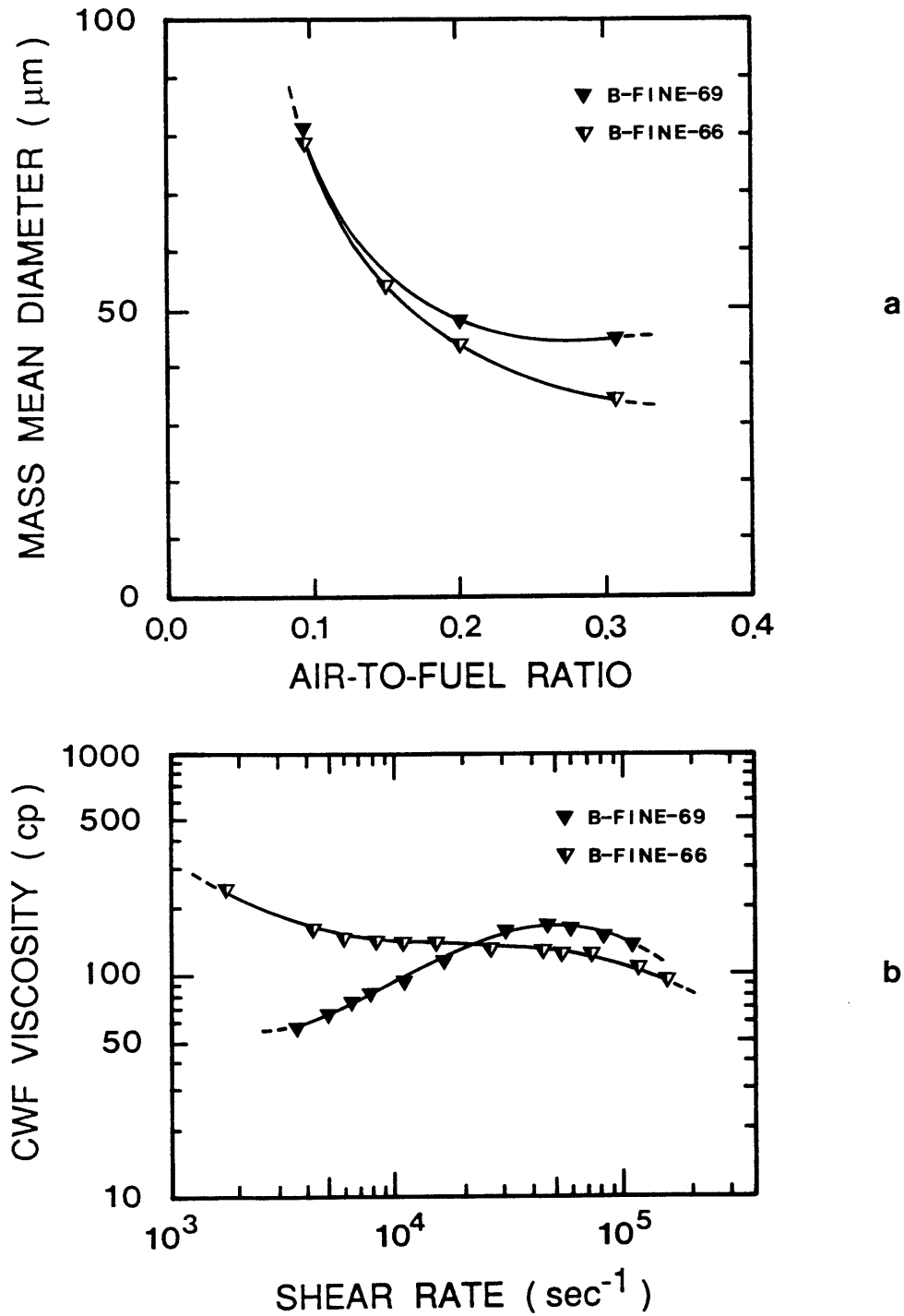
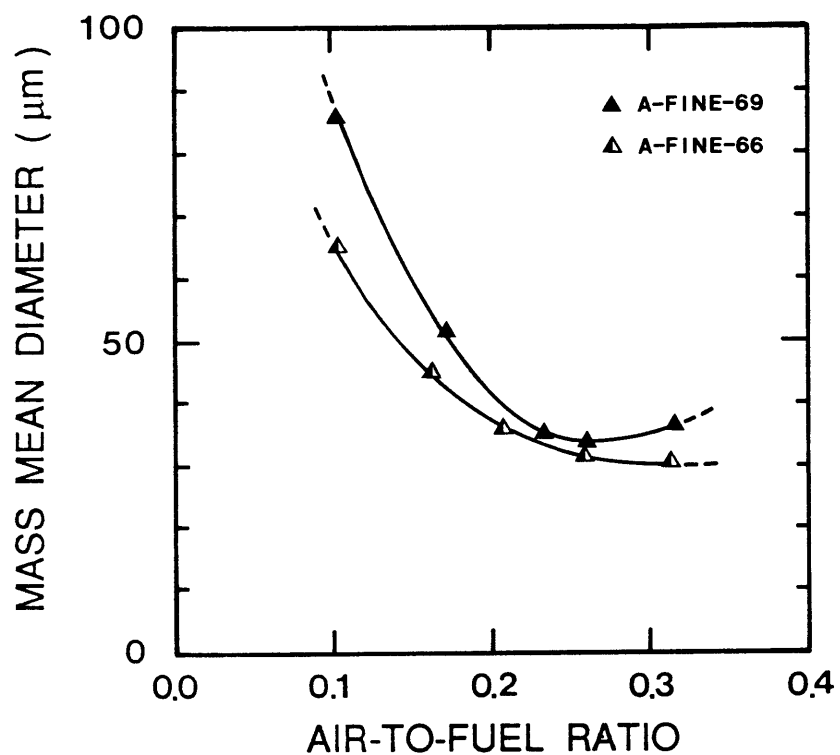
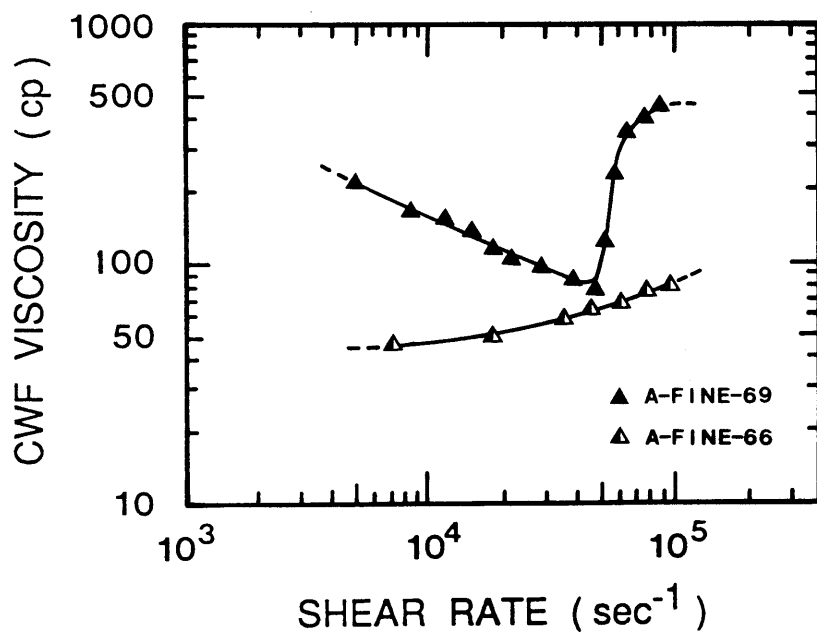


Figure 21. Effect of Dilution on MMD and Viscosity of CWF (B-Fine)  
 (a) MMD versus AFR, (b) CWF Viscosity versus Shear Rate



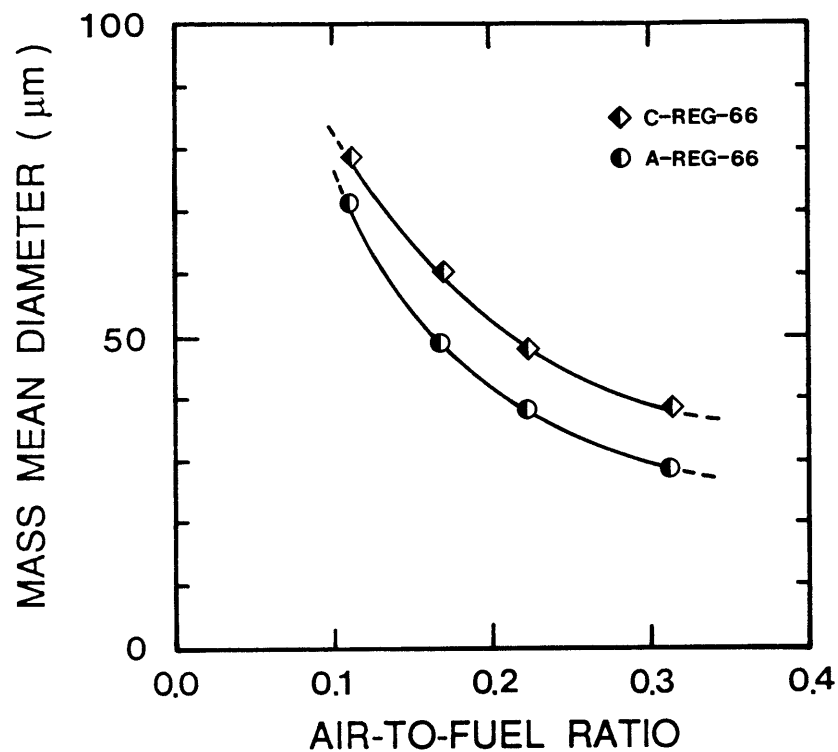


a

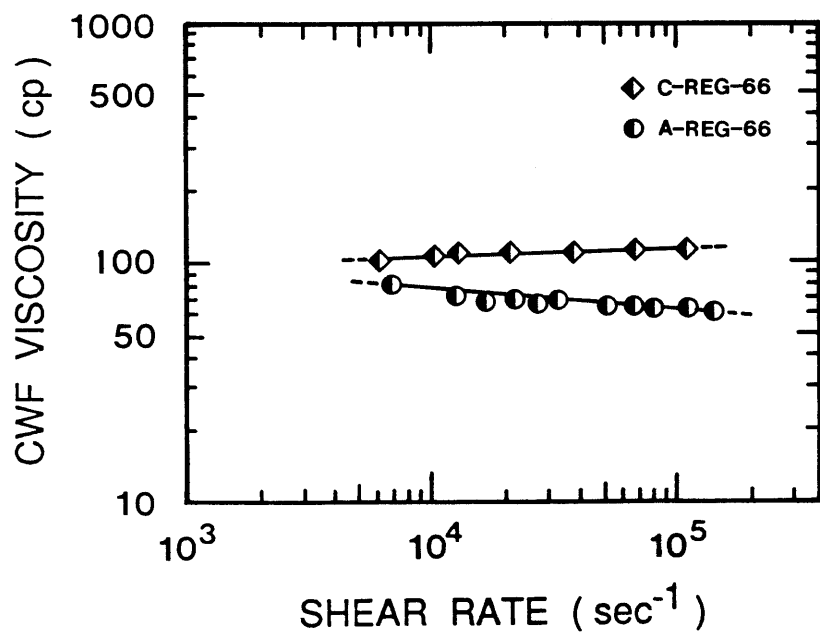


b

Figure 22. Effect of Dilution on MMD and Viscosity of CWF (A-Fine)  
 (a) MMD versus AFR, (b) CWF Viscosity versus Shear Rate



a



b

Figure 23. Effect of Chemical Additive on MMD and Viscosity of CWFs (A-Reg & C-Reg)  
 (a) MMD versus AFR, (b) CWF Viscosity versus Shear Rate

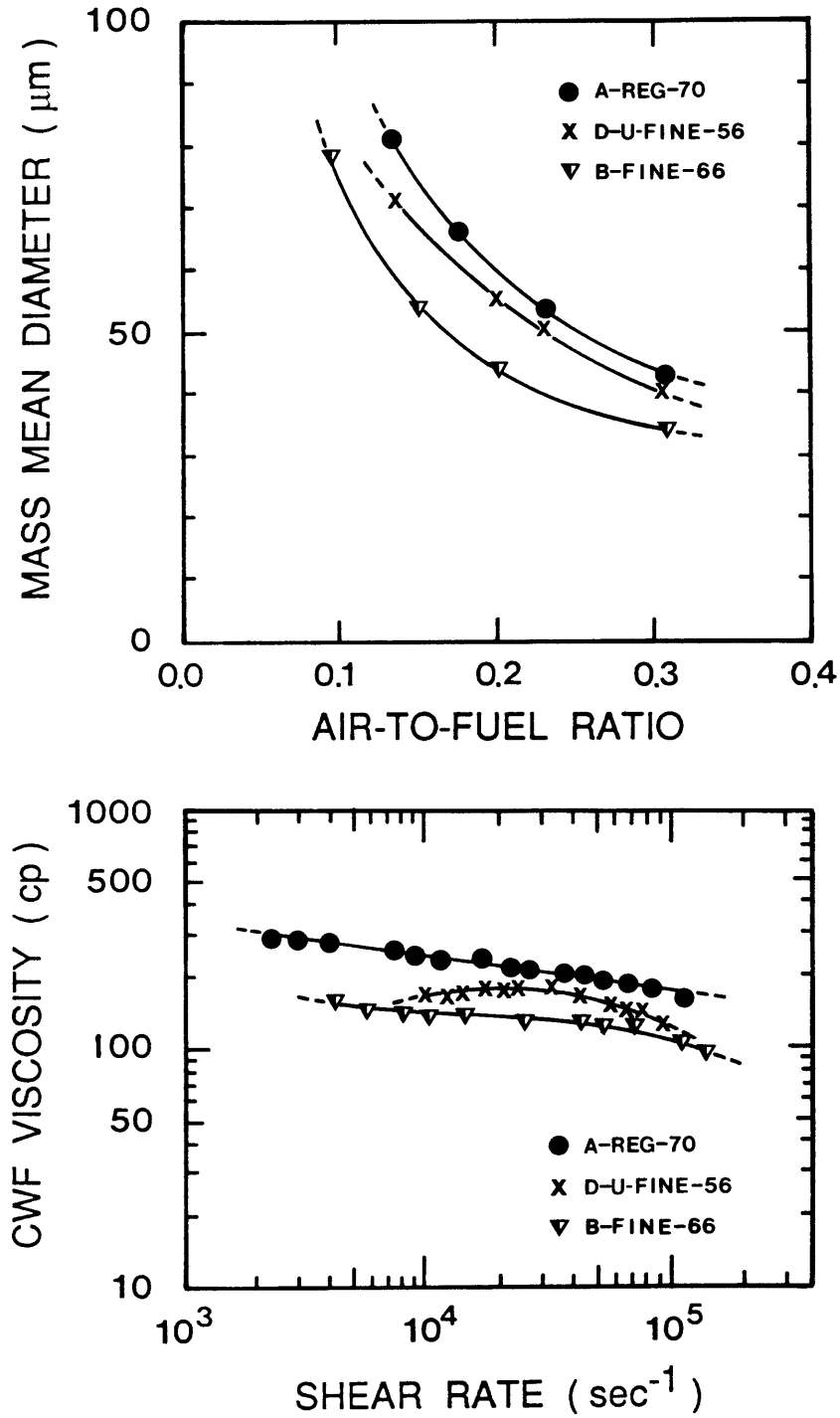


Figure 24. Effect of Coal Particle Size Distribution on MMD and Viscosity of CWFs (A-Reg, B-Fine, & D-U-Fine)  
 (a) MMD versus AFR, (b) CWF Viscosity versus Shear Rate

spray. The MMDs decrease with increasing dilution due to the decrease in CWF viscosity as shown in Figure 20-b. Figure 23 shows the effect of chemical additives (A and C) on MMD and viscosity of CWF. It is found that the chemical additives affect the viscosity, and correspondingly, the MMD of CWF.

The effect of coal particle size distribution on MMD and CWF viscosity is shown in Figure 24. In the shear rate range of  $10^4$  to  $10^5$   $\text{sec}^{-1}$ , the viscosity of A-Reg-70 CWF is the highest and that of B-Fine-66 is the lowest. This means that the coal particle size distribution influences MMD by changing the viscosity of CWF.

The viscosity at low shear rate was measured by the commercial viscometer (HAAKE RV-12) to check the consistency of viscosities at the middle range of shear rate ( $10^3$  to  $10^4$   $\text{sec}^{-1}$ ), and presented in Figures 25 and 26. These figures show that the viscosities measured by the capillary tube viscometer and the commercial viscometer (HAAKE RV-12) match reasonably well in the shear rate range of  $10^3$  to  $10^4$   $\text{sec}^{-1}$ .

Figures 21, 22, 24, and 25 show the evidences that the representative shear rates, calculated by eq. (4) in Section 3.3, closely agree with the actual shear rates during the atomization process. Therefore, it is concluded that air-to-fuel ratios (AFRs) in the range of 0.1 to 0.3 for the OR-KVB atomizer correspond to the representative shear rates in the range of  $2 \times 10^4$  to  $6 \times 10^4$   $\text{sec}^{-1}$ .

The significance of the use of high shear rate viscosities is borne out also by data in Figures 24 and 25. Reliance on low shear rate (less than  $10^4$   $\text{sec}^{-1}$ ) viscosities would lead to the wrong order in the fineness of atomized droplet sizes of the three CWFs tested, but when the correct

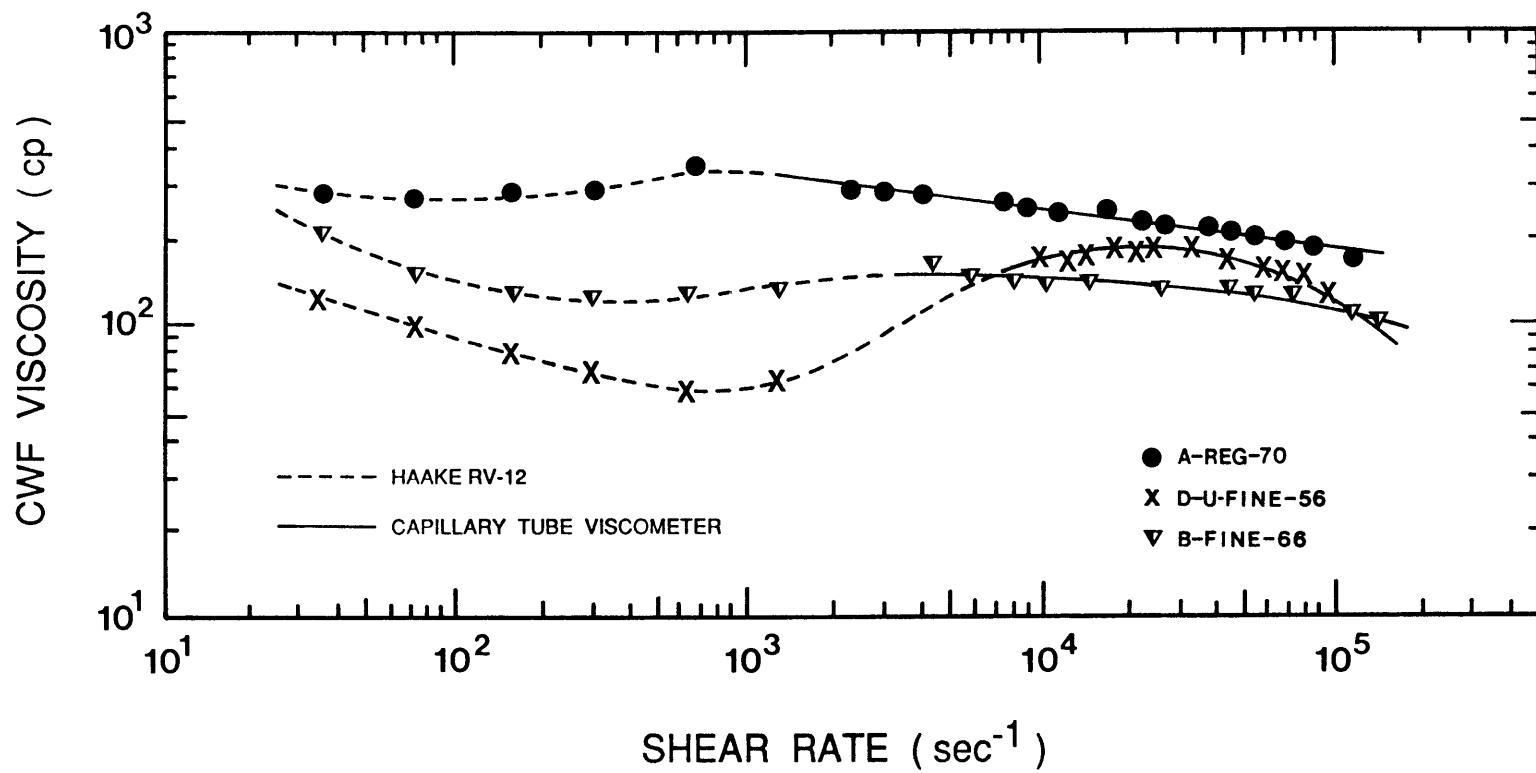


Figure 25. Effect of Coal Particle Size Distribution in CWF on CWF Viscosity at Low and High Shear Rates

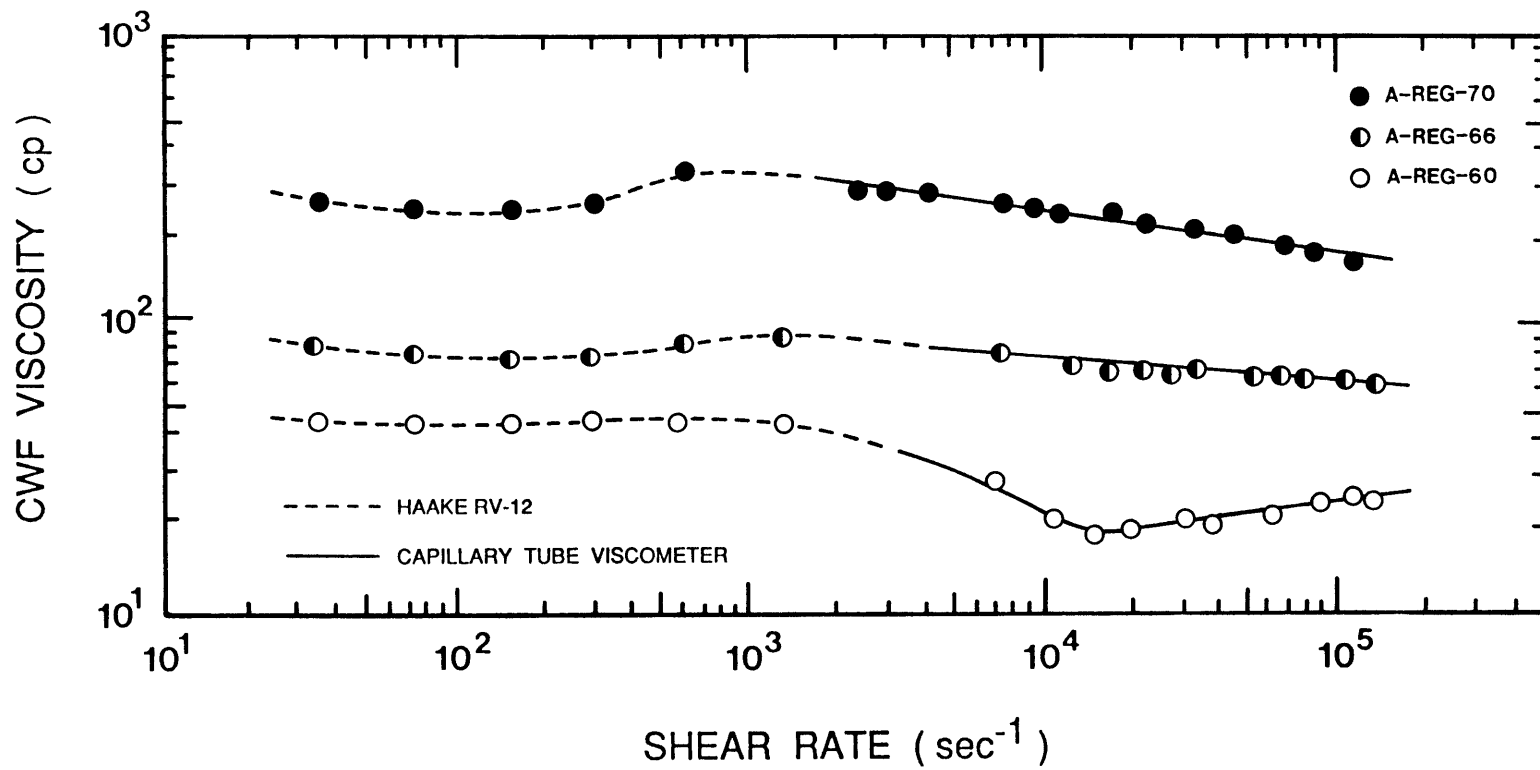


Figure 26. Effect of Dilution on CWF Viscosity at Low and High Shear Rates

values of the viscosities (at high shear rate in the range of  $2 \times 10^4$  to  $6 \times 10^4 \text{ sec}^{-1}$ ) are used, the droplet sizes and viscosities of the three CWFs appear in the same order (Figures 24 and 25).

### 3.5 Correlation of CWF Atomization

The spray's average droplet size data (Mass Mean Diameters) are correlated with the characteristic dimension of the atomizer, the air-to-fuel ratio (AFR), the relative velocity between atomizing air and CWF, and the properties of atomizing air and CWF. The basic form of the atomization correlation will be discussed in Section 3.5.1, and the atomization correlation for the OR-KVB atomizer will be established in Section 3.5.2.

#### 3.5.1 Basic Form of Atomization Correlation

Miesse<sup>(20)</sup> proposed that the atomization phenomena of liquid streams could be sufficiently described by two independent dimensionless groups: the Reynolds number (Re) and the Weber number (We). Miesse also found that the use of the Z number (or the Ohnesorge number<sup>(21)</sup>) could facilitate correlation of the experimental data.

In the case of liquid-jet disintegration due to the influence of the surrounding air, the droplet sizes obtained are governed by the ratio of the disruptive aerodynamic force  $\rho_A U_R^2$  to the consolidating surface tension force  $\sigma_L/D_o$ . This dimensionless ratio is known as the Weber number We, and expressed as

$$We = \frac{\rho_A U_R^2 D_o}{\sigma_L}$$

where  $\rho_A$  = density of surrounding air

$U_R$  = relative velocity between liquid jet and surrounding air

$D_o$  = diameter of liquid jet

$\sigma_L$  = surface tension of liquid

In the case of liquid jet breakup occurring without the influence of the surrounding air, dimensional analysis suggests that the atomization quality is dependent on the jet diameter  $D_o$  and the liquid properties: density  $\rho_L$ , surface tension  $\sigma_L$ , and viscosity  $\mu_L$ . The breakup mechanism is found to depend on the Z number, which is obtained as the ratio of the square root of the Weber number to the Reynolds number; that is,

$$Z = \frac{We^{0.5}}{Re} = \frac{\mu_L}{\sqrt{\sigma_L \rho_L D_o}}$$

According to Lefebvre<sup>(7)</sup>, the main factors governing the average droplet size of liquids of low viscosity are liquid surface tension, air density, and air velocity; for liquids of high viscosity, the effects of air properties are less significant, and the average droplet size becomes more dependent on the liquid properties, especially viscosity.

In the present study, the atomization correlation uses the Weber number  $We$  and the Z number, as follows:

$$\begin{aligned} \frac{MMD}{D_o} &= \frac{MMD_1}{D_o} + \frac{MMD_2}{D_o} \\ &= a (We)^b \left(1 + \frac{1}{AFR}\right)^c + d \left(\frac{We}{Re^2}\right)^e \left(1 + \frac{1}{AFR}\right)^f \end{aligned} \quad \text{eq. (5)}$$

where  $MMD$  = mass mean diameter of atomized CWF droplets



$D_o$  = characteristic dimension of the atomizer, defined as the diameter of fuel port

AFR = air-to-fuel mass flow rate ratio

a,b,c,d,e,f = empirical constants, determined by experimental data

The two terms in the right-hand side of eq. (5) correspond to two different mechanisms for liquid jet breakup: jet disintegration due to the influence of the surrounding air and jet breakup occurring without the influence of the surrounding air. That is, the first term represents the competition between jet-consolidating surface tension force and aerodynamic shearing force, which leads to jet destruction. The second term accounts for the competition between viscous restoring force and surface tension force, which leads to jet breakup in the absence of surrounding air effects.

The basic form of correlation [eq. (5)] can also be expressed as

$$\frac{MMD}{D_o} = a \left( \frac{\sigma_L}{\rho_A U_R^2 D_o} \right)^{-b} \left( 1 + \frac{1}{AFR} \right)^c + d \left( \frac{\mu_L^2}{\rho_L \sigma_L D_o} \right)^e \left( 1 + \frac{1}{AFR} \right)^f \quad \text{eq. (6)}$$

During the atomization tests, the surface tension  $\sigma_L$  and density  $\rho_L$  of the liquid varied little among the CWFs tested, and the fuel port diameter  $D_o$  was fixed at 3.8 mm.

### 3.5.2 Atomization Correlation for OR-KVB Atomizer

The MMDs of the atomized droplets for six CWFs are plotted as a function of high shear viscosity for the AFRs of 0.1, 0.15, 0.2, 0.25, and 0.3 in Figures 27 and 28. It can be seen that a linear relationship between MMD and CWF viscosity exists. This relationship implies that the

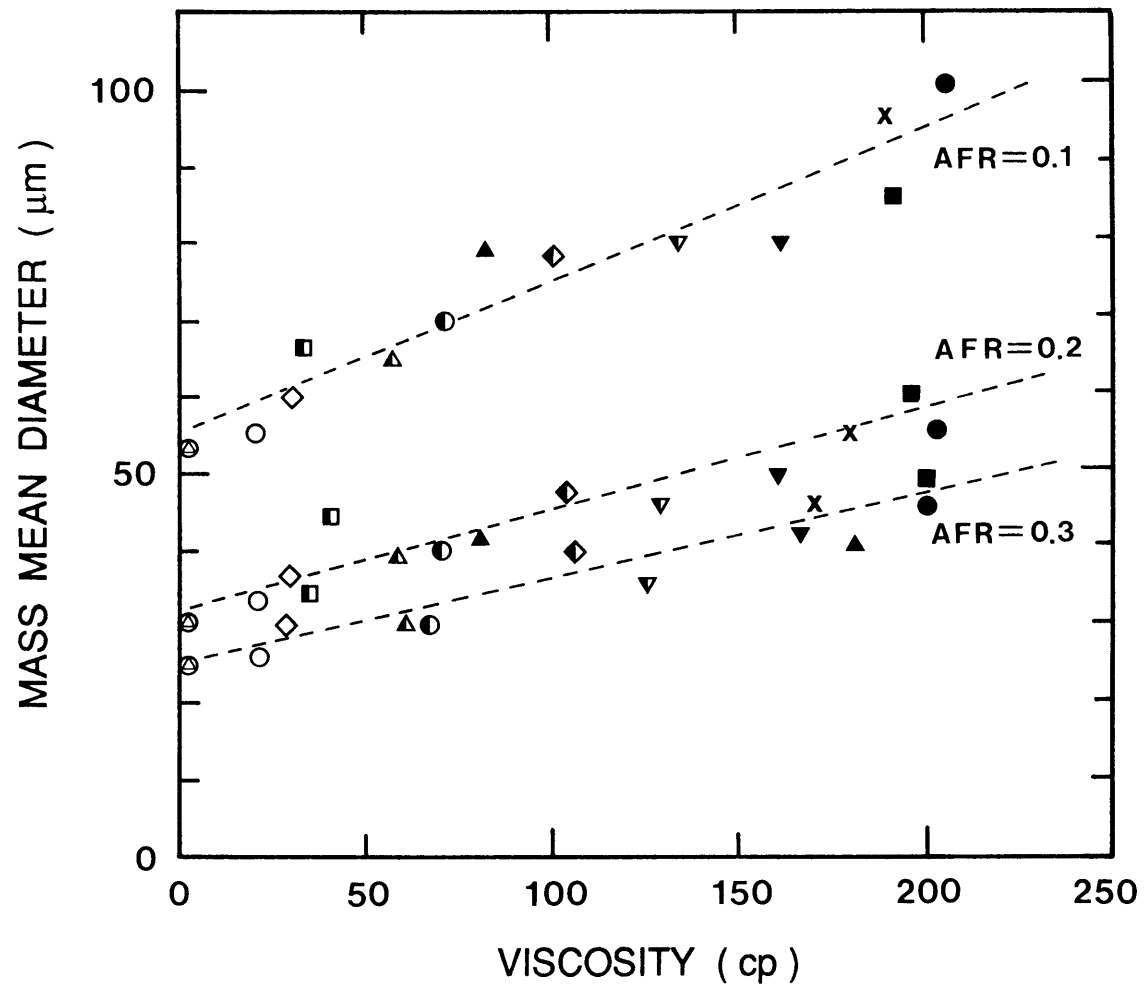


Figure 27. Mass Mean Diameter of Spray Droplets of Various CWFs versus CWF Viscosity for AFRs = 0.1, 0.2, & 0.3

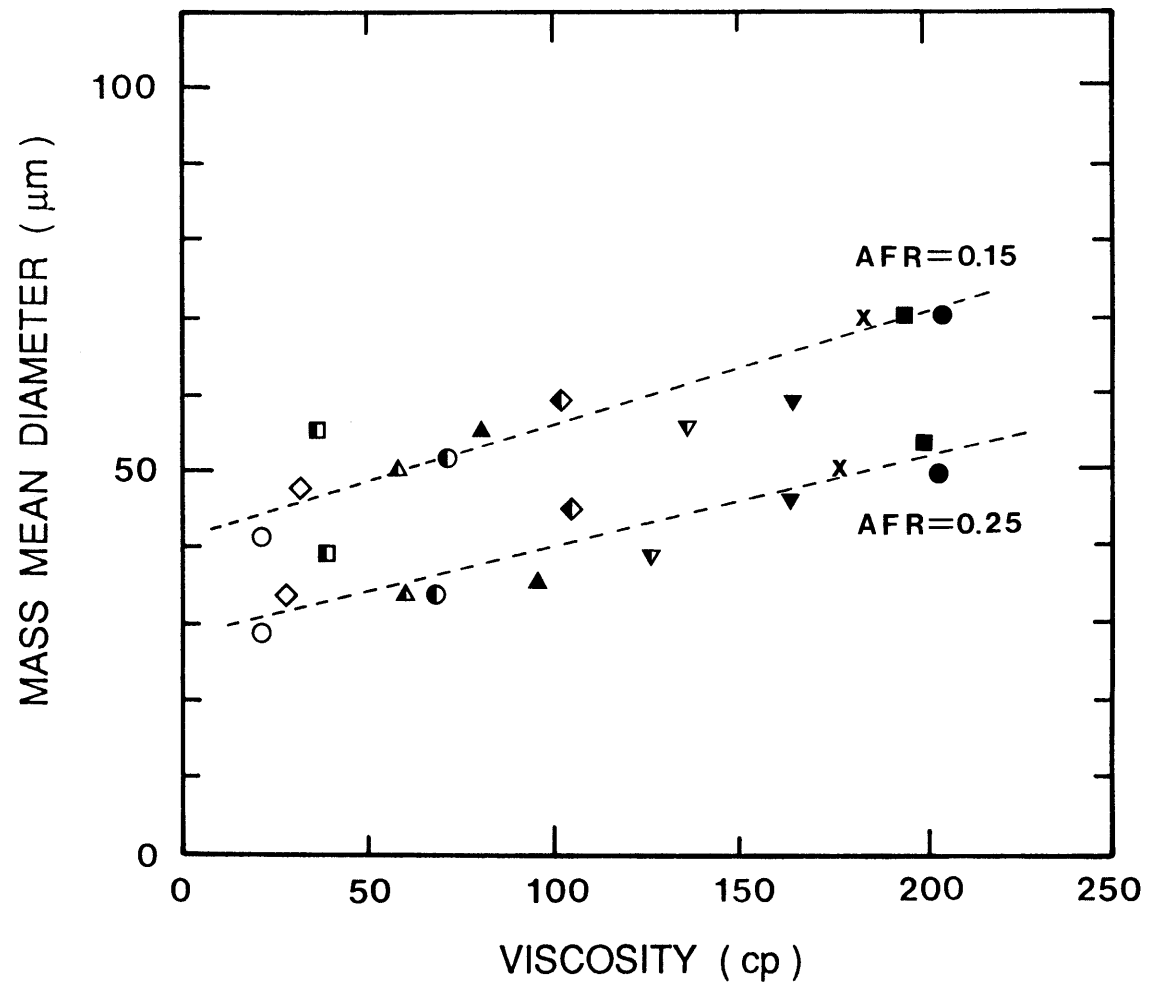


Figure 28. Mass Mean Diameter of Spray Droplets of Various CWFs versus CWF Viscosity for AFRs = 0.15 & 0.25

empirical constant 'e' in eq. (6) has the value of 0.5, which makes the exponent of the viscosity  $\mu_L$  one.

Figures 29 and 30 show the variation of MMD with  $(1 + 1/AFR)$  for various CWFs and also show that MMD decreases with increasing AFR.

The CWF atomization data were substituted into eq. (6) to determine the empirical constants a through f. Finally, the dimensionally correct equation for  $MMD/D_o$  is expressed as

$$\frac{MMD}{D_o} = 0.0263 \left( \frac{\sigma_L}{\rho_A U_R^2 D_o} \right)^{0.25} \left( 1 + \frac{1}{AFR} \right)^{0.5} + 0.0050 \left( \frac{\mu_L^2}{\rho_L \sigma_L D_o} \right)^{0.5} \left( 1 + \frac{1}{AFR} \right)^{0.75} \quad \text{eq. (7)}$$

where the unit of MMD: m

$D_o$ : m

$\sigma_L$ : kg/sec<sup>2</sup>

$\rho_A$ : kg/m<sup>3</sup>

$\rho_L$ : kg/m<sup>3</sup>

$U_R$ : m/sec

$\mu_L$ : kg/m·sec

The viscosity term in eq. (7) is replaced with the power law expression to account for the non-Newtonian rheology of CWF as follows:

$$\mu = K \dot{\gamma}^{n-1} \quad \text{eq. (8)}$$

where K  $\equiv$  consistency index

n  $\equiv$  flow behavior index

$\dot{\gamma}$   $\equiv$  shear rate

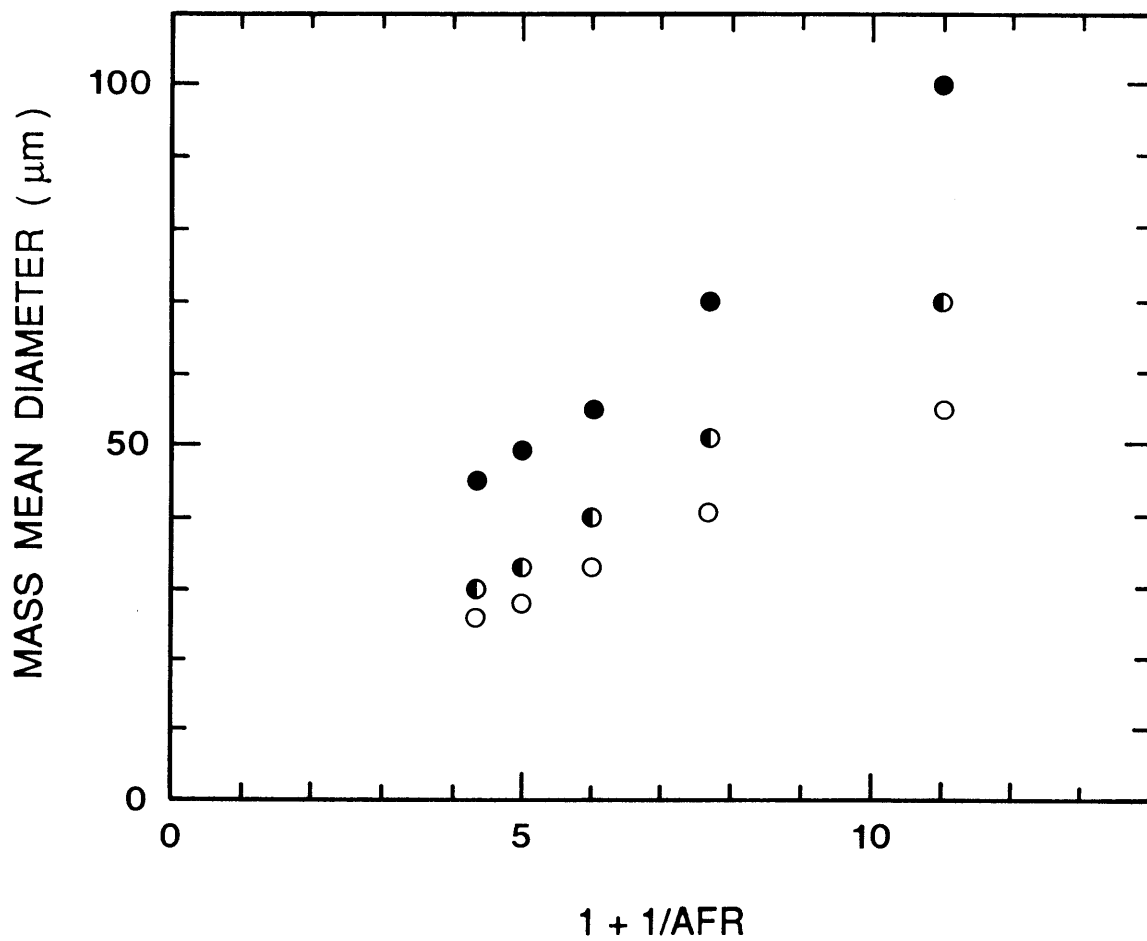


Figure 29. Mass Mean Diameter of Spray Droplets versus  $(1 + 1/AFR)$  for A-Reg-70, 66, & 60 CWFs

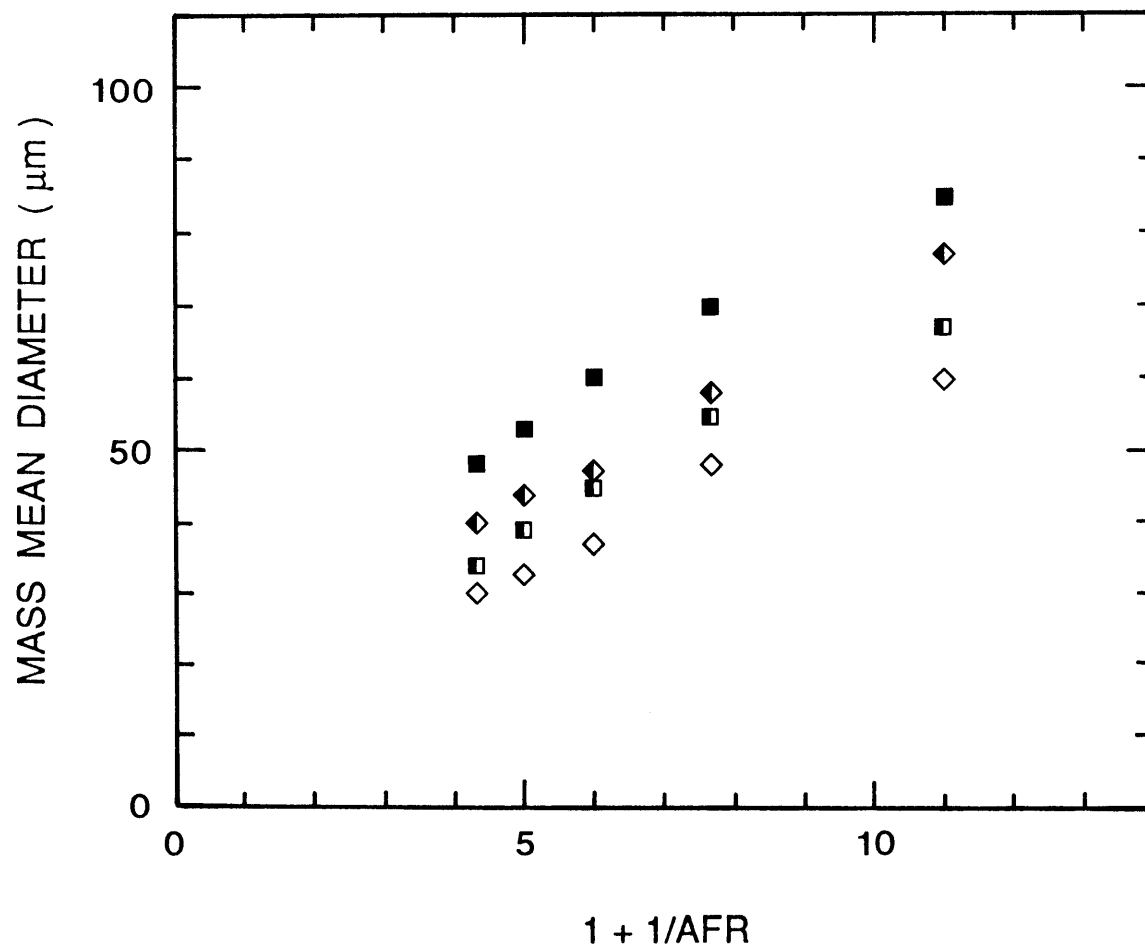


Figure 30. Mass Mean Diameter of Spray Droplets versus  $(1 + 1/\text{AFR})$  for B-Reg-70 & 66 and C-Reg-66 & 60 CWFs

From eqs. (7) and (8), the CWF atomization correlation for the OR-KVB atomizer is established as

$$\frac{\text{MMD}}{D_o} = 0.0263 \left( \frac{\sigma_L}{\rho_A U_R^2 D_o} \right)^{0.25} \left( 1 + \frac{1}{\text{AFR}} \right)^{0.5} + 0.0050 \left( \frac{(K\dot{\gamma}^{n-1})^2}{\rho_L \sigma_L D_o} \right)^{0.5} \left( 1 + \frac{1}{\text{AFR}} \right)^{0.75} \quad \text{eq. (9)}$$

The comparison of the measured MMDs with the calculated MMDs, using eq. (9), is illustrated in Figure 31. The correlation [eq. (9)] of CWF atomization for the OR-KVB atomizer is found to closely agree with experimental results if the high shear viscosity (i.e., viscosity which were obtained at the representative shear rate of the present study) of the CWF was substituted into eq. (9). The comparisons of measured MMDs, calculated MMDs which were calculated with the viscosities at a low shear rate of  $100 \text{ sec}^{-1}$  (i.e., viscosities which most of the other researchers used), and calculated MMDs which were calculated with the viscosities at a high shear rate are shown in Figure 32. It illustrates the sensitivity of the above atomization correlation to the use of the correct value of the CWF viscosity (i.e., CWF viscosity at a high shear rate).

### 3.6 Summary

The atomization study of CWF was undertaken to understand the effect of the high shear viscosity on CWF atomization. The high shear viscosity was measured by using the capillary tube viscometer. The mean droplet size of the CWF spray was measured at various relative atomizing air/CWF

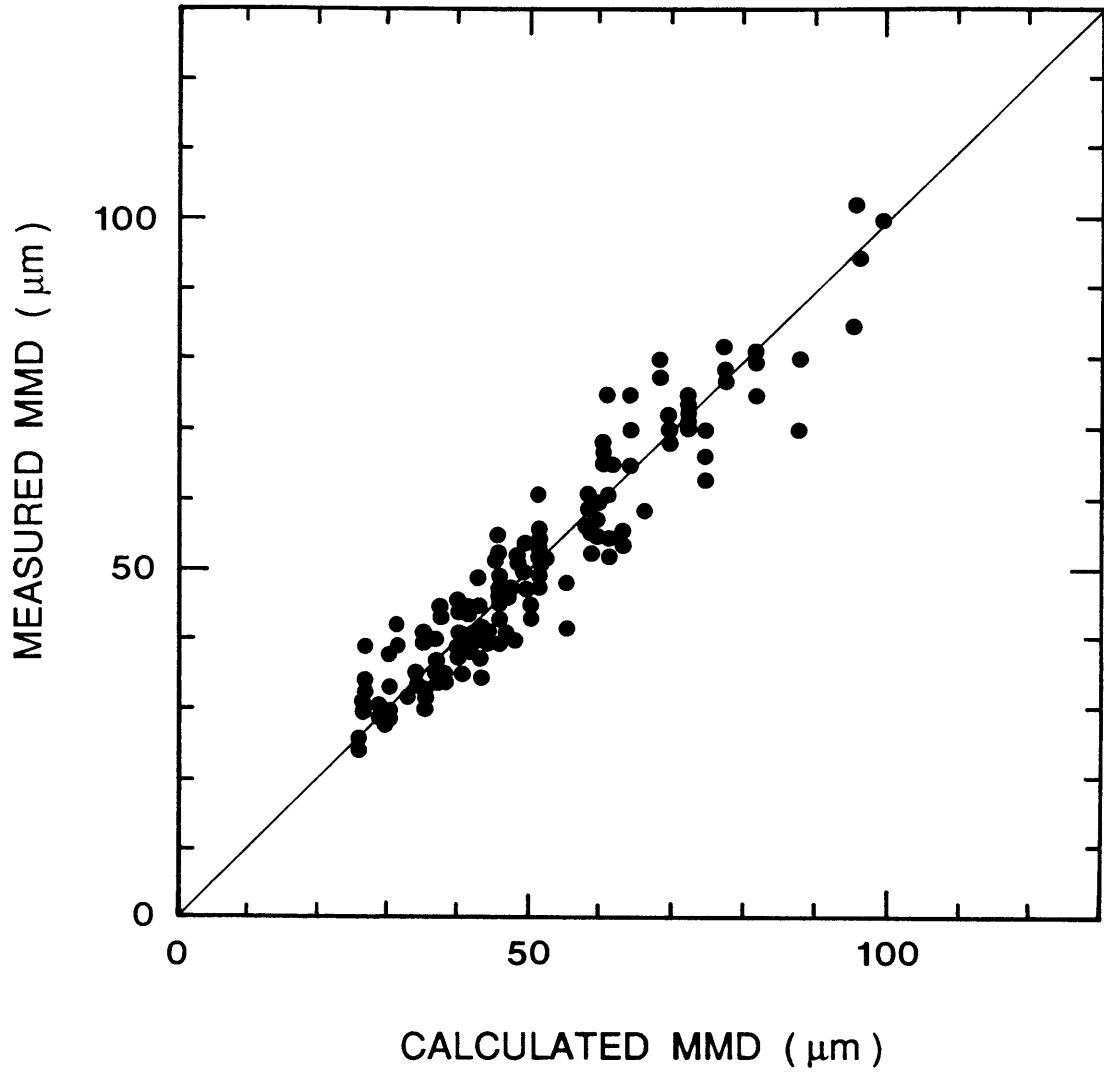


Figure 31. Comparison of Measured MMDs with Calculated MMDs



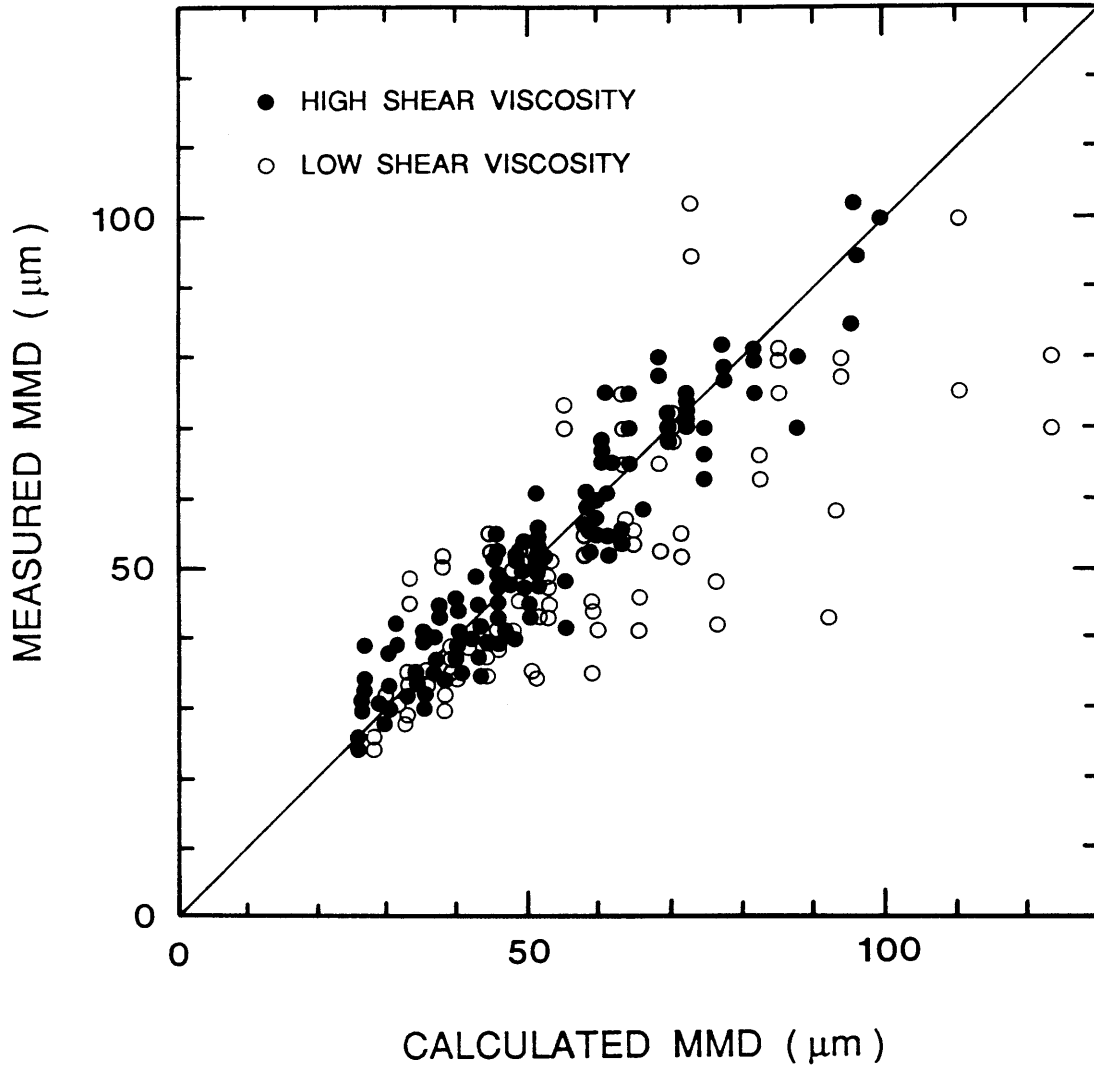


Figure 32. Comparisons of Measured MMDs with Calculated MMDs for Low Shear Viscosities and for High Shear Viscosities

velocities in the Spray Test Facility by using the laser diffraction spray analyzer.

Solids-loadings, coal particle size distributions, and chemical additives, by which CWF fuel types are often characterized, are found to have little influence on the surface tension of CWF, but a strong influence on non-Newtonian viscosity of CWF. Experimental data show that not only the atomizing air-to-fuel ratio (AFR), but also the variation of viscosity at a high shear rate, have an important effect in determining the mass mean diameter of the CWF spray. Approximate calculations of the representative shear rate for the OR-KVB atomizer give values in the range of  $2 \times 10^4$  to  $6 \times 10^4 \text{ sec}^{-1}$ . Finally, the study established the atomization correlation of mean droplet sizes (MMD) with the properties and flow parameters of CWF and atomizing air.

## CHAPTER 4

## FLASH-ATOMIZATION STUDY OF CWF

4.1 Introduction

In the CWF-fired boilers, the convective tube bank erosion could be reduced if the fly-ash particles were sufficiently small, such particles would follow the gas streamlines around tubes rather than impact on them. If finer coal particle size distribution (p.s.d.) in the CWF could permit use of smaller atomizer orifices, this might lead to finer fly-ash p.s.d. via improved atomization, with the fineness of atomization being related to the orifice dimensions of the atomizer. Unfortunately, this approach would yield reduced life of atomizer orifice because of increased erosion. Furthermore, finer coal p.s.d. in CWF leads to increased CWF viscosity for a given CWF solids loading, and this, in turn, may lead to coarser atomization, unless the CWF viscosity is reduced by means of an additive or by diluting CWF with water.

An alternative route to finer p.s.d. of CWF droplets and of the fly-ash is the use of fuel treatments to induce flash-atomization. The atomizer would deliver as fine a spray as readily achievable, but fuel treatments would cause further disintegration of the atomized CWF droplets, yielding finer CWF droplet p.s.d. for combustion.

In the following sections, the theoretical models of CWF atomization will be made and the experimental results of CWF flash-atomization will be discussed.

## 4.2 Theoretical Models of CWF Flash-Atomization

### 4.2.1 Nucleation Sites in Coal Particle during CWF Flash-Atomization

Bubble growth has two separate processes: i) the formation of bubbles (nucleation) and ii) the subsequent growth. Three types of different idealized conditions of nucleation can be considered<sup>(22)</sup>.

- (1) Pure liquid; no suspended foreign matter.
- (2) Liquid with suspended sub-microscopic non-wettable material that contains permanent gas pockets from which bubble nuclei emerge on volume heating.
- (3) Surface with cavities containing gas and/or vapor.

In general, nucleation will occur first at solid surfaces<sup>(23)</sup>.

CWF consists of micronized coal particles, water, and a small fraction of chemical additive. During flash-atomization of CWF, bubbles form and grow in the interstitial water of CWF. The possible nucleation sites can include: macropores and micropores of coal particles (heterogeneous nucleation), micropores of suspended submicroscopic coal particles in the interstitial water (heterogeneous nucleation), and interstitial water itself (homogeneous nucleation). However, heterogeneous nucleation is much more likely to occur compared to homogeneous nucleation<sup>(23)</sup>. Therefore, vapor bubble formation (nucleation) will mainly take place both at the pores of coal particles and of suspended submicroscopic coal particles during CWF flash-atomization.

#### 4.2.2 Mechanism of CWF Flash-Atomization

When CWF is heated up at high pressure (say 150°C at 690 kPa) and discharged to atmosphere through an atomizer, flash-atomization will occur in the atomized CWF droplets and/or ligaments. As discussed in Section 4.2.1, the most probable nucleation sites will be macropores and micropores of coal particles and micropores of suspended submicroscopic coal particles.

When the heated CWF undergoes sudden pressure drop, the air pocket in an active nucleation pore grows by evaporation at the liquid/vapor interface. As evaporation at the liquid/vapor interface continues, air and/or vapor bubble in the active nucleation pore will grow continuously. The total volume of rapidly growing bubbles will take up an increasing part of the total CWF droplet volume. As the radius of growing bubbles reaches a critical size, bubble growth may be restricted through mutual interference.

In this study, flash-atomization is assumed to occur when the growing bubbles in the interstitial water of CWF form a close-pack spherical array just touching each other, at which time they will coalesce into a big vapor region. Figures 33 and 34 show the sequential process of flash-atomization of the atomized CWF droplet and/or ligament. Figure 33 shows flash-atomization at the gap between each coal particle. The entrapped air pocket in the active nucleation pore grows from the bottom of the pore to the top of the pore, and forms a hemispherical bubble at the mouth of the pore (Figure 33-a). The vapor bubbles grow (Figure 33-b), until bubble growth is restricted through mutual interference (Figure 33-c). As the growing bubbles touch each other,

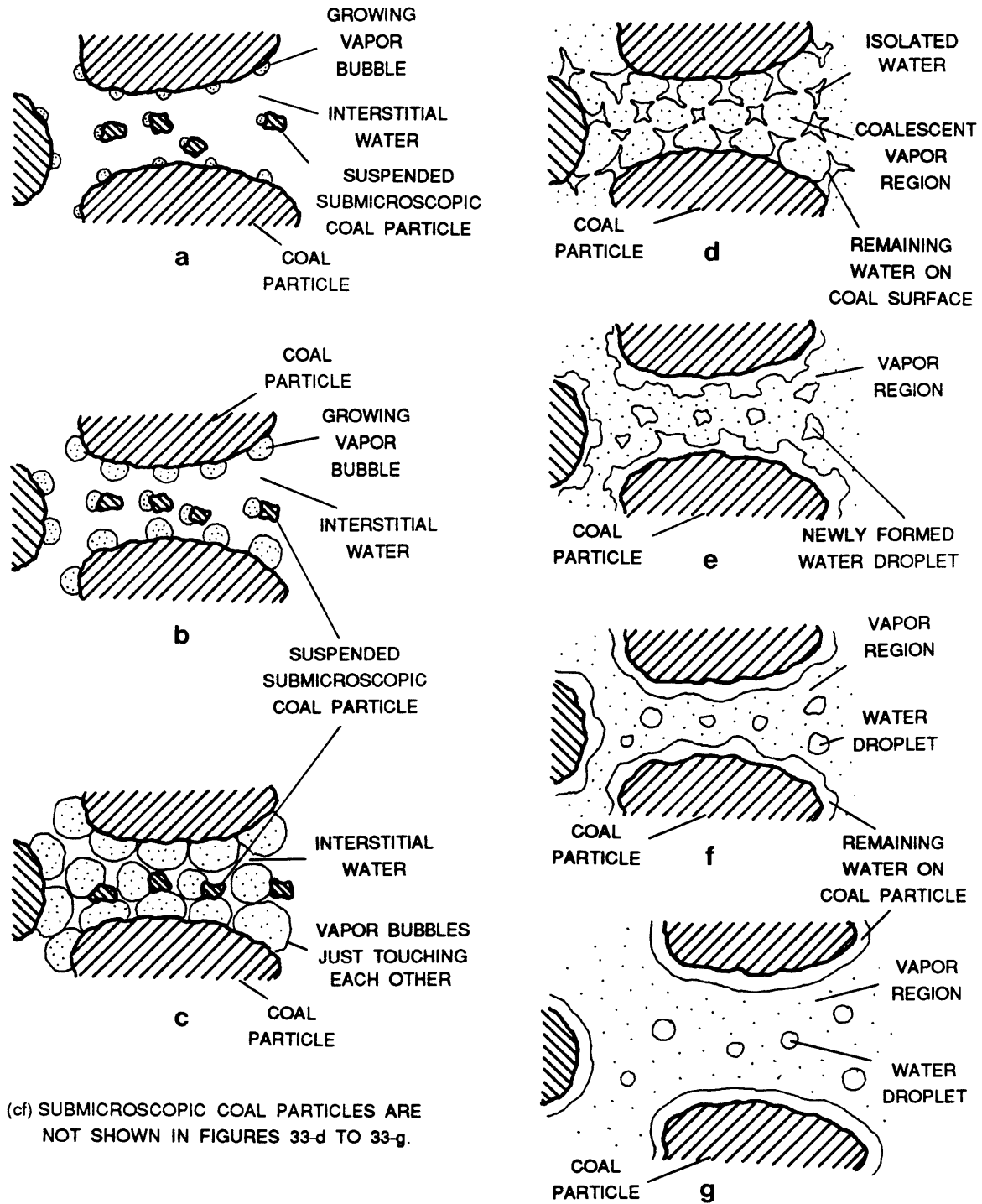


Figure 33. Sequential Process of Flash-Atomization between Each Coal Particle in CWF

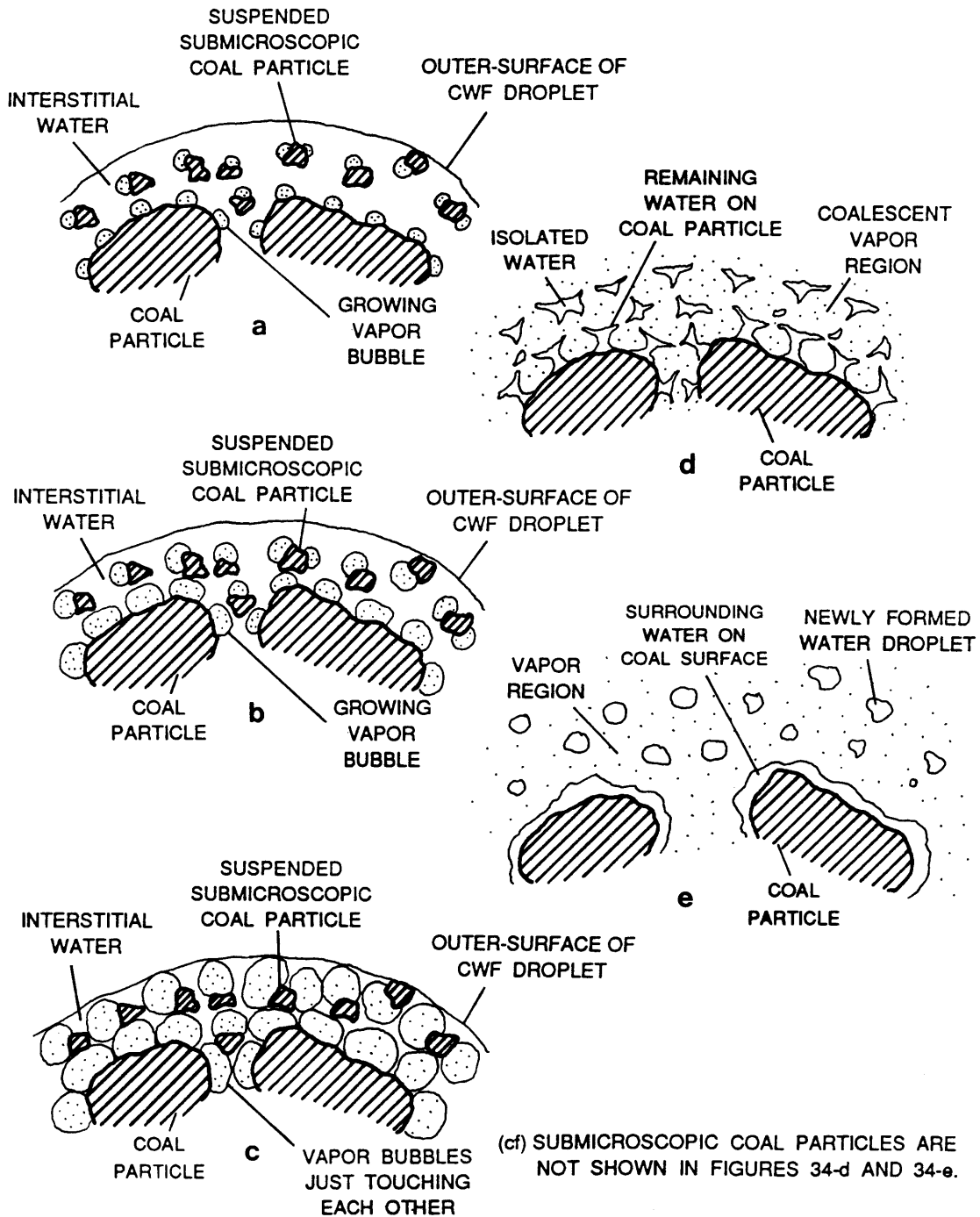


Figure 34. Sequential Process of Flash-Atomization on CWF Droplet Surface

they will start to burst and coalesce into a big vapor region (Figure 33-d). The water isolated by coalescence of vapor bubbles will instantaneously form a spherical water droplet due to the surface tension of the water and will be suspended in the vapor region for a while (Figures 33-e and 33-f). The water, which is disconnected by a coalescent vapor region and remains on the surface of the coal particle, will instantly spread on the coal surface due to wetting behavior between the water and the coal surface, and will uniformly surround the coal particle (Figures 33-e and 33-f).

Before the flash-evaporation process, coal particles in the CWF droplet attract each other due to the presence of the interstitial water. Upon completion of coalescence of the vapor bubbles, most of the coal particles in the CWF droplet are isolated by a coalescent vapor region, and small water droplets are formed instantaneously in the vapor region and scattered (Figure 33-g).

Figure 34 shows flash-atomization at the outer surface of CWF droplet. The bubble nucleation occurs both at the micropores of suspended submicroscopic coal particles and the macropores and micropores of coal particles (Figure 34-a). The vapor bubbles grow (Figure 34-b), until they touch each other (Figure 34-c). Upon contact, they will coalesce into a big vapor region and will escape into the atmosphere, and then some water isolated by a coalescent vapor region will form water droplets instantaneously and will be dispersed into the atmosphere (Figures 34-d and 34-e).

As newly formed water droplets and CWF droplets with surrounding water are scattered, some fraction of them may collide and adhere to each



other (Figure 35). The extent of adhesion during droplet scatter depends on the amount of surrounding water on the surface of a CWF droplet, which directly influences the surface tension force between coalescent CWF droplets. If the amount of surrounding water is very small, even though CWF droplets collide with each other, they fall apart easily due to weak surface tension force. However, if the amount of surrounding water is large enough, during droplet collision, CWF droplets are much more likely to adhere to each other and make large coalescent CWF droplets.

#### 4.2.3 Bubble Growth Dynamics

Bubble growth dynamics play an important role in the study of flashing evaporation. In this study, the model of bubble nucleation at the nucleation pore and the model of bubble growth limited by heat diffusion will be adopted to explain bubble growth behavior during flash-atomization of CWF.

The model of vapor bubble growth to the critical size from a pore at a solid surface, was formulated by Thirunavukkarasu<sup>(24)</sup>. His model describes the bubble growth in the early stages prior to the bubble reaching the critical size (i.e., a hemispherical shape of the vapor/liquid interface at the pore mouth) in the liquid which is suddenly superheated due to a pressure drop.

Figure 36-a shows the initial stage of the entrapped vapor and/or air pocket in the active nucleation pore. Figures 36-b and 36-c show the bubble growing up to the top of the nucleation pore. The time  $\Delta t$ , taken to reach the top of the nucleation pore (Figure 36-c) from the bottom of the pore (Figure 36-a) is derived from the energy equation in the liquid

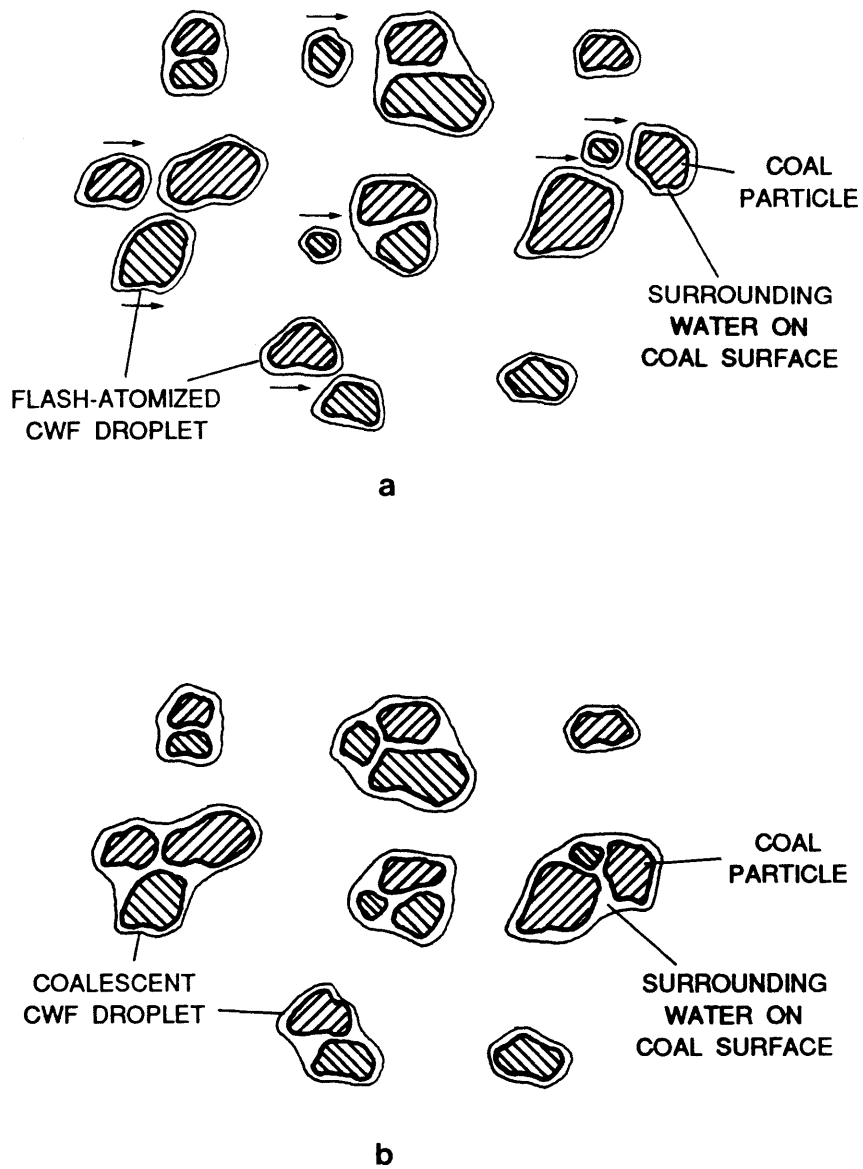


Figure 35. Adhesion Process of Flash-Atomized CWF Droplets  
(a) Before Collision, (b) After Collision

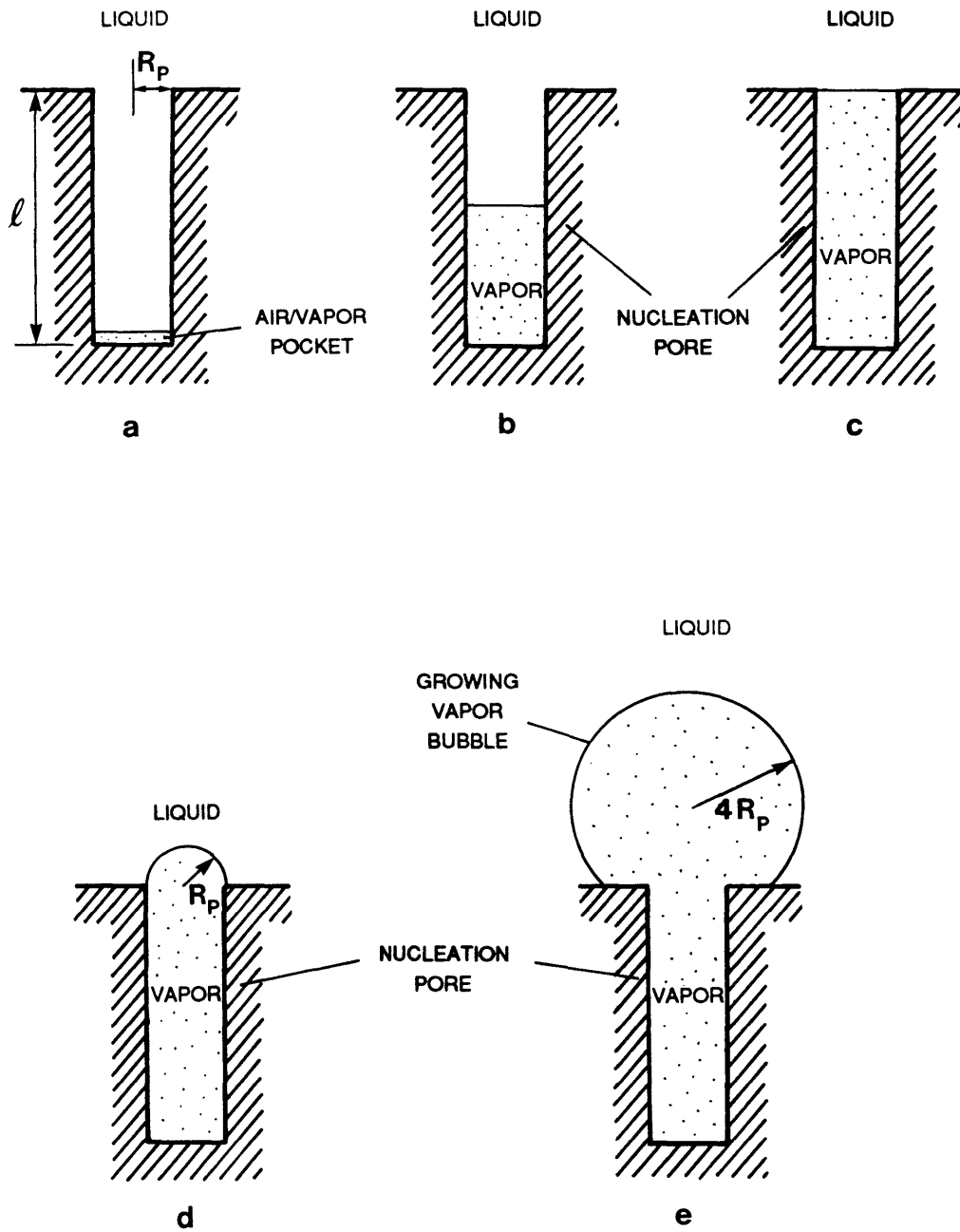


Figure 36. Sequential Process of Vapor Bubble Growth at Nucleation Pore of Coal Particle

for a plane interface, and expressed as (24)

$$\Delta t_1 = \left( \frac{\pi \rho_v^2 h_{fg}^2}{4 \rho_l^2 c_l^2 \alpha_l} \right) \left( \frac{l}{\Delta T} \right)^2 \quad \text{eq. (10)}$$

where  $l$  = depth of cylindrical nucleation pore

$\Delta T$  = superheat of liquid

$\rho_v$  = density of vapor

$\rho_l$  = density of liquid

$c_l$  = specific heat of liquid

$\alpha_l$  = thermal diffusivity of liquid

$h_{fg}$  = latent heat of evaporation

$\Delta t_1$  = time taken to reach top of the pore from bottom of the pore

The vapor bubble reached the top of the nucleation pore (Figure 36-c) grows and forms a hemispherical shape (radius of  $R_p$ ) at the nucleation pore (Figure 36-d). The bubble growth rate between the stage of Figure 36-c and the stage of Figure 36-d is obtained from the energy equations in the liquid and vapor regions, and expressed as

$$\frac{dR}{dt} = \frac{2 \pi R_p^2 k_l \rho_l c_l}{3 X Y} (\Delta T)^2 \quad \text{eq. (11)}$$

where  $\frac{dR}{dt}$  = bubble growth rate

$R_p$  = radius of nucleation pore mouth

$X, Y$  = functions of bubble radius  $R$  and vapor temperature

$k_l$  = thermal conductivity of liquid

$\Delta T$  = superheat of liquid

Hence, the time  $\Delta t_2$ , required to reach the hemispherical stage (Figure 36-d) from the bubble radius of  $R_\infty$  (Figure 36-c) is given by

$$\Delta t_2 = \int_{R_\infty}^{R_p} \frac{3 XY}{2 \pi R_p^2 k_\ell \rho_\ell c_\ell (\Delta T)^2} dR \quad \text{eq. (12)}$$

where  $R$  = radius of bubble

$R_\infty$  = radius of bubble at the pore mouth in Figure 36-c

From eqs. (10) and (12), total time taken to reach the hemispherical stage (Figure 36-d) from the bottom of the pore (Figure 36-a) is

$$\begin{aligned} \Delta t_1 + \Delta t_2 = & \left( \frac{\pi \rho_v^2 h_{fg}^2}{4 \rho_\ell^2 c_\ell^2 \alpha_\ell} \right) \left( \frac{\ell}{\Delta T} \right)^2 \\ & + \int_{R_\infty}^{R_p} \frac{3 XY}{2 \pi R_p^2 k_\ell \rho_\ell c_\ell (\Delta T)^2} dR \quad \text{eq. (13)} \end{aligned}$$

The bubble growth well beyond the hemispherical stage shows a similar behavior to that predicted by Zwick and Plesset<sup>(25)</sup>. Plesset and Zwick<sup>(26,27)</sup> as well as Forster and Zuber<sup>(28)</sup> and others<sup>(29,30)</sup> studied the asymptotic bubble growth which is limited by heat diffusion. Their results, applicable to the isobaric bubble growth, show that the bubble growth rate is proportional to superheat, and inversely proportional to the square root of bubble growth time, as follows:

$$\frac{dR}{dt} = \left( \frac{12}{\pi} \right)^{1/2} \frac{\rho_\ell c_\ell \alpha_\ell^{1/2} \Delta T}{2 \rho_v h_{fg} t^{1/2}} \quad \text{eq. (14)}$$

Hence, the asymptotic bubble growth time  $\Delta t_3$ , taken to reach a final bubble radius of  $R_2$  from an initial bubble radius of  $R_1$ , is given by

$$\Delta t_3 = \frac{\pi \rho_v^2 h_{fg}^2}{12 \rho_l^2 c_l^2 \alpha_l (\Delta T)^2} (R_2 - R_1)^2 \quad \text{eq. (15)}$$

where  $\Delta t_3$  = time taken to reach  $R_2$  from  $R_1$

$R_1$  = initial bubble radius

$R_2$  = final bubble radius

It is found<sup>(24)</sup> that the transition from the bubble growth rate in the nucleation pore [given by eq. (11)] to the bubble growth rate limited by heat diffusion [given by eq. (14)] occurs, when the bubble radius reaches around four times pore radius (Figure 36-e). (i.e.,  $R \approx 4 R_p$ ). Therefore, the total time  $\Delta t_{\text{tot}}$ , required to reach final bubble radius of  $R^*$  from the entrapped air and/or vapor pocket at the bottom of the pore can be obtained as

$$\begin{aligned} \Delta T_{\text{tot}} &= \Delta t_1 + \Delta t_2 + \Delta t_3 \\ &= \left[ \frac{\pi \rho_v^2 h_{fg}^2}{4 \rho_l^2 c_l^2 \alpha_l^2} \right] \left( \frac{l}{\Delta T} \right)^2 \\ &+ \int_{R_\infty}^{R_p} \frac{3 XY}{2\pi R_p^2 k_l \rho_l c_l (\Delta T)^2} dR + \int_{R_\infty}^{4R_p} \frac{-3 XY}{2\pi R_p^2 k_l \rho_l c_l (\Delta T)^2} dR \\ &+ \left[ \frac{\pi \rho_v^2 h_{fg}^2}{12 \rho_l^2 c_l^2 \alpha_l (\Delta T)^2} \right] (R^* - 4R_p)^2 \quad \text{eq. (16)} \end{aligned}$$

Here,  $\Delta t_2$ , given by eq. (12), is modified by substituting  $4R_p$  instead of  $R_p$  into the upper limit of integral.  $\Delta t_3$  can be also obtained by substituting  $4R_p$  and  $R^*$  into the initial and final bubble radius,  $R_1$  and  $R_2$ , in eq. (15), respectively.

The total bubble growth time  $\Delta t_{\text{tot}}$  is inversely proportional to the square of superheat  $\Delta T$ . Hence, it is concluded that as superheat  $\Delta T$  increases and final bubble radius  $R^*$  decreases, total bubble growth time  $\Delta t_{\text{tot}}$  decreases. Also, total bubble growth time  $\Delta t_{\text{tot}}$  is dependent upon the dimensions of the nucleation pore ( $R_p$  and  $\ell$ ) and the properties of liquid and vapor.

#### 4.2.4 Effect of Superheat on CWF Flash-Atomization

Coal particles within CWF droplet have lots of micropores and macropores. These pores are assumed to have the pore size distribution shown in Figure 37 which illustrates the number of pores of a particular size range versus diameter of pore.

In accordance with Staniszewski's<sup>(31)</sup> observation, as superheat  $\Delta T$  is increased, the number of activated nucleation pores will increase and more pore will become activated at diameters spread on either side of the critical diameter  $D_{\text{crit}}$  as shown in Figure 37.

As the number of activated nucleation pores increases (i.e., density of nucleation site increases), the average distance between each activated nucleation pore will decrease, and therefore, the average diameter of touching bubbles, which is defined as the average diameter of vapor bubbles when they form a close-pack spherical array just touching each other in this model of flash-atomization, will decrease.

As shown in Figures 38-a and 38-b, as the average diameter of touching bubbles decreases, the amount of remaining water on the coal surface per unit coal surface area will decrease, and the size of each isolated water droplet in the coalescent vapor region will also decrease,

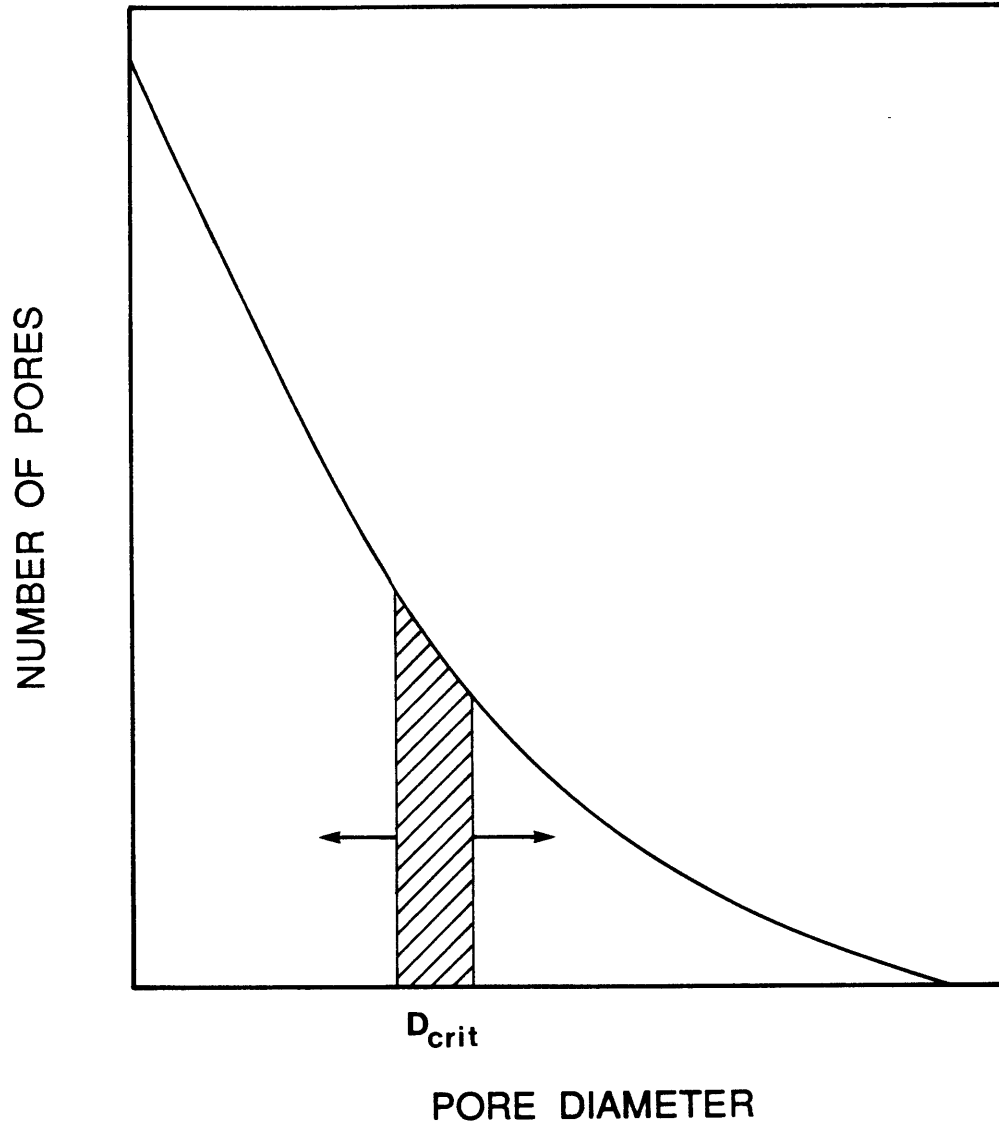
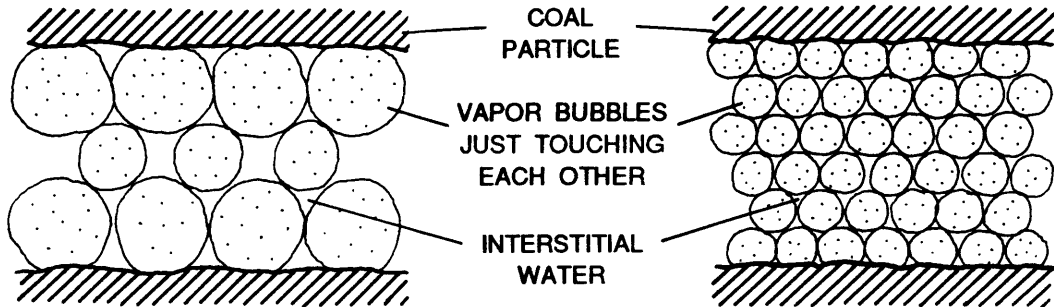


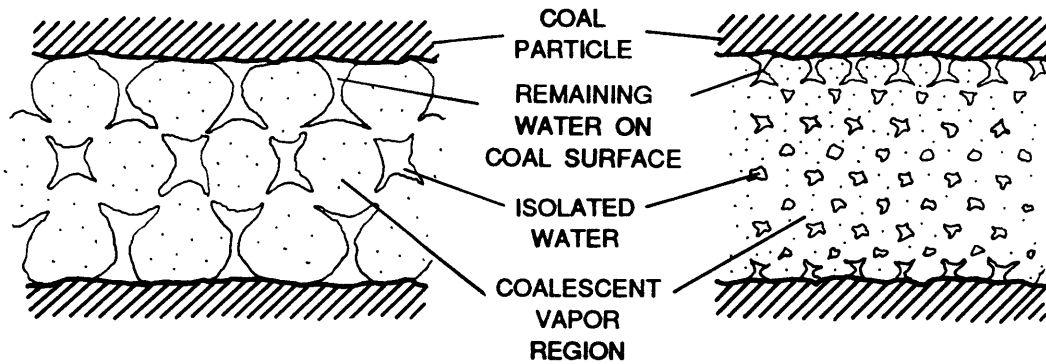
Figure 37. Pore Size Distribution of Coal Particle



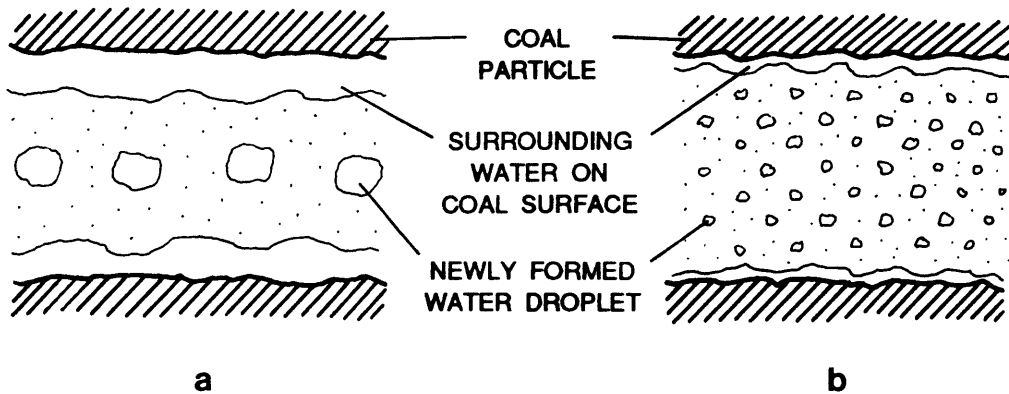
PROCESS 1: GROWING BUBBLES ARE JUST TOUCHING EACH OTHER.



PROCESS 2: WATER IS ISOLATED BY COALESCENT VAPOR REGION.



PROCESS 3: WATER ON COAL SURFACE SPREADS UNIFORMLY AND WATER IN COALESCENT VAPOR REGION FORMS DROPLETS.



a

b

Figure 38. Comparison of Amount of Remaining Water on Coal Particle Surface with Different Superheat  $\Delta T$

(a) Small Superheat  $\Delta T$ , (b) Large Superheat  $\Delta T$

however, the number of each isolated water droplet will increase. Consequently, as superheat  $\Delta T$  increases, the average diameter of newly formed CWF droplet which is the sum of original coal diameter and thickness of surrounding water will decrease due to decrease in the thickness of surrounding water.

As newly formed CWF droplets scatter and collide due to microexplosion during flash-atomization, they begin to adhere to each other. As the amount of surrounding water of each CWF droplet, which directly influences the surface tension force between coalescent CWF droplets, increases, the probability of adhesion during CWF droplet collision will increase.

As shown in Figure 39, adhesive force between each CWF droplet is given by surface tension of water ( $\gamma$ ) multiplied by circumference ( $\ell$ ) at the neck region. The circumference of the neck region is proportional to the amount of surrounding water. As the amount of surrounding water increases, adhesive force between each CWF droplet will increase, resulting in higher probability of adhesion, and therefore, larger CWF droplet size.

#### 4.2.5 Spray Angle Change during Flash-Atomization

When a superheated liquid under flashing evaporation partially evaporates to return to its stable saturation state, it has the capability of doing an amount of useful work equal to the available energy of a superheated liquid upon its surroundings.

The available energy of a superheated liquid ( $\Delta\psi$ ) in the isobaric process can be obtained as

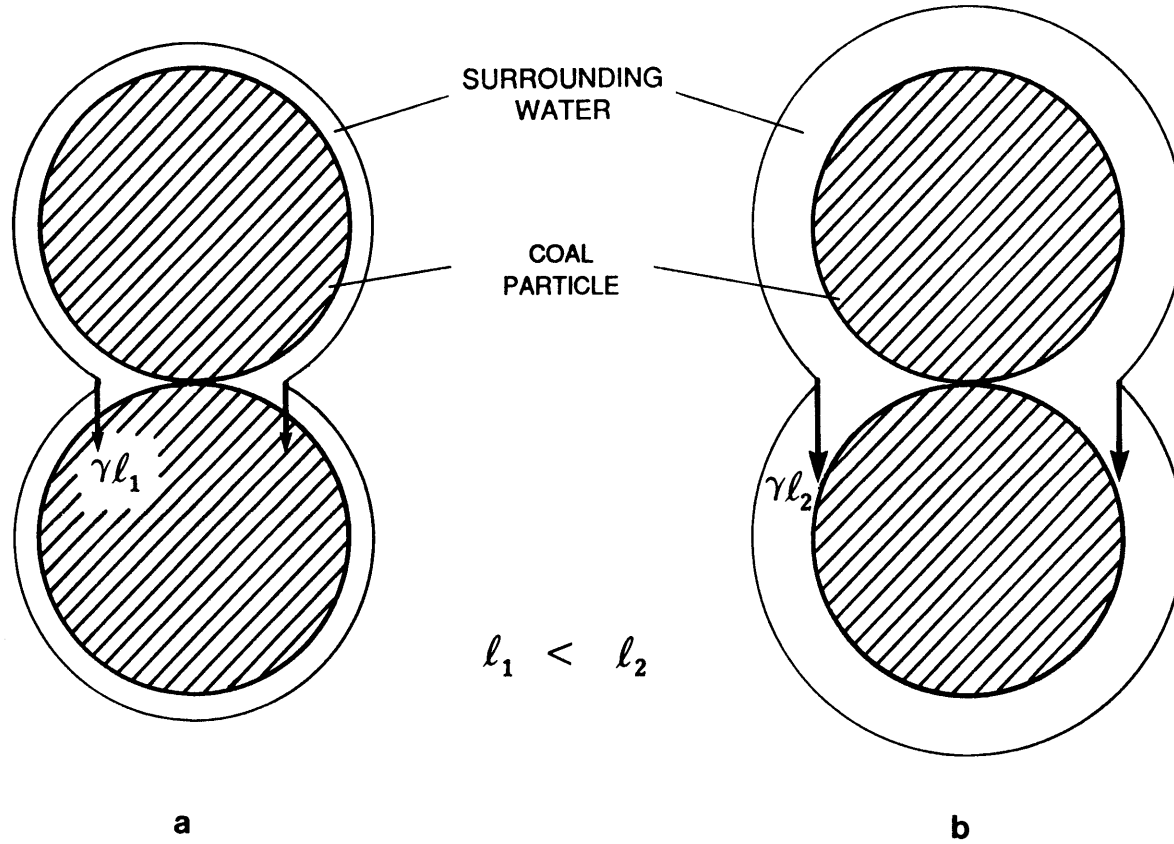


Figure 39. Comparison of Surface Tension Force with Different Amount of Surrounding Water in Coalescent CWF Droplets  
 (a) Thin Water Layer, (b) Thick Water Layer

$$\Delta\psi = \Delta h - T_{\text{sat}} \Delta s \quad \text{eq. (17)}$$

where  $\Delta h$  = enthalpy difference between superheated liquid and saturated liquid

$T_{\text{sat}}$  = saturation temperature of liquid at ambient pressure

$\Delta s$  = entropy difference between superheated liquid and saturated liquid

Specific heat  $c_p$  is nearly constant in the temperature range of interest, and therefore, eq. (17) can be expressed as

$$\Delta\psi = c_p \left[ \Delta T - T_{\text{sat}} \ln \left( \frac{T}{T_{\text{sat}}} \right) \right] \quad \text{eq. (18)}$$

where  $c_p$  = specific heat of liquid at constant pressure

$\Delta T$  = superheat of liquid

$T$  = temperature of superheated liquid, given by

$T = \Delta T + T_{\text{sat}}$

Therefore, the available energy of a superheated liquid ( $\Delta\psi$ ) in the isobaric process can be rewritten as

$$\Delta\psi = c_p \left[ \Delta T - T_{\text{sat}} \ln \left( \frac{\Delta T + T_{\text{sat}}}{T_{\text{sat}}} \right) \right] \quad \text{eq. (19)}$$

The available energy of a superheated liquid can be absorbed in the kinetic energy of the spray or as new surface energy. Lienhard<sup>(32)</sup> shows the magnitude of the new surface energy is not of primary importance compared to that of the kinetic energy.

For a twin-fluid atomization without flash-atomization, two components of spray velocity can be defined; one is the axial velocity of

spray  $V_a$ , and the other is the radially propagating velocity of spray  $V_r$  (Figure 40-a). In the case of flash-atomization, an additional velocity of spray  $V_f$ , generated by flash-atomization should be considered (Figure 40-b).

As shown in Figure 40-a, the half angle  $\alpha_0$  of the spray without flash-atomization is expressed as

$$\sin \alpha_0 = \frac{V_r}{V_a} \quad \text{eq. (20)}$$

In Figure 40-b, the half angle  $\alpha$  of the spray with flash-atomization is expressed as

$$\sin \alpha = \frac{V_r + V_f}{V_a} \quad \text{eq. (21)}$$

If all of the available energy were to go into translational kinetic energy, the maximum velocity  $V_{f_{\max}}$ , generated by flash-atomization, would be

$$V_{f_{\max}} = (2 c_p)^{\frac{1}{2}} \left[ \Delta T - T_{\text{sat}} \ln \left( \frac{\Delta T + T_{\text{sat}}}{T_{\text{sat}}} \right) \right]^{\frac{1}{2}} \quad \text{eq. (22)}$$

However, in reality, only a fraction of the superheated liquid will fully return to a saturated condition during flash-atomization. Therefore, actual velocity ( $V_f$ ) generated by flash-atomization can be given by maximum velocity generated by flash atomization ( $V_{f_{\max}}$ ) multiplied by the efficiency factor  $\xi$ .

$$V_f = \xi V_{f_{\max}} \quad \text{eq. (23)}$$

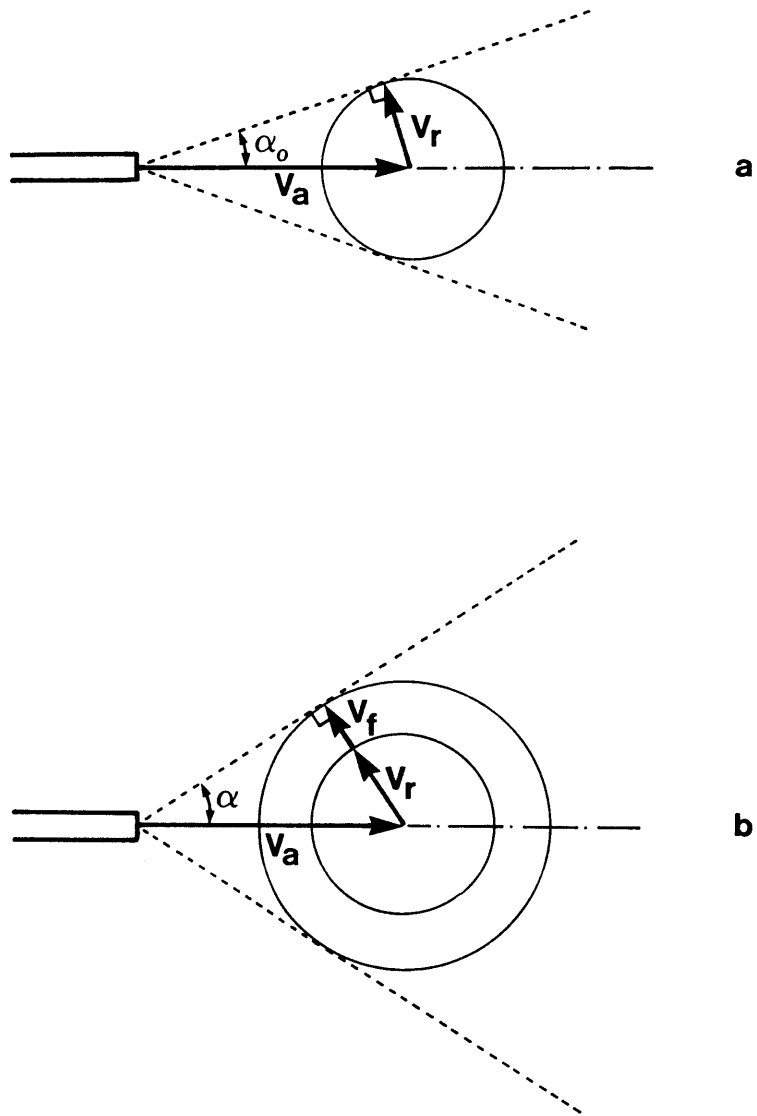


Figure 40. Schematic Diagrams of Twin-Fluid Atomization  
(a) Without Flash-Atomization,  
(b) With Flash-Atomization

Here, the efficiency factor  $\xi$  will have some value much less than unity, and will be obtained experimentally in Section 4.4.

From eqs. (20) through (23), actual velocity  $V_f$  generated by flash-atomization is correlated as

$$\begin{aligned} V_f &= V_a (\sin \alpha - \sin \alpha_0) \\ &= \xi V_{f_{\max}} \\ &= \xi (2 c_p)^{\frac{1}{2}} \left[ \Delta T - T_{\text{sat}} \ln \left( \frac{\Delta T + T_{\text{sat}}}{T_{\text{sat}}} \right) \right]^{\frac{1}{2}} \end{aligned} \quad \text{eq. (24)}$$

Hence, the half angle  $\alpha$  of the spray with flash-atomization is correlated with superheat of liquid  $\Delta T$ , efficiency factor  $\xi$ , and axial velocity of spray  $V_a$ , as follows:

$$\alpha = \sin^{-1} \left[ \frac{\xi}{V_a} (2c_p)^{\frac{1}{2}} \left[ \Delta T - T_{\text{sat}} \ln \left( \frac{\Delta T + T_{\text{sat}}}{T_{\text{sat}}} \right) \right]^{\frac{1}{2}} + \sin \alpha_0 \right] \quad \text{eq. (25)}$$

where  $\alpha$  = half angle of spray with flash-atomization

$\alpha_0$  = half angle of spray without flash-atomization

$T_{\text{sat}}$  = saturation temperature of liquid at ambient pressure

$\Delta T$  = superheat of liquid

$\xi$  = efficiency factor

$V_a$  = axial velocity of spray

$c_p$  = specific heat at constant pressure  $P_{\text{amb}}$

In a twin-fluid atomization spray, the axial velocity of spray  $V_a$  is varied with the mass flow rate of atomizing air  $\dot{m}_a$  and that of fuel  $\dot{m}_f$ . The term of  $\xi/V_a$  will be correlated with  $\dot{m}_a$  and  $\dot{m}_f$  in Section 4.4.

### 4.3 Experimental Results of CWF Flash-Atomization and Discussions

The effect of flash-atomization on CWF atomization quality was examined in the Spray Test Facility (STF) equipped with the laser diffraction spray analyzer. CWF was heated up to the temperature of 150°C at the fuel line pressure of 500 Pa by the steam-heated heat exchanger line and then sprayed into the STF at atmospheric pressure. The droplet sizes of CWF spray were measured by the laser diffraction spray analyzer and mass mean diameter (MMD) of CWF droplets was calculated from the data of laser diffraction measurement. Figure 41 shows the variation of MMD of CWF droplets with CWF temperatures and air-to-fuel ratios. The effect of superheat  $\Delta T$  on the p.s.d. of CWF droplets can be observed in this figure. For both high (0.26 - 0.32) and low (0.13) air-to-fuel ratios (AFR), the MMD decreases gradually with increasing CWF temperature up to 100°C due to the decrease in CWF viscosity with increasing CWF temperature. The further reduction in MMD observed between 100°C and 150°C is caused mainly by flash-atomization.

For the high AFR, it is seen that the measured MMD approaches the MMD of the parent coal particles in the CWF, indicating the potential of thermally assisted atomization for improvement of spray quality. For the low AFR of 0.13, there is a similar decrease in MMD with increasing CWF temperature in the CWF temperature range of 100°C to 150°C, but the smallest droplet MMD measured is much larger than that of the parent coal particles.

The extent of flash-atomization is dependent upon the geometry of the gap between each coal particle as well as original size of CWF droplet. If superheat  $\Delta T$  is large enough and the gap between each coal



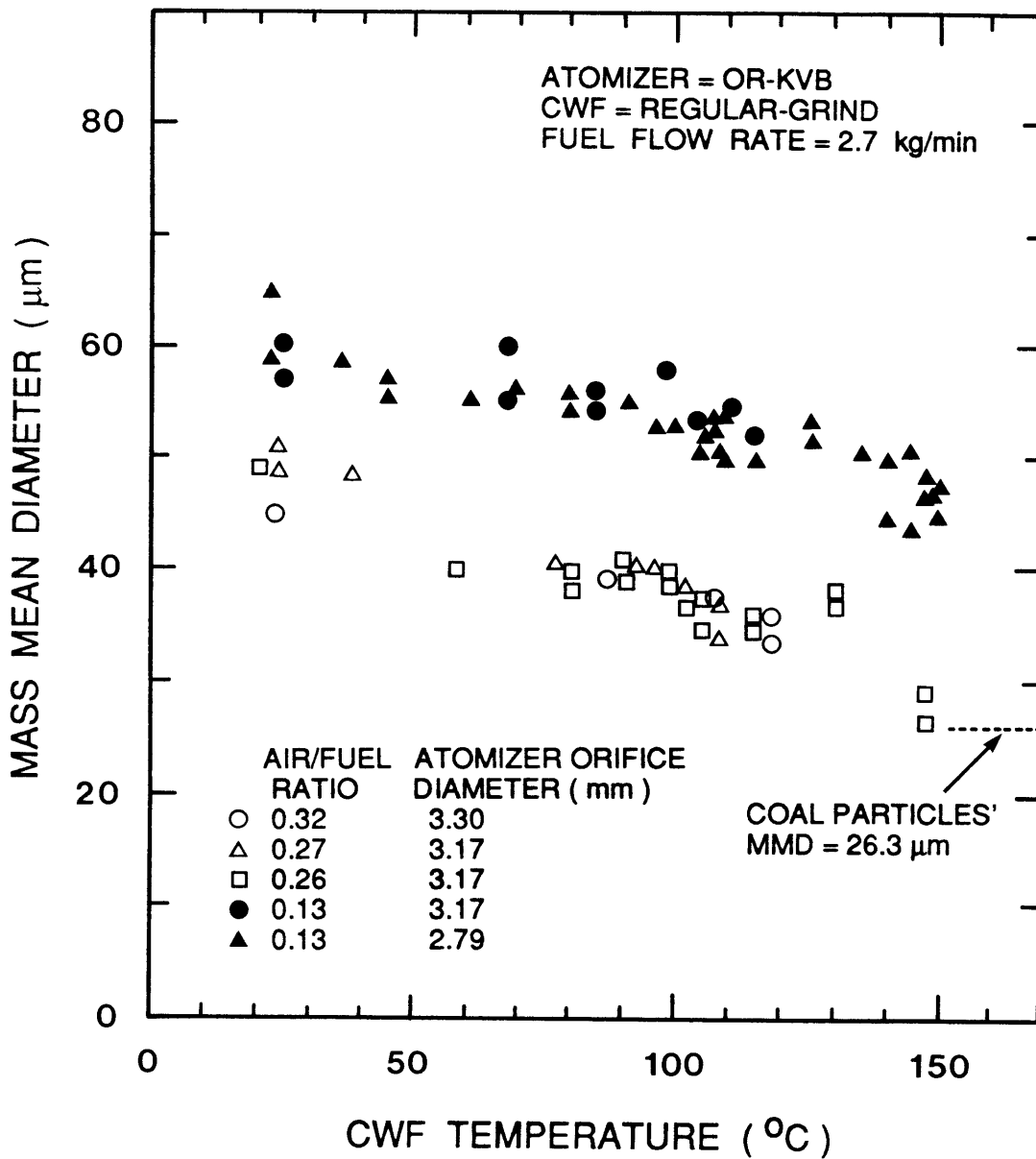


Figure 41. Effect of CWF Temperature on Mass Mean Diameter of CWF Spray

particle is uniform, and if there is no droplet adhesion due to droplet collision, then the resultant CWF droplet size will be the sum of the size of the original coal particle in the CWF droplet and the thickness of surrounding water around coal particle surface. Also, p.s.d. of water droplets formed by coalescence of vapor bubble should be added to the p.s.d. of coal particles with surrounding water to obtain the resultant p.s.d. of CWF droplets due to flash-atomization. In the above ideal case, when superheat remains constant, there will be no effect of original CWF droplet size on the resultant p.s.d. of CWF droplets during flash-atomization due to ideally uniform breakup.

However, in actuality, the gap between each coal particle in the CWF droplet is not uniform, and therefore, the touching bubble radius  $R^*$  will be different, place by place. Therefore, simultaneous occurrence of coal particle isolation by coalescence of vapor bubble cannot be expected, and flash-atomization will occur partially and non-uniformly. When the extent of flash-atomization remains constant (i.e., same  $\Delta T$ ), as the initial size of atomized CWF droplet increases, the resultant MMD of CWF droplets after flash-atomization also increases as shown in Figure 41.

The similar effect of flash-atomization on the atomization quality is also observed in the water spray test, and the changes of viscosity and MMD of water spray are plotted as a function of water temperature in Figure 42. Figure 42-b shows that MMD of water spray decreases with increasing water temperature. As shown in Figure 42-a, as water temperature increases, the viscosity of water decreases with a higher rate below 100°C and much lower rate above 100°C. Therefore, it can be concluded that the decrease in MMDs for water temperature up to 100°C is due to the

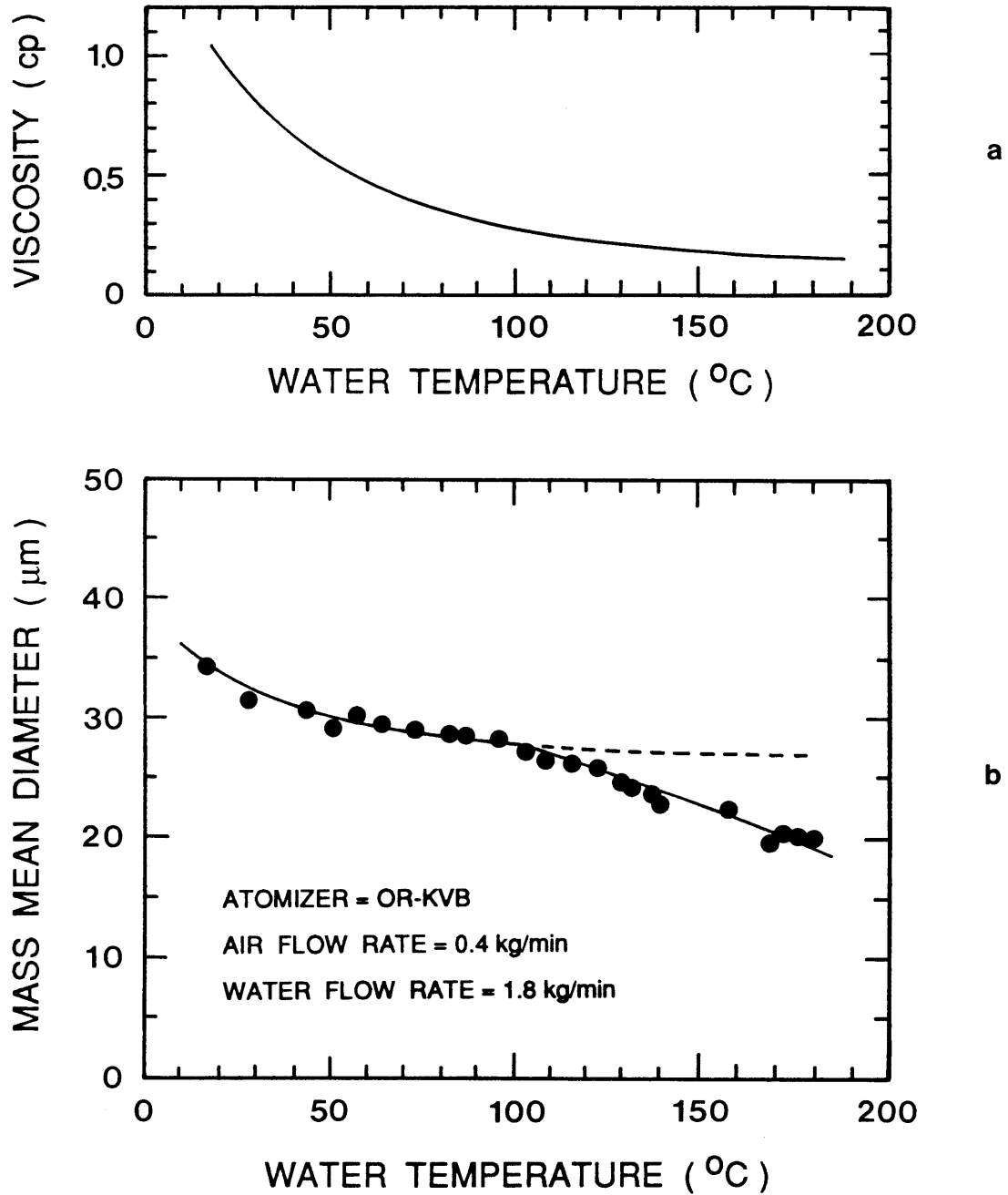


Figure 42. Effect of Water Temperature on Mass Mean Diameter of Water Spray

(a) Water Viscosity versus Water Temperature,

(b) MMD of Water Spray versus Water Temperature

corresponding reduction in water viscosity, and the steep decrease in MMDs of water spray above 100°C is mainly due to flash-atomization.

Figure 43 shows the relative mass distribution of CWF sprays at the CWF temperatures of 21°C, 100°C, and 148°C, and of the parent coal particles used in CWF. Each distribution curve has a differential form of the cumulative Rosin-Rammler mass distribution. The beneficial effect of heating CWF from room temperature to 100°C and then to 148°C can be observed in this figure. As CWF temperature increases, MMD of CWF spray decreases and the CWF spray becomes more uniform. It is seen that at the CWF temperature of 21°C, 13 % of the spray mass is contained in droplets greater than 100  $\mu\text{m}$ , whereas at the temperature of 148°C the corresponding fraction of the spray mass is 1.3 %. It also shows that the mass distribution of the spray at 148°C in the large droplet size range is close to that of the parent coal particles.

The extent of flash-atomization can be estimated using the area enclosed by two mass distribution lines of 100°C and 148°C. These two lines intersect with each other at the CWF droplet diameter of 43  $\mu\text{m}$ . The enclosed area to the right of this abscissa represents the total amount of large droplets mass loss due to flash-atomization, and it is equal to the area to the left of 43  $\mu\text{m}$ , which is the total amount of fine droplets mass gain. The fraction of this area per total area is calculated to be 0.2, i.e., it can be said that as much as 20% of the total mass of spray droplets is converted into finer droplets.

The effect of superheat  $\Delta T$  on the p.s.d. of CWF droplets, shown in Figure 43, can be explained by the model of flash-atomization which was discussed in Section 4.2, as follows: As superheat  $\Delta T$  increases, the

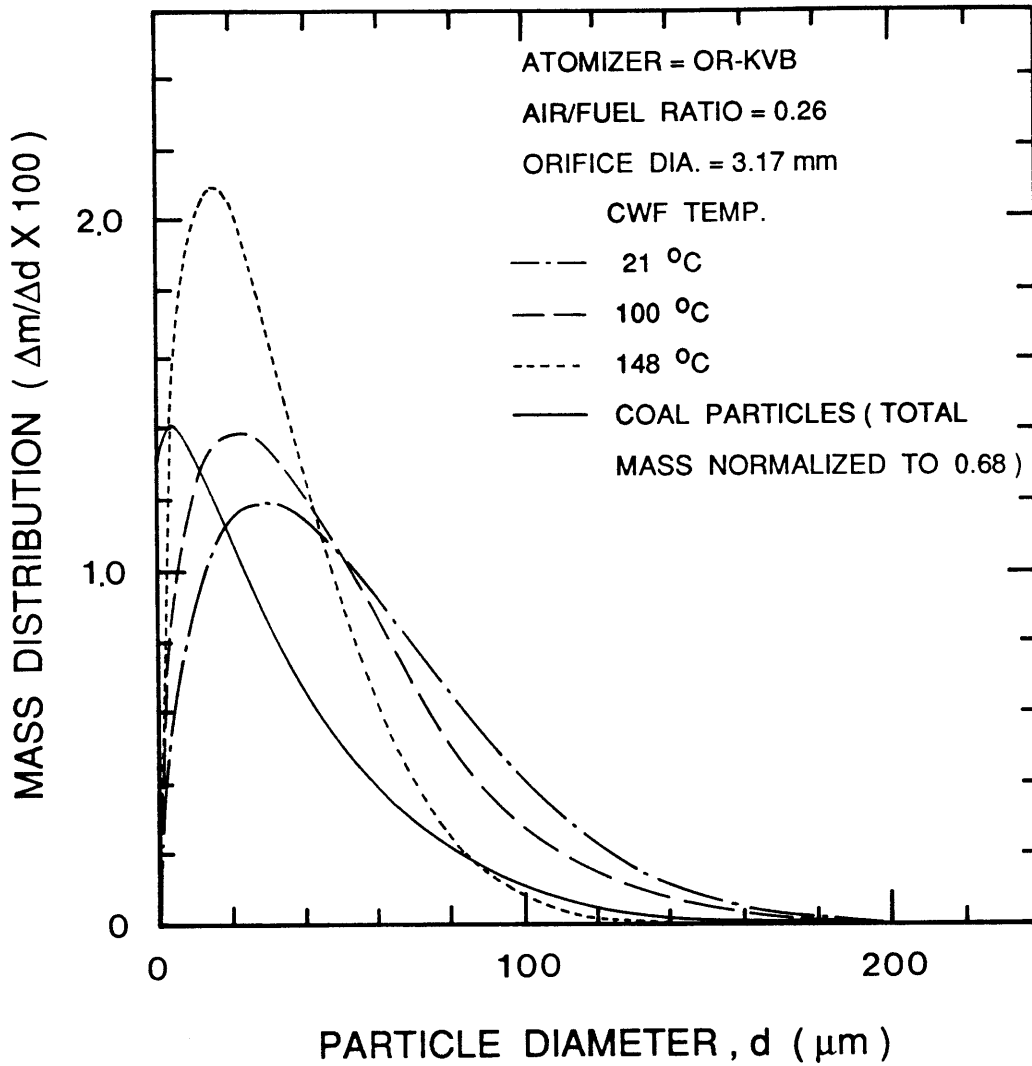


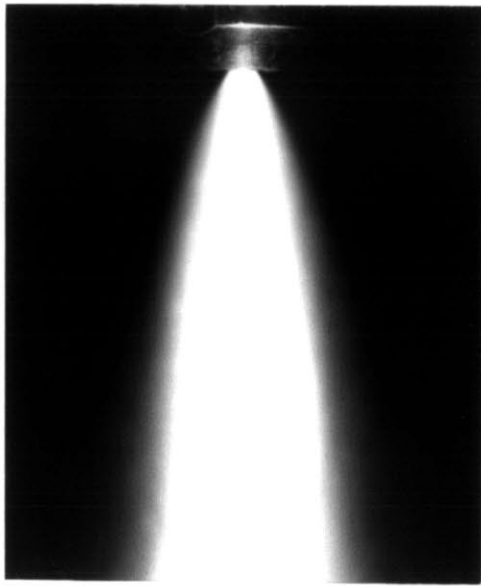
Figure 43. Comparison of Mass Distribution on CWF Sprays and Coal Particles at Various CWF Temperatures

touching bubble radius  $R^*$  will decrease due to the increase in the number of active nucleation pores. This increase in superheat  $\Delta T$  and decrease in average touching bubble radius  $R^*$  will reduce the total bubble growth time  $\Delta t_{tot}$ . If the flashing delay time, which is the same as the total bubble growth time  $\Delta t_{tot}$  required to reach touching bubble radius  $R^*$  from the entrapped air (and/or vapor) bubble, is so short that completion of bubble growth can occur earlier than the completion of evaporation of CWF droplet, flash-atomization in the CWF droplets and/or ligaments will fully occur. This results in the decrease in MMD of CWF droplets at  $148^\circ\text{C}$  in Figure 43. On the contrary, if the flashing delay time is so long that bubble growth up to  $R^*$  cannot be completed until the completion of evaporation of CWF droplet, then there is little effect of flash-atomization on the p.s.d. of CWF droplets.

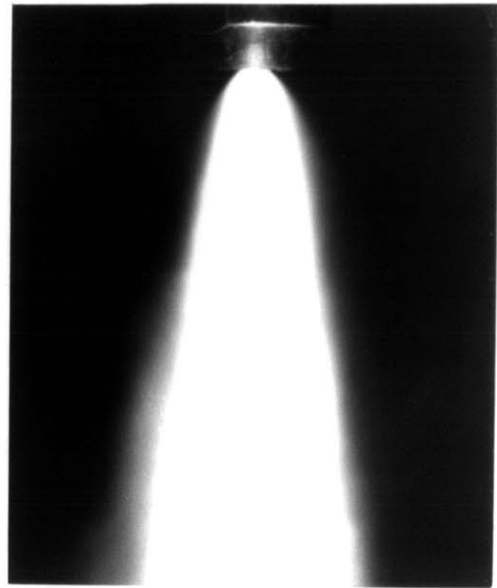
#### 4.4 Experimental Results and Correlation of Spray Angle Change during Flash-Atomization

The spray angle change during flash-atomization of water was investigated in the Spray Test Facility (STF). A 4 x 5 view camera with a 200-mm lens and extension bellows and a flash light were used for recording the spray.

Figure 44 shows the angle change of water spray with water temperature and air-to-fuel ratio (AFR). The water temperature was varied from  $100^\circ\text{C}$  to  $160^\circ\text{C}$  and AFR was varied from 0.1 to 0.3. As shown in Figure 44, spray angle increases with increasing water temperature. The rate of angle change, with temperature change, for a lower AFR (Figure 44-a) is found to be greater than that of a higher AFR (Figure 44-b).



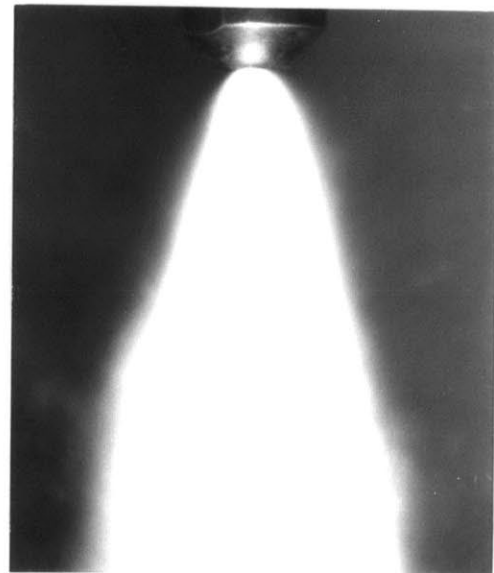
$T = 100\text{ }^{\circ}\text{C}$  ,  $\text{AFR} = 0.1$



$T = 100\text{ }^{\circ}\text{C}$  ,  $\text{AFR} = 0.3$



$T = 160\text{ }^{\circ}\text{C}$  ,  $\text{AFR} = 0.1$



$T = 160\text{ }^{\circ}\text{C}$  ,  $\text{AFR} = 0.3$

a

b

Figure 44. Photographs of Water Sprays Taken for AFRs of 0.1 and 0.3 and at Water Temperatures of 100°C and 160°C

(a)  $\text{AFR} = 0.1$  , (b)  $\text{AFR} = 0.3$

In order to complete the correlation of spray angle in eq. (25), the term of  $\frac{\xi}{V_a}$  is correlated with mass flow rates of both atomizing air and water. The spray angle was measured at the position of 4.0 cm downstream from the atomizer tip as shown in Figure 45. The spray half angle at the temperature of 100°C ( $\alpha_0$ ) and that at higher temperature ( $\alpha$ ) were obtained as functions of water temperature (T) and mass flow rates of both atomizing air ( $\dot{m}_a$ ) and of water ( $\dot{m}_f$ ). Figure 46 shows the variation of  $(\sin \alpha - \sin \alpha_0)$  with  $(2c_p)^{1/2} \left[ \Delta T - T_{sat} \ln \frac{\Delta T + T_{sat}}{T_{sat}} \right]^{1/2}$  for fixed  $\dot{m}_f$  and  $\dot{m}_a$ . The slope of the data line in this figure represents value of  $\frac{\xi}{V_a}$  for the corresponding  $\dot{m}_a$  and  $\dot{m}_f$ . These values of  $\frac{\xi}{V_a}$  are plotted as functions of  $\dot{m}_a$  and  $\dot{m}_f$  in Figure 47. Based upon the data in Figure 47, the term of  $\frac{\xi}{V_a}$  is correlated with  $\dot{m}_a$  and  $\dot{m}_f$  as follows:

$$\frac{\xi}{V_a} = \frac{0.0068}{\dot{m}_f} - \left( 2.2 \times 10^{-10} \dot{m}_a \right)^{0.0293 \dot{m}_f + 0.190} \quad \text{eq. (26)}$$

where the unit of  $\xi/V_a$ : sec/m

$\dot{m}_a$  : kg/min

$\dot{m}_f$  : kg/min

From eqs. (25) and (26), the half angle  $\alpha$  of the water spray during flash-atomization is correlated with water temperature, mass flow rates of both water and atomizing air, and the half angle  $\alpha_0$  of the water spray at the water temperature of 100°C, and expressed as



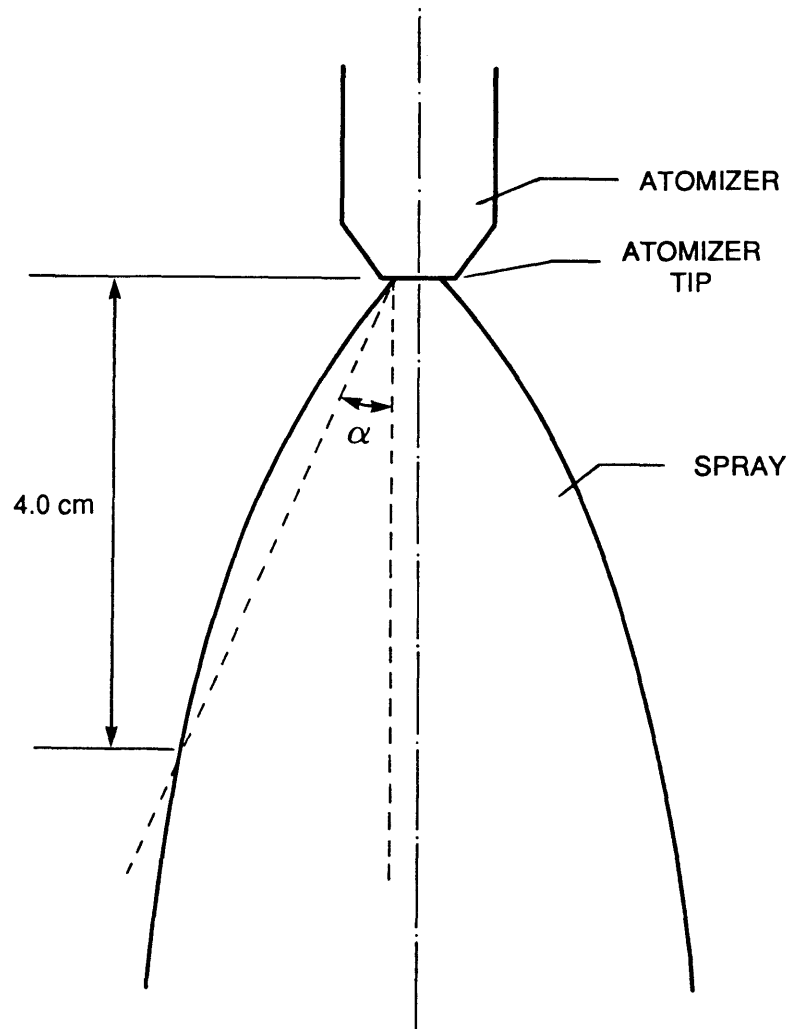


Figure 45. Measurement of Spray Angle  $\alpha$

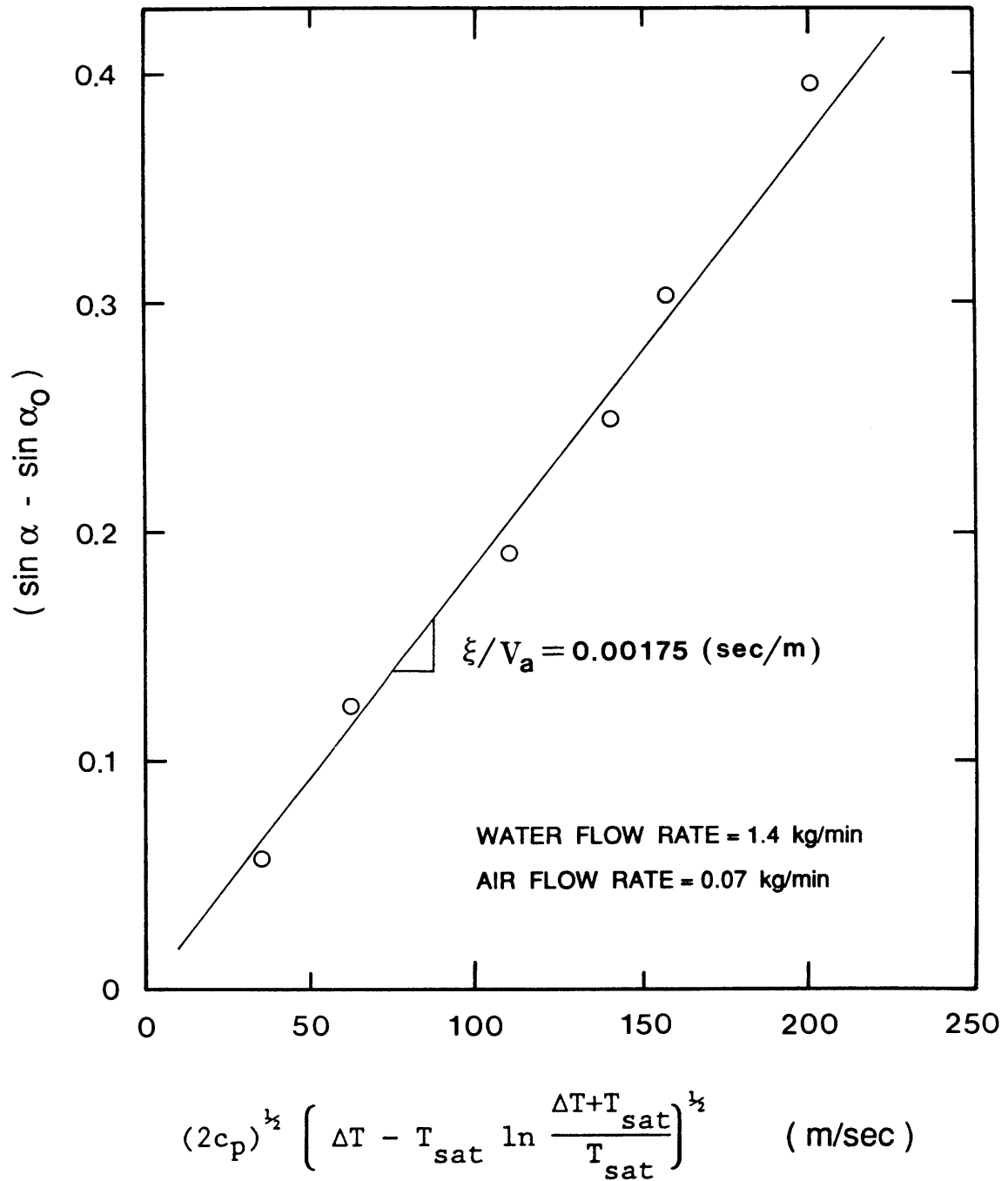


Figure 46. Variation of  $(\sin\alpha - \sin\alpha_0)$  with  $(2c_p)^{1/2} \left[ \Delta T - T_{sat} \ln \frac{\Delta T + T_{sat}}{T_{sat}} \right]^{1/2}$

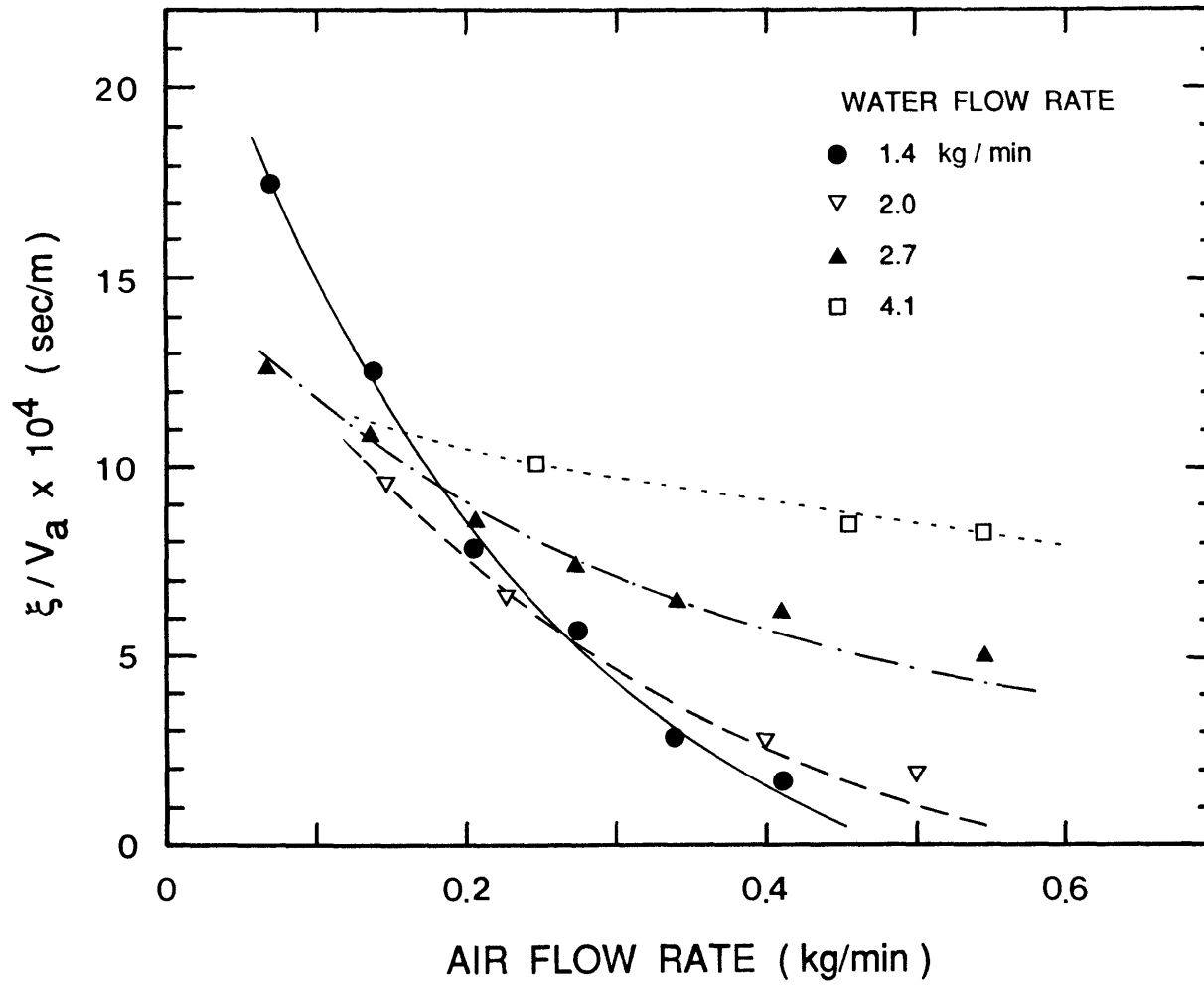
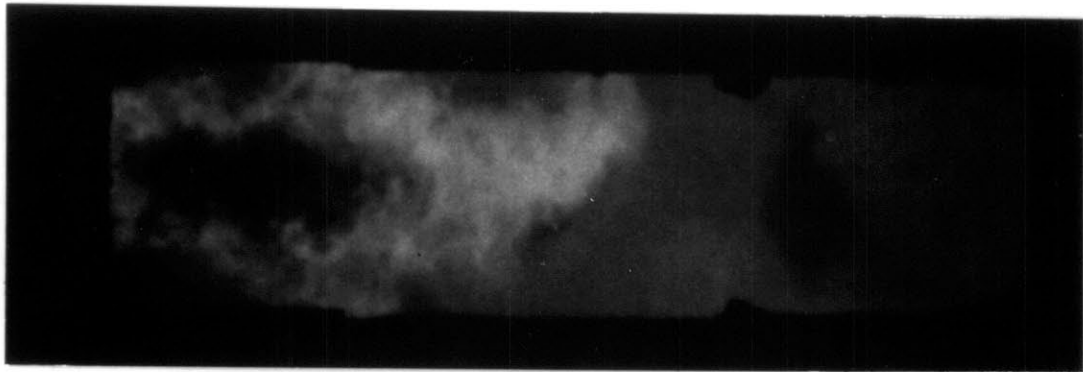


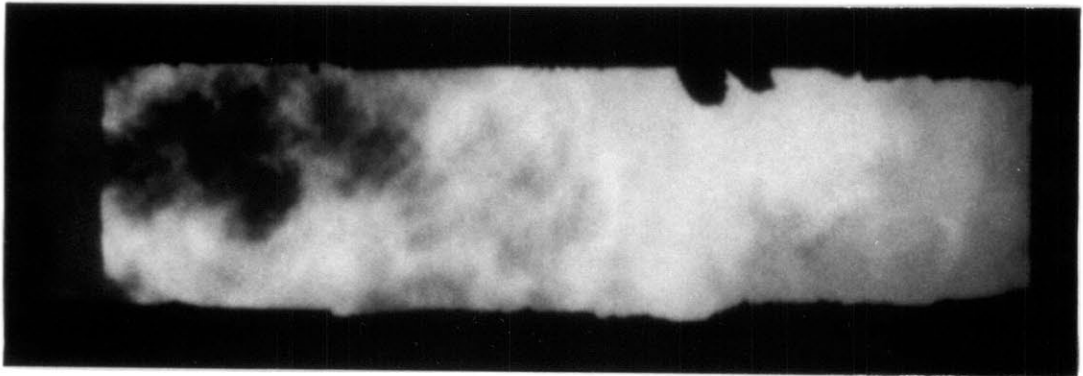
Figure 47. Variation of  $\xi/V_a$  with Flow Rates of Water and Atomizing Air

$$\alpha = \sin^{-1} \left[ (2c_p)^{\frac{1}{2}} \left( \frac{0.0068}{\dot{m}_f} - \left( 2.2 \times 10^{-10} \dot{m}_a \right)^{0.0293 \dot{m}_f + 0.190} \right) \right. \\ \left. \times \left( \Delta T - T_{\text{sat}} \ln \left( \frac{\Delta T + T_{\text{sat}}}{T_{\text{sat}}} \right) \right)^{\frac{1}{2}} + \sin \alpha_o \right] \quad \text{eq. (27)}$$

Figures 48-a and 48-b show the photographs of the flames of CWF taken in the Combustion Research Facility. Figure 48-a corresponds to the CWF flame without fuel treatment and Figure 48-b corresponds to the CWF flame with thermally assisted atomization, which induces flash-atomization. As shown in these figures, the flame angle near the atomizer with flash-atomization (Figure 48-b) is found to be greater than that without flash-atomization (Figure 48-a).



a



b

Figure 48. Photographs of CWF Flames in CRF  
(a) Without Flash-Atomization,  
(b) With Flash-Atomization

## CHAPTER 5

## COMBUSTION STUDY OF CWF WITH FUEL TREATMENTS

5.1 Introduction

The combustion characteristics of CWF with fuel treatments were investigated (33,34,35) in the MIT Combustion Research Facility. The fuel treatments, which were used to achieve CWF flash-atomization, are described as follows:

- (1) Thermally assisted atomization by CWF heating<sup>(36,37)</sup>: if a pressurized CWF is heated above its saturation temperature, the water in CWF flash evaporates as its pressure drops rapidly at the atomizer tip. This flash-evaporation of water in CWF induces further disintegration of atomized CWF droplets, yielding a substantial decrease in p.s.d. of CWF droplets.
- (2) CO<sub>2</sub>-assisted atomization by CO<sub>2</sub> injection into CWF in the fuel line<sup>(38)</sup>: injected CO<sub>2</sub>, which is dissolved into CWF, will evolve as a gaseous form at atmospheric pressure during atomization and will encourage further disruption of CWF droplets.
- (3) Chemically assisted atomization by the mixing of picric acid with CWF<sup>(39)</sup>: the water-soluble and thermally unstable chemical (e.g., picric acid), which is mixed in CWF, induces microexplosions in CWF droplets in the hot environment, resulting in further disintegration of CWF droplets.

In the following sections, the effects of three fuel treatments on CWF combustion characteristics will be evaluated in terms of carbon

conversion efficiency, flame stability, gas composition, solid concentration, and fly-ash deposition.

## 5.2 Experimental Results and Discussions

Combustion experiments were carried out in the Combustion Research Facility (CRF) to examine the effects of fuel treatments which induce flash-atomization by the preheating of CWF up to 110°C, by the CO<sub>2</sub> injection, and by the addition of picric acid. Fine-grind and regular-grind CWFs were used for the combustion tests. Specifications of these CWFs are presented in Table 3. In a baseline study, the same CWFs were used without fuel treatment. The experimental conditions during the combustion tests are presented in Table 4.

Photographs of the flames of fine-grind CWF taken during the combustion tests are shown in Figure 49. It can be observed that the different fuel treatments yield varying improvements in flame stability and air/fuel mixing. A longer flame length and a wider flame angle were especially evident when the CWF was heated; this was consistent with the measurements of better carbon burnout for the thermally assisted flames.

The effect of fuel treatments was analyzed further in terms of the particle size distribution (p.s.d.) of flame solids, which was obtained by a Pilat Mark III cascade impactor. Particles larger than 20  $\mu\text{m}$  were captured by a cyclone separator at the upstream of the cascade impactor and sieved. Particle size distributions of flame solids taken in the flames of fine-grind and regular-grind CWFs for a distance ratio  $X/D$  of 17.1 ( $X$  denotes the distance from the atomizer tip and  $D$  denotes the diameter of the combustion air nozzle, which was 17.6 cm) are plotted in

Table 3

## Specifications of CWFs\* for Fuel Treatment Study

o Regular-grind CWF

Solids p.s.d. in CWF

Size ( $\mu\text{m}$ )	850	70	20	7.6
% Passing	100	80	50	30

Weight Percentage of Coal in CWF 70.3%

Apparent viscosity (Haake): 616 cp at 21°C and 102 sec<sup>-1</sup>o Fine-grind CWF

Solids p.s.d. in CWF

Size ( $\mu\text{m}$ )	600	75	30	9.9	4.6
% Passing	100	96.9	80	50	30

Weight Percentage of Coal in CWF 69.6%

Apparent viscosity (Haake): 416 cp at 21°C and 102 sec<sup>-1</sup>o Characteristics of the Parent Coals (Splashdam) in CWF

Proximate Analysis: As received      Dry Basis

% Moisture	1.07	-
% Ash	5.50	5.56
% Volatiles	30.44	30.77
% Fixed Carbon	62.99	63.67
kJ/kg	33800	34160

Ultimate Analysis (Dry)

% Carbon	82.91
% Hydrogen	5.06
% Nitrogen	1.50
% Chlorine	0.11
% Sulfur	0.61
% Ash	5.56
% Oxygen (diff.)	4.25

\*Analyses of experimental CWF were provided by Atlantic Research Corp.



Table 4

## Experimental Conditions of Combustion Tests

Fixed Conditions

- o Atomizer: Solid Cone 50° OR-KVB Atomizer, 3.175 mm Orifice Diameter
- o Burner Type: 25° Half Angle Divergence, Refractory
- o Combustion Air Swirl:  $S = 2.8$
- o Burner Nozzle Diameter: 0.176 m
- o Atomizer Position: At the entrance of the divergent quarl
- o Combustion Chamber Configuration (from burner to outlet):
  - 7 Water-cooled refractory lined sections
  - 2 Water-cooled bare metal sections
  - 5 Water-cooled refractory lined sections

Fine-grind CWF

- o CWF Type: Fine-grind, Splashdam, 67.5% Coal Loading
- o Fuel Flowrate: 188 kg/hr (1.0 MW Firing Rate)
- o Fuel Pressure at Atomizer: 1.65 MPa (1.20 MPa with Heating)
- o Fuel Temperature: 26°C (110°C with Heating)
- o Atomizing Air Flowrate: 35.9 kg/hr
- o Atomizing Air Pressure: 1.20 MPa
- o Combustion Air Flowrate: 1119 kg/hr
- o Combustion Air Preheat: 290°C
- o Excess O<sub>2</sub>: 2%

Regular-Grind CWF

- o CWF Type: Regular-grind, Splashdam, 69.5% Coal Loading
- o Fuel Flowrate: 232 kg/hr (1.3 MW Firing Rate)
- o Fuel Pressure at Atomizer: 1.72 MPa (1.40 MPa with Heating)
- o Fuel Temperature: 27°C (110°C with Heating)
- o Atomizing Air Flowrate: 42.9 kg/hr
- o Atomizing Air Pressure: 1.34 MPa
- o Combustion Air Flowrate: 1570 kg/hr
- o Combustion Air Preheat: 310°C
- o Excess O<sub>2</sub>: 2%

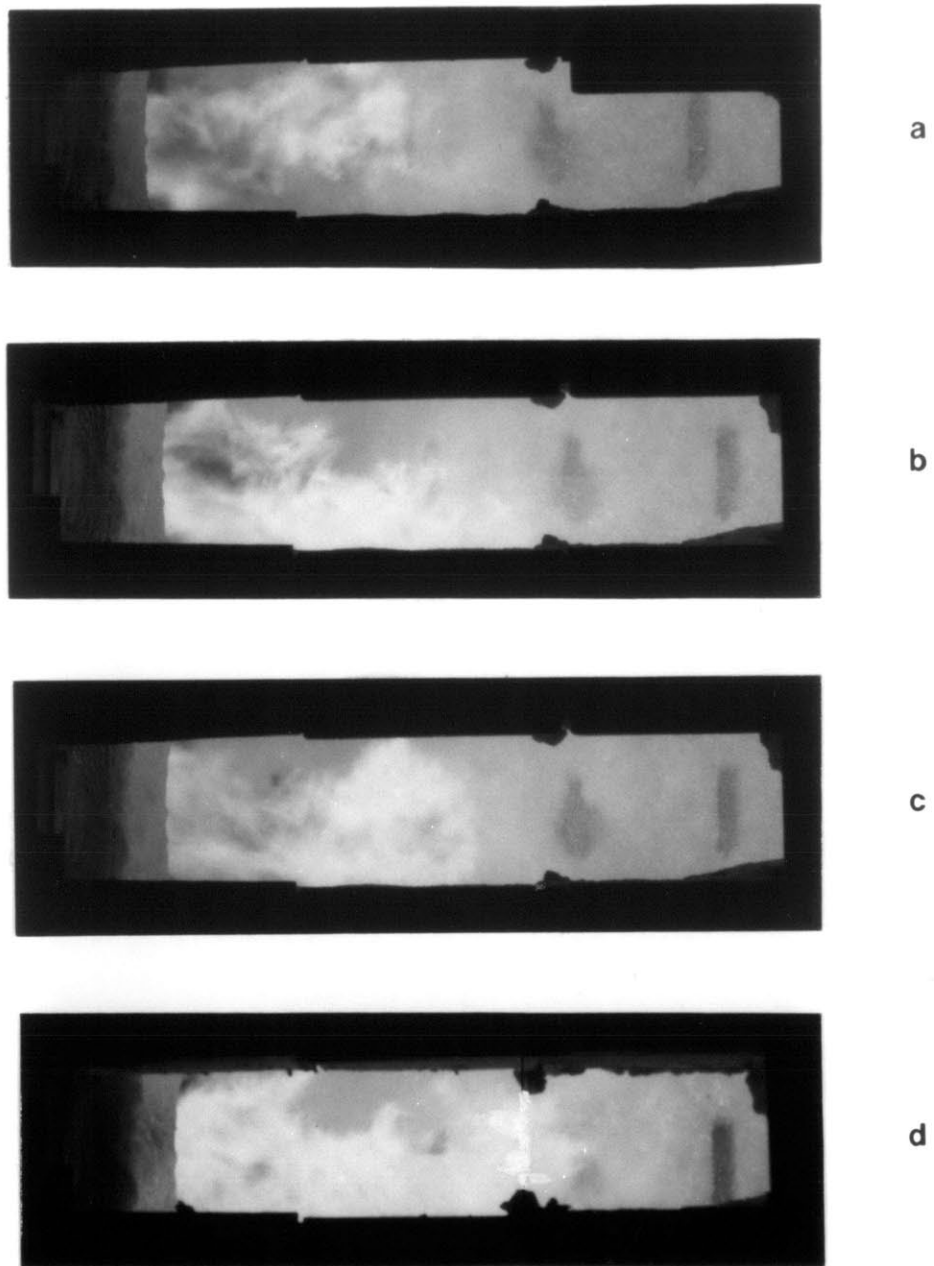


Figure 49. Photographs of CWF Flames with Various Fuel Treatments  
(a) Baseline, (b) Picric Acid, (c) CO<sub>2</sub>, (d) Heating

Figures 50 and 51, respectively. In Figure 51, the mass percentage of unburned carbon as a function of particle diameter is also plotted for the thermally assisted and baseline flames, indicating a substantial reduction in the amount of unburned carbon in the large particles for the thermally assisted flames. With the fuel treatments, improvement in particle size distributions induced by reduction in the mass fraction of the large particles and the corresponding increase in the mass fraction of the small particles can be seen for both the fine-grind and the regular-grind CWFs. CO<sub>2</sub> injection and picric acid addition resulted in appreciable improvement in p.s.d. of flame solids. However, the fuel treatment of CWF by heating produced the finest p.s.d. of flame solids.

Detailed measurements (see Appendix C) at the centerline of the flames of both fine-grind and regular-grind CWFs were made to compare the flame conditions of the baseline flames with those of the thermally assisted flames. Some radial traverse measurements were also carried out for the thermally assisted flames (Table C.2). The centerline distributions of flame velocity and temperature are plotted in Figure 52. Figure 53 shows that solids concentrations of the thermally assisted flames are lower than those of the corresponding baseline flames. Furthermore, the carbon burnout of the thermally assisted flames is better than that of the baseline flames.

As discussed in Section 4.4 and shown in Figure 48, high-speed cine films and photographs of the flames show a wider flame angle for the thermally assisted flames compared to that for the baseline flames, and the corresponding improved flame stability is manifested by the reduced ignition distance and the absence of low frequency fluctuations at the

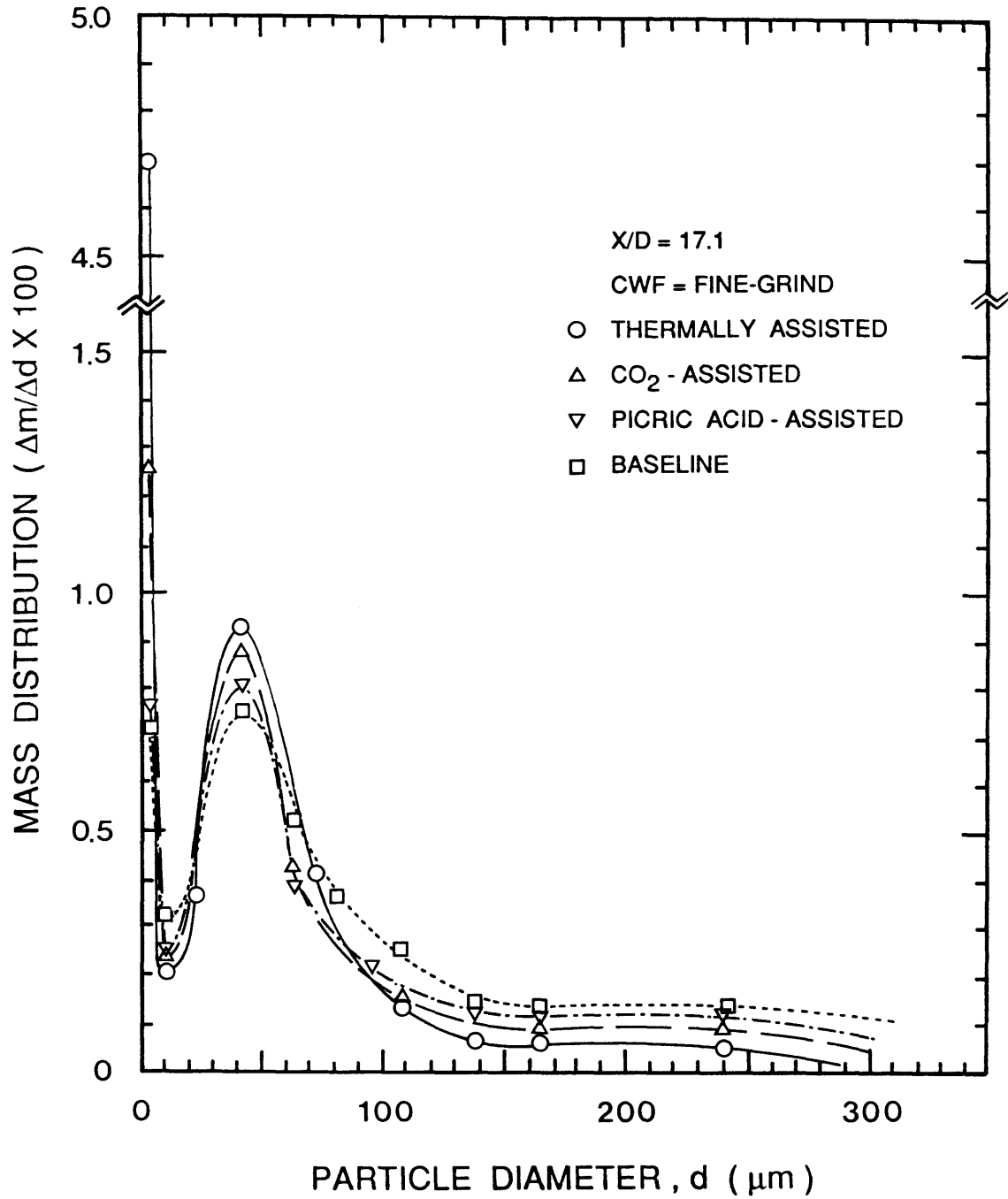


Figure 50. Particle Size Distributions of Fly-Ash and Residual Char (Unburned Carbon) for Various Fuel Treatments (Fine-Grind CWF, Flame Thermal Input = 1.0 MW)

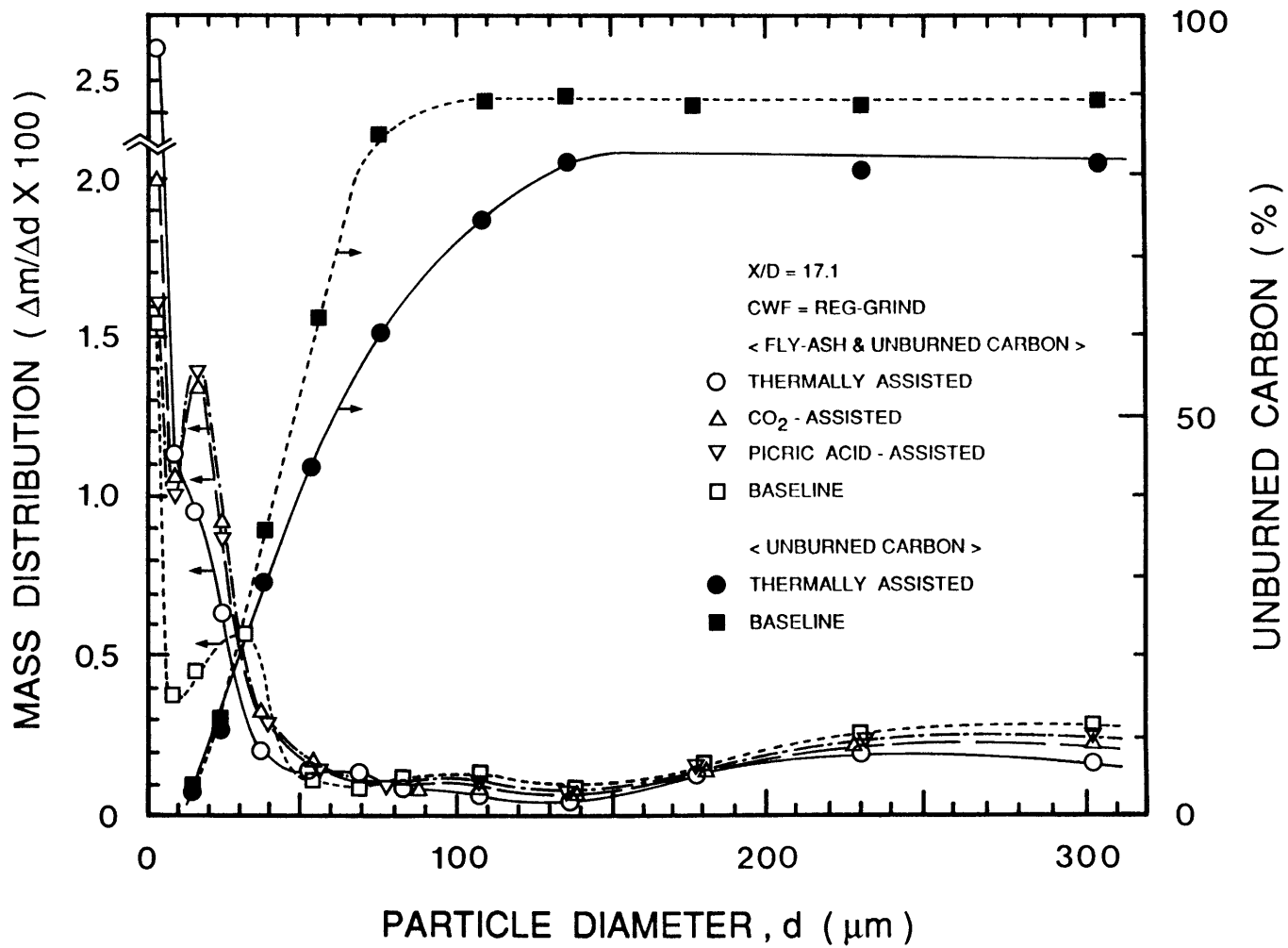


Figure 51. Particle Size Distributions of Fly-Ash and Residual Char (Unburned Carbon) for Various Fuel Treatments (Regular-Grind CWF, Flame Thermal Input = 1.3 MW)

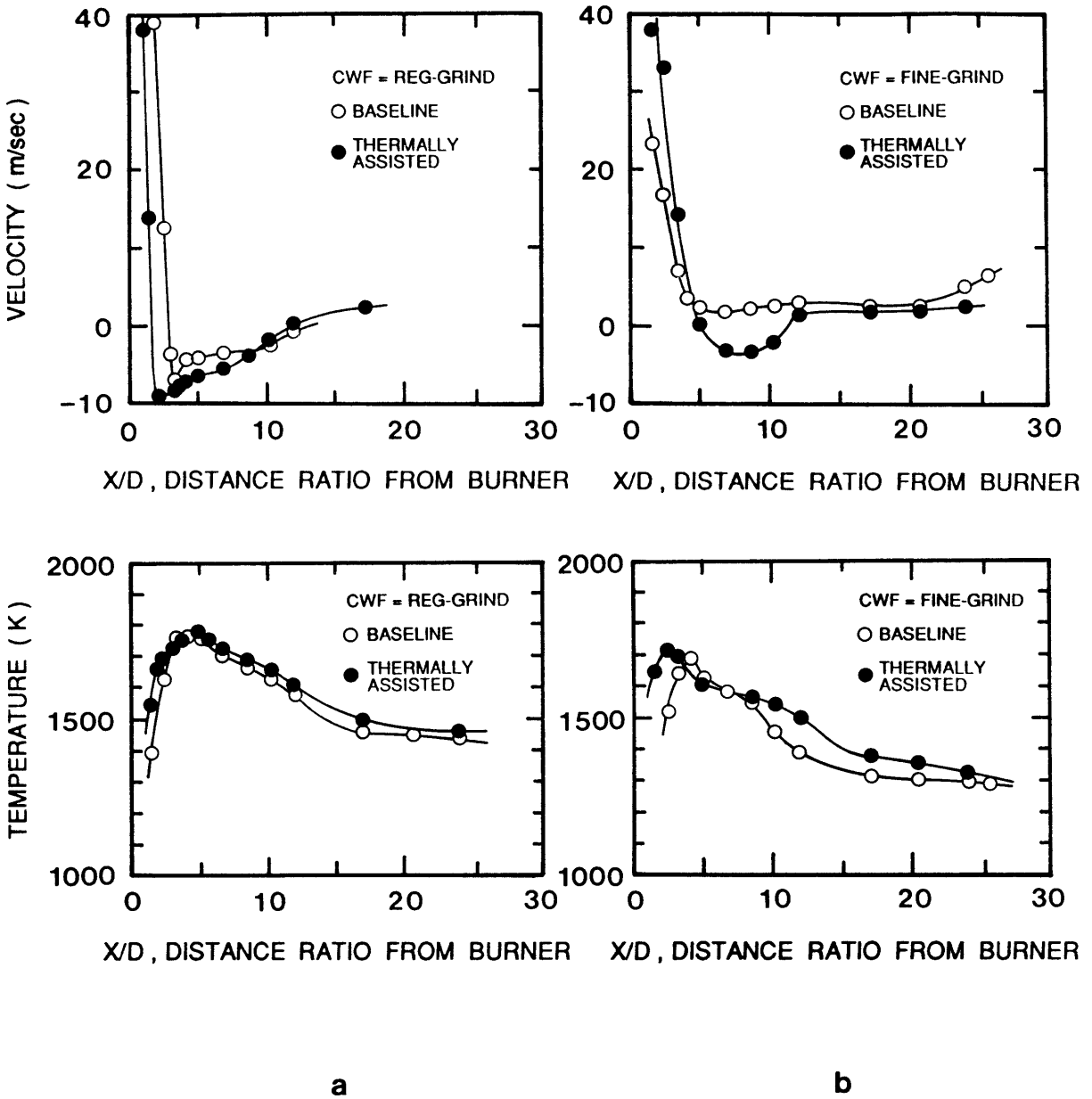
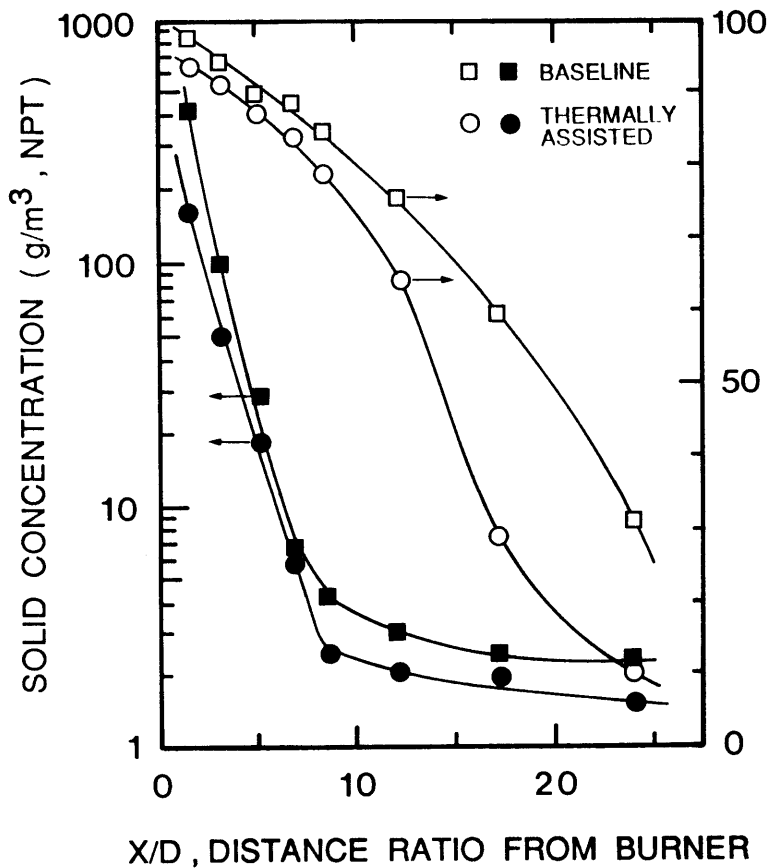
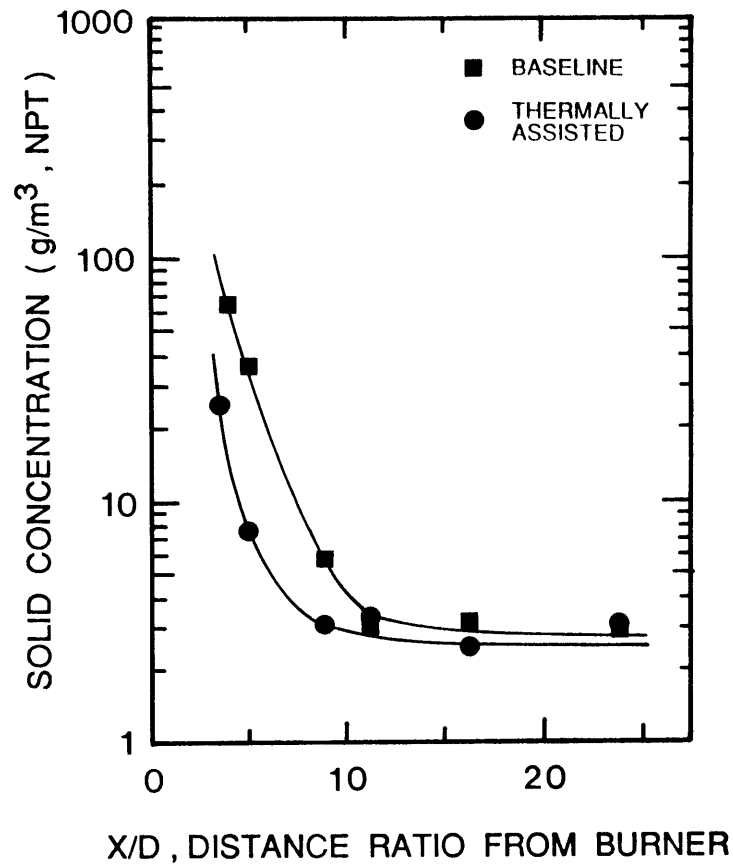


Figure 52. Comparisons of Gas Temperature and Gas Velocity at Centerline of Flames of Regular- and Fine-Grind CWFs for Baseline and Thermally Assisted Flames  
 (a) Regular-Grind CWF, Flame Thermal Input = 1.3 MW,  
 (b) Fine-Grind CWF, Flame Thermal Input = 1.0 MW



a



b

Figure 53. Solids Concentrations and Carbon Conversion Efficiencies at Centerline of Flames of Regular- and Fine-Grind CWFs for Thermally Assisted and Baseline Flames  
 (a) Fine-Grind CWF, Flame Thermal Input = 1.0 MW,  
 (b) Regular-Grind CWF, Flame Thermal Input = 1.3 MW

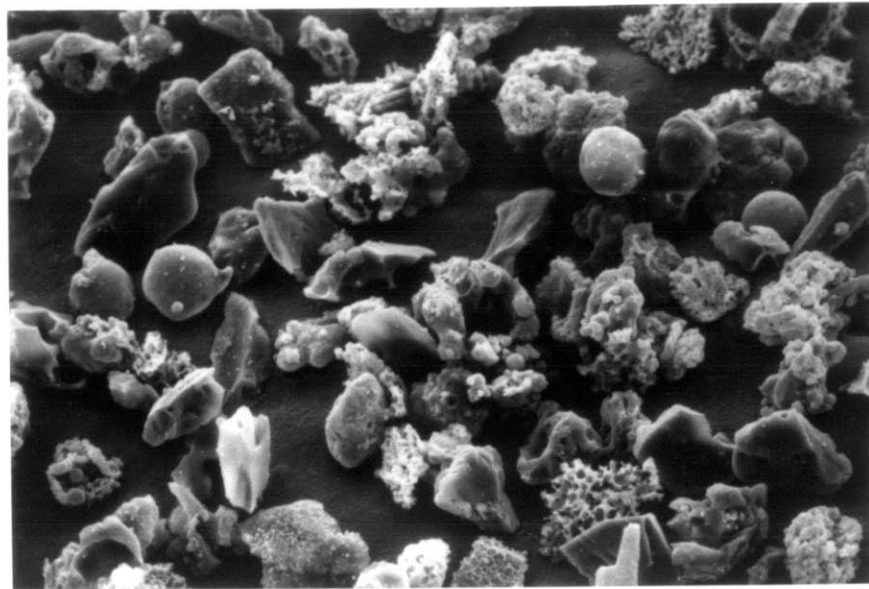
flame front. The improvement in combustion characteristics is also illustrated by Scanning Electron Micrographs (SEM) taken for the flame solids sampled at the centerline of the thermally assisted and baseline flames for  $X/D = 17.1$ . Comparisons of the SEMs of flame solids in the size ranges of 30-45  $\mu\text{m}$ , 150-212  $\mu\text{m}$ , 212-250  $\mu\text{m}$ , and 250-355  $\mu\text{m}$  in Figures 54, 55, 56 and 57, respectively. They show that the state of oxidation progressed much further in the thermally assisted flames compared to the flames without fuel treatment.

The deposition rates of fly-ash on tubes were also examined for the baseline and thermally assisted flames. The ceramic tube, which was thermally equilibrated with the flame gases, was inserted perpendicular to the flame axis for 20 minutes. The transverse distribution of the deposition rate could be determined from the amount of fly-ash deposited per unit length of deposition probe.

The effect of fuel treatment of CWF by heating on the deposition rate for tube diameters of 25.4 mm and 6.4 mm is shown in Figure 58. The deposition rate for the thermally assisted flames for the 25.4 mm tube is found to be less than that for the baseline flames at all transverse locations by a factor of 0.5 to 0.6. However, the thermally assisted flames give a higher deposition rate for the 6.4 mm tube compared to the baseline flames in the region close to the flame axis. This may be related to the reduction of the mass fraction of the larger particles which are capable of eroding the deposited fly-ash upon their impaction.

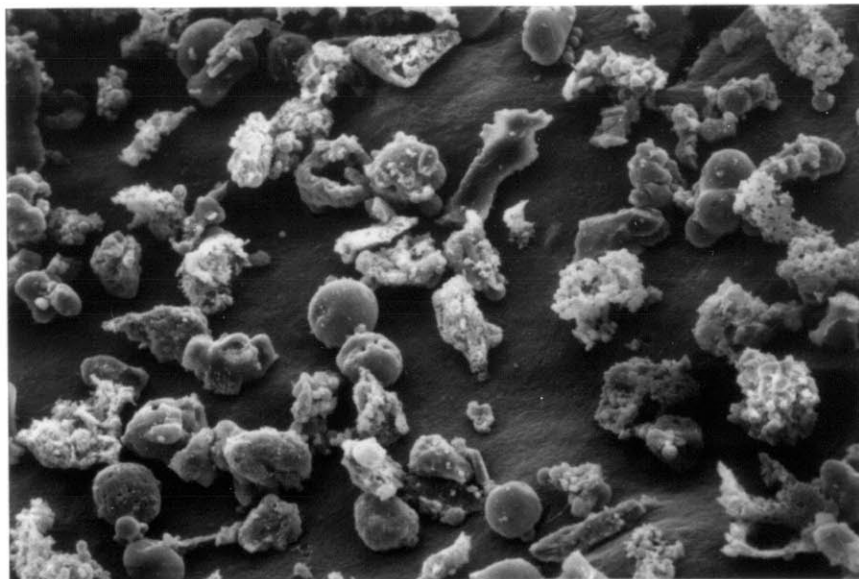
Finally, the comparisons of experimental data concerning gas composition, solids concentration, and carbon conversion efficiency for the baseline flames and for the flames with the three fuel treatments are





a

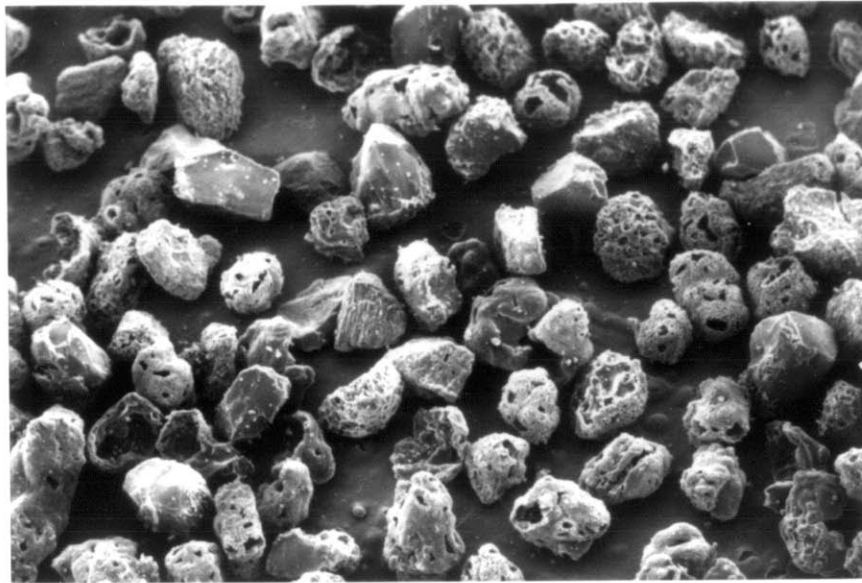
100  $\mu\text{m}$



b

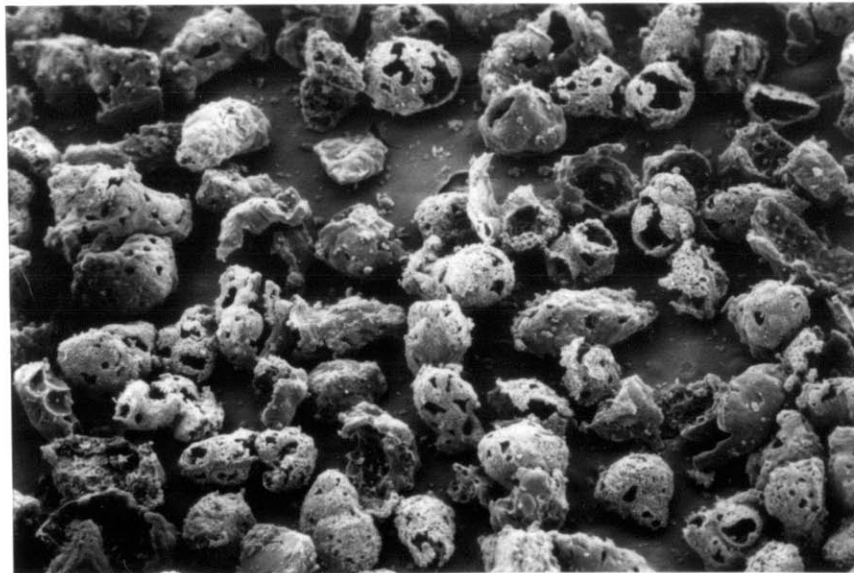
100  $\mu\text{m}$

Figure 54. SEM Photographs of Particles Collected from Centerline of Flames at  $X/D = 17.1$  (30-45  $\mu\text{m}$  Particle Size)  
(a) Baseline, (b) Thermally Assisted



a

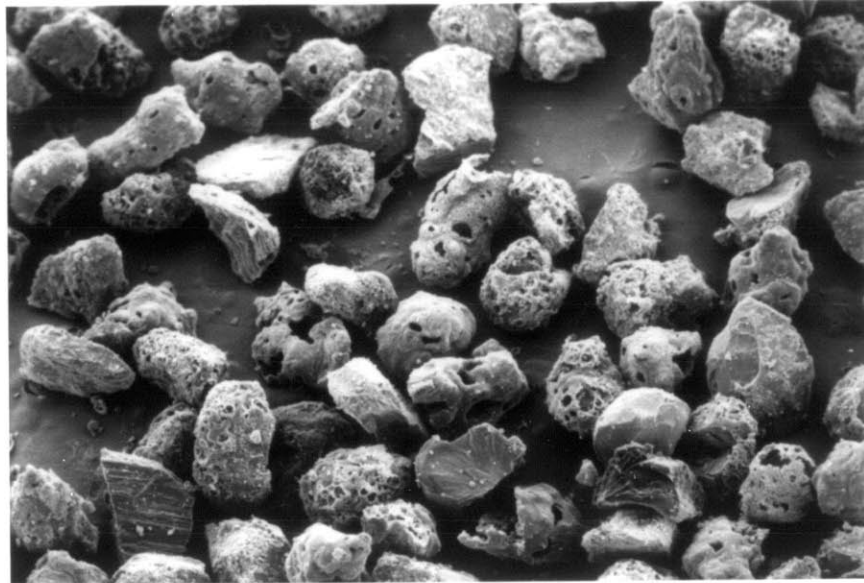
500  $\mu\text{m}$



b

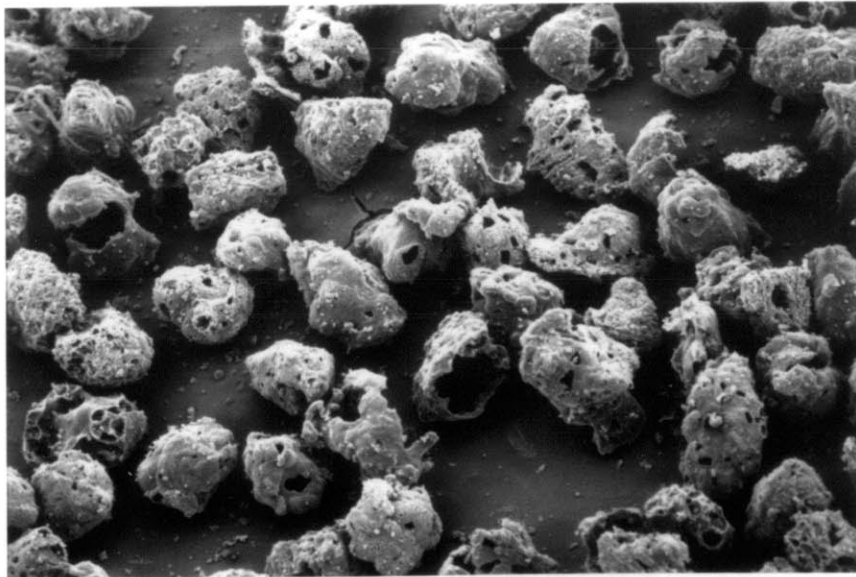
500  $\mu\text{m}$

Figure 55. SEM Photographs of Particles Collected from Centerline of Flames at  $X/D = 17.1$  (150-212  $\mu\text{m}$  Particle Size)  
(a) Baseline, (b) Thermally Assisted



a

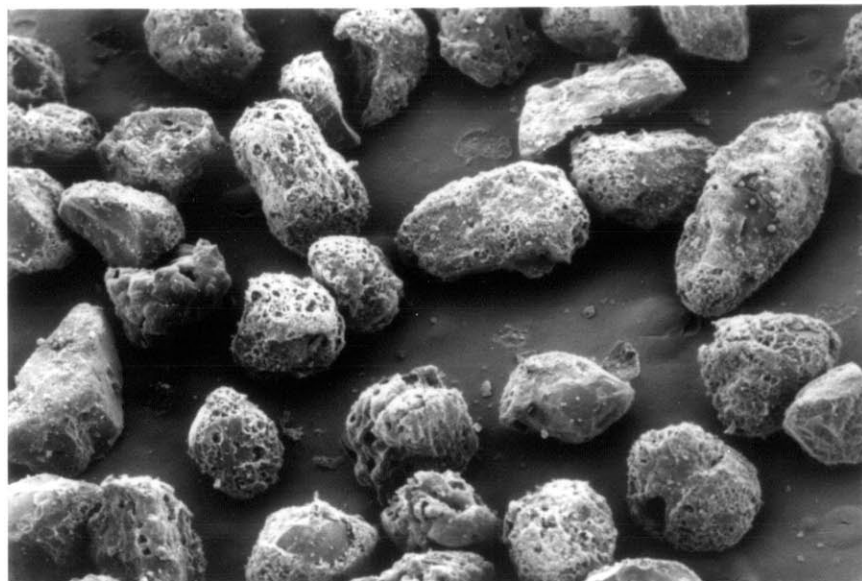
500  $\mu\text{m}$



b

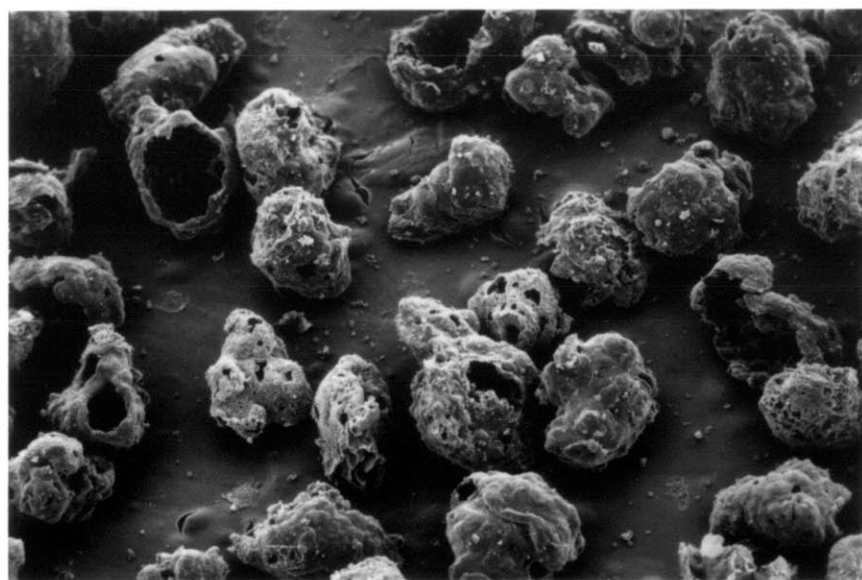
500  $\mu\text{m}$

Figure 56. SEM Photographs of Particles Collected from Centerline of Flames at  $X/D = 17.1$  (212-250  $\mu\text{m}$  Particle Size)  
(a) Baseline, (b) Thermally Assisted



a

500  $\mu\text{m}$



b

500  $\mu\text{m}$

Figure 57. SEM Photographs of Particles Collected from Centerline of Flames at  $X/D = 17.1$  (250-355  $\mu\text{m}$  Particle Size)  
(a) Baseline, (b) Thermally Assisted

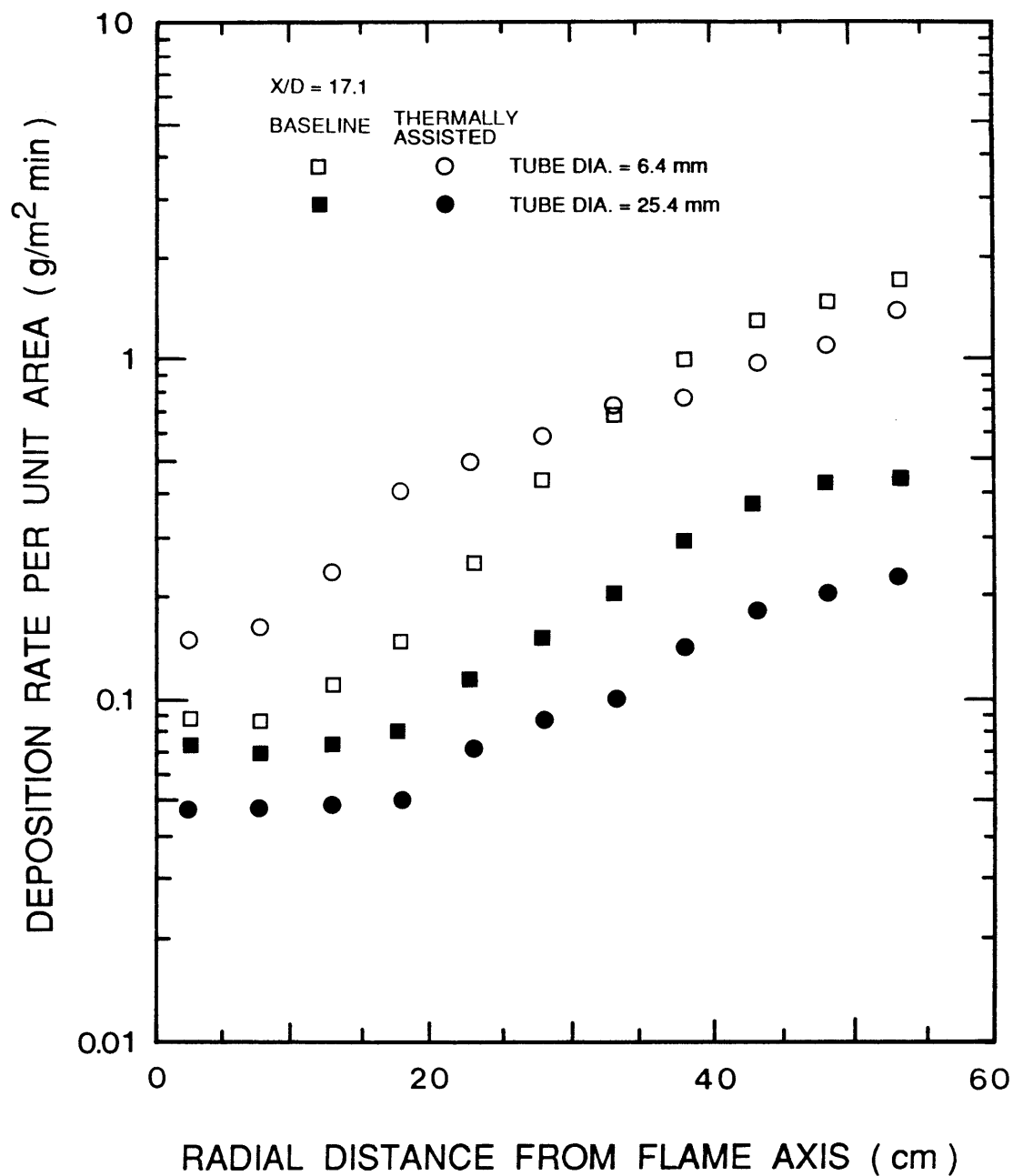


Figure 58. Transverse Distributions of Fly-Ash Deposition Rate per Unit Area of Ceramic Tubes at Axial Distance Ratio of X/D = 17.1 for Baseline and Thermally Assisted Flames

made in Tables 5 and 6 for the fine-grind and regular-grind CWFs, respectively. The improvement in carbon conversion efficiency due to fuel treatment is accompanied by the corresponding reduction in O<sub>2</sub> concentration at the furnace exit. The lower O<sub>2</sub> concentration is concomitant with the higher CO<sub>2</sub> concentration and the lower final concentration of CO. The data show that the thermally assisted atomization is the most effective method in improving the carbon conversion efficiency. CO<sub>2</sub>-assisted atomization is found to be slightly more effective than chemically assisted atomization by picric acid addition.

### 5.3 Summary

Three methods of fuel treatments which induce flash-atomization to improve the quality of spray droplet p.s.d., and thereby yield finer fly-ash p.s.d., were studied in the CRF. The three methods include 1) thermally assisted atomization, 2) CO<sub>2</sub>-assisted atomization, and 3) chemically assisted atomization. In-flame measurements made during combustion experiments in the CRF served to determine the influence of these three methods of flash-atomization on flame stability, carbon burnout, and resultant fly-ash p.s.d.

During the combustion experiments, the characteristics of the three modes of flash-atomization were studied to identify the effectiveness of each method in reducing the fly-ash p.s.d. The most effective method was the thermally assisted atomization, judging by reduction of solids concentration and p.s.d. determined along the length of the flames. While not as effective as thermally assisted atomization, CO<sub>2</sub>-assisted atomization, and chemically assisted atomization brought beneficial

Table 5

Summary of Experimental Data from Combustion Tests with  
Various Fuel Treatments for Fine-grind CWF

Treatment	Base		CO <sub>2</sub>		Picric Acid		Heating	
	27°C		3.9 g/kg CWF		0.35 g/kg CWF		108°C	
Axial Position X/D, D = 0.176 m	3.3	17.1	3.3	17.1	3.3	17.1	3.3	17.1
Temperature (K)	-	1352	-	1353	-	1354	-	1353
O <sub>2</sub> (%)	-	3.52	-	2.70	-	3.30	-	0.71
CO (%)	-	0.0202	-	0.0067	-	0.0076	-	0.0035
CO <sub>2</sub> (%)	-	14.57	-	15.57	-	14.98	-	17.21
Solid Concentration* (g/m <sup>3</sup> , NTP)	63.9	20.1	58.8	8.7	57.0	8.8	22.7	2.6
Ash (%)	5.7	-	7.9	-	7.4	-	11.0	-
Carbon Conversion † Efficiency	3.7	-	32.1	-	26.3	-	52.9	-

CWF Type: ARC Regular Splashdam

\* Water-quench solids sampling probe (X/D = 3.3)  
Steam-heated solids sampling probe (X/D = 17.1)

† Carbon conversion efficiency at combustin exit (X/D = 28)  
for all cases was greater than 99%.

Table 6

Summary of Experimental Data from Combustion Tests with  
Various Fuel Treatments for Regular-Grind CWF

Treatment	Base		CO <sub>2</sub>		Picric Acid		Heating	
	27°C		3.9 g/kg CWF		0.35 g/kg CWF		110°	
Axial Position X/D, D = 0.176 m	3.3	17.1	3.9	17.1	3.3	17.1	3.3	17.1
Temperature (K)	-	1459	-	1486	-	1490	-	1496
O <sub>2</sub> (%)								
CO (%)	-	0.0071	-	0.0071	-	0.0072	-	0.0057
CO <sub>2</sub> (%)								
Solid Concentration* (g/m <sup>3</sup> , NTP)	99.0	2.3	79.01	1.9	80.7	2.2	52.2	1.5
Ash (%)	5.8	39.0	7.4	47.6	6.7	44.0	8.0	71.5
Carbon Conversion † Efficiency	4.4	90.8	26.3	93.5	18.0	92.5	32.3	97.7

CWF Type: ARC Fine Splashdam

\* Water-quench solids sampling probe (X/D = 3.3)  
Steam-heated solids sampling probe (X/D = 17.1)

† Carbon conversion efficiency at combustin exit (X/D = 28) for all cases was greater than 99%.



results. The improvement in atomization quality by CO<sub>2</sub> injection was slightly greater in the flame than in sprays atomized into the cold environment of the STF. The chemically assisted atomization was ranked third, behind thermally assisted atomization and CO<sub>2</sub>-assisted atomization.

CHAPTER 6  
CONCLUSIONS

(Flash-) Atomization Study of CWF

- (1) Coal particle size distribution, solid loading, and chemical additive in CWF have a strong influence on the non-Newtonian viscosity of CWF, but little influence on the surface tension of CWF.
- (2) CWF viscosity at high shear rate as well as air-to-fuel ratio (AFR) are important factors to determine mean droplet size (MMD) of CWF spray.
- (3) The representative shear rate during CWF atomization is found to be in the range of  $2 \times 10^4$  to  $6 \times 10^4 \text{ sec}^{-1}$  for the OR-KVB, twin-fluid atomizer.
- (4) The mean droplet size (MMD) of CWF spray is correlated with the properties and velocities of CWF and atomizing air for the OR-KVB, twin-fluid atomizer.
- (5) Flash-atomization, induced by fuel treatments, improves the atomization quality by further disintegration of the atomized CWF droplets.

- (6) During flash-atomization the spray angle is found to increase with superheat of liquid (fuel).
- (7) The change of spray angle due to flash-atomization is correlated with superheat of liquid (fuel) and mass flow rates of both liquid (fuel) and atomizing air for water spray.

Combustion Study of CWF with Fuel Treatments

- (8) Thermally assisted atomization by CWF preheating above 100°C significantly improves carbon conversion efficiency, flame stability, and reduction of fly-ash particle size.
- (9) CO<sub>2</sub>-assisted atomization and chemically assisted atomization (picric acid additive) give measurable improvements in combustion characteristics.

## REFERENCES

1. Beér, J.M., "Coal-water Fuel Combustion: Fundamentals and Application, A North American Review", Second European Conference on Coal Liquid Mixtures, London, England, September 1985.
2. Farmayan, W.F., Walsh, P.M., Teare, J.D., and Beér, J.M., "Coal-Water Slurry Ignition and Flame Stability: Mechanisms and Effects of Major Input Variables", ASME Winter Annual Meeting, New Orleans, December 9-14, 1984.
3. Farmayan, W.F., Srinivasachar, S., Monroe, L., DiTaranto, F., Teare, J.D., and Beér, J.M., "NO<sub>x</sub> and Carbon Emission Control in Coal-Water Slurry Combustion", 6th International Symposium on Coal Slurry Combustion and Technology, Orlando, Florida, June 25-27, 1984.
4. Swithenbank, J., Beér, J.M., Taylor, D.S., Abbot, D., and McCreath, G.C., "A Laser Diagnostic Technique for Measurement of Droplet and Particle Size Distribution", AIAA 14th Aerospace Sciences Meeting, Washington, D.C., AIAA Paper No. 76-69, pp. 1-9, January 1976.
5. Dodge, L.G., "Change of Calibration of Diffraction-Based Particle Sizers in Dense Sprays", Optical Engineering, Vol. 23, No. 6, 1984.
6. Yu, T.U., Rah, S.C., Kang, S.W., and Beér, J.M., "Measurement of Viscosity of Coal-Water Fuels at High Shear Rate", 8th International Symposium on Coal Slurry Preparation and Utilization, Florida, May 1986.
7. Lefebvre, A.H., "Gas Turbine Combustion", McGraw-Hill Book Company, 1983.
8. Lefebvre, A.H., "Airblast Atomization", Progress in Energy and Combustion Science, Vol. 6, pp. 233-261, 1980.
9. Borio, R.W., Smith, D.A., and LaFlesh, R.C., "Development and Comparative Testing of Commercial Scale Atomizers for Slurry Fuels", 6th International Symposium on Coal Slurry Combustion and Technology, Orlando, Florida, June 25-27, 1984.
10. Rasfjord, T.J., "Atomization of Coal Water Mixtures: Evaluation of Fuel Nozzles and Cellulose Gum Simulant", ASME Paper No. 85-GT-88, Gas Turbine Conference and Exhibit, Houston, TX, March 1985.
11. Chigier, N. and Meyer, P.L., "Atomization of Coal-Water Slurries", 6th International Symposium on Coal Slurry Combustion and Technology, Orlando, Florida, June 25-27, 1984.

12. Chigier, N. and Meyer, P.L., "Photographic and Malvern Analysis of Coal-Water Slurry Atomization", 7th International Symposium on Coal Slurry Fuels Preparation and Utilization, New Orleans, LA, May 1985.
13. Sommer, M.T. and Matsuzaki, Y., "Mechanisms of Effective Coal/Water Slurry Atomization", American Flame Research Committee Symposium on Combustion Diagnostics, Akron, OH, October 1983.
14. Smith, C.F., Sojka, P.E., and Lefebvre, A.M., "Investigation of Spray Characteristics of Coal Water Slurry Fuels", 6th International Symposium on Coal Slurry Combustion and Technology, Orlando, Florida, June 25-27, 1984.
15. Daley, R.D., Farthing, G.A., and Vecci, S.J., "Coal-Water Slurry Evaluation Volume 2: Laboratory and Combustion Test Results", Electric Power Research Institute, CS-3413, 1984.
16. Tsai, S.C. and Knell, E.W., "Rheology and its Effects on Atomization of Coal Water Slurry", 1st Pittsburgh Coal Conference, Pittsburgh, PA, Sept 1984.
17. Lefebvre, A.H. and Miller, D., "The Development of an Air Blast Atomizer for Gas Turbine Application", CoA-Report-AERO-193, College of Aeronautics, Cranfield, Bedford, England, 1966.
18. Yu, T.U., Kang, S.W., and Beér, J.M., "Fuel Type Effects on Coal-Water Slurry Atomization", AIAA-86-0298, AIAA 24th Aerospace Sciences Meeting, Reno, Nevada, Jan. 6-9, 1986.
19. Yu, T.U., Kang, S.W., Beér, J.M., Sarofim, A.F. and Teare, J.D., "Atomization Quality and High Shear Rate Viscosity of Coal-Water Fuels", 12th International Conference on Slurry Technology, March 1987.
20. Miesse, C.C., "Recent Advances in Spray Technology", Appl. Mech. Reviews, Vol. 9, No. 8, pp 321-323, 1956.
21. Ohnesorge, W., "Formation of Drops by Nozzles and the Breakup of Liquid Jets", Z. Angew. Math. Mech., Vol. 16, 1936.
22. Rohsenow, W.M., "Nucleation with Boiling Heat Transfer", ASME 70-HT-18, pp. 2-11, 1970.
23. Rohsenow, W.M., Developments in Heat Transfer, MIT Press, 1964.
24. Thirunavukkarasu, K., "Bubble Growth from a Cavity at a Solid Surface", ASME 70-HT-13, pp. 1-9, 1970.
25. Zwick, S.A. and Plesset, M.S., "On the Dynamics of Small Vapor Bubbles in Liquids", J. Math. Phys., Vol 33, pp. 308-330, 1955.
26. Plesset, M.S. and Zwick, S.A., "A Nonsteady Heat Diffusion Problem with Spherical Symmetry", J. Appl. Phys., Vol. 23, pp. 95, 1952.

27. Plesset, M.S. and Zwick, S.A., "The Growth of Vapor Bubbles in Superheated Liquids", *J. Appl. Phys.*, Vol. 25, pp. 493-400, 1954.
28. Forster, H.K. and Zuber, N., "Growth of a Vapor Bubble in a Superheated Liquid", *J. Appl. Phys.*, Vol. 25, pp. 474-478, 1954.
29. Scriven, L.E., "On the Dynamics of Phase Growth", *Chem. Eng. Sci.*, Vol. 10, pp. 1, 1959.
30. Birkhoff, G., Margulies, R.S. and Horning, W.A., "Spherical Bubble Growth", *Phys. of Fluids*, Vol. 1, pp. 201 1958.
31. Staniszewski, B.E., "Nucleate Boiling Bubble Growth and Departure", Tech. Report. 16, DSR 7673, Office of Naval Research Contract NONR-1841 (39), MIT Heat Transfer Lab., Aug. 1959.
32. J.H. Lienhard, "An Influence of Superheat Upon the Spray Configuration of Superheated Liquid Jets", *Journal of Basic Engineering*, Transactions of the ASME, pp 685-687, Sept. 1966.
33. Yu, T.U., Kang, S.W., Toqan, M.A., Walsh, P.M., Beér, J.M., and Sarofim, A.F., "Secondary Atomization of Coal-Water Slurry Fuels", Seventh International Symposium on Coal Slurry Combustion and Technology, New Orleans, Louisiana, May 22-24, 1985.
34. Yu, T.U., Kang, S.W., Toqan, M.A., Walsh, P.M., Teare, J.D., Beér, J.M., and Sarofim, A.F., "Disruptive Atomization and Combustion of CWF", 8th International Symposium on Coal Slurry Preparation and Utilization, Orlando, Florida, May 27-30, 1986.
35. Yu, T.U., Kang, S.W., Toqan, M.A., Walsh, P.M., Teare, J.D., Beér, J.M. and Sarofim, A.F., "Effect of Fuel Treatment on Coal-Water Fuel Combustion", 21st Symposium (International) on Combustion, West Germany, August, 1986.
36. Merten, M. and Homer, M., Section in Final Report on "Combustion of Coal/Water Suspension Power Plants", Steinkohlen bergbauverein (Lignite Mining Association), Essen, Germany, January, 1972.
37. Daley, R.D., Farthing, G.A., Jr. and Vecchi, S.J., Coal Water Slurry Evaluation, Vol. 2, Final Report CS-3413, Research Project 1895-3 EPRI Palo Alto, CA 1984.
38. Reid, R.C., Sarofim, A.F., and Beér, J.M., MIT, Cambridge, MA., private communication 1983.
39. Olen, K.R., "Chemically Enhanced Combustion of Water-Slurry Fuels", U.S. Patent No. 4,445.150, June 19, 1984.
40. Skelland, A.H.P., "Non-Newtonian Flow and Heat Transfer", Wiley, New York, N.Y., 1967.

APPENDICES

## APPENDIX A

## PRINCIPLE OF LASER DIFFRACTION SPRAY ANALYZER

The operational principle of the laser diffraction spray analyzer is based on the Fraunhofer diffraction pattern superimposed on the geometrical image, produced by the droplets in the path of the monochromatic coherent light beam. The diffraction pattern is large compared to the image. The resulting light energy distribution is collected through a lens by a multi-element detector consisting of 31 semi-circular rings. The lens acts effectively as a Fourier transform lens by bringing all the scattered light from droplets at various locations in the beam into the focal plane of the lens. For monosize particles, the light distribution pattern at the focal plane would consist of alternate bright and dark fringes, the position of which would depend upon the size of the droplets. When droplets of many different sizes are present an aggregate light energy distribution is obtained from which the droplet size distribution can be calculated. The light energy falling on one ring of the photo-detector located between radii  $s_i$  and  $s_j$  can be expressed according to<sup>(4)</sup>

$$E_{i,j} = C \sum_{k=1}^M N_k X_k \left[ (J_0^2 + J_1^2)_{s_i} - (J_0^2 + J_1^2)_{s_j} \right] \quad \text{eq. (A.1)}$$

where  $C$  is a constant,  $N$  is the number of droplets of size  $X$ ,  $J_0$  and  $J_1$  are Bessel functions, and  $M$  the number of drop size ranges. The total light energy distribution is also the sum of the product of the energy distribution for each size range and the weight or volume fraction in that range. This can be expressed in the form of a matrix equation as



follows:

$$E = TW \quad \text{eq. (A.2)}$$

where  $W$  is the weight fraction and  $T$  contains the coefficients which define the light energy distribution curves for each droplet. Rewriting the above equation as  $W = T^{-1}E$ , then with the knowledge of the inverse matrix  $T^{-1}$  the weight distribution can be calculated from the measured light energy  $E$ . An approach to the solution of eq. (A.2) is to assume a form for  $W$  and adjust the parameters by iterative means until the sum of the squared errors  $\Sigma(E-TW)^2$  is a minimum. The Malvern Instrument (Model 1800) adopts a Rosin-Rammler weight distribution for  $W$ . Note that other distribution functions such as the normal distribution could be used. To determine the diffraction pattern the 30 semi-annular detectors are scanned sequentially by a solid state switch, controlled by a microprocessor, both with and without the droplets present in the beam.

If, for example, the Rosin-Rammler distribution is postulated, then in the processing of the signal the microprocessor assumes that the size distribution is a good approximation to:

$$R = 1 - v = \exp \left[ - (X/\bar{X})^n \right] \quad \text{eq. (A.3)}$$

where  $R$  is the weight fraction contained in particles of diameters greater than  $X$ ,  $\bar{X}$  is the Rosin-Rammler mean diameter (for which  $R = 36.8\%$ ), and the exponent  $n$  indicates the spread of diameters about the mean. For a fuel spray typical values of  $n$  will be between 1.1 and 3, and can increase to 15 to 20 for near monosize droplets.

The microprocessor selects initial values of  $X$  and  $n$  and the light energy distribution corresponding to the Rosin-Rammler distribution is

calculated through eq. (A.2). A least squares error criterion is used to determine the quality of fit between calculated and measured light energy distribution. The parameters  $X$  and  $n$  are then iteratively adjusted to give the best fit with minimum error. The Rosin-Rammler distribution in 15 size ranges together with the calculated and measured light energy distribution is printed by the microprocessor using the appropriate values of  $\bar{X}$  and  $n$ .

Using  $\bar{X}$  and  $n$ , the mass mean diameter (MMD), which is the droplet diameter below or above which lies 50 percent of the mass of the droplets (i.e.,  $R = 0.5$ ), can be calculated by

$$\text{MMD} = \bar{X} [\ln 0.5]^{-\frac{1}{n}} \quad \text{eq. (A.4)}$$

The Sauter mean diameter, SMD, also can be related by

$$\text{SMD} = \frac{\bar{X}}{\Gamma(1-\frac{1}{n})} \quad \text{eq. (A.5)}$$

where  $\Gamma$  is the gamma function. The SMD is the diameter of a droplet having the same volume/surface ratio as the entire spray.

The mass distribution of a spray as the weight fraction in any size increment is given by the derivative of eq. (A.3), i.e.,

$$\frac{dv}{dx} = (n/\bar{X}) (X/\bar{X})^{n-1} \exp \left[ - (X/\bar{X})^n \right] \quad \text{eq. (A.6)}$$

## APPENDIX B

## PRINCIPAL OF CAPILLARY TUBE VISCOMETER

The essential feature of the capillary tube viscometer is the measurement of the frictional pressure drop associated with the laminar flow of fluid at a given rate through a long, smooth, cylindrical tube of known dimensions. Detailed discussions on theoretical backgrounds for the non-Newtonian fluid, flowing through the capillary tube, can be found elsewhere<sup>(40)</sup>. The only results relevant to the present study are summarized here<sup>(6)</sup>.

Under conditions of steady, fully developed flow through a capillary tube, the shear stress at the tube wall can be expressed as

$$\tau_w = \frac{D\Delta P_f}{4L} \quad \text{eq. (B.1)}$$

and the shear rate at the tube wall for a steady, laminar flow of time-independent fluid can be expressed as

$$\dot{\gamma}_w = \frac{3n'+1}{4n'} \frac{8V}{D} \quad \text{eq. (B.2)}$$

where

$$n' = \frac{d \ln (D\Delta P_f/4L)}{d \ln (8V/D)} \quad \text{eq. (B.3)}$$

By analogy with Newtonian fluids an apparent viscosity is defined as

$$\mu_a = \tau_w / \dot{\gamma} \quad \text{eq. (B.4)}$$

for the corresponding shear rate.

When the measurements made on the capillary tube viscometer are converted into a logarithmic plot of  $D\Delta P_f/4L$  versus  $8V/D$ ,  $n'$  is evaluated as the slope of the curve at a particular value of  $\tau_w$ . The corresponding wall shear rate and apparent viscosity are found from eqs. (B.2) and (B.4), respectively. Eq. (B.3) shows that it is also possible to write

$$\tau_w = \frac{D\Delta P_f}{4L} = K' \left(\frac{8V}{D}\right)^{n'} \quad \text{eq. (B.5)}$$

Since eq. (B.2) is based on the assumption of laminar flow in the tube, this condition can be confirmed by checking that the generalized Reynolds number is less than 2100:

$$\text{Re}_{\text{gen}} = \frac{D^{n'} V^{2-n'} \rho}{K' 8^{n'-1}} < 2100 \quad \text{eq. (B.6)}$$

In practice the pressure drop measured over the capillary tube can be expressed as

$$\Delta P = \Delta P_f + \Delta P_{f,\text{excess}} \quad \text{eq. (B.7)}$$

where  $\Delta P_f$  is the frictional pressure drop in fully developed flow and  $\Delta P_{f,\text{excess}}$  is the excess frictional pressure drop because of entrance and additional friction effects. The excess frictional pressure drop should be constant when measurements of  $\Delta P$  are made for two tubes of different lengths,  $L_1$  and  $L_2$ , but with the same diameter and at the same flow rate (i.e. same average velocity). Therefore, the excess frictional pressure drop can be cancelled out from eq. (B.7) by subtracting the two measured values of pressure drop.

$$\Delta P_{21} = \Delta P_2 - \Delta P_1 = (\Delta P_f)_2 - (\Delta P_f)_1 \quad \text{eq. (B.8)}$$

The values of  $\Delta P_{21}$  and  $L_{21} = L_2 - L_1$  can then be used in place of  $\Delta P_f$  and  $L$ , respectively, in eqs. (B.1) through (B.5) to determine the apparent viscosity and shear rate.

## APPENDIX C

## EXPERIMENTAL DATA OF IN-FLAME MEASUREMENTS

The following four tables summarize the experimental data obtained by in-flame measurements in the Combustion Research Facility. Centerline distributions of flame temperature, velocity, gaseous species concentrations and particle concentrations are tabulated. Some radial distributions are included in Table C.2.

Table C.1

Experimental Data of In-Flame Measurements, (Fine-grind CWF, Baseline)

Distance from Air Nozzle		Gas Temp.	Gas Velocity	Mole Fractions (as measured, dry basis)					Particle Concentration (g/m <sup>3</sup> , NTP)	
X(m)	X/D	T(K)	u <sub>z</sub> (m/s)	X <sub>O<sub>2</sub></sub>	X <sub>CO<sub>2</sub></sub>	X <sub>CO</sub>	X <sub>NO</sub>	X <sub>SO<sub>2</sub></sub>	ρ <sub>coke</sub>	ρ <sub>ash</sub>
				(%)	(%)	(%)	(ppm)	(ppm)		
0.17	1.0	-	103.0	-	-	-	-	-	-	-
0.27	1.5	-	23.1	-	-	-	-	-	-	-
0.42	2.4	1515	16.0	-	-	-	-	-	-	-
0.57	3.3	1638	7.5	0.4	16.2	2.300	497	875	63.67	-
0.74	4.2	1681	4.0	-	-	-	-	-	-	-
0.88	5.0	1620	2.3	0.3	17.6	1.000	457	750	36.02	-
1.19	6.8	1580	1.9	1.7	16.7	0.111	500	625	-	-
1.49	8.5	1538	2.4	2.5	16.1	0.651	-	600	5.61	-
1.80	10.3	1450	2.6	2.3	16.3	0.028	-	500	-	-
2.09	11.9	1390	2.9	2.0	16.7	0.019	-	-	3.03	-
3.00	17.1	1309	2.5	2.0	16.6	0.006	492	0	3.20	-
3.61	20.6	1301	2.5	2.1	16.6	0.003	495	-	3.21	-
4.22	24.1	1297	5.4	-	-	-	-	-	3.23	-
4.52	25.8	1289	6.7	2.7	15.9	0.002	489	-	-	-

\*Centerline Measurement (Radial distance = 0 m)

Table C.2

Experimental Data of In-Flame Measurements, (Fine-grind CWF, Heating)

Radial Distance R(m)	Distance from Air Nozzle		Gas Temp. T(K)	Gas Velocity u (m/s)	Mole Fractions (as measured, dry basis)					Particle Concentration (g/m <sup>3</sup> , NTP)	
	X(m)	X/D			X <sub>O<sub>2</sub></sub> (%)	X <sub>CO<sub>2</sub></sub> (%)	X <sub>CO<sub>2</sub></sub> (%)	X <sub>NO</sub> (ppm)	X <sub>SO</sub> (ppm)	$\rho_{\text{coke}}$ <sup>+</sup>	$\rho_{\text{ash}}$
0	0.17	1.0	-	106.0	-	-	-	-	-	-	-
0	0.27	1.5	1645	38.2	-	-	-	-	-	-	-
0	0.42	2.4	1719	33.0	-	-	-	-	-	-	-
0	0.57	3.3	1697	14.3	1.6	14.9	1.150	700	525	26.21	-
0.1			1641	-4.1	6.4	12.5	0.056	580	513	9.47	-
0.2			1581	14.5	7.1	11.9	0.025	535	525	6.90	-
0.3			1570	11.8	6.1	12.9	0.012	550	538	4.36	-
0.4			1555	5.0	6.0	13.2	0.010	560	713	-	-
0	0.88	5.0	1600	0.0	1.8	16.1	0.320	590	650	7.24	-
0.1			1602	-3.9	2.9	15.5	0.073	610	625	5.03	-
0.2			1619	-2.9	3.7	14.8	0.017	600	625	4.78	-
0.3			1618	2.0	4.4	14.4	0.014	610	563	4.78	-
0.4			1593	7.1	5.0	13.7	0.015	600	550	-	-
0	1.19	6.2	1583	-3.4	3.0	15.5	0.040	590	650	-	-
0	1.49	8.5	1566	-3.0	3.3	15.3	0.040	570	620	2.89	-
0.2			1584	2.1	3.2	15.3	0.011	590	638	-	-
0.4			1589	2.8	3.6	14.9	0.008	600	650	2.53	-
0	1.80	10.3	1541	-1.8	3.4	15.1	0.015	-	625	-	-
0	2.09	11.9	1500	1.5	3.2	15.3	0.016	-	625	3.55	-
0	3.00	17.1	1377	2.1	2.9	15.7	0.007	505	663	2.60	-
0	3.61	20.6	1356	2.1	2.6	16.3	0.007	-	575	-	-
0	4.22	24.1	1326	2.8	2.6	15.9	0.008	-	675	3.33	-

Table C.3

Experimental Data of In-Flame Measurements, (Regular-grind CWF, Baseline)

Distance from Air Nozzle		Gas Temp. T(K)	Gas Velocity $u_z$ (m/s)	Mole Fractions (as measured, dry basis)					Particle Concentration (g/m <sup>3</sup> , NTP)	
X(m)	X/D			X <sub>O<sub>2</sub></sub> (%)	X <sub>CO<sub>2</sub></sub> (%)	X <sub>CO</sub> (%)	X <sub>NO</sub> (ppm)	X <sub>SO<sub>2</sub></sub> (ppm)	$\rho_{\text{coke}}$	$\rho_{\text{ash}}$
0.17	1.0	-	55.6	-	-	-	-	-	-	-
0.27	1.5	1393	44.6	-	-	-	-	-	423.73	-
0.42	2.4	1620	12.4	0.7	15.7	3.300	740	1125	-	-
0.57	3.3	1771	-6.9	0.8	17.0	1.600	750	775	99.00	-
0.74	4.2	1760	-4.3	0.5	17.7	0.800	690	763	-	-
0.88	5.0	1757	-4.2	0.4	18.1	0.900	630	788	28.66	-
1.19	6.8	1706	-3.7	1.8	17.2	0.093	710	600	6.92	-
1.49	8.5	1667	-3.7	3.6	15.5	0.027	740	525	4.30	-
1.80	10.3	1623	-2.6	3.1	16.1	0.016	740	538	3.04	-
2.09	11.9	1576	-0.9	2.8	16.3	0.011	720	575	-	-
3.00	17.1	1459	-	2.4	16.9	0.007	700	575	2.36	-
3.61	20.6	1450	-	2.5	16.7	0.006	710	588	-	-
4.22	24.1	1439	-	2.2	17.1	0.005	680	600	2.34	-



Table C.4

Experimental Data of In-Flame Measurements, (Regular-grind CWF, Heating)

Distance from Air Nozzle (m) X/D		Gas Temp. T(K)	Gas Velocity $u_z$ (m/s)	Mole Fractions (as measured, dry basis)					Particle Concentration ( $g/m^3$ , NTP)	
				$X_{O_2}$ (%)	$X_{CO_2}$ (%)	$X_{CO}$ (%)	$X_{NO}$ (ppm)	$X_{SO_2}$ (ppm)	$\rho_{coke}$	$\rho_{ash}$
0.17	1.0	-	43.6	-	-	-	-	-	-	-
0.27	1.5	1543	14.0	-	-	-	-	-	166.48	-
0.34	1.9	1664	-10.4	-	-	-	-	-	-	-
0.42	2.4	1688	-7.3	1.1	15.2	4.000	700	700	-	-
0.57	3.3	1727	-8.3	0.8	15.9	3.500	670	1150	52.25	-
0.63	3.6	1736	-7.8	-	-	-	-	-	-	-
0.74	4.2	1748	-7.0	0.9	16.9	1.300	700	525	-	-
0.88	5.0	1775	-6.4	0.9	17.3	0.900	690	575	19.29	-
0.94	5.4	1739	-5.7	0.7	17.8	0.700	670	575	-	-
1.19	6.8	1708	-5.5	2.1	17.4	0.175	710	575	5.84	-
1.49	8.5	1681	-4.0	2.9	15.9	0.037	710	600	2.52	-
1.80	10.3	1655	-2.1	2.5	16.8	0.025	710	625	1.44	-
2.09	11.9	1610	0	2.4	16.9	0.013	720	588	-	-
3.00	17.1	1490	2.2	2.2	16.8	0.006	710	638	2.00	-
4.22	24.1	1460	-	1.8	17.4	0.007	670	638	1.50	-

## BIOGRAPHICAL NOTE

Shin-Won Kang was born in Seoul, Korea, on September 28, 1955. He attended Kyung-Gi Middle School and Kyung-Gi High School in Seoul, Korea.

He graduated Cum Laude in Mechanical Engineering from Seoul National University in 1979. He worked for three years in the Korean Air Force Headquarters and was honorably discharged in 1982.

He received a master's degree in Mechanical Engineering from M.I.T. in 1984. His Thesis, "Pool Heat Transfer in a Simulated PWR Pressurizer", was supervised by Prof. Peter Griffith. He authored a paper on the thesis subject, "Pool Heat Transfer in a Simulated PWR Pressurizer", published in Trans. of ANS, Vol. 46, 1984.

He received a degree of Ph.D. in Mechanical Engineering from M.I.T. in 1988. His Thesis, "Combustion and Atomization Studies of Coal-Water Fuel in a Laminar Flow Reactor and in a Pilot-Scale Furnace", was supervised by Prof. János M. Beér and Prof. Adel F. Sarofim. He authored or co-authored ten related papers on the thesis subject.

In addition to working as a research assistant in the Heat Transfer Laboratory and the Energy Laboratory at M.I.T. for four years, he served as a teaching assistant in the Department of Chemical Engineering.

He expects to complete work on an MBA in the Sloan School of Management at M.I.T. in Dec. 1988. He and his wife Kyung-Hee have a four-year-old daughter, So-Yeun (Janet R.).